MITOCHONDRIA CALCIUM OVERLOAD: WHEN STRUCTURE MEETS FUNCTION

By

Jasiel O. Strubbe-Rivera

A DISSERTATION

Submitted to
Michigan State University
in partial fulfillment of the requirements
for the degree of

Pharmacology and Toxicology—Doctor of Philosophy

2023

ABSTRACT

Heart disease is a leading global cause of death and results in significant economic and healthcare burdens. A critical factor involved is mitochondrial dysfunction induced by calcium overload. This form of dysfunction plays a major role in the injuries that develop from acute myocardial infarctions. Thus, it essential to develop strategies to target these organelles to enhance overall functionality. This thesis examines the critical role of mitochondria in cellular energetics, with a focus on the effects of calcium on mitochondrial structure and function and proposes strategies to advance our understanding.

It is proposed that i) mitochondrial structure is a critical regulator of cellular energetics, and ii) inhibition of oxidative phosphorylation is a calcium-related phenomenon that involves ultrastructural changes. To investigate the mechanisms behind the inhibitory effect of mitochondrial calcium overload on ADP-stimulated respiration, high-resolution respirometry and cryo-electron microscopy were used. The findings show that calcium accumulation leads to the formation of calcium phosphate deposits, outer membrane rupture, inner membrane fragmentation, and evisceration. This results in loss of respiratory control.

High-resolution, cryo-EM images of isolated mitochondria exposed to various conditions designed to elucidate how calcium overload impacts structure and function were collected. From these data, 3D reconstructions were generated for morphometric analysis. The results show that higher levels of calcium can lead to a significant reduction in the density of the cristae network, which ultimately impacts the integrity of the cristae. The impact of calcium phosphate deposits on the mitochondrial matrix is also apparent, resulting in looser and thinner matrices in mitochondria loaded with calcium compared to control or treated-mitochondria with the permeability transition pore inhibitor Cyclosporin A. The study raises questions about the potential link between cristae destabilization and the permeability tran-

sition pore, which can lead to mitochondrial rupture and cytochrome c release.

In addition, a phase separation-based approach was used to study the dynamics of mitochondrial ultrastructure pattern formation, which defined the mitochondrial ultrastructure as a two-component system consisting of the inner membrane space and the matrix space, with the outer membrane serving as the domain boundary. The study mimicked the observed effects of calcium phosphate deposits, where calcium phosphate induces devastating remodeling effects on the inner membrane, resulting in matrix expansion, intermembrane space contraction, and cristae remodeling.

Finally, the thesis discusses a few compound libraries that were screened to find drugs capable of protecting isolated mitochondria from calcium overload and oxidative stress. Eleven compounds passed the initial screening for protection against calcium overload. Future directions for this line of research should expand the drug screening approach to validate the compound hits and investigate the potential for combination therapies using multiple drug candidates. Overall, these findings provide a promising starting point for further research into the development of effective treatments and preventative measures for mitochondrial dysfunction and related diseases.

To my Mom, Dad, and Sister: who have always been my guiding lights and unwavering pillars of support. To my friends: thank you for your unwavering encouragement and faith in me. And to the countless cups of coffee and tobacco bowls that helped fuel my late-night study sessions - this thesis is as much yours as it is mine.

ACKNOWLEDGMENTS

I am deeply grateful to my mentor, Jason, whose unwavering support and guidance made this work possible. Throughout my Ph.D. years, his high standards, keen interest, positive attitude, and timely and scholarly advice pushed me to become better at what I do. Jason, thank you for giving me a home in your laboratory and opening the world of research full of excitement in front of me.

I also want to express my gratitude to my committee members, Drs. Jackson, Lauver, Fink, and Parent, for challenging me every step of the way. Your brilliant comments and suggestions made my defense enjoyable and my future as a scholar more fruitful and full of knowledge.

To the Departments of Pharmacology and Toxicology, Physiology, and the outstanding staff, I extend my sincerest thanks for all the attention and guidance. To the BioMolecular Science and the Broadening Experiences in Scientific Training programs, thank you for believing in me and offering me such a great opportunity. I will forever be grateful.

To the National Institute of Health and the financial support of this research through the NIH F31 Ruth L. Kirschstein Predoctoral Individual National Research Service Award F31HL152623 Fellowship. I am grateful to cryo-EM facility managers, Drs. Parent and Subramanian, for their collaboration and support in obtaining high-quality mitochondrial images. Their expertise was instrumental in the success of this research project, and I am truly thankful for their assistance.

Last but not least, to my family and friends – this journey would not have been possible without your continuous support. Your encouragement and love kept me afloat, and for that, I am eternally thankful.

TABLE OF CONTENTS

LIST OF ABBREVIATIONS

- $\Delta\mu_H$ Electrochemical gradient
- $\Delta\Psi_m$ Mitochondrial membrane potential
- **ΔpH** Proton gradient
- **AA** Antimycin A (complex III inhibitor)
- **AFG3L2** AFG3 Like Matrix AAA Peptidase Subunit 2
- **ALM** Alamethicin (channel forming pepite)
- **ANT** Adenine nucleotide translocator
- **F_1F_O-ATP synthase** Adenosine triphosphate synthase or complex V
- **BKA** Bongkrekate or bonkrekic acid
- **$CaCl_2$** Calcium chloride
- **CAtr** Carboxyatractylate or carboxyatractyloside
- **CoQ** Coenzyme Q (mobile electron carrier)
- **CHE** Calcium/Hydrogen exchanger
- **CH model** Cahn-Hilliard curvature functional model
- **CI** Complex I or NADH-ubiquinone oxidoreductase/dehydrogenase
- **CII** Complex II or Succinate oxidoreductase/dehydrogenase
- **CIII** Ubiquinol-cytochrome c oxidoreductase/dehydrogenase
- **CIV** cytochrome c oxidase
- **CRC** Calcium retention capacity. Amount of calcium the mitochondria uptakes prior to permeabilization
- **Cryo-EM** cryo-electron microscopy
- **Cryo-ET** cryo-electron tomography
- **CsA** Cyclosporin A
- **CypD** Cyclophilin D
- **Cyt. c** Cytochrome c
- **EGTA** Ethylene glycol-bis(2-aminoethylether)-N,N,N′,N′-tetraacetic acid (calcium chelator)

- **EMRE** Essential MCU regulator
- **ETS** Electron transport system or chain
- **F_1** Catalytic component of the F-ATP synthase
- **Fis1** Mitochondrial fission protein 1
- **F_O** F-ATP synthase component residing on the membrane
- **GSK-3β** Glycogen synthase kinase-3β
- **GTPase** Guanosine triphosphatase protein
- **H_2O_2** Hydrogen peroxide
- **HSP90** Heat shock protein 90
- **HK2** Hexokinase 2
- **IBM** Inner boundary membrane
- **IF1** Inhibitory factor 1 protein
- **IMM** Inner mitochondrial membrane
- **IMS** Intermembrane space
- **I/R injury** Ischemia/reperfusion injury
- **JO_2** Respiratory rate
- **KD** dissociation constant
- **kDa** Kilodaltons
- **mCK** Mitochondrial creatine kinase
- **MCU** Mitochondrial calcium uniporter
- **MCUR1** Mitochondrial calcium uniporter regulator 1
- **MDM2** Mouse double minute 2
- **Mff** Mitochondrial fission factor
- **MICOS** mitochondrial contact site and cristae organizing system
- **MICU 1-3** Mitochondrial calcium uptake family
- **Mids** Mitochondria dynamics proteins 49 and 51
- **MitoPQ** MitoParaQuat (ROS inducing drug)

- **MMC** Mitochondria megachannel; also known as mitochondria multiconductance channel
- **MMPs** Matrix metalloproteinases
- **MPT** Mitochondrial permeability transition. Interchangeably used with PTP
- **mtGFP** Mitochondria green fluorescent probe
- **mtCK** Mitochondria creatine kinase
- **NADH** Nicotinamide adenine dinucleotide
- **NCLX** Sodium/calcium/lithium exchanger
- **NDUFS1** NADH:ubiquinone oxidoreductase 75 kDa Fe-S protein 1
- **OMA1** *m-AAA* protease 1
- **OMM** Outer mitochondrial membrane
- **OPA1** Optic atrophy protein 1: dynamin-like GTPase
- **OSCP** Oligomycin sensitive conferring protein
- **OXPHOS** Oxidative phosphorylation
- **PARL** Presenilin-associated rhomboid-like protein
- **PDEs** phosphodiesterases
- **Pi** Inorganic phosphate with the formula $H_2PO_4^-$
- **PiC** Mitochondrial phosphate carrier
- **pmf** Proton-motive force
- **PPIase** Peptidyl-prolyl, cis-trans isomerase
- **PTP** Permeability transition pore
- **QH2** Ubiquinol
- **ROS** Reactive oxygen species (mostly the superoxide anion ($O_2^{-\bullet}$) but also includes other species; hydroxyl radical, non-radical species)
- **RR** Ruthenium red (MCU inhibitor)
- **sAC** soluble adenylyl cyclase
- **shRNA** Short hairpin RNA
- **SIRT** Simultaneous iterative reconstruction technique

- **SIRT3** Sirtuin 3
- **SLC25A23** Solute carrier 25A23
- **SPG7** Spastic paraplegia 7
- **SQ** Semiquinone
- **SR** Sarcoplasmic reticulum
- **State 2** Resting metabolic state: energized mitochondria are supplied with NADH-linked and/or $FADH_2$-linked substrates.
- **State 3** Active metabolic state: energized mitochondria are supplied with ADP to drive the synthesis of ATP consuming high amounts of oxygen in the process.
- **State 4** Resting metabolic state following the synthesis of ATP in the presence of substrates in which the rates of mitochondrial respiration are low.
- **TRAP1** Tumor necrosis factor type 1 receptor-associated protein
- **tBID** BH3 interacting domain death agonist
- **TCA** Tricarboxylic acid cycle
- **TSPO** Translocator protein of 18 kDa
- **UCP1** Uncoupling protein 1 or thermogenin
- **UPR** Unfolded protein response
- **VDAC** Voltage-dependent anion channel
- **VSMCs** Vascular smooth muscle cells

Chapter 1

Perspectives on the PTP: How Did We Get Here?

1.1 Introduction

Cardiovascular disease is often caused by cardiac ischemia/reperfusion (IR) injury, colloquially known as a heart attack. Heart attacks lead to several types of injuries which affect cardiac tissue on different time and spatial scales. One of the most devastating injuries is known as lethal reperfusion injury. I became interested in this type of injury because it is centered on the mitochondria. Surprisingly, there are no effective drug therapies to acutely treat cardiac IR injury; therefore, understanding what governs and precipitates this type of injury is of high importance.

Under normal conditions, myocardial tissue is constantly perfused with oxygenated blood and nutrients. However, anything limiting or impeding myocardial blood flow will lead to oxygen deprivation and make the tissue ischemic. The most common technique to reestablish blood flow is known as percutaneous coronary intervention (PCI). PCI is also known as balloon angioplasty, and it alleviates blockages to allow blood flow through ischemic tissue. However, there is a paradoxical effect following reperfusion whereby more tissue damage is induced. This is called ischemia/reperfusion injury.

There are multiple factors governing tissue damage following reperfusion. Free radical

generation, altered calcium handling, and altered cellular metabolism govern the acute response. Immune activation and microvascular dysfunction constitute the delayed response. These responses precipitate reentrant arrhythmias, myocardial stunning, the no-reflow phenomenon, and lethal reperfusion injury. My thesis focuses on lethal reperfusion injury and specifically addresses how calcium overload disrupts mitochondrial function. Hence, it is relevant to understand how calcium is regulated at physiological levels at the mitochondrial level.

Mitochondria generate cellular energy through the electron transport system ending with the reduction of molecular oxygen to water molecules. This process involves the movement of protons across the inner mitochondrial membrane which generates an electrochemical gradient. This electrochemical gradient is used to generate ATP molecules in a process known as oxidative phosphorylation. Calcium uptake is also driven by this electrochemical potential. To be precise, the electrical component of this energy potential is used by the calcium uptake pathways with the primary pathway in cardiac tissue consisting of the mitochondrial calcium uniporter. Once inside the matrix, calcium accelerates mitochondrial respiration by activating three dehydrogenases in the tricarboxylic acid cycle. During ischemia, myocardial tissue is deprived of oxygen, and mitochondria become unable to sustain high rates of ATP production. Consequently, ion homeostasis breaks down and metabolic pathways are rewired in a futile attempt to sustain mechanical and electrical activity. At this stage, most cell death is necrotic and not apoptotic in nature. However, that all changes upon reperfusion.

During reperfusion, the reintroduction of oxygen to the highly reduced respiratory chain causes a burst of reactive oxygen species production. In the presence of calcium overload, this burst of oxidants triggers the permeability transition phenomenon. This phenomenon causes organelle swelling and membrane rupture and releases pro-apoptotic factors. As

such, the tissue damage is more apoptotic in nature at this stage. While this phenomenon is universally observed in many diseases and organs following IR injury, the mechanism of how calcium disrupts mitochondrial function is not well understood. From the work described in this thesis, it can be shown that calcium overload impairs metabolic function by affecting mitochondrial structure through the formation of calcium phosphate deposits within the mitochondrial matrix in the calcium overloaded state.

For this thesis, I used Hartley albino guinea pigs to measure and quantify mitochondrial function and test the effects of calcium overload on mitochondrial function and structure. Of all the common rodent species used in research, guinea pigs are excellent animal models for studies on heart metabolism for various reasons. First, the action potential of guinea pig ventricular myocytes closely resembles that of humans. Hence, other rodent models lack the pronounced plateau phase present in humans and guinea pigs. Second, calcium handling in the ventricular cardiomyocytes is closer to that in humans than other rodent models. This is, in part, due to the sodium/calcium exchanger playing a bigger role in calcium handling, whereas in other rodent species, the sarcoplasmic reticulum calcium pumps dominate calcium flow patterns. Third, the xanthine oxidase enzyme activity, involved in purine nucleotide breakdown, is very low and comparable to human hearts, whereas in other rodent models, it is highly active. Fourth, the guinea pig heart possesses a full complement of inhibitory factor 1 (IF1), an extremely relevant protein in IR injury, whereas rats and mice do not possess a full complement. Overall, the guinea pig heart has more similarities to humans than other typical rodent models used when it comes to calcium handling, myosin isoform expression, purine nucleotide metabolism, and myocardial function. Thus, it is a suitable candidate for these kinds of studies. However, this does not come without limitations, as I will address in our discussion.

My thesis explores how calcium overload impairs mitochondrial ATP production and bioenergetics which striking ultrastructural changes are also observed. It argues that mitochondrial structure is a critical regulator of cellular energetics, and the proteins and biophysical mechanism responsible for fine tuning ultrastructure are suitable drug targets capable of circumventing current therapeutic limitations. This Chapter provides a historical overview of the elusive permeability transition phenomenon, while Chapter 2 introduces the concept of calcium in mitochondrial structure and its impact on function. To complement this analysis, Chapter 3 examines the effects of calcium at the structural level using cryo-electron microscopy, and Chapter 4 provides a computational perspective on mitochondrial structure and function.

Chapter 5 delves into the impact of calcium overload at the cristae level, demonstrating how changes in structure can alter function. It also explicitly highlights the belief that calcium overload observed during acute myocardial infarction damages mitochondrial function by altering its structure, mainly due to the formation of calcium phosphate deposits that destabilize the cristae structures. Finally, Chapter 6 reports the results of a small, 5,000-compound library screened for cardioprotection against calcium overload and oxidative stress. Despite the availability of such drugs on the market, none are currently used from a mitochondrial pharmacological intervention standpoint.

Overall, this thesis lays out a project that provides a deeper understanding of the important aspects that govern mitochondrial function and ultrastructure. Given the prevalence of multiple diseases arising from mitochondrial calcium overload, developing strategies to target mitochondria to enhance overall functionality in this condition is crucial. That said, achieving this goal requires a thorough understanding of mitochondrial behavior under various conditions which can be challenging given the dynamic nature of biological systems and

the limitations of current technologies.

1.2 Role of PTP in disease

In this chapter, I review insights on the molecular candidates thought to form the permeability transition pore (PTP) phenomenon, their nature, and validated observations. The aim of this text is to provide information on the influential experiments that supported the hypothesis of certain molecular components. At the same time, I will examine the work of those who contested those hypotheses. And, while this layout holds for most of the scenarios therein, at the writing of this thesis chapter there are some molecular candidates yet to be (dis)proven and currently undergoing intense scrutiny. My proposal is that pore formation can be, to some extent, explained by changes in the mitochondrial structure leading to mitochondrial swelling, cristae destabilization, and membrane rupture. In essence, the goal of this chapter is to provide an overview on the permeability transition phenomenon which includes its role in disease, molecular discoveries, and the proposed models. I will also discuss how these PTP models shifted over time due to their inability to withstand rigorous experimental scrutiny.

When it comes to disease-associated perturbations, the PTP is in front of many pathologies including, but not limited to, Alzheimer disease, Parkinson's disease, optic atrophy factor 1 (OPA1), mitochondrial DNA disorders, multiple sclerosis, and cardiovascular diseases such as heart failure [1–7]. All of which have been extensively reviewed elsewhere [1–7]. My discussion will be focused on heart failure in the context of myocardial ischemia and reperfusion (IR) injury. The onset of IR injury is of high relevance in a clinical setting where high mortality rates and long-term organ dysfunction are observed. Injuries encompass acute coronary

artery syndrome, cerebrovascular and acute kidney injury, among others [4]. In this line myocardial IR injury is a pathological manifestation centered on the mitochondria. While the events leading to tissue injury have been reviewed elsewhere, they are briefly summarized below [8, 9]. During ischemia oxygen levels in the tissue are low to non-existent removing the electron transport system (ETS) from the equation as the main source of ATP supply to maintain cellular functions. During an ischemic insult the cytosol acidifies, and calcium levels become dysregulated. Under normal conditions, the levels of calcium are regulated between 100 nM and 1 μM by the sarco/endoplasmic reticulum Ca^{2+}-ATPase (SERCA), the plasma calcium ATPase (PMCA), and the Na^{+}/Ca^{2+} exchanger (NCLX). However, during ischemia when ATP levels are low, calcium becomes dysregulated and soars into overload conditions [10]. While there are pathways and reactions that can generate ATP during ischemia (e.g., glycolysis and creatine kinase), these ATP production pathways either run out of fuel or become impaired during long durations of ischemia. Consequently, the $\Delta\Psi_m$ collapses and NADH and $FADH_2$ accumulation near maximally reduce the ETS. In attempts of regulating the mitochondrial membrane potential ($\Delta\Psi_m$), the F_1F_O-ATP synthase reverses and further consumes ATP generating ADP + Pi as a byproduct [11]. Overflow of fumarate from the purine nucleotide breakdown and the succinate dehydrogenase (SDH) reversal exacerbates the ischemic succinate accumulation. At this stage most of the tissue damage is necrotic in nature and less associated with calcium overload [12–14]. This, in part, is due to the loss of $\Delta\Psi_m$ required to drive calcium into the mitochondria. The mitochondrial and cellular acidification inhibits the PTP activity [15, 16]. During reperfusion, oxygen levels and the $\Delta\Psi_m$ are restored. Thus, allowing mitochondria to switch from ATP consumers to ATP producers once more. The highly reduced ETS combined with succinate accumulation leads to the generation of reactive oxygen species (ROS) [14, 17]. This in combination with pH restoration

and rapid and energetically driven calcium accumulation into the mitochondria triggers the mitochondrial permeability transition pore (PTP) [15, 16]. This phenomenon is known as the oxygenation paradox in which reoxygenation of the ischemic tissue causes damage that far exceeds the tissue injury observed during ischemia. Most of the tissue damage and cell death following reperfusion is attributed to acute and delayed responses. The acute response is more apoptotic in nature whereas the delayed response further exacerbates tissue damage following the influx of inflammatory cells and complement proteins. Hence, understanding the PTP phenomenon and the relationship between ROS production and calcium overload remains a relevant topic of investigation and physiologically important [18].

1.3 The History of the PTP Concept

The permeability transition pore (PTP) is a term coined by Haworth and Hunter in 1979. However, mitochondrial calcium overload and what is now recognized as "pore-like" behavior has been a subject of vigorous debate for the last 60 years. Although different molecular models have been suggested, none have withstood the examination provided by genetic ablation. Originally, it was thought to be an artifact from experiments; however, it soon became known that his phenomenon holds physiological significance. The classical view of the PTP concept is that is a calcium-dependent phenomenon where swelling is observed. Some examples were shown in isolated rat heart muscle sarcomeres and isolated cow and rat heart mitochondria incubated in sucrose buffer with high calcium content and phosphate [19–21]. In these experiments a rapid decrease in light scattering was followed by a slower and gradual decrease. The rapid drop in light scattered is characterized by mitochondria swelling very rapidly due to rapid diffusion of sucrose across the opened membranes when chal-

lenged with calcium. This sudden decrease in scattering is also referred to as high-amplitude swelling, which is considered the benchmark for identifying the PTP opening. The gradual drop in light scattering reflects the diffusion of sucrose through narrower pores. However, this could be attributed to gradual pore opening in the more Ca^{2+}-resistant subpopulation of mitochondria. This reflects the heterogeneous nature of the mitochondrial population response to PTP activity following a calcium challenge. Later, it was discovered mitochondrial swelling was stimulated by elevated Pi, oxidative stress, and fatty acids and prevented by adenine nucleotides (including ADP) and cations such as Mg^{2+}, Sr^{2+}, Mn^{2+}, and Ba^{2+} [22]. Altogether, the PTP phenomenon is preceded by mitochondrial swelling and calcium is a prerequisite for its opening. During the initial stages of research, Haworth and Hunter proposed that mitochondrial swelling could be a regulated proteinaceous channel. Later in 1990, Halestrap and Davidson showed similar activity in which a high-conductance channel was activated by very high calcium concentrations. Around the same time, Szabó and Zoratti relied on patch clamp experiments and detected multiple conductive states inhibited by cyclosporin A (CsA) [23]. Eventually, this effect was shown to be mediated by the matrix receptor peptidyl-prolyl *cis-trans* isomerase cyclophilin D (CypD) which strengthened the hypothesis of a giant channel or pore forming unit that controls the phenomenon. Halestrap and Davidson termed this channel the mitochondrial megachannel (MMC; also referred as the multiple conductance channel) with conductance substates below a maximum of 1.3 to 1.5 nS [23]. Szabó and Zoratti further concluded that the activity attributed to the MMC and the PTP where the one and the same [24, 25]. Zoratti's group included a genetic mouse model lacking the CypD *Ppif* gene in later experiments. Despite the absence of this gene, the mitochondria still demonstrated Ca^{2+}-induced PTP opening, although at higher concentrations of calcium compared to wild type. Here, it was shown that mitochondria from the

Ppif$^{-/-}$ mouse model do not exhibit PTP inhibition by CsA [26]. Thus, providing evidence for CypD not as a molecular component but rather a PTP modulator. The significance of CypD in more recent hypotheses will be discussed later. Experiments conducted in 1996 showed a transient-like pore, thus potentially functioning as a gate for the release of calcium. All of which defined the bona fide PTP boundaries and its definition. In today's literature the PTP is a proteinaceous pore thought to form in the inner mitochondrial membrane (IMM) and is permeable to solutes of up to 1.5 kDa in size [27]. Afterwards, agents that promote PTP were discovered, which were found to work in synergy with pathophysiological calcium levels including reactive oxygen species (ROS), Pi, membrane de-energization, and matrix pH alkalinization. Regulators were also identified, acting on various sites of the mitochondria, such as ATP-synthase reversal and inhibition, and ETC complexes. Additionally, pore inhibitors such as ADP, Mg^{2+}, and acidic matrix pH were discovered. The discovery prompted the proposal of several models and mechanisms featuring candidate pore-forming units. Nevertheless, the molecular identity of the pore remains a mystery. Following this, I will explore the present models and pore modulators, starting with an overview of the mitochondrial proteins and the experiments that gave rise to many of the speculative models described in current literature. It is important to note that most of these models have not been established as fact. In this chapter, I will examine the studies that contest the proposed models and put forth an alternative perspective that emphasizes the impact of structural alterations on mitochondrial function.

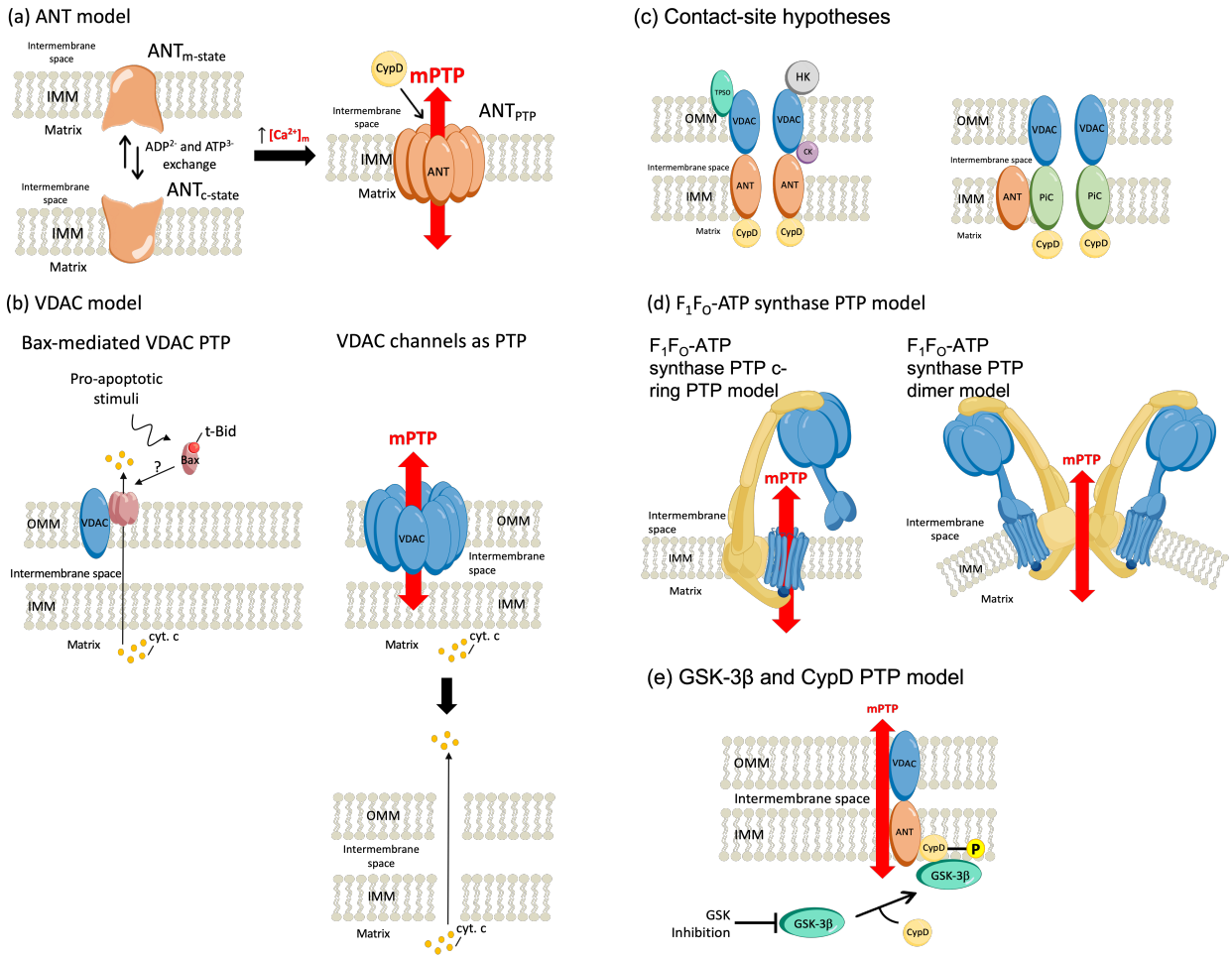

Figure 1.1: Cartoon representations of the prevalent permeability transition pore models.

1.4 Proposed Models for the PTP

The ANT as a Pore Component

The first proposed molecular component of the PTP was the adenine nucleotide translocator (ANT) as shown in **Figure 1.1a** [23]. The ANT family is a group of transporters and the most abundant protein of the IMM. It controls the exchange of ADP and ATP between the mitochondrial matrix and IMS against a large electrochemical potential generated across the IMM by exchanging nucleotides in a "ping-pong" type kinetic mechanism [28]. The negatively charged nature of adenine nucleotides is compensated by the electrostatic prop-

erties of the binding residues in the main substrate-binding site of the ANT. A recent study suggests three positively charged residues (K30, R88 and R287) serve as counter charges to achieve substrate specificity to neutralize the negative charges of ADP^{3-} and ATP^{4-} and reorient substrates during translocation [28]. The repulsion of these positive charges poses a high energy barrier when ANT is unoccupied. Upon substrate binding, the charge neutralization lowers the energy barrier and effectively minimize the electrophoretic forces during transport to allow proper nucleotide translocation [28]. Multiple ANT isoforms exist with gene expressions varying between organisms and tissue specificity. For instance, the human mitochondria contain 4 ANT isoforms (ANT1 – 4), whereas rodents express 3 genes (ANT1, 2, and 4) [22]. When it comes to tissue specificity, ANT1 dominates in skeletal muscle and heart mitochondria. Whereas ANT2 dominates most of the other tissue and organs (particularly liver and brain) and ANT4 is restricted to the sperm flagellum [29]. The nucleotide movement by the monomeric carriers is achieved by cycling between two open states: (i) the matrix-state (m-state) and (ii) the cytosolic-sate (c-state) (**Figure 1.1a**). In the m-state, the matrix nucleotide binding site is exposed making the binding site facing the IMS unavailable. Whereas on the c-state, the cytosolic nucleotide binding site allows the exchange of nucleotides towards the IMS. The involvement of the ADP/ATP carrier, also known as the ANT, as a crucial regulator of PTP has been well-documented in the literature since 1979. Studies by Haworth and Hunter shed light on the role of the ANT in the Ca^{2+}-induced transition state [30]. Two mitochondrial morphologies were observed following electron microscopic imaging: the "orthodox" and the "aggregated" form. Samples with lightly stained and swollen matrices were classified to have an orthodox form, whereas darkly stained and condensed were classified to have an aggregated form. Mitochondria in the orthodox form were characterized by having low cristae densities. In this form, mitochondria are uncoupled

and unable to generate ATP. In contrast, the aggregated form contains condensed matrices and are well-coupled and able to synthesize ATP. This pertains to the preservation of the cristae structure, which enables the ATP synthase and respiratory chain units to work in closer proximity with minimal diffusion barriers. While looking at the effect of PTP opening by uncouplers, ionophores, and NADH oxidizing agents, Hunter and Haworth noticed that the ANT inhibitors atractylate (ATR) and bongkrekate (BKA) regulated the Ca^{2+}-induced transition state in a reciprocal manner. Specifically, ATR increases PTP opening while bongkrekate (BKA) inhibits it. This was significant at the time given it placed the PTP as a physiological significant phenomenon due to the cell flexibility in regulating PTP activity [30]. The ANT hypothesis solidified in 1996 when Brustovetsky and Klingenberg purified the ANTs, using hydroxyapatite exclusion chromatography, and reconstitute them in liposomes followed by patch-clamp analysis [30, 31]. This revealed that ANT generates conducting channels in the order of 300 – 600 pS in a Ca^{2+}-dependent manner as observed previously [31]. The effect of ATR promoting Ca^{2+}-activated PTP and BKA its inhibition, potentiated by ADP, were observed. However, the unique interaction of BKA with ANT, along with the consistent *bona fide* PTP activity, led Brustovetsky and Klingenberg to concluded that the ANT was a component of the PTP. Similar conclusions were reached by others [32]. While the mechanisms for PTP opening seemed promising, the proposed models of pore assembly started to fall short when challenged with genetic models [33]. The ANT as a pore component came into question by Kokoszca et al., in 2004 when isolated liver mitochondria lacking ANT1/2 isoforms still showed PTP activity [34]. And while higher levels of Ca^{2+} where needed to induce pore activity, ANT-deficient mitochondria displayed CsA-induced PTP inhibition and higher cytochrome c (cyt. c) content release. Hence, Kokoszca et al., concluded that ANT is not an essential component but rather a regulator of the pore. However, as

discussed above, mice possess 3 *Ant* genes (*Ant1*, *Ant2*, *Ant4*) which raised questions as to whether other *Ant* genes could compensate in the original knockout models. More recently, Karch et al. generated a double ANT1/ANT4 knockout model with a conditional, liver specific ANT2 knockout. While these models where resistant to PTP, large amplitude swelling was still observed at higher calcium loads in a CsA-sensitive fashion [35]. Similar results were shown in quadruple gene-deleted mice additionally lacking the *Ppif* gene that encodes CypD (a target of CsA). As expected, these mitochondria where resistant to Ca^{2+}-induced PTP opening. They concluded that the data supports a "multi-pore model" in which PTP is composed of *at least* two components. However, the data conflicts with the proposal given that the triple ANT knockout models still responded to ADP addition and wild type traces of oxygen consumption rates, along with membrane potential analysis and swelling assays, were not included (referring the reader to ref. [35] Supplemental Figure 1B). Here they concluded that the ANT function could be compensated by the mitochondria by another *Slc25a* family member.

VDAC Joins the PTP Model as a Component

In the early 1990s, Szabó and Zoratti's experiments led them to propose the pore was made up of voltage-dependent anion channel (VDAC) molecules (**Figure 1.1b**) [36]. At the time this sounded promising given VDAC is the most abundant outer mitochondrial membrane (OMM) protein. And when it comes to mitochondrial bioenergetics, its role is essential. VDAC controls the flux of small solutes, metabolites, and protein diffusion. There are three mammalian isoforms VDAC1 – 3; with VDAC1 mostly expressed in cardiac mitochondria. While VDAC allows the movement of cations, it preferentially allows anions to flow through. This is significant given the anionic nature of most metabolites. This effect

is attributed to the electrostatic environment of the channel (charged channel walls) and the conformational changes induced to the channel by the passing metabolites [37]. The channel has a 1.8 or 2.5 nm diameter in its open or closed state, respectively [37]. Ion flux through VDAC is tightly regulated by an electrical potential that controls VDAC channel opening and closing. It is fully opened at voltages of 0 mV and preferentially moves inorganic anions over cations. Whereas higher voltages favor the closed state and preferentially moves cations over inorganic anions [38]. However, given the aqueous pore size some suggest it has evolved to control metabolic fluxes in and out of the mitochondria, particularly ATP and ADP [37]. ATP flux studies performed in VDAC reconstituted in liposomes showed that the open probability linearly increases at greater ATP concentrations [37]. Hence, VDAC serves as a gatekeeper for biochemical function and compartmentalizes signaling events between the cytoplasm and mitochondria. Shortly after the proposal of the VDAC model, multiple experiments provided evidence that ANT and VDAC copurify with the translocator protein (TSPO), also known as peripheral benzodiazepine receptor [39]. A second study looking at the effect of benzodiazepines targeting TSPO show the ability to inhibit permeability transition pore opening and suggested the ANT-VDAC-TSPO complex is associated with the contact-site hypothesis [40]. The idea of the contact site hypothesis emerges from protein-protein interactions between the outer membrane protein VDAC and inner membrane protein ANT. At the time, this was of relevance given the PTP was attributed to this interaction and a third unknown component (later attributed to CypD or other proteins). This model is accredited to Le Quoc, Halestrap, and Crompton's work [41–43]. Studies by Crompton et al. in 1996 were the first to show that CsA inhibits pore activity. CsA was also key on identifying CypD as a potential pore component. CypD is a mitochondrial matrix protein of ∼22 kDa consisting of a sequence of 207 amino acids that is further cleaved to a ∼19 kDa

protein in the mitochondrial matrix with a cyclophilin domain that imparts the peptidyl-prolyl *cis-trans* isomerase (PPIases) activity [24, 44]. Its activity is conserved across the cyclophilin gene family and many organisms within the eukaryotic and prokaryotic kingdom [24]. Inspired in the findings of Fournier et al. and Jung et al., Crompton et al. confirmed and extended that CsA inhibits a Ca^{2+}-dependent pore in the IMM [24, 45]. This matched quite well with the *bona fide* PTP activity. Indeed, several studies confirmed CsA interaction with CypD abrograted PTP opening. This suggested that CypD was the pore component by interacting with the pore regulator ANT [23, 46–48]. The strongest case for CypD as a pore component came from the *Ppif* genetic knockout mice model where mitochondria resisted swelling and PTP opening in Ca^{2+} overloaded states, ROS, and cardiac I/R-induced injury [46]. These findings also made the distinction that while PTP inhibition is not closely related to cellular apoptosis, it does not exclude its participation given that CypD knockout models prevented Ca^{2+}- and ROS-induced cytochrome c (cyt. c) release [46]. A distinction that is made in the literature by some is that PTP opening is mediated by necrosis and not apoptosis [46, 49]. This idea came from genetic CypD knockout studies showing the lack of involvement of proapoptotic factors, i.e., the Bcl-2 family, during Ca^{2+}-induced PTP activity [49]. Despite this evidence, earlier studies showed that proapoptotic factors interact with PTP regulators including VDAC and the ANT to regulate apoptotic events and cyt. c release [50–53]. Hence, both apoptotic and necrotic signaling events should be considered and valid when PTP is concerned. A CypD deficient model showed a lack of caspase activity while conferring protection from I/R-induced injury. This effect is exacerbated when overexpressed [54]. Similar conclusions were reached by others which strengthened the CypD hypothesis as a PTP component [55]. When it comes to VDAC, it has been shown to interact with Bax to form large non-selective conducting channels of 1.8 to 2.3 nS (**Figure 1.1b**) [56]. This was

of relevance as it matched the *bona fide* conductance state ranges for pore formation. This idea connected well with the notion that cell death by the pro-death Bcl-2 family member Bax was directly related with pore formation. However, a recent report in *Vdac*1-, *Vdac*3- and *Vdac*1 – 3-null mice yet exhibited calcium tolerance, oxidative stress, cyt. c release, caspase release and PTP activity similar to wild type animals [57]. Furthermore, mouse models lacking VDAC still exhibited cell death in a Bax dependent fashion. Altogether, these results suggest that VDAC function for PTP activity and pro-apoptotic signaling is dispensable and it serves a modulatory role for the so-called pore opening. It did not take long to test this mode of regulation with known models in attempts of unifying previous observations.

The Contact-Site Hypothesis

As such, the contact-site hypothesis started emerging as a strong candidate for the PTP phenomenon. This work is mainly attributed to Le Quoc, Halestrap, and Crompton's work [41–43]. Studies by Crompton in reconstituted proteoliposomes from VDAC, ANT, and CypD, from rat heart mitochondria, revealed an apparent triprotein complex whose binding is unaffected by calcium and a 10-fold CsA treatment (**Figure 1.1c**) [42]. Despite this, proteoliposomes displayed PTP activity, sensitive to CsA inhibition, when exposed to calcium and phosphate. Interestingly, either calcium or phosphate did not induce PTP activity by themselves. This begs the question whether calcium phosphate precipitation takes place and disrupt the interaction of these proteins to induce PTP opening. The idea of calcium phosphate precipitates, however, will be of relevance later in **Chapters 2**, **3**, and **4**. Others suggested that the mitochondrial creatine kinase (mCK), hexokinase II (HKII), and translocator protein (TSPO) stabilize the VDAC and ANT channel in conjunction with

CypD (**Figure 1.1c**) [58]. However, conditional knockouts of TSPO and genetic deletion of all VDAC isoforms, in mice and fibroblasts, still exhibited calcium induced-PTP [57, 59, 60]. By the same token, genetic loss of function studies on *CypD* knockout models classified CypD as pore modulator but not essential for PTP formation [24]. Evidence for CypD as a pore modulator came from knockout models where mitochondria displayed a remarkable ability to withstand high amounts of calcium and its uptake prior to permeabilization [61].

The PiC Link to the PTP

Shortly after the contact-site hypothesis, Herick et al. show that the phosphate carrier (PiC) was able to generate Ca^{2+}-dependent currents [62]. The PiC is a ∼31 – 34 kDa size mitochondrial solute carrier that is a part of the solute carrier family SCL25A that includes the ANT, oxoglutarate carrier, and uncoupling proteins, citrate carrier, mitoferrins, among others [63–66]. It catalyzes the movement of Pi/H^+ symport (or Pi/OH^-) and Pi/Pi antiport in an electroneutral fashion across the IMM [63, 64]. The mammalian phosphate carrier has two isoforms (PiC-A and PiC-B) that share a common 6 helix structure with conserved motifs [67]. Isoform A predominates mostly in the heart, diaphragm, and skeletal muscle [63]. Whereas isoform B is ubiquitous and expressed in all tissues. The less than 30 % difference comes from the alternative exon 3A splicing affecting amino acids 4 – 45 from the total sequence comprising the PiC. Hence, alternative splicing determines and explains the divergence in affinity and transport activity between the isoforms. When it comes to Pi affinity, the isoform PiC-B has ∼3-fold higher affinity than PiC-A [63]. A recent study suggests that the ubiquitous expression of PiC-B and its affinity for Pi allows the anion handling in high energetic tissue. Such that when this system saturates, at increasing Pi levels, PiC-A Pi affinity activates the carrier to continue compensating the energetic demand [63].

Following the experiments by Herick et al., in 1997, Halestrap's group proposed a model for PTP whereby the PiC undergoes conformational change upon calcium exposure facilitating binding to CypD [62, 64]. The PiC-CypD interaction was CsA-sensitive which may or may not include ANT binding, depending on the isoforms described earlier (**Figure 1.1c**). Phosphate has been shown to possess potent PTP opening properties, and overexpression of the PiC has been observed to trigger apoptosis [68, 69]. However, according to other studies, Pi is a PTP inhibitor [70]. Leung et al. suggested the PiC may be a critical component of the PTP and proposed a model whereby CypD interacts with PiC to induce pore opening (**Figure 1.1c**) [64]. However, PiC from *Saccharomyces cerevisiae* reconstituted into giant liposomes have a conductance of 25 ± 5 and 40 ± 10 pS in the presence and absence of divalent cations, respectively [62]. The conductance of the channel formed by the PiC is about 50 times too low to account for the PTP. Additionally, $PiC^{-/-}$ mice display similar oxygen consumption rates and Ca^{2+}-induced PTP relative to the non-transgenic mouse models [71]. Altogether, these results suggests that PiC is not an essential component of the PTP phenomenon. The field has since become static following the genetic ablation studies that harpooned the old consensus PTP models. The latest PTP models now include F_1F_O-ATP synthase.

The F-ATP Synthase

The F_1F_O-ATP synthase, also known as complex V, is a 600 kDa multisubunit complex in charge of producing and consuming ATP based on the mitochondrial energetic demand. It is composed of a catalytic part (F_1) and a membranous component (F_O) connected by a central and peripheral stalk (**Figure 1.2**) [72]. The mammalian F_1 consists of a catalytic $\alpha_3\beta_3$ domain arranged alternately and connected internally to the rotatory central stalk γ. At the

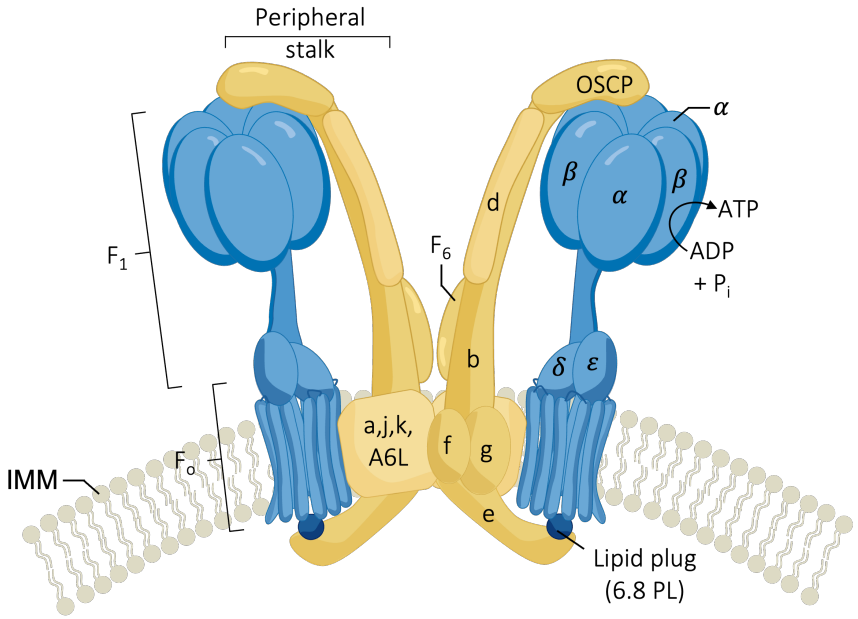

Figure 1.2: Cartoon representation of the F_1F_O-ATP synthase structure. Updated model adapted from Bonora, Giorgio, and Pinton [59].

bottom, the central stalk interacts with the F_O inner mitochondrial membrane-embedded complex c-ring subunits through subunits δ and ϵ [73]. The F_O domain is comprised of subunits e – g, and A6L embedded in the inner mitochondrial membrane and one copy of subunits a, b, d, F6 and the oligomycin sensitivity-conferring protein (OSCP) [73]. The latter subunits (a, b, d, F6, OSCP) form the peripheral stalk in one side of the complex and it is thought to serve the purpose of a stator countering the rotatory movement upon ATP synthesis/hydrolysis termed "rotatory catalysis" [73]. Briefly, the pumping of protons established an electrochemical gradient ($\Delta\mu_H$) across the IMM. It can be broken up into two components: the electrical potential ($\Delta\Psi_m$) and the pH gradient (ΔpH). Together, when expressed in mV units, these two components sum up to what we call the proton motive force (pmf). The pmf is the ($\Delta\mu_H$) but in voltage units instead of units of Gibb's free energy (joule/mol). The potential energy generated from the electrochemical gradient powers the rotation of the c-ring subunits within the F_O domain and the central stalk

allowing ATP to be synthesized/hydrolyzed within the β subunits of the F_1 domain [73]. This catalysis requires the $\alpha_3\beta_3$ domain to remain static relative to the c-subunit ring which is achieved by the peripheral stalk. The synthesis of ATP requires ADP and inorganic phosphate (Pi:H_2PO^{4-}) binding whereas its hydrolysis requires and yields the opposing reaction. When conditions are unfavorable (i.e., wasteful hydrolysis of ATP), the inhibitory protein IF1 binds to the ATP synthase to halt its activity at the expense of $\Delta\Psi_m$. IF1 interacts as a homodimer with the F_1 ATP synthase catalytic sectors through subunits β and γ with increasing effectiveness at lower pH values. Hence, it plays a protective role in pathophysiological conditions as those observed in cerebral, myocardial, and kidney during hypoxic ischemic insults [74, 75]. Interestingly, the levels of IF1 expression can vary by tissue level, with the heart tissue having one of the highest. Therefore, the expression variability of IF1 might dictate the extent or degree of protection that occur on different tissues [74].

F-ATP Synthase Dimers, Oligomers, and Cristae Structures

The F_1F_O-ATP synthase forms dimeric and oligomeric arrays in the inner mitochondrial membrane stabilized by IF1 [72]. The assembly of two identical monomers forms V-like shape dimeric structures that provides stabilization to the complex, facilitates ATP synthesis, and shapes the inner mitochondrial membrane [73, 76]. The dimeric assembly can then organize into oligomeric arrays across the IMM giving the membrane its shape and the apex of the cristae its typical curvature. Interestingly, various PTP models of the ATP synthase have been proposed. This is interesting given that cristae formation is highly dependent on the F_1F_O-ATP synthase membrane organization. IF1 also regulates mitochondrial structure and function. This was observed on a recent study looking at IF1 overexpression, or lack thereof, in a population of cells cotransfected with a mitochondrial green fluorescent probe (mtGFP)

using electron microscopy [74]. It was observed that mitochondria in the absence of IF1 had disorganized cristae structures whereas in its presence mitochondria displayed densely packed cristae structures relative to control [74]. In addition, IF1 was shown to modulate F_1F_O-ATP synthase at rest by increasing the proton flux and NADH oxidation [74]. Altogether, these results suggested that alterations in the F_1F_O-ATP synthase structure and activity can destabilize structure and function. However, additional evidence suggests that the ATP synthase enzymatic activity is also regulated by the CypD.

CypD and its Relationship with the F-ATP Synthase

As previously mentioned, CypD is the only generally accepted modulator of the mitochondrial PTP. Hence, the field focused on possible interaction with the ATP synthase. To understand recent models of CypD and ATP synthase on regulating pore activity, I will discuss CypD regulation on the ATP synthase at a structural level. Recent evidence suggest CypD regulates scaffolding function to effect changes in mitochondrial physiology [44]. Initial experiments seeking answers on CypD interactions with complex V showed that CypD binds to F_1F_O-ATP synthase oligomers through its interaction with subunits OSCP, b, and d from the peripheral stalk and decreases the enzymatic activity of the complex [72]. The inhibitory effect was potentiated by Pi and reduced by CsA. The effect of Pi inhibition might come from conformational changes upon binding to the catalytic site of the F1 subunit. Whereas CsA presumably displaces CypD from the OSCP subunit favoring ATP synthesis. The involvement of the lateral stalk and CypD is intriguing given that the former stabilizes the rotation of the F_1F_O-ATP synthase and dimeric and oligomeric assembly in an IF1 independent fashion. Hence, the authors speculated that CsA might enhance oligomerization explaining the increased activity of the F_1F_O-ATP synthase. Subsequent studies, investi-

gating the effect of CsA on isolated rat kidney or liver mitochondrial respiration, found CsA can inhibit energized mitochondria fed with complex I and II substrates following an ADP bolus [24, 77]. Although CsA appears to inhibit respiration in a concentration-dependent manner, our group and others have reported similar maximal ADP-stimulated respiration responses between mitochondria treated with CsA and those not treated with CsA [78, 79]. Discrepancies on these measurements with our results might be due to the mitochondrial protein quantity or CsA concentration. In agreement, the capacity of CsA to accumulate higher loads of calcium prior to PTP has been observed and well-documented by our lab and others [78, 79]. Recently, the paralogue of the heat shock protein 90 (Hsp90) tumor necrosis factor receptor associated protein 1 (TRAP1) was shown to form a complex with CypD and subunits α, β, γ, d, g, and OSCP of the F_1F_O-ATP synthase [61, 80]. TRAP1 is mainly restricted to mitochondria, exerts its chaperone activity using ATP, and, while highly expressed in tumors, its expression in normal tissue is low [81]. While its physiological function is still in the nascent stages, TRAP1 has been linked in mitochondrial dynamics regulation, mitophagy and antioxidant capacity [82]. Recently, TRAP1 has been associated with controlling PTP opening where its inhibition or downregulation led to cell death, apoptogenic factor release, and membrane potential collapse [61]. Furthermore, the TRAP1/CypD complex was shown to be inhibited by CsA and p53 but not with agents that abrogate its ATPase activity [61]. Given that TRAP1 interacts with CypD and binds to several subunits of the F_1F_O-ATP synthase, this begs two questions 1) whether the complex disruption between TRAP1 and CypD are inhibited by competitive binding between p53 and CsA and 2) whether the protective effects of TRAP1 on PTP activity are exerted by binding to CypD and inhibiting the latter binding to the F_1F_O-ATP synthase.

F-ATP Synthase as a PTP Component

In recent years, several models have been proposed that link the F_1F_O ATP synthase to the pore. One of the earlier models, put forth by Giorgio and Bernardi et al., suggested that F_1F_O ATP synthase dimers constitute the pore (**Figure 1.1d**) [83, 84]. A newer model from Mnatsakanyan and Jonas et al. proposes that a single F_1F_O ATP synthase can produce the pore by detachment of the c-ring subunit of F_O from F_1 to form an aqueous pore (**Figure 1.1d**). This model was later updated by Gerle, who proposed a "death-finger" mechanism involving the displacement of a lipid plug embedded in the center of the c-ring [85]. According to Gerle's model, this plug dissociates from the enzyme when Ca^{2+} binds to subunit β of F_1, a process that is enhanced when CypD binds to the OSCP subunit [22, 85]. Another PTP model involves a tripartite protein complex consisting of the tumor suppressor p53, CypD, and IF1 [22]. However, this tripartite model was later discredited [72]. Altogether, various models of F_1F_O-ATP synthase were proposed and updated to constitute the pore. However, only the mono- and dimeric mode of pore regulation were mostly accepted. The F_1F_O-ATP synthase also interacts with the PiC and the ANT (and mtCK in striated myocytes) to form the "ATP synthasome" [86]. Protein binding occurs adjacent to the F_O domain in a 1:1:1 F_1F_O:PiC:ANT stoichiometry [87]. In addition, the oligomeric assembly of synthasomes elongates tubular cristae structures [86, 88]. This assembly is thought to increase the efficiency of ATP production. From a bioenergetic standpoint, these protein-protein interactions could enhance energy transfer rates in an on-demand basis [86]; however, these complexes could increase protein subunit stability via hydrophobic interactions. Another perspective includes cristae-mediated protein interactions that enhance ATP synthesis via kinetic and thermodynamic arguments [86, 89–91]. This idea goes accordingly with the

proposed respirasome assembly in which certain complexes of the ETS interact with each other to form super complexes. The super complexes are the assembly of mitochondrial respiratory complexes I, III, and IV into a bigger complex of varying stoichiometry. The stoichiometry I:III_2:IV_n ($n = 1 - 4$), also known as the synthasome, is commonly discussed [92, 93]. However I:III_2 and III_2:IV_n ($n = 1$ or 2) are not rare [94]. These complexes are presumed to increase the ETS efficiency and lowers ROS production [95]. While the existence of these types of supercomplexes is intriguing, we do not have the necessary data to conclude that they are indeed functionally relevant. Recent studies suggest the regulation of synthasome assembly by CypD. The synthasome is a macromolecular complex thought to play a critical role in oxidative phosphorylation (OXPHOS) by facilitating the interaction between respiratory complexes and ATP synthase. Using the mouse heart homogenates and the blue native gel technique, Beutner et al. found that the opening of the mitochondrial PTP disrupted synthasome formation, whereas promoting OXPHOS or removing CypD maintained the integrity of the synthasomes [86]. This suggests that CypD is a key regulator of PTP activity and thereby influences the formation of the synthasome complex. This led them to propose that CypD is a master regulator of PTP activity. CypD interaction can be modified through post-translation modifications to regulate PTP opening. Studies led by Miura et al. showed that inactivation of glycogen synthase kinase-3β (GSK-3β) inhibits PTP opening and protects the cardiomyocytes against reperfusion-induced necrosis [96]. Miura et al. suggests that phosphorylation of the GSK-3β might suppress the ANT-CypD interaction. The mechanism involves phosphorylated GSK-3β interaction with ANT and not with CypD. However, studies on tumor cell lines including epithelial prostate RWPE-1, osteosarcoma SAOS-2, and metastatic prostate cancer DU145 cells, show that GSK-3β phosphorylates CypD and promotes PTP opening [97]. Whereas inhibiting GSK-3β protects from PTP activity [97]. This

mode of inhibition will be relevant in **Chapter 6** when discussing therapeutic strategies. Parks and colleagues conducted a study using a mouse model with a mitochondrial calcium uniporter (MCU) knockout, in which increased phosphorylation of serine residue 42 (CypD-S42) on CypD sensitizes PTP opening to calcium [98]. Hurst et al. further evaluated CypD phosphorylation on PTP opening using HEK cells lacking endogenous CypD and rescued with either a wild type or a serine to alanine CypD S38-43A mutant [99]. In this study S191A, and not S38-43A mutations, completely abolished phosphorylation and increased the calcium uptake threshold before PTP opening. Thus, suggesting the S191A mutant gives similar protection as the CypD inhibition in the regulation of pore opening [99]. The authors proposed a model in which the S191 residue phosphorylation through GSK-3β induces CypD binding to the OSCP subunit of the F_1F_O ATP synthase; this favors PTP activity. Overall, these studies provide insight into the regulation of PTP opening by CypD following post-translational modification and potential mechanism for CypD interaction with the F_1F_O-ATP synthase.

Clash of the Titans

The British biochemist John E. Walker is known for his work on elucidating the enzymatic mechanism of ATP synthase. For this work, he received and shared the Nobel Prize in Chemistry in 1997 with Jens C. Skou and Paul D. Boyer. In 2017, Walker and his team entered the PTP field and made some substantial contributions. They demonstrated that p^0 cells lacking mitochondrial DNA, as well as cells in which the genes for subunits of the F_1F_O-ATP synthase have been disrupted, can still exhibit PTP activity. [100–102]. This provided strong evidence against the F_1F_O-ATP as the pore component. In a series of back-and-forth commentaries, Walker and Bernardi debated the molecular mechanism of pore

formation using results generated from transgenic animal studies. Bernardi pointed out that cells lacking F_1F_O-ATP synthase, mitochondrial swelling is slower than control cells, and the channel conductance was a fifth ($\sim$0.3 nS) relative to control. Bernardi interprets these observations as evidence in support of his argument that the F_1F_O-ATP synthase is indeed the pore [103]. This led Bernardi to suggest that mitochondria possess at least two pathways for permeabilization: one inhibited by CsA and not BKA and the second inhibited by both agents [104]. Bernardi's viewpoint remains unchanged and believes that the F_1F_O-ATP synthase remains a strong candidate as the molecular identity of the pore. In a follow-up letter to Bernardi, Walker reiterated his findings and strongly suggested the ATP synthase is not associated with the PTP [104]. That said, John Walker maintains an open mind and correctly points out that this controversy would not be solved until the native, dimeric structure of the enzyme complex is revealed. If F_1F_O-ATP synthase dimers do form the pore, there should be an aqueous channels within the complex of approximately 20 – 30 Åin diameter [105]. Overall, the genetic ablation of the proposed putative components of the PTP did not prevent the occurrence of PTP opening. Hence, many unanswered questions await an explanation or require further evaluation. Thus far, CypD is the only generally accepted PTP modulator. For this reason, CypD is used as a bait for newly proposed PTP candidates [103]. Altogether, this shows a striking ability of the mitochondria to devise mechanistic redundancies to display PTP activity when calcium homeostasis is heavily disrupted. However, I present an alternative hypothesis that explains how calcium overload alters the mitochondrial structure and hence function [79, 106].

1.5 The Lesser of Two Evils: F-ATP Synthase and ANT Mediate Distinct Permeability Pathways

A recent experiment in HAP1-A12 mitoplasts lacking the c-subunit of the F_1F_O-ATP synthase recorded a pore conductance of ∼300 pS [107]. Mitoplasts are swollen mitochondria that do not possess an outer membrane. The F_1F_O-ATP synthase pore conductance is between 4 to 5 times lower than the currently accepted *bona fide* pore conductance of 1.3 – 1.5 nS and surprisingly still sensitive to BKA. The channel clamped on to in the HAP1-A12 experiments resembled the 300 – 600 nS conductance from purified heart mitochondria. This conductance range matched those obtained from studies using ANT enriched proteoliposomes [29, 31, 108]. Similarly, addition of BKA to control mitoplasts generates currents about 300 pS which could be inhibited by CsA and ADP [61, 107]. Experiments by Carrer et al. showed that mitoplasts were sensitive to CsA and refractory to BKA [61]. This supports the F_1F_O-ATP synthase as the pore mediating pathway. Whereas ablating subunit g, and by extension subunit e, reflects mitoplasts sensitive to CsA but not BKA [61]. This supports the ANT as the pore mediating pathway. Altogether, this led to a new PTP regulation model in which pore formation occurs by, at least, two CypD-dependent pathways: 1) The F_1F_O-ATP synthase assembling the pore and, in the absence of c-subunits, 2) the involvement of the ANT to assemble the pore. While the two CypD-dependent pathways involving the F_1F_O-ATP synthase and the ANT are currently the most well-supported models for the PTP, there are other proposed mechanisms that don't fit into these categories.

1.6 PTP Caused by Protein Misfolding

Lemasters and colleagues proposed that the process of pore opening may involve protein misfolding with two basic modes of operation [109]. The first mode occurs when there is sufficient chaperone-like proteins, such as CypD, available to bind and block the conductance generated by misfolded proteins to minimize PTP formation. The production of misfolded proteins is triggered by severe insults, such as oxidative stress and calcium overload. Higher levels of calcium can regulate pore opening, whereas CsA inhibits pore formation. However, the second mode of PTP formation is unregulated and insensitive to CsA, if the number of misfolded proteins exceeds the binding capacity of chaperone-like proteins. Overall, this hypothesis suggests that a delicate balance exists between the binding capacity of chaperones like CypD and the number of misfolded proteins to inhibit pore activity. When this balance is disrupted, the unregulated and CsA-insensitive component of the pore ensues, leading to pore opening and ultimately cell death. Although this idea of PTP regulation seems unlikely, Lemasters et al. correctly anticipated the involvement of heat shock proteins, a large family of molecular chaperones, in regulating pore function through cyt. c release [109]. Recent research indicates that the heat shock protein TRAP1 might play a role in controlling PTP opening. Despite this, the validity of this model of PTP modulation remains unproven.

1.7 Fatty Acids Alter Mitochondrial Bioenergetics and Promotes PTP Opening

Fatty acids (FA) play a crucial role in various cellular processes, including cell signaling pathways, membrane composition, and energy production. Esterified FAs serve as the primary energy storage and are a component of phospholipids. On the other hand, non-esterified

FAs can be associated with membranes, bound to FA-binding proteins, or free. Although FAs are an efficient source of energy production, their dysregulation can result in changes in membrane permeability and energy coupling [106]. Recent studies have suggested that FAs are involved in proapoptotic signaling events and PTP opening [110]. PTP activity by FA is influenced by the number of saturations and hydrocarbon chain length. Increasing unsaturation across the hydrocarbon chain leads to mitochondrial membrane depolarization and cell cytotoxicity *in situ* [110]. This effect may be due to the ability of FAs to uncouple mitochondrial respiration, which increases with the number of unsaturation and chain length. However, the protonophoric activity, i.e., H^+ cycling through the IMM, of long-chain FAs occurs over several minutes and does not significantly affect the proton motive force [110]. This may be due to the slow movement of FAs across hydrophobic membrane barriers, which are dependent on their protonated, unprotonated, or anionic states, and have low permeability. The uncoupling effect of FAs has been known since 1965 when exposure to cold conditions led to a burst of heat production in skeletal mitochondria from pigeons [111, 112]. This is known as nonshivering thermogenesis; a process regulated by the uncouple protein 1 (UCP1 or thermogenin). UCP1 are expressed in brown and beige adipose tissue [113]. Other UCP homologues, including UCP2 and UCP3, have been identified in other tissues with poorly understood roles. The uncoupling effects of FAs was later proposed to occur through interactions with ANT [111]. Interestingly, adding FA to isolated mitochondria leads to mitochondrial swelling, cytochrome c release, and OMM rupture in a concentration-dependent manner, suggesting a potential PTP role [110]. When CsA is added to inhibit PTP activity following FA exposure, various responses are observed *in situ* and *in vitro*. For example, CsA-insensitivity is seen in C14-C16 FAs, whereas CsA-sensitivity is seen in C18-C20 FAs [110]. This sets up a scenario where both FA-dependent and independent

PTP mechanisms may be involved. Penzo and Bernardi et al. suggest that the difference on PTP activity and cytotoxity between saturated and unsaturated fatty acids arise from their availability for biosynthesis and esterification [110]. On the one hand, differences between saturated FAs arise from esterification. Whereas differences between unsaturated FA may arise from physicochemical properties, their role in signaling pathways, and the biosynthesis process of a given FA along with its transport and delivery mechanisms [110]. To summarize, FAs seem to play a role in PTP but requires further investigation.

1.8 The Metalloprotease SPG7 as a Regulator of the PTP

The nuclear-encoded mitochondrial metalloprotease spastic paraplegia 7 (SPG7) is found in the inner mitochondrial membrane and is associated with hereditary spastic paraplegic patients with SPG7 mutations [114]. SPG7 forms homo-oligomeric complexes with the metalloprotease AFG3 Like Matrix AAA Peptidase Subunit 2 (AFG3L2) [22], and both proteins are involved in IMM protein quality control [22, 115]. Furthermore, SPG7 interacts with CypD and VDAC to promote PTP formation [114]. To identify the PTP component, experimental models of HEK293T and HeLa cells silenced by short hairpin RNA (shRNA) were developed. While mitochondria exhibited an enhanced mitochondrial calcium retention capacity, these models were not exempt from PTP opening [114]. Interestingly, cells with shRNA of SPG7 exhibited elongated mitochondria without altered calcium handling. However, mitochondria elongation might be attributed to AFG3L. A recent study showed that AFG3L mutation destabilizes fusion proteins by hyperactivating specific metallopeptidases involved in cristae remodeling [115]. These cells displayed similar calcium retention

to cells exposed to VDAC1 and CypD shRNA. Therefore SPG7 is a pore modulator rather than a PTP component.

1.9 An Abandoned Model: Complex I and PTP Regulation

Fontaine et al. were among the first to demonstrate the involvement of complex I with PTP [116]. In their experiments, skeletal muscle mitochondria were energized with either complex I substrates (NADH-linked) or complex II substrates ($FADH_2$-linked), followed by the addition of calcium in the presence or absence of CsA. The researchers recorded various mitochondrial parameters, such as $\Delta\Psi_m$, calcium retention capacity (CRC), oxygen consumption rate, and pyridine nucleotide pools. The results showed that complex I substrates sensitized the mitochondria to PTP opening, while complex II substrates did not. The authors concluded that PTP opening is regulated by the rate of electron flow through complex I and not by differences in $\Delta\Psi_m$, matrix pH, Ca^{2+} uptake, oxidation-reduction status of pyridine nucleotides, or production of hydrogen peroxide. These results are surprising given all of these are hallmarks of *bona fide* PTP. However, inhibiting complex I activity using rotenone inhibited the Ca^{2+}-dependent PTP opening, and the addition of catalase suggested that ROS are not involved in complex I substrate-dependent PTP opening [116]. The Fontaine et al. study results show that there exist substrate-dependent nucleotide redox status. The pyridine nucleotide pool is highly reduced with complex I substrates which could be associated with lower oxygen consumption rates, preserved $\Delta\Psi_m$, and enhanced CRC. Similar effects were observed with complex II substrates; however, the authors did not provide details of the nucleotide pool redox state between the substrates. Therefore, it is unknown to

what degree the ETS circuitry is rewired, which is relevant given that the major sources of ROS in mitochondria come from complex I and III. This is relevant given that most studies suggest the superoxide production is enhanced when the NAD^+ pool is reduced [117–121]. Overall, this study obfuscates the already complicated regulatory landscape of the PTP.

1.10 Concluding Remarks

Throughout the 65 years of research on PTP, numerous molecular models of varying depth and complexity have been proposed, but many have failed to withstand genetic scrutiny while others remain unproven. Despite the confusion and difficulty in navigating the literature on PTP, understanding this phenomenon is crucial in developing effective therapeutic interventions for diseases where PTP is prominent. The handling of calcium is a common feature among these models and influences mitochondrial function. To seek answers, my proposal is focused on understanding the effects of calcium-induced mitochondrial function from a structural perspective. Recent findings suggest that cristae structure is highly disrupted during calcium overload, leading to loss of function. In the following chapters, I propose a morphological argument that links mitochondrial structure with the observed loss of function during calcium overloaded states, potentially explaining some of the proposed models.

Chapter 2

Calcium Overload and Mitochondrial Metabolism

2.1 Introduction: Mitochondrial Calcium - The Good and the Bad

ATP is coupled to nearly every reaction in the body and is necessary for an organism's survival. This essential energy metabolite is primarily produced by mitochondria in a process known as oxidative phosphorylation. Oxidative phosphorylation is regulated in a manner that ensures the optimal rate of mitochondrial ATP production. ATP breakdown products, ADP, and inorganic phosphate (Pi) are the most potent regulators of oxidative phosphorylation. That said, calcium is also an important regulator but acts as a double–edged sword regarding oxidative phosphorylation [78, 122]. Calcium ions enter and leave mitochondria through a variety of specialized channels and transporters in a tissue-specific manner [123]. Moreover, mitochondria possess a unique ability to accumulate massive quantities of calcium in their matrix with devastating consequences [78, 122, 124, 125]. While relatively low amounts of calcium ($0 \leq 40$ nmol/mg mitochondria) are essential for energy production, high levels of calcium (≥ 500 nmol/mg) leads to the total collapse of energy homeostasis (**Figure 2.1**) [126]. In between, a state known as calcium overload (40 – 500 nmol/mg), calcium impairs oxidative phosphorylation and presumably contributes to long–term organ dysfunction. These ranges were identified using guinea pig cardiac mitochondria, and exter-

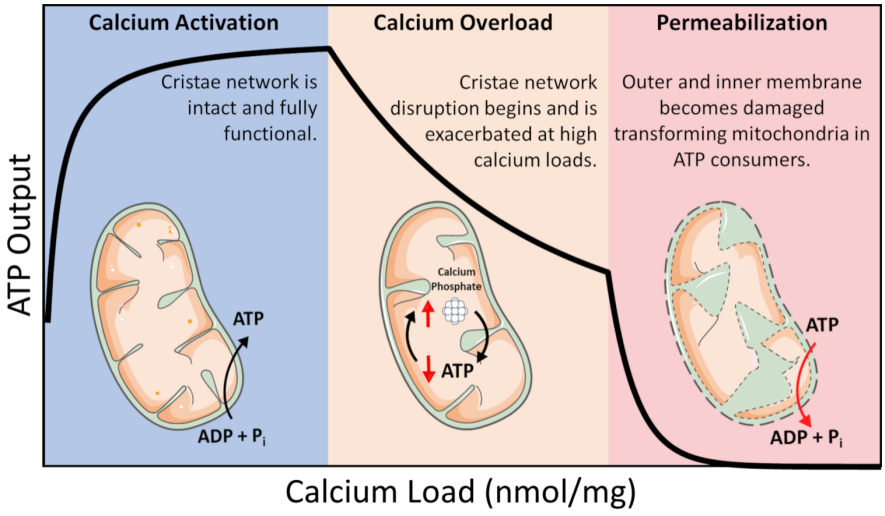

h]

Figure 2.1: Calcium overload. In low amounts, calcium enhances mitochondrial function by activating several Ca^{2+}–sensitive catabolic enzymes. In moderate amounts, depressed rates of oxidative phosphorylation become observable. In extreme amounts, mitochondria become structurally compromised and consume ATP in a futile attempt to restore homeostasis.

nal effectors such as cyclosporin A (CsA) can modulate them [122, 127]. Thus, the regulation of mitochondrial calcium content is of utmost importance for living tissue.

In this intermediate calcium overloaded state, ATP synthesis is inhibited by total mitochondrial calcium in a titratable manner [78, 122, 128]. This inhibition is relieved after calcium is removed from mitochondria if the total content is below 500 nmol/mg, and calcium removal only partially recovers ATP synthesis capacity at higher loads [125]. Phosphate facilitates mitochondrial calcium uptake but can ultimately lead to cell death via the mitochondrial permeability transition phenomenon [125, 129]. While phosphate is thought to act as a permeability transition inducer, it may also serve a dual purpose as a desensitizer under certain conditions [130]. While the molecular details of the mitochondrial permeability transition phenomenon are still debated, the current consensus revolves around the idea of the formation of a proteinaceous pore [127, 131]. That said, the conditions required to open this pore *in vitro* are extreme and would result in irreversible cell death *in vivo*. Thus, it

may not play a significant role in how calcium regulates energy metabolism in living tissue. There are numerous review articles discussing our current understanding of this phenomenon [132, 133]. Discussed herein, and previously by our group [122, 125], is an emerging idea that views this phenomenon from a different perspective which involves a conceptual link between mitochondrial ultrastructure and function.

2.2 Materials and Methods

Mitochondria isolation and protein quantification

Cardiac mitochondria were obtained from Hartley albino guinea pig hearts weighting 350 – 450 g (4 – 6 weeks old). The animals were injected with heparin (500 units/mL) in the intraperitoneal cavity and subjected to anesthesia with 4 – 5 % isoflurane prior to guillotine decapitation. The heart was obtained following a thoracotomy procedure and perfused with a cold cardioplegia solution. The heart tissue was minced into ∼10 mm pieces and homogenized using a handheld homogenizer at 18,000 rpm for 20 seconds. Mitochondria were isolated using differential centrifugation as described in [122, 125, 127]. The mitochondrial protein quantification was performed using the BIORAD bovine serum albumin (BSA) standard set kit and the bicinchoninic acid (BCA) assay. The mitochondrial suspension was diluted to 40 mg/mL and kept on ice throughout the duration of the experiments (4 - 5 hours).

Mitochondrial quality control

The mitochondrial respiratory control ratio (RCR) was determined using an Oxygraph 2k (Oroboros Instrument Corp., Innsbruck, Austria) by loading 2 mL of a respiratory buffer containing 130 mM KCl, 5 mM K_2HPO_4, 20 mM 3-(N-morpholino) propanesulfonic acid

(MOPS), 1 mM $MgCl_2$, 1 mM ethylene glycol-bis(β-aminoethyl ether)-N,N,N′,N′-tetraacetic acid (EGTA), and 0.1 % (w/v) BSA at a pH of 7.1 and 37 °C. Before the addition of 0.1 mg/mL mitochondria, 5 mM sodium pyruvate and 1 mM L–malate (pH 7.0) were added. All the following experiments were performed using the described conditions and buffer. The leak state was recorded for 5 minutes following the addition of 0.1 mg/mL mitochondria. Here, we define leak state as the rate of oxygen consumption by the mitochondria in the presence of substrate and absence of ADP. At 5 minutes, a bolus of 500 µM ADP was added to determine the maximum ADP-stimulated respiratory rate. The mitochondrial quality was assessed by computing the RCR obtained by dividing the maximal ADP–stimulated respiration rate by the leak respiration rate. Only Mitochondria with RCR values greater than or equal to 16 met the quality criteria and used for experiments.

Calcium Effects on Mitochondrial Respiration

To assess the effects of calcium on mitochondrial function, leak state was recorded after the addition of 5 mM sodium pyruvate and 1 mM L–malate and 0.1 mg/mL mitochondria. At 5 minutes, water vehicle, 25 µM $CaCl_2$, or a 50 µM $CaCl_2$ bolus was injected into the oxygraphy chamber. For the zero Ca^{2+} conditions, 1 mM EGTA was present throughout the experiment. When the water vehicle is used, it is important to note that 4 µM residual Ca^{2+} from buffer contaminants is initially present. At 10 minutes, a 500 µM ADP bolus was injected to induce maximal ADP-stimulated respiration rates.

Cryo–Electron Microscopy (Cryo–EM) Sample Vitrification and Tomographic Acquisition

Isolated mitochondria were suspended at a concentration of 0.1 mg/mL in 2 mL of respiration buffer containing 5 mM sodium pyruvate and 1 mM L–malate. At 5 minutes, water vehicle, 1 mM EGTA, 25 µM $CaCl_2$, or a 50 µM $CaCl_2$ bolus was injected into the oxygraphy chamber. For the cyclosporin A (CsA) treatment, 1 µM CsA was added to the suspension before the addition of mitochondria. At 10 minutes, 5 µL samples were pipetted from the mitochondrial suspension and deposited on Quantifoil R2/2 holey carbon grids pretreated with a Pelco EasiGlo glow discharge unit for 1 minute. The grids were set on a Vitrobot Mark IV chamber with automated temperature regulation (4 °C), blotting (3 seconds), and humidity control (100 %). Samples were blotted to thin the water layer, plunged into liquid ethane, then transferred and stored in liquid nitrogen until imaging. The imaging and tomographic acquisition was collected using a FEI Talos Artica at 200 keV in low dose conditions on a Falcon 3EC direct electron detector with an electron dose of ∼2 e-/Å^2 per tilt image. The tomographic images were collected at 22,000 x magnification obtaining a final product of 4.7 Å/pixel with a total electron dose of ∼100 e^-/Å^2.

Tomogram Alignment and 3D Reconstruction

Motion correction was performed on each individual micrograph using Motioncor2 v1.2.6 with an index factor of 7. Briefly, a cross-correlation algorithm was performed to identify the translation and rotation of the 7 images with respect to the reference image. This information was used to align all the images to reduce the motion blur and increase the signal-to-noise ratio. The tilt series alignment was performed using IMOD v4.9.12 and the Simultaneous Iterative Reconstruction Technique (SIRT) feature with 7 – 10 iterations. The

3D reconstruction tracings were performed using IMOD (3dmod) drawing tool functionality [134].

Statistics

All data were analyzed and plotted using MATLAB 2022a (Mathworks, Inc., Natick, MA, USA). The data in **Figure 2.4** are presented as a mean ± standard deviation from at least $n \geq 8$ independent observations.

2.3 Calcium Homeostasis, Entry, and Exit Pathways

Mitochondrial calcium homeostasis is primarily regulated by three pathways: the mitochondrial calcium uniporter (MCU), $Na^+/Ca^{2+}/Li^+$ exchanger (NCLX), and calcium hydrogen exchanger (CHE). The MCU is the dominant uptake pathway and is comprised of a heteromeric protein complex composed of various subunits including the mitochondrial Ca^{2+} uptake family (MICU 1, 2, and 3), essential MCU regulator (EMRE), MCU regulator 1 (MCUR1), MCU dominant negative β–subunit (MCUb), and the solute carrier 25A23 (SLC25A23) [135]. These subunits form a complex on what appears to be an on demand basis [135–138]. While an in–depth review on the molecular structure and function of these subunits are beyond the scope of this mini review/perspective, we would like to refer our readers to references [135, 136, 138]. Other pathways for Ca^{2+} uptake including the rapid mode calcium uptake and ryanodine receptors are also speculated to play an important role under certain conditions [139–141]. The MCU channel has a high affinity for Ca^{2+} (Kd $\leq$ 2 nM); however, it has a low half activation constant ($K_{0.5}$ ~20 mM) [142]. In other words, it is highly selective for Ca^{2+} but requires high levels of calcium in the millimolar range

to activate. As a result, the MCU is less active at lower concentrations of calcium (0.1 – 1 µM) and more active at higher extramitochondrial calcium loads as defined by the Kd [141]. The efflux pathways are primarily controlled by the NCLX and CHE. The NCLX is an electrogenic exchanger that swaps 3 Na^+ (or Li^+) for 1 Ca^{2+} [143, 144]. Consequently, this reaction is electrogenic and sensitive to the mitochondrial membrane potential. Under physiological conditions, the CHE swaps calcium out for protons in the matrix in a manner that is presumed to be an electroneutral ratio of 1 Ca^{2+} per 2 H^+ [128]. The calcium hydrogen exchanger functions independently of sodium and is present at much lower activities in tissues with high energy demand [145]. For instance, the CHE is dominant in the liver and other relatively quiescent tissues, while NCLX is predominant in the heart, brain, and other high activity tissues [131, 146–150]. Under basal conditions, cytosolic Ca^{2+} concentrations are maintained in the 100 nM range [151]. For cardiomyocytes and skeletal myocytes, the range of global or average cytosolic Ca^{2+} concentrations during peak contraction that mitochondria are exposed to fall within 1 µM but can peak two to three times higher under stimulatory conditions [152]. That said, some mitochondria are exposed to higher concentrations ($\sim$10 – 100 µM) in microdomains associated with mitochondrial–SR contact sites [153–155]. In either the basal or stimulatory condition, intramitochondrial Ca^{2+} levels remain low as long as mitochondria remain coupled [156]. This form of calcium regulation is attributed to the mitochondrial calcium buffering system, which refers to the ability of mitochondria to store large amounts of calcium in their matrix [65]. As a result, mitochondria are particularly relevant in scenarios of calcium overload, where their ability to buffer and regulate calcium helps maintain cellular homeostasis

This is of relevance in high–energy demand tissue as the mitochondrial membrane potential, Ca^{2+}, and Na^+ are the main regulators of mitochondrial calcium homeostasis. And

while Ca^{2+} uptake is very sensitive to changes in membrane potential, Ca^{2+} efflux is less sensitive [157]. As a result, the MCU channel can load Ca^{2+} into the matrix at a rate far exceeding the NCLX matrix calcium clearance (1,400 and 20 nmol Ca^{2+} min^{-1} mg mitochondrial $protein^{-1}$, respectively) [158]. Hence, under conditions that disrupt cytosolic calcium homeostasis, Ca^{2+} uptake through MCU floods the matrix of energized mitochondria with massive amounts of Ca^{2+} [128]. Left unchecked, membrane potential loss precipitates a catastrophic collapse in energy homeostasis [122, 159]. This phenomenon is often ascribed to the permeability transition phenomenon and has detrimental consequences for cell health and longevity [124, 129, 132, 158, 160]. This scenario places mitochondria in a vulnerable position, leading some to view the permeability transition phenomenon as a calcium overload release valve [104, 161]. Regardless, the mitochondria Ca^{2+} uptake and removal processes are highly regulated with compensatory mechanisms in place to ensure cellular homeostasis and survivability. When such regulatory mechanisms fail, mitochondria become overloaded with calcium, and energy homeostasis collapses.

2.4 Calcium TCA and ETC

Calcium also influences mechanisms driving mitochondrial energy production and metabolic activity. For example, calcium regulates the activity of metabolic enzymes in the TCA cycle including pyruvate dehydrogenase, isocitrate dehydrogenase, and α–ketoglutarate dehydrogenase [125]. The TCA cycle generates reducing equivalents (such as NADH and UQH_2) used by the proton pumps that establish the membrane potential and alkalize the mitochondrial matrix relative to the cytoplasm [26]. This, in turn, biases ATP synthase away from its more favorable ATP hydrolysis set point to an operating regime conducive for ATP produc-

tion via oxidative phosphorylation. Therefore, in high–energy demanding tissue where cells are constantly exposed to transient Ca^{2+} signals, calcium homeostasis is intrinsically linked to ATP production both through the TCA cycle and oxidative phosphorylation (OXPHOS) to regulate cellular bioenergetics. Under most conditions, the membrane potential is the primary determinant of the ratio of matrix ATP to ADP and inorganic phosphate (i.e., the matrix ATP/ADP/Pi ratio). As Ca^{2+} is injected into mitochondria, matrix ATP/ADP ratios decline, the membrane potential depolarizes to a degree, and matrix pH increases [160, 162]. As the matrix pH becomes more basic, dihydrogen phosphate ($H_2PO_4^-$) is effectively driven into the mitochondria in symport with H^+ in an electroneutral fashion. The phosphate carrier facilitates his symport, and when $H_2PO_4^-$ enters the matrix, it undergoes a deprotonation event and forms HPO_4^{2-} [163]. Under these conditions, elevated Pi levels in the matrix facilitate the formation of calcium phosphate complexes. The formation of these complexes involves the deprotonation of HPO_4^{2-} into the phosphate trianion (PO_4^{3-}) further releasing a H^+. This helps counteract the significant alkalizing effect of accelerated proton pumping and charge replacement caused by Ca^{2+} uptake. Overall, a slight depolarization will alkalize the matrix pH which has the net effect of enhancing mitochondrial Ca^{2+} sequestration [159]. However, when the current generated by Ca^{2+} uptake exceeds the proton pumping current, thermodynamic driving forces reverse the F_1F_O ATP synthase activity and pumps protons out of the matrix via ATP hydrolysis [126]. When ATP is hydrolyzed from this reversal, the phosphate released can participate in phosphate precipitate formation until ATP is exhausted and the metabolic system collapses [65, 164]. This is just one possible scenario as ATP hydrolysis isn't a required source of inorganic phosphate during precipitate formation. In the presence of oligomycin, ATP synthase is inhibited and mitochondria still possess the ability to take up massive amounts of Ca^{2+} when sufficient Pi is present [165].

Ultimately, when matrix Ca^{2+} concentrations exceed a threshold level, the formation of calcium phosphate precipitates in the matrix has the effect of reducing the mitochondrial free Ca^{2+} levels to manageable amounts via a type of buffering mechanism but at the expense of oxidative phosphorylation capacity [78, 141].

2.5 Mitochondrial Calcium Buffering

We know that the consequences of precipitate formation operate on a spectrum (**Figure 2.1**), but we do not fully comprehend the mechanism. At low concentrations, calcium phosphate precipitates can have a protective effect. Whereas at high concentrations, precipitates can destabilize the mitochondrial cristae network [122, 125]. This has been confirmed by others in which mitochondria loaded with Ca^{2+} resulted in calcium phosphate precipitates occupying more than 20 % of the matrix volume [122]. One potential mechanism that leads to metabolic dysfunction is that precipitates may mechanically destabilize membrane structures by disrupting proteins involved in maintaining the cristae structure [125]. Another idea is that precipitates may serve as physical barriers limiting metabolite and substrate diffusion across the matrix [78]. The regulatory characteristics of the phosphate precipitation buffering mechanism remain enigmatic, but one concept boils down precipitate formation to a simple thermodynamic argument [65, 164]. A second concept includes the idea that precipitate formation requires nucleation sites [129]. Full occupancy of these sites might dampen the extent of phosphate buffering within the mitochondrial matrix and send free Ca^{2+} high into pathological concentrations. The unknown nature of these potential nucleation sites makes it challenging to devise effective genetic and pharmacological approaches to manipulate mitochondrial calcium buffering. Thus, further study is required to resolve

some of these unknowns.

2.6 Potential Role of Annexins in Mitochondria

Under appropriate conditions, when the mitochondria are energized, and magnesium and phosphate are present, adenine nucleotides are taken up with Ca^{2+} during precipitate formation [166]. However, the mechanism as to how precipitate formation is accomplished is yet to be elucidated but may be linked to annexins [167, 168]. These proteins consist of a multigene family of Ca^{2+}–regulated proteins with a calcium and lipid–binding modules known as the core domain. Some even possess GTP/ATP binding capabilities that enhance Ca^{2+}/lipid interactions [169, 170]. Their ubiquitous nature covers a variety of cellular functions including membrane transport, membrane–domain organization, anti-inflammatory and fibrinolytic activities, membrane repair, Ca^{2+} signaling pathways and even mitochondrial morphogenesis [165, 171–173]. Others have theorized that annexins can act as a "lipid patch" to aid in injury repair [174]. And while the various annexin affinities for Ca^{2+} are different, it was demonstrated that increased annexin Ca^{2+} binding is correlated with plasma membrane repair [175]. Initially, annexins most sensitive to Ca^{2+} are bound and as the healing process proceeds, Ca^{2+} concentrations increase and the annexins presented are less sensitive to Ca^{2+}. That said, annexins may also bind to the inner membrane and form nucleation sites for precipitate growth [168]. In doing so, annexins can reduce free Ca^{2+} concentrations and prevent the activation of Ca^{2+}–dependent degradation processes in the matrix. Hence, annexins may be involved in signaling related to mitochondrial calcium overload, but the extent of which is currently unknown. Perhaps the biggest question is whether annexins are linked to the permeability transition phenomenon or the Ca^{2+} buffering system. Hence,

functional studies, coupled with structural assessments, looking at the expression and activity of annexins with respect to Ca^{2+} handling in cardiac mitochondria could prove fruitful. However, the connection between mitochondrial ultrastructure and energy transduction is an emerging field. That said, we are still quite limited today, but cryo–EM has shed new light on the subject.

2.7 Structure/Function Axis

Mitochondrial ultrastructure undergoes dramatic changes during metabolic perturbations or in the presence of certain genetic modifications [176–183]. As such, calcium overload is a way to induce mitochondrial structural modifications. The response of mitochondria to Ca^{2+} was first reported about a half-century ago and was shown to decouple mitochondrial ATP production in extremely overloaded states via the permeability transition phenomenon [44, 59, 60, 72, 75–77, 184–188]. A different perspective on the matter involves the incorporation of structural information with coincident function data which is summarized in **Figure 2.1**. The idea linking structure to function is not new; however, the effect of Ca^{2+} on ultrastructure is novel and warrants further investigation. The importance of this concept is borne out through two simple facts. The first involves matrix contracture following ADP binding [111]. This presumably enhances energy transduction, a theory yet to be experimentally or computationally verified. The second encompasses ultrastructural changes induced by the presence of excess Ca^{2+} [17, 122, 189]. From this mechanism, the intriguing phenotypes reported in prior work can be explained by a metabolic flux imbalance caused by Ca^{2+}-induced cristae network disruption via metabolite permeability changes induced by cristae junction modifications. Following up on our previous modeling study [78], we have identified

novel structural changes associated with calcium overload and treatments known to protect against its devastating effects [125]. We hypothesize that differential cristae junctional protein processing underly the differences in these phenotypes. **Figure 2.2** shows that as the Ca^{2+} load increases, the ultrastructural changes become more and more pronounced. These changes in ultrastructure are responsible for depressed ATP synthesis rates [127]. In the calcium overloaded state, the cristae network becomes "stringy", and the matrix volume expands with embedded Ca^{2+} phosphate precipitates located within the matrix near cristae junctions [122]. Intriguingly, the impact of cyclosporin A (CsA) on ultrastructure aligns with prior work which shows that this compound causes cristae membrane condensation and enhances metabolic flux [125, 190]. These morphological changes are independent of the permeability transition pore [127] and require new approaches capable of demystifying the links between membrane morphology and energy transduction.

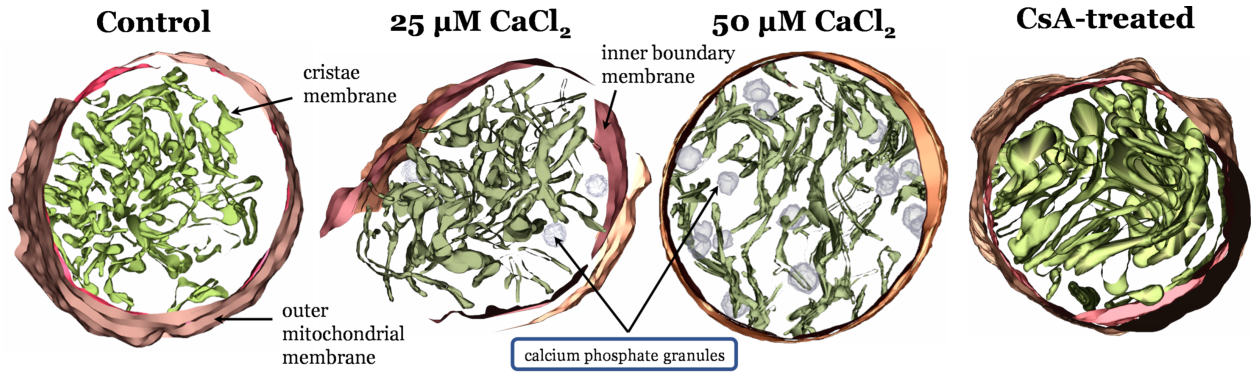

Figure 2.2: Mitochondrial ultrastructural changes associated with calcium overload. From left to right, IMOD [134] 3D mitochondrial reconstructions from cryo–electron tomography data where mitochondria were exposed to zero Ca^{2+}, a bolus of 25 µM $CaCl_2$, a bolus of 50 µM $CaCl_2$ [125], and 1 µM CsA. Calcium causes a decrease in cristae volume in a titratable manner. CsA leads to an expanded cristae volume and altered outer membrane morphology.

While these images reveal a striking effect of calcium and CsA on the ultrastructure of isolated mitochondria, they only provide possible explanations for the observed reduction

of maximum rates in oxidative phosphorylation in the calcium overloaded state. One clue lies within the O_2 respiratory dynamics during oxidative phosphorylation in the various conditions.

2.8 Oxygen Utilization in the Calcium Overloaded State

Prior studies have identified that when mitochondria are in a calcium overloaded state, their ability to oxidatively phosphorylate ADP is compromised [127, 130]. This could be due to transient permeability transition events which decouples proton pumping from ATP synthesis. Alternatively, ultrastructural changes could underly the altered respiratory dynamics that occur during oxidative phosphorylation. One way to test this is to estimate the amount of O_2 utilized per ADP phosphorylated. Estimating these values is difficult and requires the right protocols. Since we collected our data with a different objective in mind, we developed a suitable alternative approach. Using the information of the time derivative of the respiratory rate (JO_2), we estimated the duration of oxidative phosphorylation in a manner that is robust against experimental condition. The method is summarized in **Figure 2.3**. At the time point when oxidative phosphorylation is winding down, there is a transition that marks when the system is entering its final approach to a new steady state. This method was robust with respect to environmental conditions and produced ATP/O_2 ratios close to the theoretical value. That said, the exact time or transition point in the vicinity of our selection is not critical if the respiratory phase or transition is the same between conditions.

Figure 2.4 summarizes the effect of calcium overload on oxygen utilization during oxidative phosphorylation in the absence and presence of CsA. The apparent ATP produced per O_2 consumed for each condition are shown in **Figure 2.4A**. This was calculated based on a

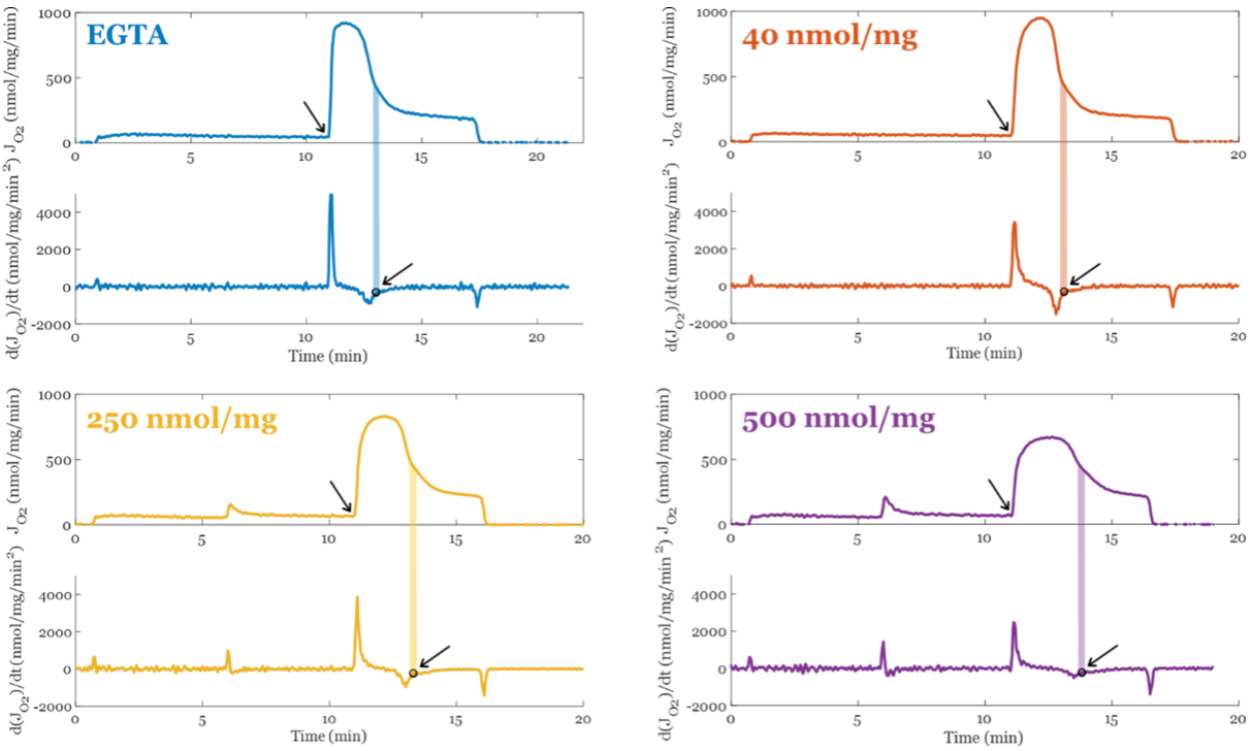

Figure 2.3: Method used to calculate the duration of oxidative phosphorylation. The transition is marked with an open circle and a shaded area for each condition that was used to estimate the point the majority of the O_2 flux switches from oxphos using the original ADP bolus to futile ATP cycling. This ATP cycling occurs when the rate of mitochondrial ATP efflux matches the ATP hydrolysis rate from extramitochondrial ATPase contaminants. All mitochondrial preparations when Mg^{2+} is present contain these contaminants. The arrows point to the start and end of oxphos for each condition.

total ADP bolus of 500 µM and assuming enough is converted to ATP before ATP cycling occurs at an appreciable rate so that a reliable estimate of O_2 cost may be calculated. CsA has little to no effect on these values; therefore, the permeability transition phenomenon is not relevant here. As the Ca^{2+} load increases, fewer ATP molecules are produced from the same number of O_2 molecules. This occurs because background cation cycling (H^+, Na^+, K^+, and Ca^{2+}) draws current from the electron transport pumps and thus consumes O_2. **Figure 2.4B** shows the estimated ATP/O_2 calculated using the following assumptions: i) Total O_2 cost only includes O_2 used for oxidative phosphorylation and O_2 used to power cation cycles. The O_2 consumed by the electrode is assumed to be negligible at these flux

rates. Assuming the average excess O_2 utilization (waste) shown in **Figure 2.4C** is representative for each calcium load, this relationship was used to correct for total O_2 utilization shown in **Figure 2.4A** to remove O_2 used to run futile cation cycles during oxidative phosphorylation. This relationship was approximated from the actual O_2 use and the theoretical amount for the given bolus of ADP. **Figure 2.4D** shows how excess O_2 utilization correlates strongly with duration of oxidative phosphorylation, which supports the idea that the O_2 waste during oxidative phosphorylation occurs at a relatively constant, calcium load specific, and predictable rate. Lastly, **Figure 2.4E** shows that after a threshold, calcium load begins to impair oxidative phosphorylation rates and forces mitochondria to phosphorylate ADP at a slower rate relative to when calcium is low or absent.

In addition, CsA tends to lower this duration back towards baseline, yet it did not impact the apparent or estimated ATP/O_2 ratio. This effect of CsA is intriguing and is not likely to be related to its effect on the permeability transition phenomenon (i.e., pore gating). The effect is still present at low calcium loads, albeit very subtly. An alternative explanation of this effect ties into the role CsA plays in modulating mitochondrial ultrastructure [125]. Cryo–EM imaging reveals that CsA leads to a more condensed cristae network and presumably enhances energy transduction rates, and this observation lines up with the shorter durations of oxidative phosphorylation. All that said, the inhibitory role calcium plays during oxidative phosphorylation is becoming clearer and is still a potential target for ischemia/reperfusion (I/R) injury and other metabolic–related disorders.

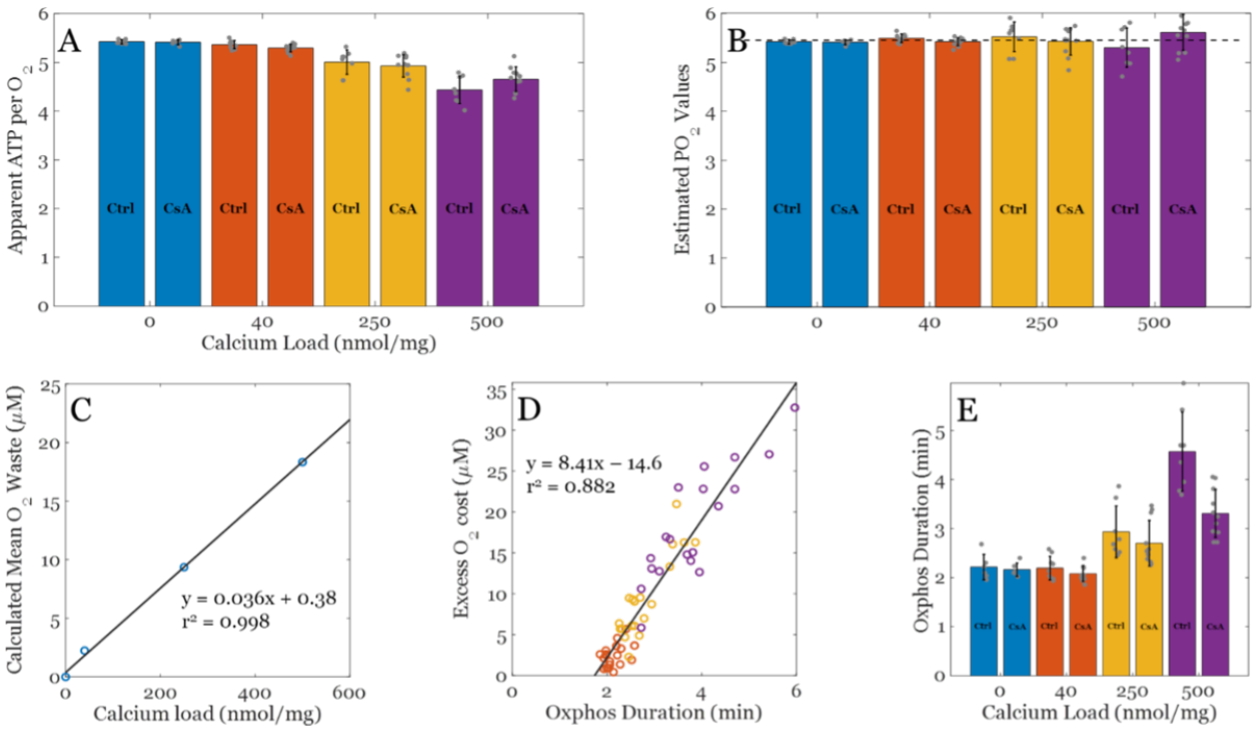

Figure 2.4: Analysis of O_2 cost for each experimental condition. A) Observed ADP consumed (ATP produced) per O_2 across a range of calcium loads with and without CsA. B) Estimated ATP/O_2 ratios across a range of calcium loads with and without CsA. The theoretical PO_2 value for NADH linked substrates is approximately 5.46 assuming $\frac{8}{3}$ + 1 H^+ per ATP generated and exported and 20 H^+ per O_2 consumed. C) Calculated mean O_2 waste during the oxphos period used to correct apparent ADP per O_2 data shown in panel A to estimate the PO_2 values shown in panel B. D) Calculated excess O_2 cost plotted against oxphos duration from panel C. E) Oxphos duration estimated from data for each condition. Color key: blue, EGTA; orange, 40 nmol/mg, yellow, 250 nmol/mg, and purple, 500 nmol/mg Ca^{2+} condition. Data are presented as the mean ± standard deviation for a sample size of $n \geq 8$.

2.9 Concluding Remarks

How exactly do calcium phosphate precipitates impair oxidative metabolism? Do they directly or indirectly affect mitochondrial ultrastructure? Are the observed ultrastructural changes causal to the reduced capacity of calcium loaded mitochondria to produce and export ATP? These precipitates have been seen in rather tame cell culture conditions [191], but do they exist in cardiac mitochondria in living cardiac tissue? They have been found

in infarcted cardiac tissue [192], but EM processing artifacts cannot be ruled out. As experimental techniques are limited, computational modeling is necessary to answer these questions related to metabolic functional capacity and ultrastructural features. The results presented herein reveal that the inhibition of oxidative phosphorylation is a calcium related phenomenon and is not caused by a direct decoupling of energy metabolism. In the calcium overloaded state, oxidative phosphorylation becomes rate limited by a yet to be determined mechanism that point towards either enzyme activity changes [78], ultrastructural modifications [122, 125], or a combination of the two. As these questions are quite challenging to answer using today's technology, detailed biophysical modeling of this phenomenon is the next best approach. Fortunately, several promising models [122, 193–195] are available to establish a solid foundation from which to pursue the answer to these questions.

Chapter 3

The Mitochondrial PTP Elucidated by Cryo-EM: The Impact of Calcium Overload on Mitochondrial Structure and Function

3.1 Introduction

Mitochondria regulate cell fate through a variety of means [23, 134, 136, 190, 196]. Their extensive networks and dynamic architecture facilitate metabolic signaling to ensure proper cellular function and survival. Mitochondria achieve this by integrating intracellular cues and physiological stimuli to regulate ATP production, metabolite oxidation, Ca^{2+} signaling, phospholipid and steroid hormone biosynthesis, and mitochondrial fission and fusion processes [125, 146, 148, 197–201]. As such, mitochondria must operate under a range of physiological conditions including transient changes in energy demand, oxidative stress, and moderate Ca^{2+} overload. For example, in highly metabolic organs such as heart, brain and kidney, their response to these conditions is crucial for cell survival [202]. However, in pathological conditions, such as during an ischemia/reperfusion event, mitochondria undergo a phenomenon known as the mitochondrial permeability transition (MPT). MPT is a gateway mechanism of cell death and involves the opening of a non-selective pore that allows small molecules and metabolites up to 1.5 kDa in size to [2] freely diffuse across the inner

mitochondrial membrane [203]. When the pore is open, the membrane potential ($\Delta\Psi_m$ is dissipated, there is a loss of respiratory control, ATP is hydrolyzed, and osmotic swelling occurs [196]. The swelling causes inner membrane unfolding, outer membrane rupture, and eventually release of apoptogenic molecules, including cytochrome c (cyt. c) that ends in cell death.

While the consequences of MPT are well appreciated, the molecular composition of the pore is currently unknown. The MPT phenomenon was first observed nearly seven decades ago when early studies in the mid 1950's to early 1960's demonstrated massive mitochondrial swelling under certain conditions [94, 188, 189, 204, 205]. These conditions involved Ca^{2+} overload, high inorganic phosphate concentrations, fatty acids, oxidative stress, and adenine nucleotide pool depletion. Interestingly, acidosis, adenine nucleotides, divalent cations (e.g., Mg^{2+}, Mn^{2+}, Ba^{2+} and Zn^{2+}), and some metabolic cofactors [202] prevent pore opening. In the late 1970's, Haworth and Hunter introduced the term 'permeability transition' and highlighted two important points: 1) pore opening is triggered by Ca^{2+}, and 2) it is closed when Ca^{2+} is removed from the environment [206]. Their results were later confirmed by Crompton et al. [207] who further proposed that the pore may have a protein identity with some physiological role [196, 203, 206, 208]. Soon after, other pioneering studies demonstrated that this phenomenon was involved in many pathophysiological diseases and conditions such as neurological disorders, aging, response to toxins, cancer, muscular dystrophy, and ischemia-reperfusion injury [27, 29, 202, 209, 210]. Despite the well-known effects of Ca^{2+} overload on mitochondrial function, the specific details remain a mystery.

As of now, the current dogma of mitochondrial Ca^{2+} overload is that mitochondrial dysfunction arises from the opening of a Ca^{2+}-dependent, free radical sensitized, and proteinaceous molecular pore whose molecular identity thus far remains elusive. Unfortunately,

efforts to identify the gene products responsible have been a rollercoaster ride of misleading discoveries and dashed hopes [100, 211, 212]. Instead of focusing on the pore, we sought to investigate the consequence of excessive Ca^{2+} overload on a population of isolated mitochondria by analyzing cryo-electron microscopy (cryo-EM) time-course data. This powerful imaging technique was coupled with high-resolution respirometry and spectrofluorimetry to structurally analyze the effect of Ca^{2+} overload on mitochondrial function. We identified a novel mechanism that links Ca^{2+} phosphate granule formation to cristae structural changes, inner membrane fragmentation, and ultimately mitochondrial permeabilization. This mechanism is not mutually exclusive with the current dogma as it integrates many past findings in a concise, overarching theoretical framework. However, our new data add exciting therapeutic targets for mitochondrial-protective therapies.

3.2 Methods

Ethical Approval

This work conformed to the National Institutes of Health's Guide for the Care and Use of Laboratory Animals and was approved by Michigan State University's Institutional Animal Care and Use Committee.

Mitochondria Isolation and Protein Quantification

Cardiac mitochondria were isolated from guinea pig hearts using differential centrifugation as described in Wollenman et al. [213] Briefly, Hartley albino guinea pigs weighing 350 – 450 g (4 – 6 weeks) were injected with heparin (500 units/mL) into the intraperitoneal cavity to

prevent blood clotting during the cardiac mitochondrial isolation. Before heart removal, the animals were deeply anesthetized with 4 – 5 % isoflurane. Prior to decapitation by guillotine, a noxious stimulus (paw pinch and eyelid reflex) confirmed the animals were fully sedated. After decapitation, a thoracotomy was performed. The heart was then perfused with cold cardioplegia solution and homogenized as described previously [213]. Mitochondrial protein content was quantified using the BIO-RAD Bovine Serum Albumin (BSA) Standard Set Kit and the BCA assay. The mitochondrial suspension was diluted to a working concentration of 40 mg/mL and kept on ice for the duration of the experiment (4 – 8 hours). Substrate stock solutions were neutralized to pH 7.0.

Mitochondrial Quality Control

The mitochondrial quality was determined using an Oxygraph 2k (Oroboros Instruments Corp., Innsbruck, Austria) under constant stirring. The O2k chambers were loaded with 2 mL respiratory buffer containing 130 mM KCl, 5 mM K_2HPO_4, 20 mM MOPS, and 1 mM $MgCl_2$, 1 mM EGTA, 0.1 % (w/v) BSA at a pH of 7.1 and 37 °C. All subsequent experiments were done using this buffer and temperature. At 0 mins, 5 mM sodium pyruvate and 1 mM L-malate were added followed by 0.1 mg/mL mitochondria. Here we defined leak state as the rate of oxygen consumption by mitochondria only in the presence of substrates. At 5 mins a bolus of ADP (500 μM) was added to induce maximal ADP-stimulated respiration. Quality was assessed by computing the respiratory control ratio (maximal ADP-stimulated rate divided by the leak rate). Only mitochondria with an RCR value greater than or equal to 16 were used in the experiments.

Ca^{2+} Contamination and Buffer Ca^{2+} Measurements

The amount of contaminating Ca^{2+} present in the respiratory buffer was 4.0 μM $\pm$ 0.43 μM which comes from reagent impurities [213]. This was measured using a perfectION^{TM} Ca^{2+} selective electrode (Mettler Toledo, Columbus, OH). Results were further confirmed using 1 μM Ca^{2+} fluorescent indicator Ca^{2+} Green 5N (503 nm excitation and 531 nm emission) using an Olis® DM245 spectrofluorimeter (Olis, Inc., Bogart, GA, USA).

Ca^{2+} Effects on Respiration and Oxidative Phosphorylation

Ca^{2+} effects on mitochondrial leak and ADP-stimulated respiration were determined by quantifying changes in leak and ADP-stimulated respiration rates after a Ca^{2+} challenge in the presence or absence of cyclosporin A (CsA). At 0 mins, 5 mM sodium pyruvate, 1 mM L-malate, 1 μM CsA, 0.1 mg/mL mitochondria were injected into each 2 mL chamber containing respiratory buffer. At 5 mins, a Ca^{2+} bolus of either 75 or 100 μM Ca^{2+} chloride was injected. At 10 mins, 500 μM ADP was added induce maximal ADP-stimulated respiration.

Mitochondrial Swelling Assay

Mitochondrial swelling was quantified by measuring absorbance at 540 nm using an Olis® DM245 spectrofluorimeter with a dual-beam absorbance module. At 0 mins, 5 mM pyruvate and 1 mM L-malate was added to a polystyrene cuvette with respiration buffer containing 1 μM CsA followed by the addition of 0.1 mg/mL mitochondria. At 5 mins, a 75 or 100 μM Ca^{2+} chloride bolus was added and the absorbance was recorded for a total of 15 mins. The minimum absorbance signal was determined by adding the uncoupler FCCP (1 μM) and the channel forming peptide Alamethicin (10 μg/mg). To normalize the raw traces, we used the

minimum absorbance value followed by the absorbance just before the addition of a Ca^{2+} bolus.

Ca^{2+} Uptake Dynamics

Ca^{2+} uptake dynamics were quantified using the fluorescent dye, Ca^{2+} green 5N (CaGr5N). Fluorescence was measured using an Olis® DM245 spectrofluorimeter. The dye was excited at 506 nm and the emission recorded at 531 nm. To minimize variability in dye concentration, 1 μM CaGr5N was added to 50 mL stocks of respiration buffer as opposed to adding small volumes to the 2 mL assay volume. At 0 mins, 1 μM CsA, 5 mM sodium pyruvate and 1 mM L-malate, and 0.1 mg/mL mitochondria were added to a polystyrene cuvette. At 5 mins, a bolus of either 75 or 100 μM Ca^{2+} chloride was added and the fluorescence was recorded for 15 mins.

Cryo-EM Sample Vitrification and Imaging

Isolated mitochondria were suspended at a concentration of 0.1 mg/mL in 2 mL respiration buffer with 5 mM sodium pyruvate and 1 mM L-malate. At the collection times indicated, 5 μL samples were pipetted from the mitochondrial suspension and deposited on Quantifoil R2/2 Holey Carbon grids that had been plasma-cleaned for 20 seconds using a Fischione Instruments model 1020 plasma cleaner. Grids were blotted to thin the water layer, and subsequently plunged into liquid ethane at room temperature using a manual plunge-freezing device (Michigan State University Physics Machine Shop). Grids were then transferred and stored in liquid nitrogen until imaging. Data for the 75 μM Ca^{2+} chloride experiments were collected in the cryo-EM facility at the University of Pittsburgh School of Medicine using

an FEI Polara G2 cryo-electron microscope with a field emission gun operating at 300 kV at nominal magnification of 9,400x with a post-column magnification of 1.4x to obtain a ∼12 – 10 Å/pixel resolution. Images were recorded on a FEI Falcon 3 direct electron-detecting camera. Data for the 100 μM Ca^{2+} chloride experiments were collected in the cryo-EM facility at the University of Pittsburgh School of Medicine using a FEI TF20 cryo-electron microscope with a field emission gun operating at 200 kV. The images were collected using a nominal magnification in the range of 5,000x on a TVIPS XF416 CMOS camera with a post-column magnification of 1.4x to obtain a 22 Å/pixel resolution. At these magnifications, the electron dose (e-/$Å^2$) is low enough to avoid significant sample destruction.

Ca^{2+} Phosphate Granules, Posner's Clusters, and Mitochondrial Structure Quantification

The program EMAN2 [163] was used to quantify the total number of granules for each mitochondrion under each condition from TEM images. A total of 1345 individual mitochondrial images were acquired in the presence and absence of CsA for two Ca^{2+} treatments. For the 75 μM Ca^{2+} chloride treatment, there were 235 images of control mitochondria and 645 images of CsA-treated mitochondria. For the 100 μM Ca^{2+} chloride treatment, there were 231 images of control mitochondria and 234 images for CsA-treated mitochondria. Mitochondrial and phosphate granule diameters were computed from three averages of two diagonal and one horizontal diameter measurement. Pixel resolution was converted to nanometers based on the magnification level. The fractional area that the Ca^{2+} phosphate granules occupy per mitochondrion was calculated by multiplying the number of granules within a mitochondrion times the sum of all the granule areas divided by the area of the mitochondrion ($\frac{Ngranules*Agranules}{Amito}$). The Ca^{2+} phosphate nanoclusters ($n = 227$) were determined

by measuring the electron-dense regions located within the granules using ImageJ (NIH, Bethesda, MD, USA).

Statistics

The Shapiro-Wilks test was used to confirm data normality. All data were analyzed and plotted using MATLAB 2019a (Mathworks, Inc., Natick, MA, USA). The data in **Figures 3.1**, **3.2**, and **3.3** (n = 3 – 4) and stats presented for the Ca^{2+} phosphate nanoclusters are presented as mean ± standard deviation. Mitochondrial images with Ca^{2+} phosphate granules were only included for the histogram analysis (n value in the figures). To assess the statistical significance of the differences between the distributions of control and CsA histograms, a two-sample Kolmogorov-Smirnov test was performed (see **Supplemental Table A.2** for the analyses). For the respirometry data at 75 µM and 100 µM $CaCl_2$, a Levene's test was conducted to assess the equality of variances between the two group and followed by a t-test was used to compare the CsA treatment with the control group. A p value of $\leq$0.01 was assumed to be statistically significant. An n-way ANOVA was run to determine significant effects between treatments at various Ca^{2+} loads and different time-points. A p value $\leq$0.05 was assumed to be statistically significant.

Reagents

All reagents were purchased from Sigma-Aldrich unless otherwise stated. Ca^{2+} Green^{TM} 5N hexapotassium salt was purchased from Thermo Fisher Scientific.

3.3 Results

Respiratory Inhibition by Ca^{2+} Overload is Reversible in Low-to-Moderate Ca^{2+} Overload

While mitochondrial Ca^{2+} concentrations lower than 100 nmol Ca^{2+}/mg mitochondria supports ATP production [125, 199, 214], levels above 500 nmol/mg mitochondria depress oxidative phosphorylation [78, 151, 215, 216]. In one of these studies, it was proposed that Ca^{2+} phosphate precipitates form in the mitochondrial matrix at high Ca^{2+} loads and reduce ATP production rates by either impeding metabolite transport and diffusion or destabilizing cristae, the functional units of mitochondria. However, the lasting effects of significant Ca^{2+} accumulation were not explored in either of these studies. To test this, we monitored mitochondrial respiration rates following the addition of the Ca^{2+} chelator EGTA under various Ca^{2+} boluses in the range of 0 to 500 nmol/mg as shown in **Figure 3.1**.

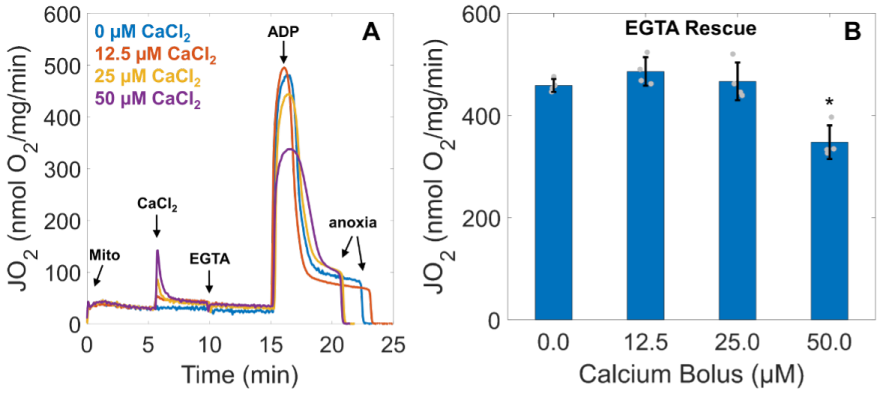

Figure 3.1: EGTA rescues mitochondrial function at low-to-moderate Ca^{2+} loads but not high loads. (A) Representative traces of ADP-stimulated respiration from Ca^{2+} loaded mitochondria following the addition of EGTA. Mitochondria (0.1 mg/mL) were energized with 5 mM sodium pyruvate and 1 mM L-malate and exposed to various Ca^{2+} boluses (0, 12.5, 25, and 50 μM). Five mins after Ca^{2+} uptake, 1 mM EGTA was added to chelate all Ca^{2+} in the system. Following an additional 5 mins, a bolus of 500 μM ADP was added to induce maximal ADP-stimulated respiration. (B) ADP-stimulated mitochondrial respiration is recovered after EGTA addition for all but the 50 μM Ca^{2+} bolus. Data are presented as mean $\pm$ standard deviation for a sample size of $n = 4$. Statistical comparisons are made with respect to 0 μM Ca^{2+}. * represents a p value less than 0.01.

The results in **Figure 3.1** show that the inhibitory effect of Ca^{2+} overload is reversible for all but high Ca^{2+} loads. As expected, the respiratory rates – the amount of oxygen consumed per mitochondrial content at a given time – before Ca^{2+} addition were equal across conditions. After a transient increase in respiration due to Ca^{2+} uptake, respiration remains elevated because of the activation of Ca^{2+}-sensitive matrix dehydrogenases and sodium/Ca^{2+} cycling. When 1 mM EGTA was added to chelate buffer Ca^{2+}, the ADP-driven respiratory rates were similar across all conditions except for the highest dose tested. These results suggest that when Ca^{2+} overload exceeds a certain threshold, mitochondrial oxidative phosphorylation is irreversibly inhibited. This effect does not involve mitochondrial calpains [78] and may involve some sort of structural change that lowers ATP production rates. Thus, the effect of Ca^{2+} overload lies on a spectrum whereby higher levels of Ca^{2+} result in detrimental changes in mitochondrial bioenergetic pathways.

CsA Preserves the Mitochondrial Function Under High Ca^{2+} Loads

We then measured mitochondrial respiratory rates during excessive Ca^{2+} overload by adding a 75 μM or 100 μM Ca^{2+} bolus in the presence or absence of CsA, a known PTP inhibitor (**Figure 3.2A** and **3.2B**). In agreement with results from **Figure 3.1**, increasing the extent of Ca^{2+} overload impairs oxidative metabolism. However, the depressive effects of Ca^{2+} on ADP-stimulated respiration is much more severe at these higher doses. The respiratory rate after ADP addition drops below 50 nmol O_2/mg/min after the 75 μM $CaCl_2$ bolus and drops below 20 nmol O_2/mg/min for the 100 μM $CaCl_2$ bolus. When CsA was present, this Ca^{2+}-dependent inhibitory effect is partially mitigated with the rate reaching nearly 320 nmol O_2/mg/min after the 75 μM bolus and 280 nmol O_2/mg/min for the 100 μM bolus. These results are statistically significant as shown in the **Supplemental Table A.2**.

Therefore, as others have found, CsA partially preserves mitochondrial function in the face of overwhelming Ca^{2+} overload [143, 175, 211, 217, 218]. This effect is typically attributed to the ability of CsA to inhibit PTP opening; however, our structural data shown in the following sections suggest the existence of a novel protective effect of CsA.

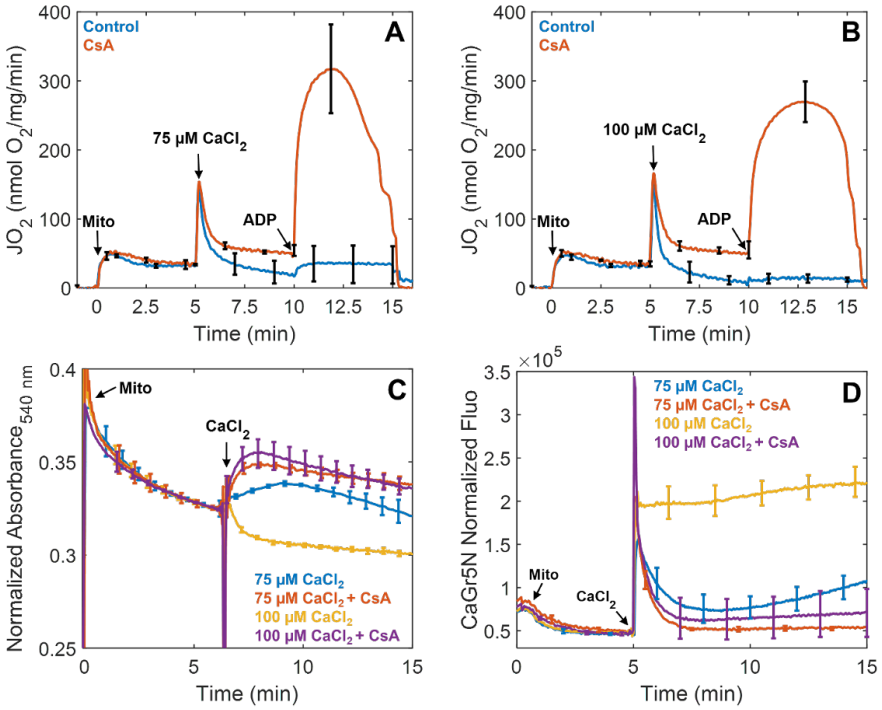

Figure 3.2: CsA preserves ATP synthesis, increase the absorbance, and enables Ca^{2+} uptake in a Ca^{2+} dependent manner. (A) and (B) The addition of 1 µM CsA prevented a near-total collapse of ADP-stimulated respiration after a bolus of 75 or 100 µM $CaCl_2$. Mitochondria were energized as described in **Figure 3.1**. (C) Mitochondrial swelling was monitored in parallel by quantifying absorbance at 540 nm. Large amplitude swelling was only observed in the 100 µM Ca^{2+} bolus group when CsA was absent. (D) Experimental conditions for Ca^{2+} uptake were similar except these experiments were performed in a cuvette open to atmosphere and tracked using CaGr5N (1 µM). In the absence of CsA, both Ca^{2+} boluses were not completely taken up by the mitochondria. In some instances, mitochondria can uptake Ca^{2+} followed by release as shown after the addition of a 75 µM $CaCl_2$ bolus. In contrast, CsA enables near-complete Ca^{2+} uptake of either bolus. Data are presented as mean ± standard deviation for a sample size of $n = 3 - 4$.

In addition to the respirometry studies, mitochondrial absorbance data obtained in parallel (**Figure 3.2C**) shows that only the 100 μM Ca^{2+} chloride bolus elicited large amplitude swelling, a classic indicator of mitochondrial permeability transition [219]. In contrast, the

addition of a 75 μM Ca^{2+} chloride bolus induced an increase in absorbance due to the formation of Ca^{2+} phosphate granules scattering light at this wavelength [220]. The gradual decrease in absorbance that follows is attributed to mitochondria fragmenting over time in response to the Ca^{2+} insult. For both CsA-treated groups, the Ca^{2+}-dependent increase in absorbance was sustained followed by a much slower decrease. However, the decrease in signal is not due to mitochondrial fragmentation but rather due to the inner membrane reorganization and matrix expansion [26, 191]. This phenomenon is discussed in latter sections of this report when classifying CsA-treated mitochondria. These results are similar to findings from a recent study that looked at the effects of the mitochondria-targeting peptide SS-31 on reducing infarct size of reperfused ischemic hearts [171]. In that study, the changes in absorbance after CsA treatment following addition of Ca^{2+} chloride are very similar to our results.

Our interpretation of the absorbance data is supported by our Ca^{2+} uptake data shown in **Figure 3.2D**. These data also demonstrate the profound beneficial effects of CsA on mitochondrial Ca^{2+} sequestration. When CsA was absent, mitochondria were not able to maintain Ca^{2+} homeostasis and Ca^{2+} was released into the buffer. For the 75 μM Ca^{2+} chloride challenge, this release was gradual and suggests there is a snowball-like effect in which mitochondria with lower Ca^{2+} tolerances release their Ca^{2+} loads and force other mitochondria to take up even more Ca^{2+} [125, 203, 221]. This results in additional mitochondria losing their ability to retain Ca^{2+}, and the process repeats until the entire mitochondrial population is compromised. In contrast, mitochondria were not able to effectively take up and store the 100 μM Ca^{2+} bolus at all when CsA was absent. This level of Ca^{2+} overload is sufficient to rapidly compromise the entire population in short order.

The Effects of Ca^{2+} Overload on Mitochondrial Ultrastructure

To capture mitochondria undergoing MPT during Ca^{2+} overload, we used the sampling scheme shown in **Figure 3.3**. These samples were drawn from a cuvette of isolated mitochondria at the indicated time points and subsequently vitrified in liquid ethane and imaged using cryo-EM. A total of 1345 cryo-EM images were analyzed and organized by sample time-point; before adding Ca^{2+} (t0) and 1.5 mins (t1), 4 mins (t2), and 10 mins (t3) after adding a Ca^{2+} bolus.

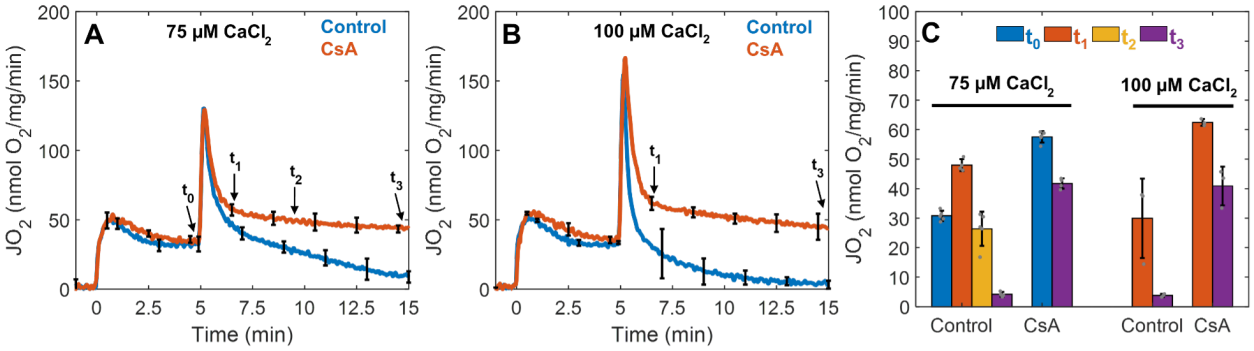

Figure 3.3: Cryo-EM sample collection protocol and time-points. (A) For the 75 μM $CaCl_2$ bolus, 5 μl of the mitochondrial suspension were collected and deposited on the Quantifoil holey-carbon grid at 5 mins just before Ca^{2+} addition (t0), approximately 1.5 mins after Ca^{2+} addition (t1), 4 mins after Ca^{2+} addition (t2), and 10 mins after Ca^{2+} addition (t3). (B) For the 100 μM $CaCl_2$ bolus, the mitochondrial suspension was sampled at t1 and t3. In all conditions, mitochondria (0.1 mg/mL) were energized with 5 mM sodium pyruvate with 1 mM L-malate. (C) The effect of Ca^{2+} in the presence or absence of CsA was quantified for each time-point. In the absence of CsA, mitochondrial respiration decreases dramatically as a function of time and the effect is exacerbated at greater Ca^{2+} loads. In the presence of CsA, mitochondrial respiration was maintained. Data are presented as mean $\pm$ standard deviation for $n = 3 - 5$ biological replicates.

We found that many mitochondria shared certain features at each time point and grouped them into 5 stages based on morphology and structure. Each stage represents the transition leading towards complete fragmentation and loss of function in the context of Ca^{2+} phosphate granules abundance, growth, outer membrane rupture, cristae integrity, and inner membrane fragmentation (**Table 3.1**). These panels represent the typical process induced

by a 75 μM bolus of Ca^{2+} in a population of isolated mitochondria.

Stage	Characterization	n
1	Rounded mitochondria, intact IMM/OMM with small or no granules present	33
2	Large granules are present, initial localized OMM rupture, altered OMM morphology	59
3	OMM partially or completely lost, IMM evisceration begins, granules dissolve	48
4	Significant IMM fragmentation, granules mostly dissolved	69
5	Complete IMM fragmentation and granules completely dissolved	65

Note: IMM - inner mitochondrial membrane; OMM - outer mitochondrial membrane.

Table 3.1: Mitochondrial Stages of Permeabilization Inferred from Structural Data

Figures 3.4 shows the effects of calcium on mitochondria. Adding a 75 µM calcium bolus induces the formation of calcium phosphate granules in the mitochondrial matrix, as seen in representative images from stages 1-4. The lighter circle is the hole of the Quantifoil carbon grid. Mitochondria typically adhere to the carbon support film that is made hydrophilic after plasma treatment, so they are often either entirely on the carbon or half-on and half-off as shown in these images. The images from stage 2-4 contain ice contamination. These ice crystals appear as dark spots with a white fringe or halo outside and below or to the side of the mitochondria. These are easily distinguishable from Ca^{2+} phosphate granules located in the mitochondrial matrix. Mitochondria in stage 1 have intact inner and outer membranes and are typically round (**Figures 3.4A** and **Supplemental Figure A.1**). Cristae structures in this set of images are hard to distinguish; however, some are identifiable. Before the addition of a Ca^{2+} bolus mitochondria are smaller and their inner and outer membranes remain intact as shown by the insets in **Figure 3.4B** – **D**. The number of Ca^{2+} phosphate granules is relatively low with sizes averaging less than 100 nm in size. After the addition of 75 µM Ca^{2+} chloride, mitochondria begin to fragment and lose bioenergetic competency. The beginning of this process is characterized by stage 2 (**Figures 3.4** and **A.2**).

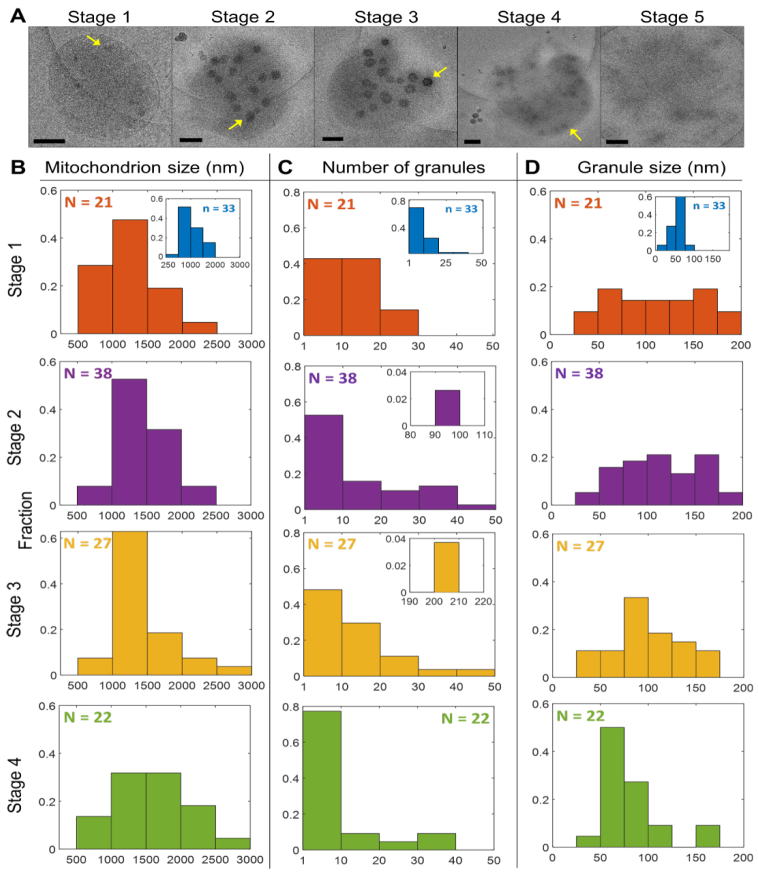

Figure 3.4: Ca^{2+} induces Ca^{2+} phosphate granule formation, OMM rupture, and IMM evisceration. (A) Representative images of mitochondria from stages 1-5 show Ca^{2+}. Scale bars: 250 nm. The insets for Stage 1 histograms (B-D) were calculated from images collected before a 75 µM Ca^{2+} bolus, where granules resulted from ∼4 µM Ca^{2+} contamination. A 75 µM Ca^{2+} bolus leads to larger, abundant granules. (B-D) Mitochondrial size and Ca^{2+} phosphate granule number and size were quantified. Mitochondrial size is constant, and granule abundance decreases by stage 4. Granules dissolve following IMM fragmentation and loss of $\Delta\Psi_m$. n represents the analyzed images per stage. Histogram data represents only mitochondria with granules. Arrows point to Ca^{2+} phosphate granules.

In this stage, regions of localized outer membrane rupture are observed and are always accompanied by the appearance of Ca^{2+} phosphate granules. While the size of granules within a mitochondrion does not vary significantly, differences between mitochondria are common and noticeable (**Supplemental Figure A.3**). During the transition from stage 2 to stage 3, outer membrane definition is lost and the inner membrane is released. The inner membrane also begins to fragment in this stage. In some instances, Ca^{2+} phosphate

granules are still present indicating that the inner membrane is still energized. However, there are also images of this stage showing granules in the middle of dissolution (**Supplemental Figure A.4**), so this stage is when depolarization begins. Unexpectedly, the granules appear to dissolve from the inside out. In stage 4, the outer membrane is almost entirely gone, and inner membrane is extensively fragmented. Stage 5 is characterized by the complete fragmentation of the mitochondrial inner membrane and is the dominant stage at the 15 min time point. In this stage, mitochondria are deenergized and contain no Ca^{2+} phosphate granules. Therefore, Stage 5 mitochondria was excluded from the analysis.

Interestingly, there were no large differences in mitochondrion sizes between the time points (ranging 500 – 3000 nm with mean values ∼1400 nm), but there were some clear differences in the size and number of granules (**Figure 4.4A – D**). As mitochondria transition from stage 1 to stage 3, the increase in absorbance shown in **Figure 3.2C** is caused by the increases in numbers and sizes of Ca^{2+} phosphate granules. In fact, the number of Ca^{2+} phosphate complexes per mitochondrion reaches a maximum by stage 3 and decreased in the following stage as shown in **Figure 4.4C**. The decrease in size and abundance by stage 4 is due to more complete mitochondrial permeabilization and fragmentation. Hence, for the first time to our knowledge, the MPT phenomenon now has direct visual confirmation of the processes proposed to occur. However, our results elucidate a mechanism that pinpoints cristae remodeling and inner membrane fragmentation as the key determinant of mitochondrial dysfunction as discussed further below.

CsA Preserves the IMM, Promotes Granules of Greater Size, and Increases their Abundance

Next, we repeated the calcium overload imaging experiments in the presence of CsA

to understand how mitochondrial respiration and calcium handling were preserved from an ultrastructural perspective (**Figure 3.5** and **Supplemental Figure A.5**).

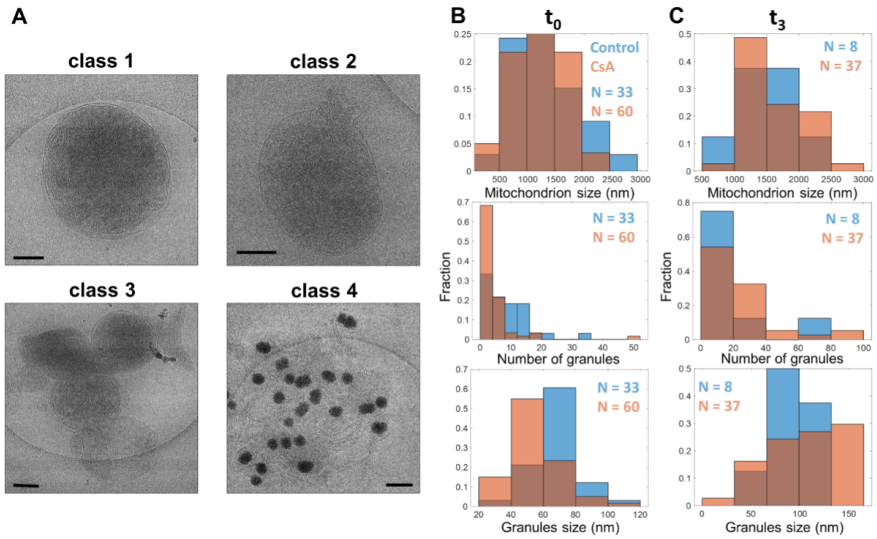

Figure 3.5: The effects of CsA on mitochondrial morphology and calcium-induced calcium phosphate granule formation. The images were taken before the addition of a 75 µM calcium bolus (t0) in the presence of 1 µM CsA. (A) Four classes of CsA-induced mitochondrial morphological changes are described in **Table 3.2**. (B) The mitochondrial size was significantly greater in the absence of CsA before the addition of calcium, but not after its addition (see **Supplementary Table A.2**). Furthermore, the group treated with CsA exhibited significantly larger and more calcium phosphate deposits compared to the control group before the addition of calcium, but not after (see **Supplementary Table A.2**). The scale bars are 250 nm. In this study, the scale bars used to represent the images were set at 250 nm. A total of 33 and 60 images were analyzed for the control and CsA groups, respectively, before the addition of calcium (t0), while 8 and 37 images were analyzed for the control and CsA groups, respectively, after calcium was added.

Similar to control mitochondria, CsA-treated samples were grouped into 4 classes based on morphology (**Table 3.2**). However, the classes are not related to a sequence of events like the stages, rather they are descriptive. Many of the images showed normal looking mitochondria with well-defined inner and outer membranes. These are class 1 mitochondria. Some of these mitochondria contained granules caused by uptake of low levels of contaminant calcium. In addition, some mitochondria had a condensed inner membrane that was sometimes localized to one side of the mitochondrion. These electron-dense regions are presumably

area of high cristae density. Interesting, some images showed mitochondria with the outer membrane ruptured with the inner membrane partially or more completely ejected from the mitochondrion. These mitochondria are classified as class 2 mitochondria. In other images, mitochondria were clustered together and are defined as class 3 mitochondria. Lastly, after the calcium treatment, images revealed mitochondria with no outer membrane, large calcium phosphate granules, and the inner membrane spread across the carbon grid. These mitochondria are classified as class 4 mitochondria. Because of morphological changes induced by CsA and calcium addition, the sizes of these mitochondria are larger than mitochondria in the other classes. In addition, mitochondria in this class had granules of heterogeneous sizes between but rarely within a single mitochondrion (**Supplemental Figure A.6**). Despite these radical changes in ultrastructure, the mitochondria remain functionally competent as shown in **Figure 3.2**. The best explanation for this observation is that the cristae junctions and inner membrane integrity is preserved by the CsA treatment.

Class	**Characterization**	**n**
1	Intact mitochondria with defined OMM and condensed OMM ± granules	215
2	IMM ejection	48
3	Clustered mitochondria	81
4	IMM spread out but intact with granules present	219

Note: IMM = inner mitochondrial membrane, OMM = outer mitochondrial membrane.

Table 3.2: Mitochondrial Classes of Inferred After CsA Treatment

The results showed that before the addition of calcium (t0), the average mitochondrial size, abundance, and size of calcium phosphate granules per mitochondrion are significantly lower and smaller in the presence of CsA compared to the control group (see **Figure 3.5**). Specifically, the average size of control mitochondria was 1319 ± 550 nm (n = 33), the average granule size was 68 ± 14 nm (n = 33), and the average number of granules per mitochondrion was 9.7 ± 3.1 (n = 33). In contrast, the average size of CsA-treated mitochondria was 1180

± 400 nm (n = 60), the average granule size was 55 ± 16 nm (n = 60), and the average number of granules per mitochondrion was 5.1 ± 2.3 (n = 60) (**Supplemental Figure A.12**. Although noticeable differences were observed following calcium administration (t3), these differences were not statistically significant (see **Supplemental Table A.2**). At t3, the average mitochondrial size for control mitochondria was 1473 ± 530 nm (n = 8), the average granule size was 90 ± 22 nm (n = 8), and the abundance was 18.0 ± 4.3 (n = 8) per mitochondrion, while the CsA-treated group had an average mitochondrial size of 1625 ± 400 nm (n = 37), an average granule size of 102 ± 36 nm (n = 37), and an abundance of 26.0 ± 5.1 (n = 37) per mitochondrion (**Supplemental Figure A.12**). Notably, only a small number of control mitochondria survived until the last time point (see **Figure 3.5C**).

Mitochondrial Membrane Fragmentation Occurs More Rapidly at Greater Ca^{2+} Loads but is Mitigated by CsA

Seeking to understand the observed large amplitude swelling for the control group after the addition of a 100 µM calcium chloride bolus, 8 images of intact control mitochondria were collected after a 100 µM calcium bolus addition. Most of the images displayed outer membrane rupture at multiple regions suggesting a rapid expansion of the inner membrane compared to the 75 µM calcium bolus (**Figure 3.6** and **Supplemental Figures A.7** and **A.8**). Thus, at this high of a calcium bolus, the morphological changes were caused by what appears to be *bona fide* permeability transition pore opening. As expected, CsA prevented this rapid expansion and led to the formation of numerous and large calcium phosphate granules. This effect was observed consistently in all 33 intact mitochondrial images that were analyzed. Without CsA, the size and abundance of the granules were noticeably decreased (**Figure 3.6B** and **Supplemental Figure A.12**). While there were no differences

in mitochondrion sizes between treatments shortly after calcium addition (1315 ± 370 nm (n = 17) vs 1487 ± 380 (n = 68)), the average control mitochondrial size decreased to 1163 ± 440 nm (n = 12) in the last time point (**Figure 3.6C** and Supplemental Figure A.12). In contrast, the average CsA-treated mitochondrion size increased to 1710 ± 440 nm (n = 83). The average number of granules in control mitochondria as a function of time was reduced from 9.6 ± 3.1 (n = 17) to 6.6 ± 2.6 (n = 12). The average size of these granules marginally increased from 84 ± 32 (n = 17) to 90 ± 37 nm (n = 12). The average number of granules in CsA-treated mitochondria increased from 46.1 ± 6.8 (n = 68) to 107 ± 10 (n = 83) with average sizes increasing from 121 ± 21 (n = 68) to 133 ± 28 nm (n = 83). These values are greater compared to the values measured after a 75 µM calcium bolus was given. This is consistent with CsA increasing calcium accumulation and preserving mitochondrial function even at these high calcium loads. However, the oxygen consumption rate after the 100 µM calcium bolus was significantly lowered compared to the 75 µM calcium bolus (**Figure 3.2A** and **3.2B**). Hence, we conclude that calcium induces irreversible effects on mitochondrial function and CsA, although not entirely protective, delays complete loss of function and allows more calcium uptake.

Calcium Phosphate Deposits are Composed of Smaller Structural Units

Calcium phosphate complexes are considered the main component of the mitochondrial calcium sequestration system [78, 164, 222]. Pioneering studies by Posner and others suggested that amorphous calcium phosphate consists of many smaller spherical elements with a chemical composition of $Ca_9(PO_4)_6$ [223–226]. These elementary calcium phosphate units were named as Posner clusters with a diameter ranging from 0.7 to 1.0 nm [226]. In the

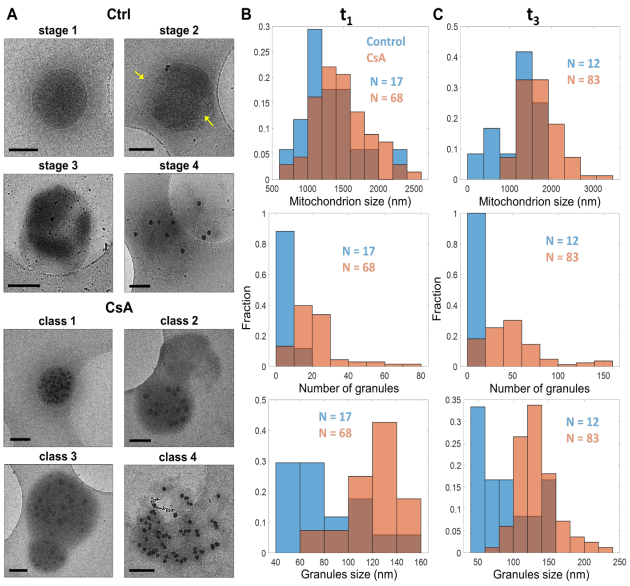

Figure 3.6: At extreme calcium loads, CsA preserves the IMM. Representative images before a 100 µM $CaCl_2$ ± 1 µM CsA. (A) Granules of various sizes between but not within a mitochondrion are observed following a 100 µM $CaCl_2$ bolus. Membrane rupture ensues in control mitochondria in multiple location as shown by the arrows. However, mitochondria treated with CsA were protected. (B) There are no differences in the mitochondrial size following Ca^{2+} addition between control and CsA-treated mitochondria at t1 (see **Supplemental Table A.2**). (C) At 10 mins following a $CaCl_2$ bolus, the mitochondrial and granule size and number become larger following CsA treatment. The opposite is true for control mitochondria due to membrane fragmentation and evisceration. A total of 17 and 68 images were analyzed for the control and CsA groups, respectively, shortly after the addition of calcium (t1), while 12 and 83 images were analyzed for the control and CsA groups, respectively, 10 minutes after calcium was added (t3). Scale bars are 250 nm.

present study, we lack the image resolution to resolve individual Posner clusters. However, our data show that the calcium phosphate granules are composed of highly electron-dense regions that resemble Posner clusters stacked together forming a higher order granule structure as shown in **Figure 3.7**. Our data also reveal that these structures are independent of CsA treatment or sampling time with the only major difference between clusters being their size. Assuming that these higher order granule structures are packed in a body-centered cubic lattice, the volume fraction of solid calcium phosphate is approximately 70 %. Computing the total volume fraction of these granules by multiplying the volume of individual

granules and their numbers per estimated mitochondrial volume (based on measured diameters and approximate thickness of 300 nm) gives an average volume fraction of 0.025. The thickness is a constraint applied after thinning the water layer before vitrification. Then by assuming a Posner cluster volume of 0.32 nm^3, the average calcium load per mitochondrion is 796 nmol/mg. To convert from mitochondrial volume to mitochondrial mass, we used the estimate of $6x10^9$ mitochondria/mg reported in Beavis and Garlid [191]. This value, 796 nmol/mg, is strikingly similar to the expected value of 750 nmol/mg calculated from the calcium uptake data shown in **Figure 3.2D**. Thus, these images yield expected values of calcium uptake and show the overwhelming majority of calcium taken up by mitochondria is stored in these calcium phosphate granules.

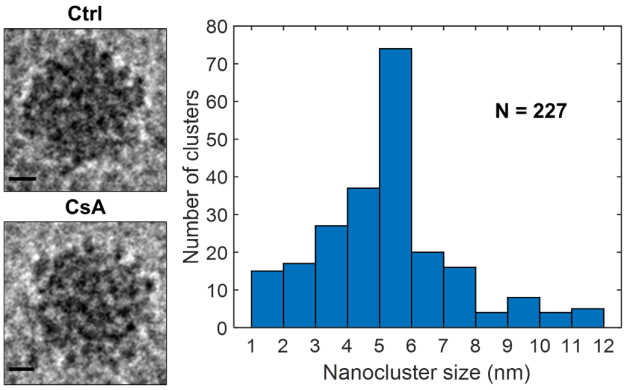

Figure 3.7: Calcium phosphate granule structure. (Left) Representative images of calcium phosphate granules for each calcium condition in the presence or absence of CsA shows near identical structure. (Right) Each granule consists of many individual electron-dense calcium phosphate nanoclusters with a diameter of 5.3 ± 2.1 nm. Scale bars are 25 nm.

While most of the isolated mitochondria contained calcium phosphate granules following the calcium addition, a few did not. There are two possible explanations for this phenomenon; either this group of mitochondria is 1) de-energized preventing calcium uptake or 2) they lack mitochondrial calcium uniporters (MCU). Based on the following statistical arguments, the latter is a more likely explanation. Assuming there are 40 MCUs per mitochondrion

[125] with an estimated standard deviation of 20, the probability of randomly selecting a mitochondrion without an MCU channel is 2.3 %. This corresponds to 11 mitochondria in our total set of 502 images. In agreement with this estimation, our data show that 17 mitochondria do not possess granules after either calcium bolus was given which corresponds to 3.4 % of the number of mitochondria imaged. This percentage is independent of treatment with 3.5 % of control mitochondria and 3.6 % of CsA treated mitochondria without any calcium phosphate granules. These results also match the respirometry data given in **Figure 3.2** whereby even after a large bolus of calcium chloride, some mitochondria are bioenergetically competent and synthesize ATP after the ADP bolus. Assuming that the boluses of calcium were enough to elicit MPT in the mitochondria with an MCU channel, the measured ADP-stimulated respiratory rate increase must be due to mitochondrial lacking an MCU. In line with this observation, the maximum ADP-stimulated respiratory rate for each calcium treatment relative to the maximum rate without calcium (as shown in **Figure 3.2**), is 11.1 % ± 4.6 (n = 3, p = 0.0007) and 6.9 % ± 1.4 (n = 3, p = 0.00004) for the 75 µM and 100 µM calcium bolus, respectively. These values are strikingly close to the value estimated from the imaging data.

A New Sequence of Events that Leads to Mitochondrial Dysfunction

The current leading hypothesis of calcium-induced mitochondrial dysfunction involves the peptidyl-prolyl *cis-trans* isomerase, cyclophilin D (CypD), interacting with as yet to be identified inner membrane proteins to form the permeability transition pore [132, 139, 207, 211, 227]. When open, the pore results in sustained membrane depolarization, large amplitude swelling, and calcium release [149, 206], and loss of mitochondrial respiratory control.

However, CsA can bind to CypD and sequester it so that its interaction with its target is prevented [143]. However, CsA is not fully protective. It is thought that it only increases the calcium threshold required to open the pore. This idea is based on studies that show CsA increases the calcium retention capacity by nearly 3-fold [220]. While an attractive hypothesis, this model has problems that are easier to explain using a different mechanism. As an alternative, we propose a novel mechanism of action whereby CsA enables robust calcium accumulation in the context of promoting calcium uptake and calcium phosphate granule formation. This mechanism involves the interaction between putative CsA-regulated proteins, and cristae structural proteins to preserve the inner membrane intactness. While the calcium phosphate granules may induces changes in morphology by mechanically disrupting membranes, it is plausible that free calcium interacts with proteins regulating inner membrane and cristae maintenance (namely the optic atrophic factor 1 and the mitochondrial contact site and cristae organizing system; known as OPA1 and MICOS) or additional regulators of this system. For instance, the stress-sensing overlapping activity with *m-AAA* protease 1 (OMA1) is a zinc metallopeptidase found in the inner mitochondrial membrane regulating mitochondrial dynamics through OPA1 processing [123, 131, 228]. OMA1 is activated under stress conditions including $\Delta\Psi_m$ dissipation, decreased ATP levels, and oxidative stress, among other insults [131]. Upon activation, OMA1 cleaves the long isoform inducing cristae remodeling and cyt. c release [123, 229–232]. This mechanism can explain the morphological and functional changes included by calcium overload that we observed in our cryo-EM images and bioenergetics data.

Indeed, we demonstrated that calcium overload impairs mitochondrial ATP production at greater calcium loads and depleting mitochondria of calcium did not fully restore function which indicates an irreversible component. These data revealed an underappreciated

energetic consequence of calcium overload on the mitochondrial function that supports a direct role of the mitochondrial calcium buffering system. In cardiac tissue, the steady-state cycling of calcium across plasma membranes maintains cytosolic calcium levels at ∼100 nM during diastole; however, the peak calcium concentration during systole can rise to the low micromolar range [155, 197, 214]. Whether the mitochondria can respond to these transient changes to meet metabolic demand is a subject of debate (reviewed in [197]) that revolves around the mitochondrial calcium uniporter (MCU) being unable to approach maximum flux rates in the transient rise of cytosolic calcium due to its low affinity for calcium [78]. Alternative hypotheses regarding calcium microdomains have been proposed in an attempt to argue in favor of significant mitochondrial calcium uptake during systole [127, 154, 164, 166, 233]; however, direct imaging studies do not support this [155, 234]. A recent study by Wescott et. al found that physiological cytosolic calcium transients causes a gradual, step-wise increase in matrix calcium concentration per beat rather than large transient peaks [125]. They also showed that at high pacing rates, the matrix calcium concentration did not change any further. Indeed, further studies are required to determine whether these results are due to equal influx and efflux of calcium per cycle or due to calcium buffering. At this point, we think the calcium buffering in the form of calcium phosphate granules system becomes relevant. In a separate study, calcium phosphate granule deposits were observed in the matrix near cristae junctions in a variety of different eukaryotic cells under physiological conditions [222]. Given the relevance of calcium in bioenergetics, the presence of these calcium deposits may exert some degree of control over mitochondrial signaling and metabolism.

In **Figure 3.8**, we present a model that accounts for various characteristics of membrane fragmentation before the MPT onset. This model integrates findings from our cryo-EM analysis with mitochondrial function and recapitulates the effects of calcium on the mito-

chondrial structure. Based on our findings, we think that changes in mitochondrial ultrastructure can explain the loss of mitochondrial function in calcium overload as well as the protective effects of CsA. Our results suggest that mitochondrial outer membrane rupture and inner membrane fragmentation are caused by calcium overload whereas the formation of granules are a consequence of calcium uptake and accumulation. In the present study, the detrimental effects of calcium overload on mitochondrial function are mitigated when CsA is present. Regardless of the calcium bolus, the number and size of granules in CsA-treated mitochondria increased, suggesting that CsA increases the mitochondrial calcium buffering capacity, thus explaining why CsA allows robust calcium uptake and increases the threshold for permeability transition pore activation [143, 175, 211, 235].

To interpret these results, we sought confirmation of our findings from work by others. A study by Pinton's group [217] studied the effect of calcium overload on mitochondria in HeLa cells. Exposing HeLa cells to the ionophore ionomycin resulted in mitochondrial network fragmentation. However, in the presence of CsA, the mitochondrial network condensed and maintained its integrity after ionomycin treatment. In addition, a study looking at mitochondrial swelling using light transmittance in a single mitochondrion showed that calcium induces mitochondrial swelling in a concentration-dependent fashion [223]. CsA decreased this effect in a calcium-dependent manner, which led the authors to conclude that either CsA induces mitochondria shrinkage or calcium accumulation induces light scattering. We show that CsA increases the absorbance in a calcium-dependent manner and induces changes in mitochondria ultrastructure including condensed inner membranes and loss of outer membrane that often led to inner membrane unraveling. Therefore, our results are consistent with these studies but quantitatively describe the ultrastructural changes associated with calcium overload and how these changes are linked to mitochondrial function.

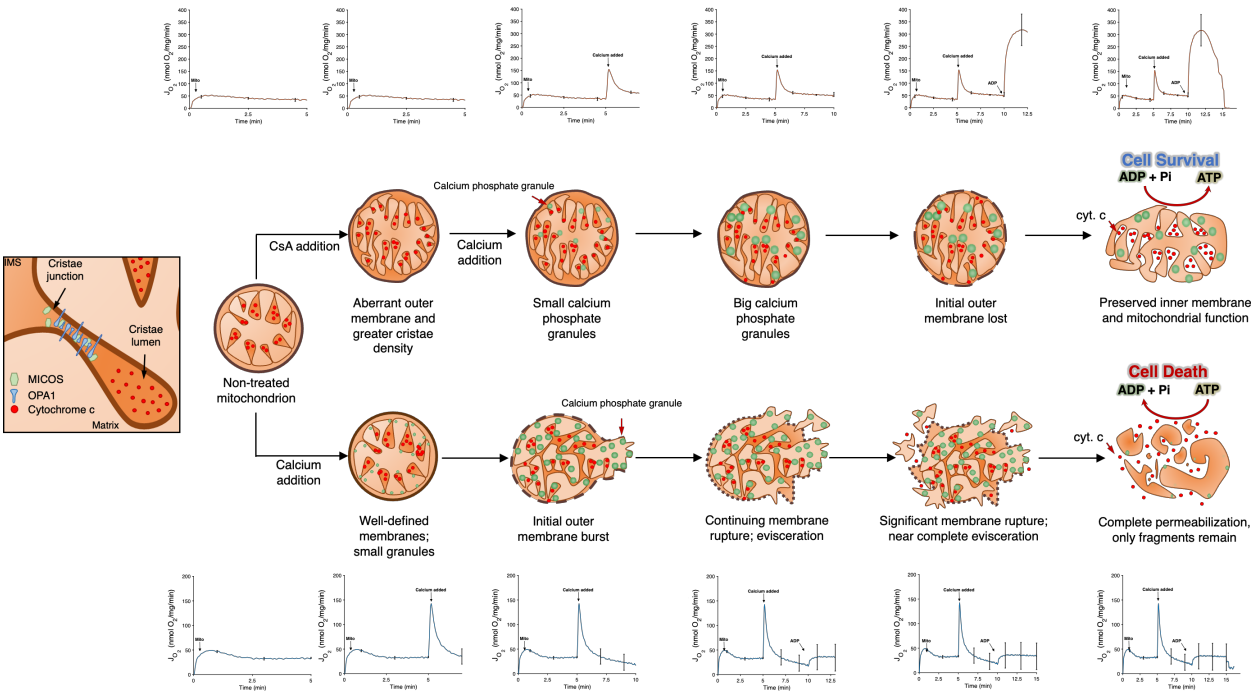

Figure 3.8: Schematic representation of calcium overload leading to mitochondrial fragmentation and permeabilization. In energized mitochondria, the $\Delta\Psi_m$ creates the driving force for calcium to accumulate in the mitochondrial matrix. This induces mitochondrial swelling and outer membrane rupture, IMM fragmentation and cyt. c release. This causes $\Delta\Psi_m$ dissipation and calcium-phosphate complex disassembly. CsA, however, alters the membrane morphologies and allows for robust calcium uptake after the addition of a $CaCl_2$ bolus. The IMM remains tethered and the cristae junctions intact. This avoids cyt. c remodeling and preserves the bioenergetic status despite the calcium effects on mitochondrial respiration. The representative respirometry traces are shown for each stage.

A major challenge in this study is the lack of cristae structural definition in our set of images. As dynamic structures, cristae are the functional units of mitochondria that lock cyt. c in the cristae lumen and provide sufficient membrane surface area to sustain oxidative phosphorylation at high rates [147, 232]. Under certain conditions when the cristae junctional width is enlarged, cyt. c escapes the lumen and causes loss of mitochondria function and cell death [236, 237]. While the expected outcomes during calcium overload were addressed, intricate details of the cristae structure including junction width, length, density, and shape must be incorporated to better understand the implications of cristae remodeling as key mediators in mitochondrial function. Earlier studies looking at calcium phosphate granule

composition relied on staining, fixing or dehydrating samples, which introduce artifacts and make them less reliable [135, 238–241]. More recently, changes in mitochondrial structure were analyzed using high-pressure techniques and freeze-substitution to minimize sample structural distortion resulting from fixation or dehydration [242]. However, structural details such as granule space distribution and structure are not as well defined with this method relative to the latest advanced cryo-EM techniques. Hence, visualization of the mitochondria in 3D by cryo-electron tomography (cryo-ET) would be an avenue for future studies to address. Nonetheless, our finding that CsA preserves the inner membrane integrity suggests that cristae remodeling and cyt. c release from the cristae lumen is likely avoided. This poses a new approach by which therapies targeting cristae remodeling can be identified to prevent pathological mitochondrial dysfunction leading to tissue injury.

3.4 Conclusion

Mitochondrial calcium overload causes mitochondrial respiratory dysfunction through the well-established mitochondrial permeability transition phenomenon. However, the precise and quantitative causal mechanisms are only recently coming into focus. In this study, we have shown that calcium-induced inhibition of ADP-stimulated respiration is reversible for low-to-moderate calcium loads (0 – 250 nmol/mg) but only partially reversible for higher calcium loads (more than 500 nmol/mg). Accumulating large quantities of calcium leads to the formation of calcium phosphate precipitates, outer membrane rupture, and eventually inner membrane fragmentation and evisceration. This results in loss of respiratory control and poor ATP synthesis rates. However, in the presence of CsA, the mitochondrial outer membrane is lost, but the ability of mitochondria to sequester significant amounts of calcium is retained with more abundant and larger calcium phosphate granules that persist. Here we

conclude from our functional and structural data that CsA preserves the inner membrane integrity and mitochondrial function by preventing detrimental cristae remodeling associated with calcium overload. These findings mechanistically link mitochondrial function to ultrastructure in the context of calcium overload and brings a new understanding of the calcium sequestration system in relation to energy metabolism, structure, and potential targets to prevent mitochondrial dysfunction.

Chapter 4

Modeling the Effects of Calcium Overload on Mitochondrial Ultrastructural Remodeling

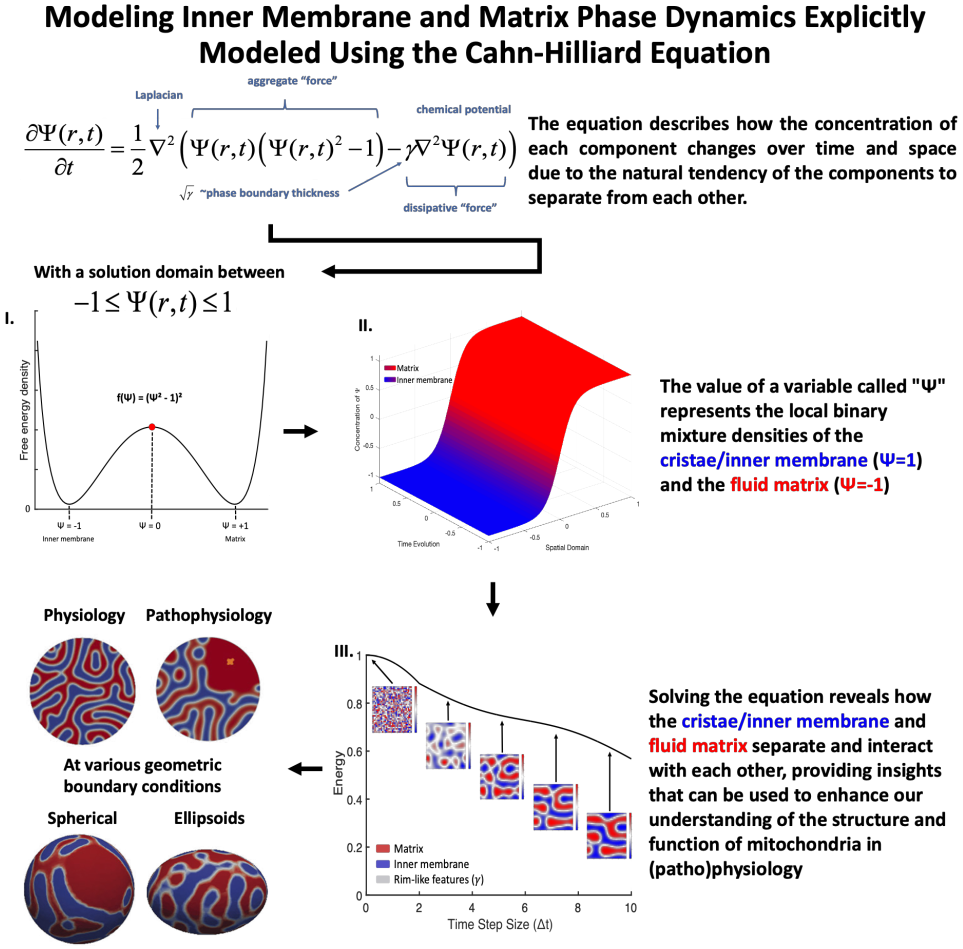

Figure 4.1: Graphical Abstract.

4.1 Introduction

Mitochondria are small organelles that provide the bulk of the energy requirements for nearly all cells in most eukaryotic organisms. They convert chemical energy in foodstuffs into a chemical potential called the ATP hydrolysis potential. Cells use this potential to synthesize proteins, power mechanical motion, sustain homeostasis, and perform other life-supporting functions. In the heart, the essential importance of mitochondria is evidenced by the fact that they constitute up to 30 % of the total cardiomyocyte volume. For example, in the absence of functional mitochondria, the heart will exhaust all of its ATP reserves in less than a minute [243], so even brief interruptions in mitochondrial ATP production have devastating consequences on energy homeostasis. Such interruptions in ATP production are caused by a myriad of diseases and conditions, with calcium overload being one of the more prominent causes. While low matrix-free calcium ($\leq$5 µM) activates matrix dehydrogenases and improves oxidative phosphorylation [244–246], calcium overload decreases ATP synthesis in a variety of ways [78, 247–263]. In extreme cases of calcium overload, there is a complete loss of mitochondrial ATP production caused by mitochondrial rupture and fragmentation [264–266]. The precise mechanisms responsible for these effects are unknown but appear to be associated with ultrastructural changes caused by calcium overload [78, 266]. Mitochondria consist of two compartments formed by two separate membranes: the outer membrane and the inner membrane. The outer membrane encases the inner membrane and serves as the gateway between the cytosolic and mitochondrial environments. This membrane forms transient connections with extra-mitochondrial organelles, such as the endoplasmic reticulum, ribosomes, nucleus, and inner membrane. The intermembrane space (IMS) compartment is between the outer and inner membrane, and the matrix compartment is encapsulated by

the inner membrane. The inner membrane surface area is approximately five to ten times that of the outer membrane and forms compartments called cristae that fit within the envelope of the outer membrane. Cristae are invaginations of the inner membrane that contain the bulk of the metabolic enzymes required to produce and deliver ATP to the cell. Both membranes are under the active control of fission and fusion proteins that react to external stimuli and energy demand cues to coordinate ATP production [267–269]. While the major fission and fusion proteins of the outer membrane are known, much less is known about the key proteins involved in inner membrane dynamics. Even less is known about regulation of the inner membrane structures, such as cristae and cristae junctions. While we still lack a complete picture of cristae formation and how they are regulated, some of the key proteins involved have been identified [270]. Cristae are not static structures [271]; they are dynamically formed in a manner dependent on a variety of known and unknown factors which control ATP synthesis rates [272]. That said, the main proteins that exert some control over the cristae's shape are the mitochondrial contact site and cristae organizing system (MICOS) [273–275], optic atrophy factor 1 (OPA1) [274, 276, 277], and ATP synthase [273, 278–280]. The MICOS proteins are necessary to form proper cristae junctions, a region in mitochondria that connects the inner boundary membrane to the cristae lumen. OPA1 is a protein with several isoforms and proteolytic variants that serves multiple roles [281]. These proteins coordinate with the MICOS proteins to form the cristae junction and help shape the cristae's morphology. ATP synthase dimers contribute to cristae morphology by inducing inner membrane curvature. Cardiolipin also plays an important role in regulating the cristae shape and membrane curvature [282]. A layer of regulation above this includes proteases and chaperones that process these structural proteins, such as OMA1 [283], YME1L [283], and prohibitins [284, 285], which are also intricately involved in a signaling network that

controls cristae morphology. However, the precise biophysical mechanisms that govern the shape of the inner membrane, including inner membrane fission and cristae structure, remain elusive. A few modeling studies have explored the potential role of mitochondrial proteins in the inner membrane architecture and metabolic function [286–295]. These studies investigate a range of phenomena, including how proteins and effectors influence inner membrane curvature and intra matrix diffusion anomalies. However, none have looked at the dynamics of the IMS and matrix volumes under healthy and diseased conditions. In addition, there are no computational studies focusing on how the inner membrane morphology influences ATP synthesis rates. Therefore, we propose a novel computational modeling approach capable of predicting the intermembrane and matrix space geometry under physiological and pathophysiological conditions. The spontaneous pattern formation and evolution of a two-component system can be described by several models, including the Canham–Helfrich curvature functional model, the Ginzburg–Landau theory, and the Cahn–Hilliard (CH) free energy [296–299]. Among them, the Canham–Helfrich model is typically used to describe cell membrane pattern formation in a water-based environment, driven by the curvature energy per unit area of the closed lipid bilayer, osmotic pressure, and surface tension [300]. This model captures cell membrane patterns without the molecular dynamics of the lipid bilayer. The Ginzburg–Landau theory describes the phase transition of type-I superconductors, the superconducting state, and the normal state without examining their microscopic electronic and magnetic properties. In the setting of a complex vector bundle over a compact Riemannian manifold, the Ginzburg–Landau theory interconnects differential geometry, quantum field theory, Yang–Mills–Higgs equations, and string theory, among others [301, 302]. The CH model is widely used in material science, chemistry, and biology to describe the phase separation of a binary mixture [303]. It is the simplest model among the aforementioned

theories. The CH model can be derived from the classic conservation law and free energy minimization, with the free energy function determining the final composition of the binary system [304, 305]. The pattern and morphology of the binary system is further determined by the domain size and geometric shape [234, 306]. The CH model can be modified to describe the nucleation dynamics and process of a specific species in the mixture [307, 308]. Additionally, multicomponent CH equations have been proposed to account for the phase separation of a system consisting of more than two species [309, 310]. These variations of the CH model enable researchers to develop CH-based theories and algorithms to understand the chemistry, physics, biology, and material sciences in a complex system that is intractable with detailed microscopic descriptions. For this study, we analyzed a set of cryo-electron tomograms of healthy and calcium overloaded mitochondria. These data show that the mitochondrial ultrastructural morphology undergoes dramatic changes in the presence of mitochondrial calcium phosphate granules. However, it is unclear how mitochondrial calcium phosphate granules regulate the mitochondrial ultrastructure. The tomographic data, combined with the respirometry data presented herein, support the concept that such morphological changes lead to a significant reduction in the mitochondrial ATP production rate. Based on these data, we speculate that the mitochondrial ATP production rate correlates with the types and numbers of cristae and cristae junctions. Our data show that a calcium overload causes significant remodeling of the inner membrane, which likely explains the decrease in mitochondrial respiration. To explore the dynamics of the pattern formation and phase separation of the mitochondrial ultrastructure, we used the CH model as a framework. We initially modeled the mitochondrial ultrastructure as a two-component system, consisting of the inner membrane space and the matrix space. The mitochondrial outer membrane served as the domain boundary of the system. We used a free energy function for the inner

membrane and a fluid matrix to demonstrate that minimizing the free energy inside a given outer membrane generates spontaneous folding of the inner membrane and the formation of layered structures, namely cristae. Next, we modeled the mitochondrial ultrastructural remodeling caused by calcium phosphate granules by using a volume exclusion approach in the CH model. By using this phase separation-based modeling approach, we show that the presence of calcium phosphate granules exerts a devastating remodeling effect on the inner membrane, which results in matrix expansion, IMS contraction, and cristae remodeling. These morphological changes correlate well with the observed changes in the ATP production rates. Future studies will further elucidate this structure–function relationship and mechanize how the inner membrane morphology impacts mitochondrial metabolism.

4.2 Methods

Ethical Approval

This work conformed to the National Institutes of Health's Guide for the Care and Use of Laboratory Animals and was approved by Michigan State University's Institutional Animal Care and Use Committee.

Mitochondria Isolation and Protein Quantification

Cardiac mitochondria were isolated from guinea pig hearts using differential centrifugation, as described previously [78, 255, 258]. Briefly, Hartley albino guinea pigs weighing 350–450 g (4–6 weeks) were injected with heparin (500 units/mL) in the intraperitoneal cavity. The animals were anesthetized with 4–5 % isoflurane and decapitated by a guillotine. After

decapitation, a thoracotomy was performed, and the heart was perfused with a cold cardioplegia solution and homogenized using a handheld electronic homogenizer at 18,000 rpm for 20 s. The mitochondrial protein content was quantified using the BIO-RAD bovine serum albumin (BSA) standard set kit and the bicinchoninic acid (BCA) assay. The mitochondrial suspension was diluted to a working concentration of 40 mg/mL and kept on ice for the duration of the experiment (2 - 3 h). The substrate stock solutions were neutralized to a pH of 7.0.

Mitochondrial Quality Control

The mitochondrial quality was determined using an Oxygraph 2k (Oroboros Instruments Corp., Innsbruck, Austria). The O2k chambers were loaded with 2 mL of a respiratory buffer containing 130 mM KCl, 5 mM K_2HPO_4, 20 mM 3-(N-morpholino) propanesulfonic acid (MOPS), 1 mM $MgCl_2$, 1 mM ethylene glycol-bis-(aminoethyl ether)-N, N, N′,N′-tetraacetic acid (EGTA), and 0.1 % (w/v) BSA at a pH of 7.1 and 37 °C. All subsequent experiments were done using this buffer and temperature. At 0 min, 5 mM sodium pyruvate and 1 mM L-malate were added, followed by 0.1 mg/mL of mitochondria. Here, we defined the leak state as the rate of oxygen consumption by mitochondria only in the presence of substrates. At 5 min, a 500 µM bolus of adenosine diphosphate (ADP) was added to induce maximal ADP-stimulated respiration. Quality was assessed by computing the respiratory control ratio (maximal ADP-stimulated rate divided by the leak rate). Only mitochondria with a respiratory control ratio (RCR) value greater than or equal to 16 were used in the experiments.

Calcium Effects on Respiration and Oxidative Phosphorylation

The calcium effects on mitochondrial leaking and ADP-stimulated respiration were determined by quantifying changes in the proton leak and ADP-stimulated respiration rates after a calcium challenge. At 0 min, 5 mM sodium pyruvate, 1 mM L-malate, and 0.1 mg/mL of mitochondria were injected into each 2 mL chamber containing the respiratory buffer. At 5 min, a calcium bolus of 50 µM of calcium chloride was injected. At 10 min, 500 µM of ADP was added induce the maximal ADP-stimulated respiration.

Cryo-EM Sample Vitrification and Imaging

Isolated mitochondria were suspended at a concentration of 0.1 mg/mL in a 2 mL respiration buffer with 5 mM sodium pyruvate and 1 mM L-malate. At the collection times indicated, 5 µL samples were pipetted from the mitochondrial suspension and deposited on Quantifoil R2/2 holey carbon grids that were pretreated for 1 min using a Pelco EasiGlo glow discharge unit. Prior to the mitochondria addition, 5–10 µL of 10 nm nanogold markers were applied to the grids, which were then air dried. These beads provided markers for fiducial alignment of the tilt series. The grids were blotted to thin the water layer and subsequently plunged into liquid ethane at room temperature using a Vitrobot Mark IV with automated temperature regulation, blotting, and humidity control (Fisher Scientific). The Vitrobot chamber was set at 4 °C with 100 % humidity, and the grids were blotted with a blot force of 1. The grids were then transferred and stored in liquid nitrogen until imaging. Tilt series were performed using an FEI Talos Arctica at 200 keV in low-dose conditions, operated using Thermofisher's Tomography software. Images were collected in linear mode on a Falcon 3EC direct electron detector with an electron dose of $\sim$2e-/Å^2 per tilt image. The images were collected at

22,000 X magnification (4.8 Å/pixel). The total electron dose was approximately 100 e-/$Å^2$ for each tomogram.

Tomographic Reconstruction

Motion correction was performed for the individual micrographs and binned by an index factor of 6 using Motioncor2 v1.2.6. Tilt series alignment was performed using IMOD v4.9.12 and standard tomographic reconstruction particles, using the Simultaneous Iterative Reconstruction Technique (SIRT) strategy. Key features of the tomograms were traced using the drawing tools functionality in IMOD (3dmod) [311].

Statistics

The Shapiro–Wilks test was used to confirm data normality. All data were analyzed and plotted using MATLAB 2020a (Mathworks, Inc., Natick, MA, USA). The data in **Figure 4.2** (n = 3–4) are presented as a mean standard deviation. An unpaired Student's t-test was used to compare the calcium treatment with the control group. A value of $p \leq 0.05$ was assumed to be statistically significant.

Modeling

$$\frac{\delta \Psi}{\delta t} = \frac{1}{2}\nabla^2(-\gamma\nabla^2\Psi - \Psi + \Psi^3) \tag{4.1}$$

Equation (4.1) describes how the scalar order parameter Ψ changes over time. It is a complex equation that cannot be solved using simple math and requires numerical simulation. In this context, Ψ is a measure of the difference between the densities of two substances, phases, or domains in a specific region. In our model, these two substances are the mitochon-

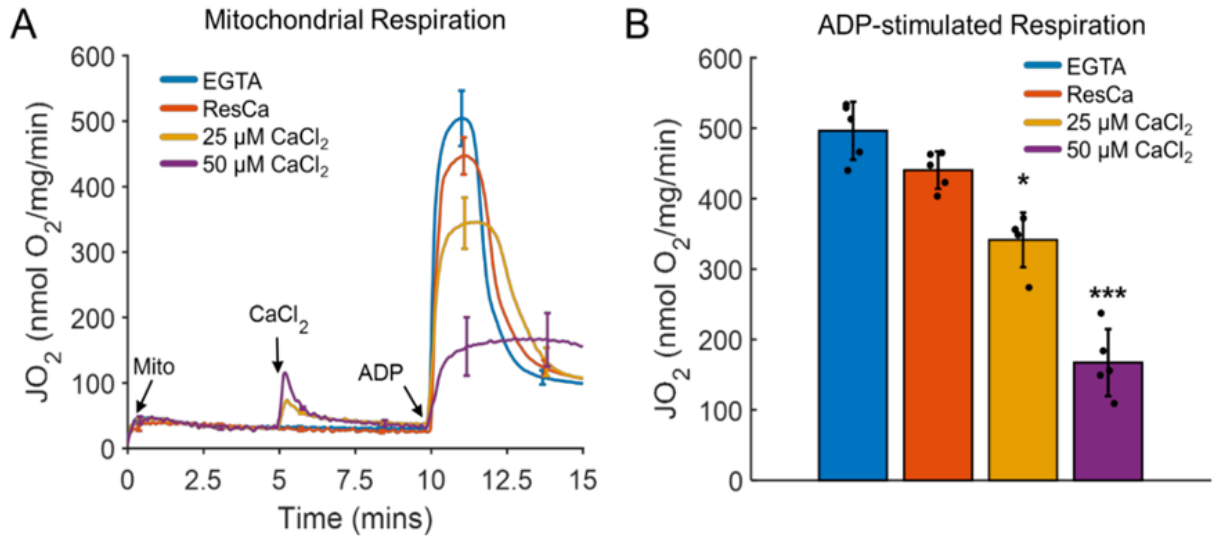

Figure 4.2: Oxidative phosphorylation decreasing proportionally with the calcium load. (A) Representative mitochondrial respiration profiles in the presence of the calcium chelator EGTA (∼4 µM residual calcium (ResCa)) and after a 25 µM or 50 µM bolus of calcium. The mitochondrial calcium loads for these conditions were 0, 40, 250, and 500 nmol calcium/mg mitochondria, respectively. Mitochondria were energized with 5 mM sodium pyruvate and 1 mM L-malate. (B) The average maximum ADP-stimulated respiration rate decreased dramatically at higher calcium doses. Maximal ADP-stimulated respiration was induced following the addition of a 500 µM ADP bolus. Data are presented as the mean ± standard deviation for a sample size of five biological replicates. Here, an * and *** represent p values ≤ 0.01 and ≤ 0.001, respectively.

drial fluid matrix and the inner membrane. Specifically, $\Psi(\mathbf{r}, t)$, where $(\Psi(\mathbf{r}, t) \vee \leq 1)$, is a scalar order parameter chosen to be the difference between the local densities of the inner membrane [Ψ = -1] and the fluid matrix [$\Psi = 1$]. The region is called a domain, and there is a transition region between the domain and the surrounding area, which is called a transition length. The length of this transition region is denoted by $\sqrt{\gamma}$ and represents the distance over which the density varies from that of the inner membrane to that of the fluid matrix. The Cahn–Hilliard equation is a fourth-order nonlinear partial differential equation (PDE), and it does not admit a general analytical solution. Therefore, numerical simulation is the primary approach to obtaining the solution of the Cahn–Hilliard equation. However, some theoretical analysis can offer a basic understanding of its behavior and underlying physics.

First, it is important to note that **Equation 4.1** can be cast in its conversational form:

$$\frac{\partial \Psi}{\partial t} = -\nabla \cdot \boldsymbol{J} \tag{4.2}$$

Where the flux vector $\boldsymbol{J}$ represents the flow of the scalar order parameter Ψ in space, and how it changes over time. The **equation** (4.2) states that the rate of change of Ψ with respect to time is proportional to the divergence of the flux vector $\boldsymbol{J}$. The flux vector $\boldsymbol{J}$ is defined as -$\frac{1}{2}\nabla\mu$, where μ is the chemical potential of the binary system. The chemical potential describes the potential energy of a substance in a given environment, and is related to the concentration of the substance. The equation (4.3) gives the expression for the chemical potential μ of the binary system, which depends on the value of the scalar order parameter Ψ and the Laplacian of Ψ. Therefore, the flux vector $\boldsymbol{J}$ represents the flow of the scalar order parameter driven by the gradient of its chemical potential, and the equation (4.2) represents the conservation of the scalar order parameter.

$$\mu = (\Psi^2 - 1 - \gamma\nabla^2)\Psi \tag{4.3}$$

In **Equation** (4.3), μ represents the chemical potential of the binary system. It is a function of the scalar order parameter Ψ and the parameter γ. The term $(\Psi^2 - 1)$ represents the deviation of Ψ from its equilibrium values ($\Psi = \pm 1$), and the term $\gamma\nabla^2\Psi$ accounts for the interfacial energy due to the spatial variation of Ψ. The equation describes the potential-driven flow in the system, which has a trivial solution at $\Psi = 0$ where both phases are in equilibrium and two nontrivial solutions at $\Psi = \pm 1$ representing two different phases each pure in its own phase. In other words, either all fluid matrix or inner membrane. The characteristic length of the crista is assumed to be one in this setting, and the domain size

should be chosen accordingly based on experimental data. The boundary condition for μ and Ψ is the usual zero-flux condition.

$$n \cdot \nabla \mu(r,t) = 0 \text{ and } n \cdot \nabla \Psi(r,t) = 0, \quad r \in \Gamma \tag{4.4}$$

where $\boldsymbol{n}$ is normal to the boundary and Γ is the boundary of the geometrical shape. When introducing calcium into the mitochondria system, the boundary condition around the calcium is given as

$$n \cdot \nabla \mu(r,t) = 0 \text{ and } \Psi(r,t) = C, \quad r \in \Gamma' \tag{4.5}$$

where $\boldsymbol{C}$ is a constant and Γ' is the boundary of the region $[\Psi = \boldsymbol{C}]$ corresponding to the calcium region. Moreover, the Cahn–Hilliard equation is related to the time-dependent Ginzburg–Landau equation, which can be derived from the free energy minimization. Similarly, the Cahn–Hilliard equation can also be derived from the minimization of the Ginzburg-Landau-type free energy functional $\boldsymbol{F}$:

$$F(\Psi) = \int_\Omega \left[f(\Psi) + \frac{\gamma}{2} (\nabla \Psi)^2 \right] dr \tag{4.6}$$

where Ω is the domain of interest and $f(\Psi) = \frac{1}{4}(\Psi^2 - 1)^2$ is the free energy per unit of volume. It is easy to show that the Ginzburg–Landau-type free energy functional decays with respect to time:

$$\frac{dF}{dt} = -\int_\Omega |\nabla \mu|^2 dr \tag{4.7}$$

This allows us to set various initial values, such as random noise, when solving the CH

equation.

Furthermore, we can linearize the CH equation to understand its long wavelength instability in spatially extended settings. Let us assume that the system is near the trivial solution $\Psi(\boldsymbol{r},\ \mathrm{t}) = 0$, implying a uniform steady state corresponding to the homogeneous mixture. Consider the following form of solution for a small fluctuation of the order parameter:

$$\Psi(\mathbf{r}, t) = \Psi_0 e^{\omega t} e^{i\mathbf{k}\cdot\mathbf{r}} \tag{4.8}$$

where $\boldsymbol{k}$ is the wavevector, $k = |\boldsymbol{k}|$ is the wavenumber, and *w(k)* is the angular frequency. The stability of the solution depends on the angular frequency. The system is linearly unstable when *w(k)* >0 and decays when *w(k)* <0. By substituting this solution into the linearized Cahn–Hilliard equation, we have the dispersion relation

$$\omega(k) = -\frac{1}{2}\left(k^4 - k^2\right) \tag{4.9}$$

Therefore, long wavelength states with $k < 1$ will be linearly unstable. Such a long wavelength instability is exploited by the nonlinear CH system. Short wavelength states with $k > 1$ will decay in a linear fashion and convert short wavelength modes (i.e., large domains) into spatiotemporal patterns. The system regulates the exponential growth tendency of long wavelength modes caused by random noise and organizes them into spatially coherent states. Therefore, the spatiotemporal patterns of certain characteristic wavelengths are stabilized in the CH equation. Due to computational challenges, most simulations were carried out in rectangular domains. Motivated by the microscopic phase separation and pattern formation of the spherical and cylindrical molecular assembly, Guan et al. considered the Cahn-Hilliard equation in a circular domain [280]. In the circular domain geometry, certain symmetric

patterns occurred frequently during the simulation. These authors found that the solution of the Cahn-Hilliard equation could be effectively analyzed with Fourier–Bessel modes [281]. In the current work, the finite element method (FEM) was considered due to its advantage in dealing with irregular domains. The Cahn-Hilliard equation is a fourth-order equation whose weak form would result from the presence of second-order spatial derivatives. Solving such a form with a standard Lagrange finite element basis is problematic. Therefore, **Equation 4.1**, with the boundary condition **Equation 4.4**, is reformulated as two coupled second-order equations:

$$\frac{\partial \Psi}{\partial t} - \frac{\gamma}{2}\nabla^2 \mu = 0, \quad \mathbf{r} \in \Omega \tag{4.10}$$

$$\mu - \frac{df(\Psi)}{d\Psi} + \nabla^2 \Psi = 0, \quad \mathbf{r} \in \Omega \tag{4.11}$$

where the unknowns are Ψ and μ. Then, the variational forms of **Equations 4.10** and **4.11** are

$$\left(\frac{\partial \Psi}{\partial t}, u\right) + \frac{\gamma^2}{2} a(\mu, u) = 0, \quad \forall u \in V \tag{4.12}$$

$$(\mu, v) - \left(\frac{df(\Psi)}{d\Psi}, v\right) - a(\Psi, v) = 0, \quad \forall v \in V \tag{4.13}$$

In Equations (**4.12** and **4.13**), μ represents the solution field and v is a test function from the trial space V. The term (μ, v) is the L_2 inner product, which represents the integral of the product of μ and v over the region. The term $\frac{df(\Psi)}{d\Psi}$ represents the derivative of the free energy functional $f(\Psi)$ with respect to Ψ. This term is subtracted from the inner product

to ensure that the equation is satisfied for any μ and v.

The term $a(\Psi, v)$ represents the bilinear form, which is defined as $a(\Psi, v) = (\nabla\Psi, \nabla v)$. This term is responsible for enforcing the diffusion of the solution and is essential for numerical stability.

To discretize this equation in time, the theta method is applied to the variational forms. This involves interpolating the solution field at two consecutive time steps and weighting the integral with a parameter θ, which controls the balance between the explicit and implicit terms. The resulting system of equations is then solved using appropriate numerical techniques, such as finite element or finite difference methods as follows:

$$\left(\frac{\Psi_{n+1} - \Psi_n}{\Delta t}, u\right) + \frac{\gamma}{2} a\left(\mu_{n+\theta}, u\right) = 0, \quad \forall u \in V \tag{4.14}$$

$$(\mu_{n+1}, v) - \left(\frac{\partial f_{n+1}}{\partial \Psi}, v\right) - a(\Psi_{n+1}, v) = 0, \quad \forall v \in V \tag{4.15}$$

where $\Delta t = t_{n+1} - t_n$ and $\mu_{n+\theta} = (1-\theta)\mu_{n+1} + \theta\mu_n$. The simulations operate on 2D triangle meshes and 3D tetrahedral meshes. In the following tests, we first present the simulations of a mitochondrial system without calcium using the CH models and then give the simulations of the system with calcium. Numerical implementation is done by applying the FEniCS [294], and simulation plots are generated by ParaView [295].

4.3 Results and Discussion

Oxidative phosphorylation was inhibited in the calcium overload state [78, 247–263]. As the calcium load increased, the maximal ADP-stimulated respiration was significantly inhibited,

as shown in **Figure 4.2**. This phenomenon is not associated with the well-known mitochondrial permeability transition phenomenon [258]. At these calcium loads, the mitochondrial calcium, membrane potential, and respiration were stable [78, 258]. The inhibitory effect began at calcium loads of around 50 nmol/mg of mitochondrial protein. This value was calculated based on the quantified calcium uptake dynamics of the residual calcium in one of our prior studies [255]. This inhibition got progressively worse as the calcium load increased up to 500 nmol/mg. Therefore, calcium loads in the range of 50 – 500 nmol/mg maximally stimulated the ADP-respiration rates to decrease in a titratable manner. The cause of this inhibition was suspected to originate from calcium phosphate granule-induced cristae remodeling in an earlier study [78]. Below this range, calcium is beneficial for mitochondrial function as it stimulates matrix dehydrogenases [246]. Above this range, mitochondria undergo mitochondrial permeability transition, deenergize, and become net ATP consumers. Specifically, the mitochondrial inner membrane becomes permeable to solutes in the low kDa range, effectively preventing their ability to store chemical energy in the form of a proton electrochemical gradient. Decades of research has been done on this phenomenon [312–315], but little is known about how mitochondria respond to calcium loads below the level which induces this phenomenon and above those used for energy homeostasis. Therefore, we explored how calcium loads that do not cause permeability transition but inhibit oxidative phosphorylation alter the mitochondrial ultrastructure. In the absence of calcium, mitochondria possess an intact and dense cristae network, as shown in **Figure 4.3**. The cryo-electron micrograph and a ∼10 nm thick portion of the corresponding 3D reconstruction show that in the normal state, the internal structure of the cristae network is highly interconnected. In the cryo-EM image, rows of ATP synthase molecules can be seen spiraling down the cristae, with their F_1 portion sticking out into the matrix space. The intermembrane and cristae

spaces are nearly equal to that of the matrix space. This ensures near-optimal metabolic efficiency by maximizing both the inner membrane surface area and the matrix water space. The inner membrane houses all the proton pumps, transporters, and enzymes required to establish, maintain, and utilize the proton electrochemical gradient for ATP production. The matrix space contains nearly all the enzymes that produce the reducing equivalents used to run the proton pumps. In addition, the cristae junction widths are tight and around 10 nm in diameter (see **Figure 4.4D**). The cristae junction serves as a gateway to allow some metabolites, such as ATP, ADP, and Pi into the cristae lumen to be rapidly transported outside the cristae and mitochondria. These junctions also serve to lock key metabolites such as cytochrome c in the cristae lumen. Cytochrome c is a small ($\sim$15 kDa) mobile electron carrier that is analogous in function to nicotinamide adenine dinucleotide in the matrix and ubiquinone in the membrane lipid space. By maintaining the cristae network and matrix spaces in the form discussed above, mitochondrial ATP production rates are maximized.

In the calcium-overloaded state, the mitochondrial ultrastructure was significantly altered, as is shown in **Figure 4.4**. The presence of calcium phosphate granules in the matrix space had a devastating effect on the intermembrane and cristae spaces. The matrix space was significantly expanded, with the intermembrane and cristae spaces being dramatically reduced when comparing the reconstructed 3D tomogram to the control mitochondrion. The matrix space expanded due to the increased osmotic pressure in the matrix that occurred when large amounts of calcium were taken up by the mitochondria. In addition, the cristae junctions were significantly wider, being about 17 nm when calcium phosphate granules were present in the matrix (**Figure 4.4D**). Based on this finding and our previous analyses in **Chapter 3**, we think that this increase in the cristae junction width can cause a redistribution of cytochrome c from the cristae lumen to the intermembrane space. A recent modeling

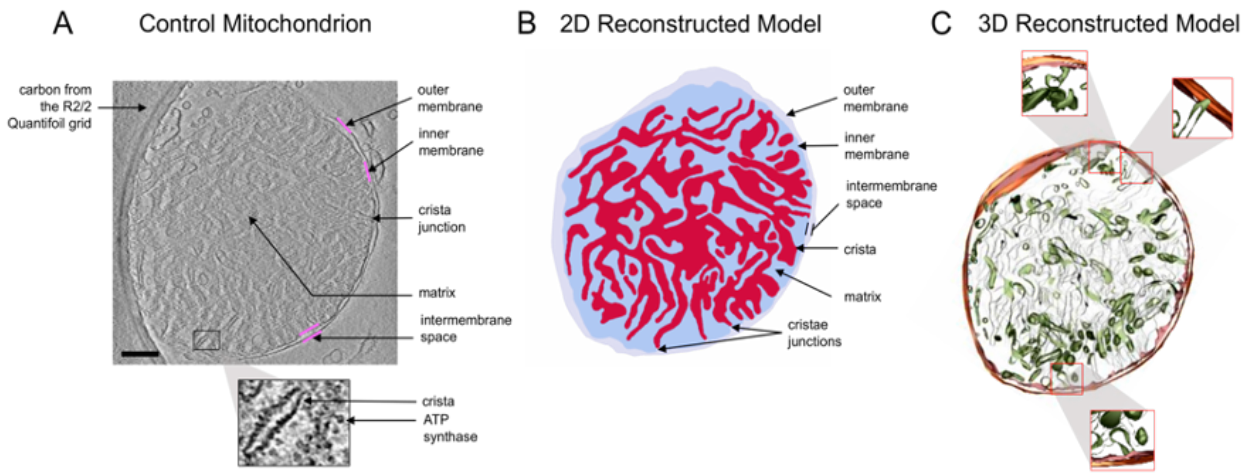

Figure 4.3: Mitochondrion with an abundant, interconnected cristae. (A) Representative portion of the tomogram from a mitochondrion in the absence of calcium. The sample was taken approximately five minutes after mitochondria were added to the respiration buffer. To remove all calcium from the system, 1 mM EGTA was added before the addition of the mitochondria. The image resolution is approximately 4 Åper pixel. The solid magenta lines highlight inner or outer membrane boundaries. Structures of interest, including the ATP synthase, crista, and crista junctions, are labeled. (B) The reconstructed model shows a complex cristae distribution, occupying nearly half of the total volume. The small, black, dot-like structures are ATP synthase molecules. (C) The 3D reconstructed model shows a densely packed, interconnected cristae network. Scale bar = 250 nm.

study demonstrated that a small decrease in the cytochrome c concentration in the cristae lumen or an increase in the diffusion distance between complexes III and IV may result in a kinetic disadvantage and lower the maximum electron flux through the respiratory system [294].

This would lead to a decrease in the maximum oxygen consumption rates we observe in calcium-loaded mitochondria. We speculate that the cristae remodeling we saw in our vitrified, isolated mitochondria impaired mitochondrial function by limiting the ability of mitochondria to 1) establish and maintain a large proton electrochemical gradient and 2) impede metabolite diffusion and transport. Additionally, calcium uptake leads to a drop in the membrane potential and an increase in the matrix pH [78, 258]. This limits the ability of mitochondria to generate a strong membrane potential and thus lower ATP synthesis

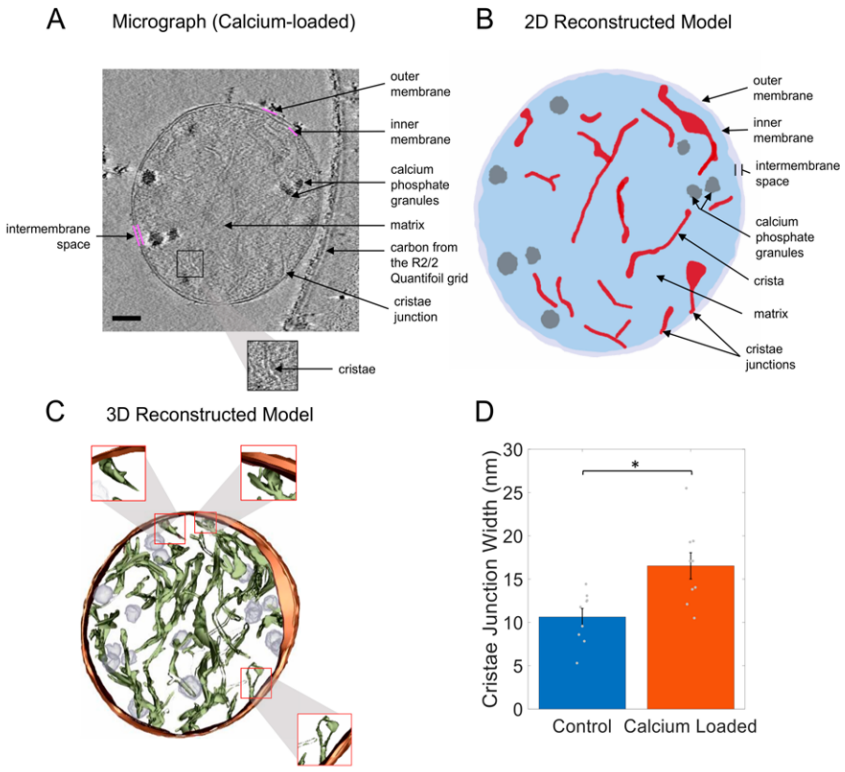

Figure 4.4: Calcium-loaded mitochondria with granules alters cristae structure. (A) Representative portion of a tomogram from a mitochondrion with calcium phosphate granules exposed to a 50 µM bolus of calcium at ∼4 Å-resolution. The solid magenta lines highlight the IMM and OMM boundaries. (B) 2D reconstructed model showing that calcium phosphate granules disrupted the cristae membrane surface area. (C) 3D reconstructed model showing a densely packed, interconnected cristae network. (D) Calcium-loaded mitochondria have wider cristae junctions than control. ∼10 cristae junctions from each type of mitochondrion were selected at random and measured. The bars are plotted as means of the data, with error bars representing the standard error of the mean. A * signifies a p value less than 0.01. Gray dots are individual data points for a sample size of n = 10. Scale bar = 250 nm.

rates [246]. In addition, the opening of the cristae junctions leads to a redistribution of cytochrome c from the cristae lumen to the inner membrane space. This further limit the ability of the proton pumps to maintain a local chemiosmotic gradient to support high rates of ATP production.

The mitochondrial morphology and the effects of calcium phosphate granules were simulated using the well-established CH model framework. The CH equation was first im-

plemented in the absence of calcium. In this simulation, the parameter γ represents the transition region length in the CH equation and is responsible for creating the white, rim-like features seen in **Figure 4.5**, which indicate the transition between the fluid matrix and the inner membrane. In other words, the value of γ determines the width of the interface between the fluid matrix and the inner membrane, and it affects the accuracy and resolution of the simulation. A larger value of γ would create a smoother transition region, while a smaller value would result in a more abrupt change. In this simulation, γ was set to one, resulting in a transition region with a moderate width. **Figure 4.5** presents four snapshots of the CH equation simulation with a time step $\Delta t = 0.001$ for **Equations 4.14** and **4.15** on a circle domain with a radius of four, relative to the unit circle with a radius of one. Of note, the time step Δt is considered dimensionless because it is a relative measure of time in the numerical simulation, which is not related to any physical time unit. In other words, the time step is chosen to control the accuracy and stability of the numerical simulation, and the unit of time used in the simulation is arbitrary and does not correspond to any specific physical time unit

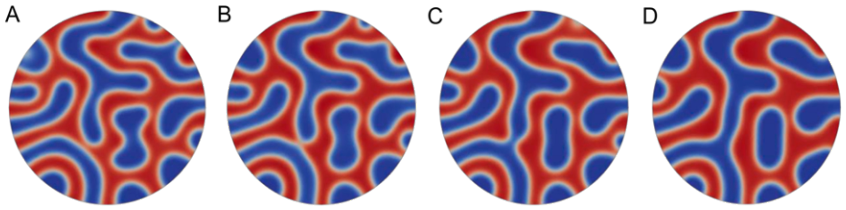

Figure 4.5: In the absence of calcium, the simulation of mitochondria using a circle domain with a radius of four showed that the inner membrane and fluid matrix were initially randomly and uniformly distributed within the domain. The time step Δt = 0.001 for (A) t_{750}, (B) t_{1250}, (C) t_{1750}, and (D) t_{2250}. Merging and splitting of the matrix and intermembrane spaces are observed as the simulation time is lengthened.

In **Figure 4.6**, a larger circle domain with radius of five is demonstrated. The parameter γ is one for the transition region length, which is indicated by the white, rim-like features

in **Figure 4.6**. The red domain of **Figure 4.6** is the fluid matrix, while the blue domain is the inner membrane part, which includes the cristae lumen. Compared with **Figure 4.5**, thinner cristae can be observed in **Figure 4.6**. This was caused by the high-frequency phase interactions introduced by imposing a larger domain. In the comparison with the experimental image, a similar pattern can be observed in **Figure 4.6**, in which cristae are randomly and uniformly distributed within the domain.

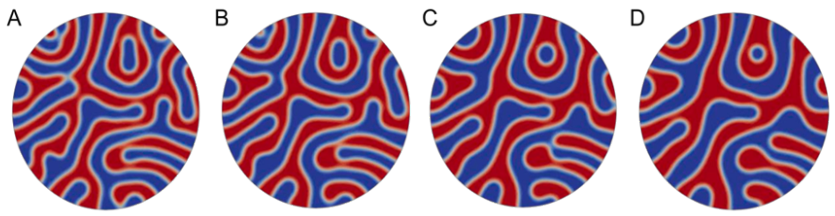

Figure 4.6: Calcium-free mitochondria simulation by a circle domain with a radius of five. The time step $\Delta t = 0.001$ for (A) t_{750}, (B) t_{1250}, (C) t_{1750}, and (D) t_{2250}. As shown in **Figure 4.5**, merging and splitting of the phase spaces are observed as the simulation time increases.

Implementation of the CH model on a mitochondrial structure can help us understand a plausible mechanism that explains the dramatic and titratable decrease in mitochondrial ATP production as a function of calcium overloading. **Figure 4.7** demonstrates the simulations of calcium load cases. In case one, a single calcium phosphate granule was loaded in the first quadrant. In the second case, and additional calcium phosphate granule was loaded in the fourth quadrant. In each panel, the orange objects indicate the location of the calcium phosphate granules. In a fascinating similarity with the experimental observations, the simulations revealed a dramatic reorganization of the cristae membrane because of the presence of calcium phosphate granules. In addition, the matrix space around the granules dramatically expanded. In the simulations, these effects were a result of an energy minimization problem. The presence of these granules near cristae membranes acted as a repulsive

force which led to matrix fluid filling the vacated space.

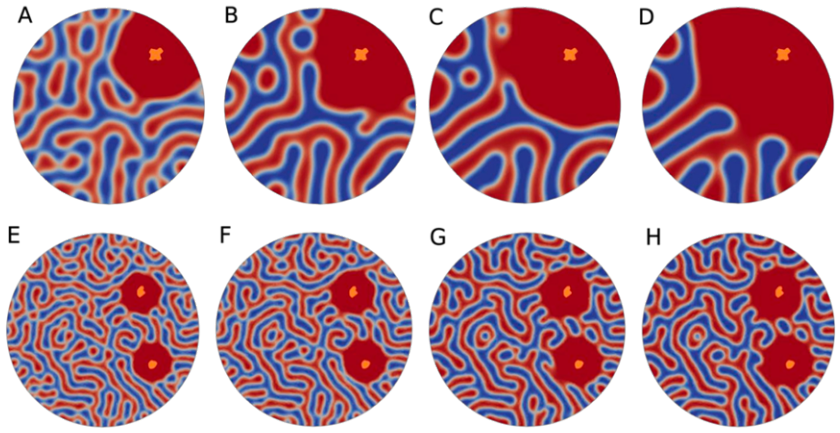

Figure 4.7: The effect of calcium phosphate granules on the inner membrane morphology. (A–D) Simulations on the effect of a single calcium phosphate granule on the mitochondrial cristae network. The Cahn–Hilliard (CH) equation was solved on a circle domain with a radius of five. The object with a white rim is the location of the calcium phosphate granule. The time step $\Delta t = 0.005$ for (A) t_{300}, (B) t_{800}, (C) t_{200}, and (D) t_{1400}. (E–H) Two calcium phosphate granule loads of the Cahn–Hilliard equation on a circle domain with a radius of eight. The orange objects are the locations of the loaded calcium phosphate granules. The time step $\Delta t = 0.001$ for (A) t_{375}, (B) t_{400}, (C) t_{850}, and (D) t_{900}. As with **Figure 4.4**, the matrix and inter membrane spaces can be observed changing dynamically in response to the presence of calcium phosphate granules.

Figure 4.8 shows the extension of the 2D simulations of the effects of calcium phosphate granules on the inner membrane topology to 3D. In this figure, colored surface plots as well as inside contour plots are presented. It can be seen from the inside contour plots in **Figure 4.8B**, **D** that the granule's location was at the center of the concave down domain. As the time increased from t_{500} to t_{1500}, the concave down domain enlarged as a direct result of the presence of the calcium phosphate granule. Changing the geometric boundary conditions from circular and spheroid to elliptical and ellipsoid resulted in a similar inner membrane topology. These results are shown in **Figure 4.9**. Simulations of a 2D elliptical mitochondrion with a major axis of 10 and minor axis of 8 are given in **Figure 4.9A**, **B**. In **Figure 4.9C**, **D**, the 3D simulation results of an ellipsoid mitochondrion are presented.

A similar pattern can be observed to that in the experimental image, which substantiates the use of the CH model and demonstrates that it can be used to characterize the internal ultrastructural features of mitochondrion with more irregular boundary conditions.

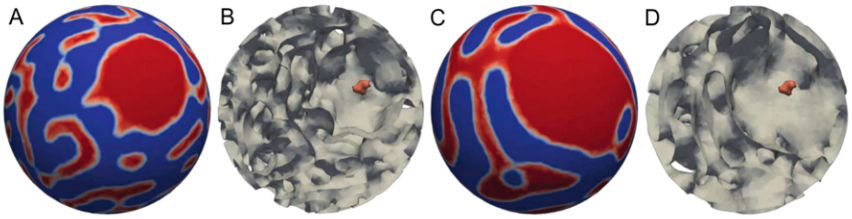

Figure 4.8: Simulation results on a 3D sphere domain with a radius of five and a single calcium phosphate granule. The time step $\Delta t = 0.001$ for (A) t_{500}, (B) the inside contour of (A), (C) t_{1500}, and (D) the inside contour of (C). The orange object represents the calcium phosphate granule.

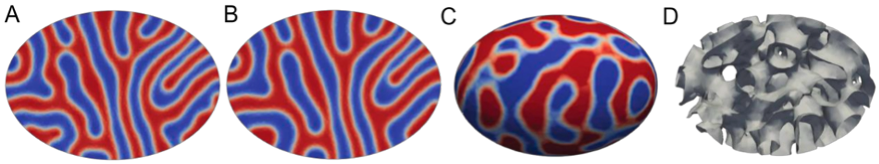

Figure 4.9: Calcium-free mitochondrial ultrastructure simulation for 2D ellipse and 3D ellipsoid domains. The time step $\Delta t = 0.005$ for (A) t_{800}, (B) t_{1000}, (C) t_{60}, and (D) the inside contour of (C). The boundary domain did not strongly regulate the inner membrane topology.

From these observations, a preliminary mechanism of calcium-induced mitochondrial dysfunction comes into focus and is presented in **Figure 4.10**. The mechanism explains how progressive calcium loading disrupts cristae, the functional units of a mitochondrion, and redistributes key oxidative phosphorylation metabolites. In this model, a calcium overload harms the mitochondrial structure by inducing inner membrane fragmentation and widening cristae junctions, which leads to the inefficient coupling of energy released during substrate oxidation and captured during oxidative phosphorylation. The mitochondrial morphology is not only affected by calcium phosphate granules [316]. In the 1960s, Hackenbrock showed that mitochondrial ultrastructure configurations lie on a spectrum ranging from the ortho-

dox to the condensed conformation [317]. He later demonstrated that these ultrastructural changes were not associated with the chemical fixation required for electron microscopy [318]. The orthodox conformation is historically defined as the ultrastructural configuration seen under an electron microscope whereby the matrix space is expanded. The inner membrane space reciprocally shrinks in a manner that appears conducive for cristae formation. This conformation is typically observed in the presence of respiratory substrates and the absence of ADP. In the condensed conformation, the matrix is characterized as having a dense or compacted matrix and a reciprocally expanded intermembrane space. This conformation is observed in the presence of ADP or respiratory poisons. Hackenbrock originally proposed that these conformations were explicitly part of a mechanochemical ultrastructural transformation model which facilitated mitochondrial ATP production. This idea was borne out in an era before Peter Mitchell's chemiosmosis principle was widely accepted [319]. That said, Hackenbrock's idea was not far off. Configurational changes to the mitochondrial membrane and enzyme localization may indeed be linked with more efficient energy transduction [320]. A common underlying principle coming out of Hackenbrock's studies reveals that the mitochondrial membrane potential appears to be necessary, but it is not sufficient when it comes to the transition from condensed to orthodox. Therefore, electrostatic effects or volume regulatory elements may be the key to unraveling the ultrastructural changes seen under the electron microscope.

4.4 Conclusion

The model presented herein is only the first of many steps being taken to understand the biophysical and biochemical regulatory mechanisms controlling cristae formation and mor-

phology. That said, cristae are specialized compartments of dynamic inner membrane folds whose curvatures are dictated by the dimerization of F_1F_O-ATP synthases [278]. In addition to ATP synthase, these specialized microcompartments contain within their membrane the respiratory machinery, or the-so-called electron transfer chain, in addition to energy-linked transhydrogenase, uncoupling proteins, and metabolic carriers. Such a rich environment in ATP synthases not only dictates the cristae shape, but it also supports ATP synthesis by the chemiosmotic coupling resulting from the electrochemical gradient generated by the movement of electrons across the various complexes of the electron transport chain. The sac-like structure shape is stabilized by the mitochondrial contact site and cristae organizing system (MICOS) [321]. This complex is composed of a myriad of proteins, known as Mic proteins, with a variety of roles including membrane shaping, contact site formation, lipid trafficking, protein biogenesis, cristae stability, and scaffolding [321]. While dynamic, the cristae shape has been mostly divided into two main morphotypes: lamellar and tubular. The former is known for its elongated, plate-like three-dimensional appearance, whereas the latter has a blob- or tube-like three-dimensional appearance. Despite the vast knowledge gathered since the discovery of cristae, little is known about how such a dynamic system is tightly regulated or the impact of the multiple morphotypes. It has been hypothesized that the dynamic adaptation of the cristae shape is dependent on the energetic demand, stage of development of the cell, and the cell type [321]. The latter adds a layer of complexity, provided that cells can have predominantly one kind of cristae morphology over the other or a mixture of them [322]. A recent study by Harner et al. showed that while these morphotypes are stabilized by dimers of F_1F_O-ATP synthase and MICOS complexes [323], a lamellar —but not tubular— cristae morphology involves the optic atrophy factor 1 (OPA1), which is known for driving inner membrane fusion events and establishing the cristae junctions [324], whereas studies

conducted by Gottschalk et al. using super-resolution structured illumination microscopy identified mitochondrial calcium uptake 1 (MICU1), a protein involved in controlling the activity of the mitochondrial calcium uniporter complex, as a calcium-dependent regulator of the cristae junction [324]. These studies revealed that knocking down MICU1 caused widening of the cristae junctions, membrane depolarization, and higher levels of matrix-resting calcium, similar to the results obtained upon OPA1 knockdown. Hence, while calcium exerts some control over cellular bioenergetics and metabolism [266], these studies revealed a role for calcium in cristae dynamics. While the modeling approach described herein faithfully reproduced the inner membrane morphology in the normal and calcium-overloaded states, it did have some limitations. For example, we did not include the possible effect that free calcium (Ca^{2+} in the solution) may have had on the proteins that regulated the cristae structure. While we do not yet know of any direct binding of calcium to the putative cristae regulators (e.g., OPA1 and MICOS), there are published studies that indirectly link calcium ions to cristae remodeling [324–328]. We intend to explore this in future studies, identifying the relationship between the total calcium content, ultrastructural changes, and ATP production rates. In this study, the total mitochondrial calcium content was not varied in the cryo-EM studies. If done, we would expect to see the total number and size of the granules play a direct role in the maximal rate of ATP production, as described in **Figure 4.10**. In addition, it was not coupled to reaction–diffusion equations to simulate the effects of the ultrastructure on metabolic fluxes, and the location and ultrastructural shaping effects of F_1F_O-ATP synthase and other mitochondrial enzymes were not accounted for. An additional limitation of the current model was the absence electrostatic effects on the membrane structure and curvature. The model was constructed by incorporating insights gained from analyzing cryo-EM structural data of isolated mitochondria, thereby provid-

ing a representation of mitochondrial morphology and function. It is important to note that the mitochondrial ultrastructural details presented herein may differ substantially from those seen *in situ*. However, we are exploring how geometric boundary constraints impact cristae morphology and intend to address this situation. In future and ongoing work, each of these limitations will be addressed to elucidate their overall impact on the mitochondrial ultrastructure and function. In conclusion, we presented a novel, phase separation-based approach to model the intermembrane and matrix spaces of mitochondria. These simulation results elucidate a plausible and likely mechanism by which mitochondrial ATP production is compromised at high calcium loads. Future studies will extend this work to simulate the volumetric changes and redistribution of key metabolites to test the hypothesis that cristae remodeling caused by calcium loading is the cause of the experimentally observed decrease in the maximum ATP synthesis rates.

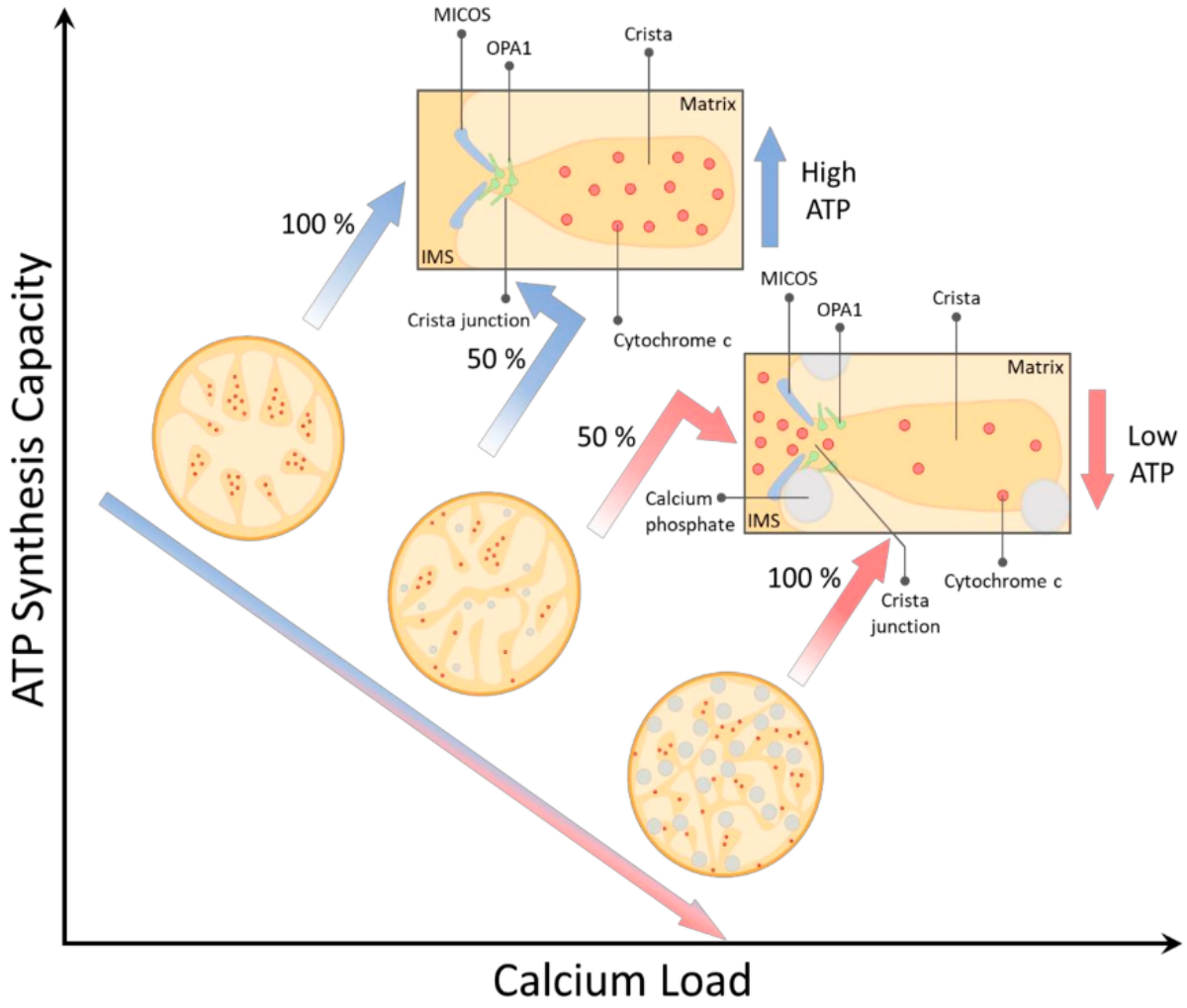

Figure 4.10: Model of calcium overload-induced mitochondrial dysfunction. We hypothesize that a calcium overload causes cristae remodeling, redistributes cytochrome c, and lowers the ATP synthesis capacity in a manner that is proportional to the calcium load.

Chapter 5

Unveiling the Role of Calcium Phosphate in Mitochondrial Cristae Dynamics

5.1 Introduction

In **Chapters 3** and **4**, I provided a broad overview of how the structure of mitochondria is affected by the local environment and discussed the consequences of calcium overload on mitochondrial function. These chapters revealed that mitochondrial respiration decreases as calcium loads increase and that the addition of the calcium chelator EGTA does not restore OXPHOS (as demonstrated in **3.1** and **Figure 4.2**. The data also suggested that mitochondria can uptake calcium concentrations as high as 50 μM, indicating that the decline in OXPHOS is not due to mitochondrial permeabilization but rather calcium's interference with function, potentially by modifying the mitochondrial ultrastructure (as shown in **Figure 3.2**).

In this chapter, I delve deeper into the proteins that control mitochondrial morphology through fission and fusion to gain a better understanding of what happens during patho-physiological conditions when high levels of calcium are present. To support this, I present cryo-electron tomography (cryo-ET) data showing how calcium disrupts the mitochondrial structure and directly affects the cristae junction and matrix volume. The preliminary data

presented herein supports the underlying hypothesis that calcium overload disrupts mitochondrial function by altering the mitochondrial structure.

Mitochondria Morphology, ETS, and ATP Synthasomes

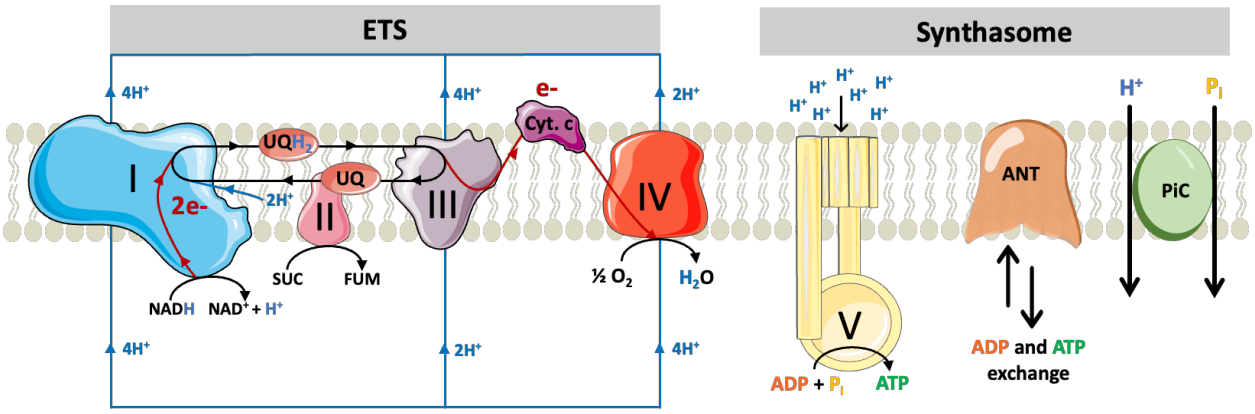

Figure 5.1: The Electron Transport System and ATP Synthasomes.

Mitochondria undergo morphological transitions based on cellular energetic demand. Because they are double-layered membrane organelles with outer and inner mitochondrial membranes (OMM and IMM), the list of molecular players involved during these transitions is numerous yet incomplete. The space between the OMM and IMM forms the intermembrane space (IMS) compartment where molecular transport and maintenance functions are exerted. The IMM further compartmentalizes into pockets called cristae. These pockets are caused by the invagination of the inner membrane which contain electron transport system (ETS) and ATP synthasome (OXPHOS) related proteins. The cristae are where the bulk of the ATP biochemistry occurs inside mitochondria. The ETS consists of four major macromolecular complexes: complex I through complex IV with complex I being the largest of the four complexes, with a molecular mass of approximately 1 megadalton. The ATP synthasome proteins consist of the F_1F_O-ATP synthase, adenine nucleotide translocase, and inorganic

phosphate carrier (**Figure 5.1**). The energy used for ATP synthesis is stored in a thermodynamic potential called the proton electrochemical gradient. This energy potential gradient is generated by the ETS. We refer to this energy potential gradient as the protonmotive force (pmf) when expressed in voltage units or $\delta\mu H^+$ when the units are in joule per mol (**Figure 5.1**).

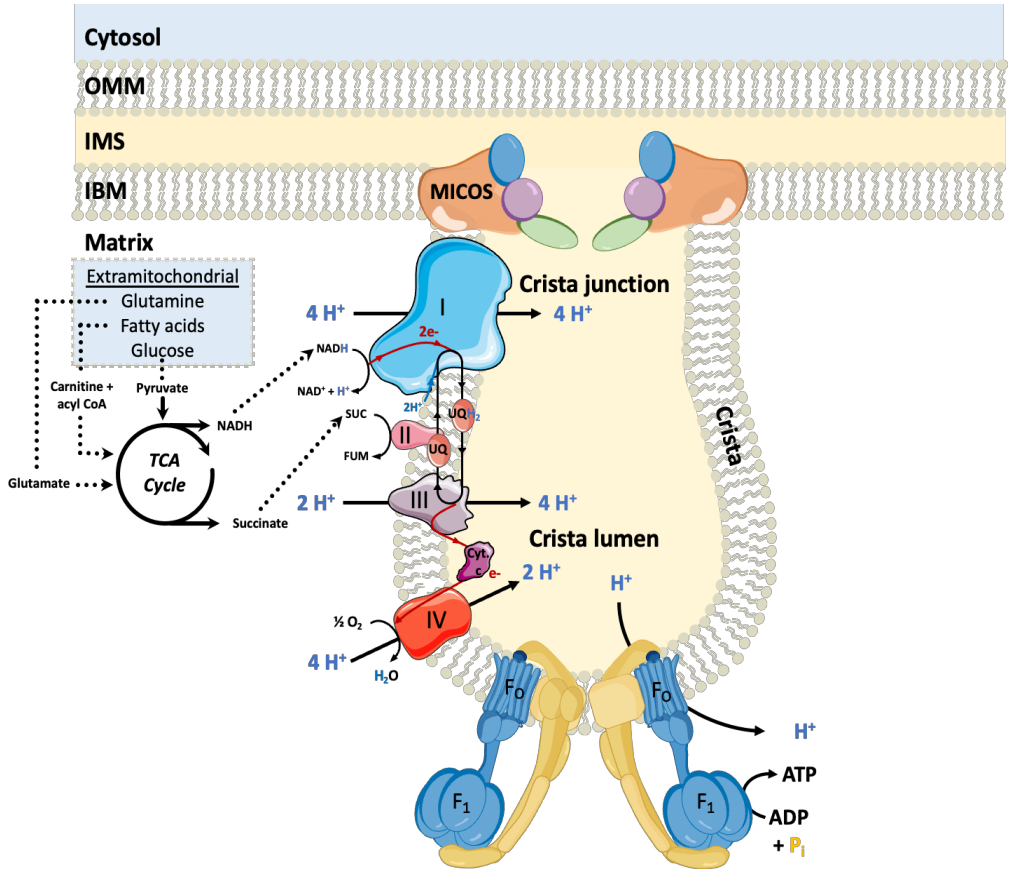

Figure 5.2: Schematic representation of a crista. The mitochondria is compartmentalized primarily by the OMM and IMM. The IMM is divided into two domains: the inner boundary membrane (IBM) and the cristae membranes. The cristae membranes further divides into the crista junctions, which connect the IBM and cristae. These junctions are tightly sealed and regulated by the mitochondrial contact site and cristae organizing system (MICOS) among others. The cristae lumen house the electron transport system (ETS), which includes complexes I, II, III, and IV. The TCA cycle machinery produces the reducing equivalents from various metabolic carbon sources and feeds electrons to the ETS. The ETS generates a proton gradient across the IMM, which drives the F_1F_O ATP synthase to produce ATP from ADP and inorganic phosphate. Dimerization of the F_1F_O complex gives the crista junctions the typical curvature known as crista rims. Adapted from [329].

Inside the cristae lumen, approximately 85 % of the mobile electron carrier cytochrome c (cyt. c) and coenzyme Q (CoQ) (**Figure 5.2**) [232, 330, 331]. Here, the tricarboxylic acid cycle (TCA) machinery resides and produces reducing equivalents (electron carriers) in the form of NADH and $FADH_2$ from the metabolic carbon sources generated in the biosynthetic pathways including glycolysis, fatty acid beta oxidation, among others. The initial region of the cristae fold is known as the cristae junction and keeps the membrane tight. The region of IMM that do not fold into cristae is known as the inner boundary membrane (IBM) and contain proteins that participate in IMM and OMM stability, as well as fission and fusion processes. Altogether, the cristae structures are the fundamental units of the mitochondria and disrupting their structure and function yields fatal consequences in the form of dysregulated cellular energetics.

Mitochondrial Dynamics and Cristae Junctions: Composition, Function, and Stability

Mitochondria are dynamic. Mitochondrial membranes continuously reshape the reticular network through fission and fusion following changes in the cell metabolic and energetic status, cell cycle, or deleterious stress causing mitophagy or apoptosis [332]. Under severe stress (e.g., starvation or overabundance of fuel) the mitochondrial reticular network can range from a hyperfused network to a highly fragmented and disconnected network. Thus, the relevance on understanding how mitochondrial dynamics are altered during pathophysiology is of relevance for the development of preventive measurements.

In mammals, mitochondrial fission is controlled by the Dynamin-related protein (Drp1) following recruitment from the cytoplasm [333]. Drp1 anchors and polymerizes into helical

oligomers in the OMM in a ring-shape fashion. Its GTPase activity constricts and divides the OMM following the hydrolysis of GTP. This event is also known to play a role in mitochondrial degradation through mitophagy; a selective autophagic elimination of mitochondria [334]. While in yeast there are several proteins characterized in the recruitment of Drp1 to the OMM, mammals' orthologues are yet to be identified [334]. In general, Drp1 recruitment is exerted by the OMM fission 1 protein (Fis1), mitochondrial fission factor (Mff), and mitochondrial dynamics protein 49 and 51 kDa (Mid49 and Mid51) [334, 335].

However, Drp1 regulation is under scrutiny and its recruitment is a debated subject. For instance, a conditional knockout model of Fis1 in HeLa, MEF and CKO cells, still shows Drp1 recruitment still occurs which argues against Fis1 mediating mitochondrial fission [336]. Whereas fission was not observed in cells lacking Mff. Similarly, a Drp1 middle domain mutation renders Drp1 interaction with Mff and impairs mitochondrial fission [333, 336]. An overly enhanced GTPase activity of Drp1 causes unrestricted mitochondria hyper-division as those observed in Huntington's disease and some cardiomyopathies [334, 337]. This suggests that Mff is essential for Drp1 recruitment [336]. *DRP1* global knockouts are embryonically lethal [335]. Whereas adult mice lacking the fission protein quickly develop heart failure and premature death [331, 335, 338]. Altogether, mitochondrial fission is controlled by several proteins and dysregulating its activity can lead to severe pathologies.

OPA1: the Long Story Short

Mitochondrial fusion, on the other hand, opposes fission and is also regulated by several IMM and OMM proteins. Fusion in the OMM is controlled by the GTPases mitofusin 1 (Mfn1) and 2 (Mfn2). They do so by tethering the OMM of adjacent mitochondria following homo- or heterodimers assembly. The Optic atrophy factor 1 (OPA1) controls both OMM

and IMM fusion [339]. The OMM is fused through Mfns interaction whereas IMM fusion occurs following OPA1 tethering to adjacent IMMs where the GTPase activity is exerted. Additionally, the IMM fusion requires OPA1 to interact with cardiolipin; the latter which composes ∼18 % of the mitochondrial inner membrane [332]. OPA1 has four different isoforms containing up to two proteolytic cleavage sites targeted by several metalloproteases that cleave long OPA1 (L-OPA1), residing in the IMM, into a shorter and soluble version. Site 1 is recognized by YME1-like ATPase and site 2 by the overlapping with the m-AAA protease 1 homolog (OMA1) [340]. Both metalloproteases yield a soluble fragment known as short OPA1 (S-OPA1) whose function is yet to be determined [332]. Studies suggest that OPA1 is a master regulator of cristae structure and ensures cristae junction tightness along with the mitochondrial calcium uptake 1 (MICU1) [235, 341].

Recently, a study looking at mitochondrial swelling, either through calcium overload or with the aid of the pharmacological channel-forming peptide alamethicin (ALM), shows higher and lower levels of S-OPA1 and L-OPA1 respectively [340]. The latter can be inhibited with sanghliferin A which inhibits pore opening [340]. This seems to suggest that L-OPA1 protects the mitochondrial integrity and allows fusion whereas the S-OPA1 derails functionality. However, proper mitochondrial fusion extends beyond mitochondria requiring a higher ratio of L-OPA1 over S-OPA1. The key relies on the cleavage site and, by extension, the metalloproteases involved.

Cleavage by YME1L occurs at site 1 and couples metabolism while allowing IMM fusion [342]. This means that YME1L cleavage is required for proper fusion of the IMM and for the proper functioning of oxidative phosphorylation (OXPHOS). In contrast, cleavage by OMA1 at site 2 disrupts mitochondrial function through membrane depolarization [342]. This effect is directly related to the energetic status of the mitochondria, with significant

membrane depolarization required to induce OMA1 proteolytic cleavage at site 2. This might explain why observed fractions of S-OPA1 are elevated in mitochondria treated with agents that disrupt the mitochondrial membrane potential and function, such as alamethicin or the Complex III inhibitor Antimycin A (AA), and why some studies associate S-OPA1 with loss of function while others highlight the necessity for fusion.

It is important to consider the energetic status parameters when interpreting the data, as the necessity of L-OPA1 proteolytic cleavage at either site 1 or site 2 for fusion could be related to enhanced GTPase activity to drive membrane fusion. For example, under transient depolarizations, OMA1 activation might be beneficial to distribute workload by promoting mitochondrial fusion. Similarly, at high working loads, YME1L activation can enhance work capacity, coupling, and ATP synthesis. However, it is yet to be determined if L-OPA1 by itself can drive membrane fusion at either basal or high energetic states [340]. Overall, the activity of OPA1 is essential for proper mitochondrial fusion and cristae junction stability.

MICOS is a crucial regulator of cristae formation and is composed of several proteins, including Mitofilin, MINOS1, CHCHD3,6, and 10, APoO and ApoL, and Qil1 in humans [341]. In yeast, the homologs are known as Mic [341]. MICU1 and OPA1 interact with MICOS to stabilize the cristae structures [343]. Studies have shown that genetic ablation of OPA1 and MICU1 or depletion of OPA1 leads to destabilization of the cristae structures [343, 344]. As discussed in **Chapters 3** and **4**, changes in the mitochondrial network through fission and fusion allow for cellular adaptability in response to energetic demand and also regulate mitochondrial damage, recycling, and degradation to attenuate damage or remove dysfunctional mitochondria [341].

Recent research has investigated the regulation of OPA1 by the PTP and showed that L-OPA1 levels drop following calcium-induced swelling and pore formation. This effect can

be inhibited by the pore inhibitor sanghliferin A. However, at very high calcium levels, sanghliferin A does not prevent L-OPA1 levels from dropping, suggesting that OPA1 levels are altered by membrane disruption induced by extremely high levels of calcium. These findings suggest that the mitochondrial structure can be altered by increasing calcium loads.

MICU1 plays a crucial role in regulating calcium uptake into the mitochondria, as it serves as the gatekeeper for the MCU channel [345]. Recent studies have shown that MICU1 localizes exclusively in the IBM and de-oligomerizes upon binding with Ca^{2+}, acting as a diffusion trap for calcium and helping to activate the MCU in the IBM [343, 346]. Therefore, the growth of calcium phosphate deposits in the regions where MCU and MICU1 localize could potentially lead to cristae destabilization in the face of calcium overload. It is important to note that calcium phosphate deposits may arise in regions rich in calcium uniporters where most of the calcium entry occurs. However, conventional confocal microscopy and cryo-EM lack the spatial resolution required to differentiate between the localization of these proteins in the IMM and IBM. Theoretically antibodies attached to gold beads that can target MCU and MICU1 can be designed to spatially detect whether the distribution of these proteins is associated with the observed granular formation. The localization and dynamics of MCU and MICU1 in relation to calcium granule formation could provide valuable insights into the mechanisms of cristae destabilization during calcium overload.

The data presented here indicates that calcium overload can lead to severe disruption of the cristae network. Specifically, we observed that a 25 μM calcium bolus did not result in significant changes to cristae junction width compared to control but did lead to a substantial reduction in matrix density. Moreover, we found that higher calcium loads resulted in exacerbated disruption of both the cristae junction width and matrix density. These findings suggest that the cristae network is highly sensitive to calcium overload, and that even moder-

ate increases in calcium levels can have significant consequences for mitochondrial structure and function.

5.2 Methods

Mitochondria Isolation and Protein Quantification

The method described in Wollenman et al. was used to obtain cardiac mitochondria from guinea pig hearts, using differential centrifugation [255]. To prevent blood clotting during isolation, Hartley albino guinea pigs weighing 350 - 450g and aged 4 - 6 weeks were injected with heparin (500 units/mL) into the intraperitoneal cavity. The animals were deeply anesthetized with 4 - 5 % isoflurane before the heart was removed by decapitation with a guillotine, following confirmation of full sedation using a noxious stimulus (paw pinch and eyelid reflex). The heart was then perfused with a cold cardioplegia solution and homogenized, as described previously [79, 255]. The mitochondrial protein content was determined using the BIO-RAD Bovine Serum Albumin (BSA) Standard Set Kit and the BCA assay. The mitochondrial suspension was diluted to a working concentration of 40 mg/mL and kept on ice for 4 - 8 hours during the experiment. The substrate stock solutions were neutralized to pH 7.0.

Mitochondrial Quality Control

The mitochondrial quality was determined using an Oxygraph 2k (Oroboros Instruments Corp., Innsbruck, Austria) under constant stirring at 37 °C. Chambers were loaded with 2 mL respiratory buffer containing 130 mM KCl, 5 mM K_2HPO_4, 20 mM MOPS, and 1

mM $MgCl_2$, 1 mM EGTA, 0.1 % (w/v) BSA at a pH of 7.1. All subsequent experiments were done using this buffer and temperature. At 0 mins, 5 mM sodium pyruvate and 1 mM L-malate were added as substrates. This was followed by 0.1 mg/mL mitochondria. The leak state was defined as the rate of oxygen consumption by mitochondria only in the presence of substrates. This measurement is taken after 5 mins. At 5 mins a bolus of ADP (500 μM) was added to induce maximal ADP-stimulated respiration. Quality was assessed by computing the respiratory control ratio (maximal ADP-stimulated rate divided by the leak rate). Only mitochondria with an RCR value greater than or equal to 16 were used in the experiments.

Calcium Tolerance Test on OXPHOS

The tolerability of the mitochondria for calcium was measured by quantifying changes in leak and ADP-stimulated respiration following a calcium challenge with and without CsA. At 0 mins, 5 mM sodium pyruvate, 1 mM L-malate, ± 1 µM CsA, 0.1 mg/mL mitochondria were injected into each 2 mL chamber containing respiratory buffer. At 5 mins, a calcium bolus of either 25 or 50 µM $CaCl_2$ was injected. At 10 mins, 500 µM ADP was added induce maximal ADP-stimulated respiration. Mitochondria with a JO_2 equal or greater than ∼200 nmol/mg/min for the 50 µM $CaCl_2$ bolus were considered for Cryo-EM imaging.

Cryo-Electron Microscopy (Cryo-EM) Sample Vitrification and Imaging

Isolated mitochondria were suspended at a concentration of 0.1 mg/mL in a 2 mL respiration buffer with 5 mM sodium pyruvate and 1 mM L-malate. At the collection times indicated,

5 µL samples were aliquoted from the mitochondrial suspension and deposited on Quantifoil R2/2 holey carbon grids pretreated for 1 min using a Pelco EasiGlo glow discharge unit. Prior to depositing the mitochondrial suspension on the carbon grid, 5–10 µL of 10 nm nanogold markers were applied to the grids and air dried. These beads serve as markers for fiducial alignment of the tilt series. The grids were blotted to thin the water layer and subsequently plunged into liquid ethane at room temperature using a Vitrobot Mark IV with automated temperature regulation, blotting, and humidity control (Fisher Scientific). The Vitrobot chamber was set at 4 °C with 100 % humidity. The grids were blotted with a blot force of 1 for 2.5 to 3 secs, transferred, and stored in liquid nitrogen until imaging. Tilt series were performed using an FEI Talos Arctica at 200 keV in low-dose conditions, operated using Thermofisher's Tomography software. Images were collected in linear mode on a Falcon 3EC direct electron detector with an electron dose of ∼2e-/ Å^2 per tilt image. The images were collected at 22,000 X magnification (4.7 Å/pixel) with a total electron dose of ∼100 e-/ Å^2 per tomogram.

Tomogram Reconstruction and Modeling

Motion correction was performed for the individual micrographs and binned by an index factor of 7 using Motioncor2 v1.2.6. Tilt series alignment was performed using ETOMO v4.9.12 [134]. Standard tomographic reconstruction particles were performed using the Simultaneous Iterative Reconstruction Technique (SIRT) strategy. At least 10 - 15 iterations were performed for each tomogram. Key features (e.g., membranes, cristae junctions, granules, size analysis) of the tomograms were traced using the drawing tools functionality in IMOD (3dmod) [134].

Statistics

All data were analyzed and plotted using MATLAB 2020a (Mathworks, Inc., Natick, MA, USA). The Shapiro-Wilk test was used to determine the normality of the data, and a One-way ANOVA was performed to determine if there were significant differences between treatments at various calcium loads and different treatments. Post-hoc analysis was done using the Tukey-Kramer test. Results of these statistical tests can be found in **Appendix B**.

Reagents. All reagents were purchased from Sigma-Aldrich unless otherwise stated.

5.3 Results and Discussion

Mitochondrial Micrographs and Cryo-EM features

To better understand the effect of calcium on the mitochondrial structure, cryo-ET were collected with the following conditions: without calcium (EGTA), with a 25 and 50 μM $CaCl_2$ bolus, or in the presence of CsA. A representation of the analysis performed for the tomograms collected is shown in **Figure 5.3**. The micrograph in **Figure 5.3** shows the details that can be gathered. Each tomogram is composed of multiple micrographs and the cristae, calcium phosphate granules, and outer and inner membrane structures are traced in 2 dimensions (2D) from top to bottom (**Figure 5.3B**). The 2D traces are then stacked to create a reconstructed 3-dimensional (3D) model of the mitochondria (**Figure 5.3C**). Finally, membrane features, such as the cristae junction width, are gathered and analyzed for every single condition (**Figure 5.3D**).

Figure 5.4 shows a micrograph representation for the tomograms collected at a given condition. Panel A contains a representative micrograph of the collected tomograms. Whereas

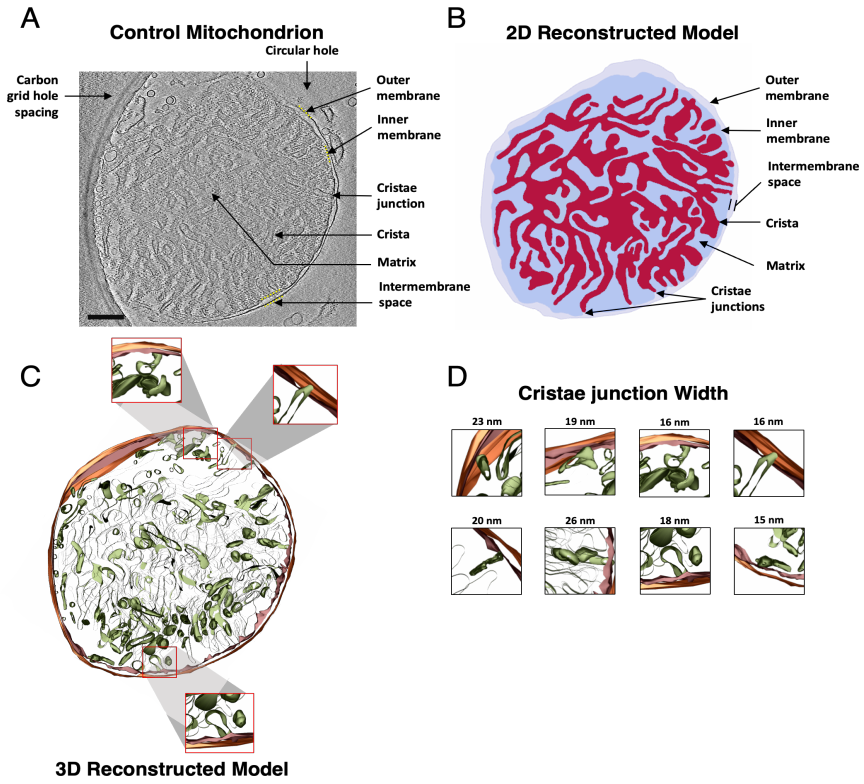

Figure 5.3: Representation on the tomogram reconstruction flowchart.

Panel B displays the 3D reconstructed models from the collected tomograms with several cristae junctions identified. There are several apparent observations to be made between control, calcium overloaded or CsA treated mitochondria. Control group was collected in the presence of the calcium chelator EGTA. Hence no calcium is present in the buffer. This group shows a typical ovoid-shape appearance with regular OMM, IMM, and cristae (**Figure 5.4**).

In contrast, the formation of calcium phosphate deposits is apparent when either a 25 or 50 μM $CaCl_2$ bolus is added to the buffer. These granules can be observed in the micrograph as dark electron dense spots within the mitochondrial matrix (**Figure 5.4A**) and as lighter grey spheres in the 3D reconstructions (**Figure 5.4B**). Following calcium uptake, the matrix expands, or swells and the cristae network looks stringy or thinner. This effect is exacerbated at increasing calcium loads. The presence of calcium phosphate deposits within

the mitochondrial matrix seems to displace cristae formation in the region. Among all the collected tomograms, cristae formation does not seem to occur in the vicinity of the granules. This goes accordingly to the observations made in **Chapter 3**. The CsA-treated group was collected in the presence of EGTA. As expected, no calcium phosphate deposits were generated. However, CsA-treated mitochondria displayed an aberrant morphology and compact cristae compartment relative to control group. A similar effect was previously recorded in **Chapters 3** and **4**. This CsA treatment effect is apparent in additional 3D reconstructed tomograms as shown in **Appendix B**. Altogether, this data confirms 1) calcium overload leads to calcium phosphate deposits and 2) significant remodeling of the cristae structures is observed at high calcium levels.

Calcium overload widens cristae junctions

To investigate the effect of calcium or CsA on the cristae junctions, we measured at least 10 cristae per mitochondrion for each condition, as depicted in **Figure 5.5**. The control group showed a typical cristae junction width of ∼10 nm. Surprisingly, the mitochondria treated with 25 μM $CaCl_2$ had similar junction widths to the control and CsA-treated groups. This might suggest that the reduction in mitochondrial respiration under this condition is related to the decreased cristae network rather than the widening of the junctions and subsequent cyt. c release. However, it is very likely that calcium inhibition of OXPHOS is more complex in nature and multifactorial. Whereas the addition of a 50 μM $CaCl_2$ bolus resulted in a thinner cristae network and wider junctions, with the width increasing by nearly 66 % following calcium accumulation. In contrast, the CsA-treated group exhibited cristae junction widths comparable to the control group, with denser mitochondrial matrices relative to control. These findings, combined with the known protective effect of CsA on mitochondria, may explain why CsA treatment can prevent calcium overload-induced damage. Neverthe-

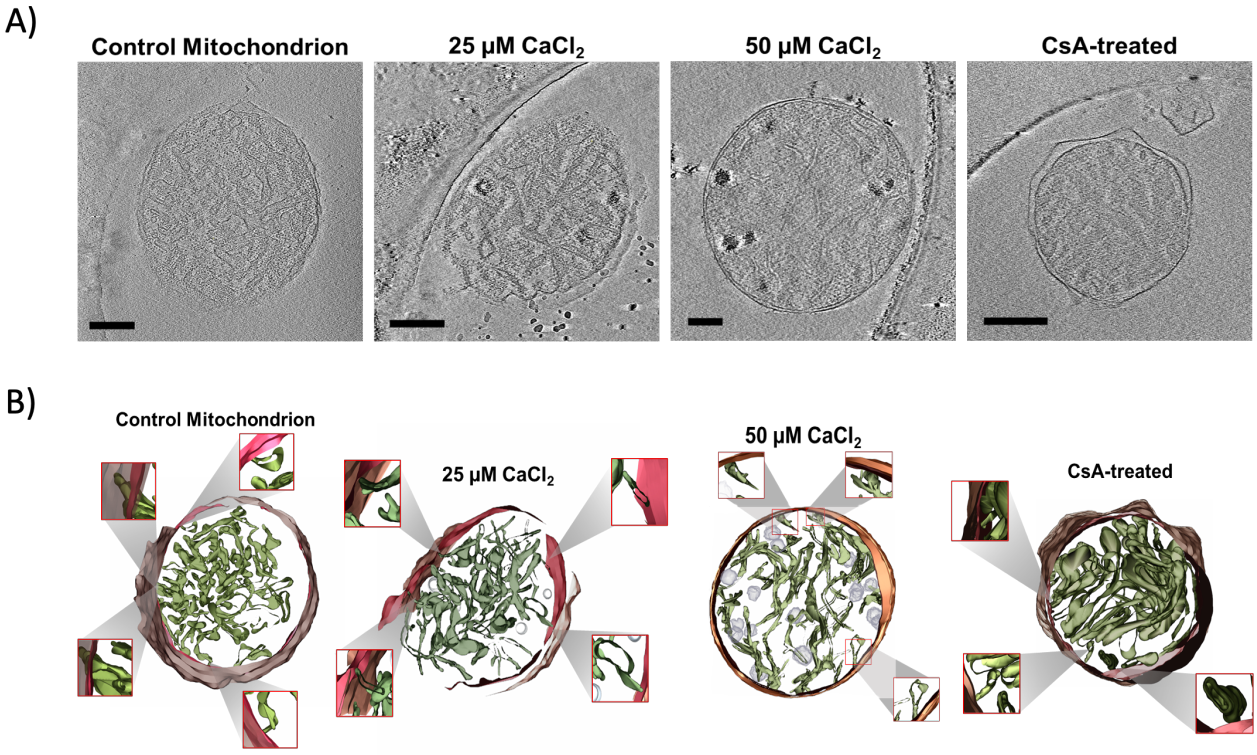

Figure 5.4: Representative micrographs with the respective 3D reconstructed tomograms from **Chapter 2**. Control group with 1 mM EGTA. The formation of calcium phosphate deposits is apparent following a 25 or a 50 μM $CaCl_2$ bolus. CsA-treated mitochondria in the presence of 1 mM EGTA displayed an aberrant morphology and compact cristae compartment. Scale bars are set at 250 nm. In the 3D models, orange represents the OMM, red the IMM, green the cristae network, and grey the calcium phosphate deposits.

less, the tomographic reconstructions for the CsA-treated group following calcium uptake require further analysis and were not included in this report.

The preliminary data presented in this study has shed light on the strong correlation between calcium overload and changes in mitochondrial morphology. Specifically, our results show that toxic levels of calcium have deleterious effects on the density of the mitochondrial cristae network. Furthermore, the effect of calcium phosphate deposits on the mitochondrial matrix is evident, with mitochondria loaded with calcium displaying thinner cristae networks relative to control and CsA treatment. Given the impact of calcium overload on the cristae network, it is not surprising that our results indicate a potential impairment in

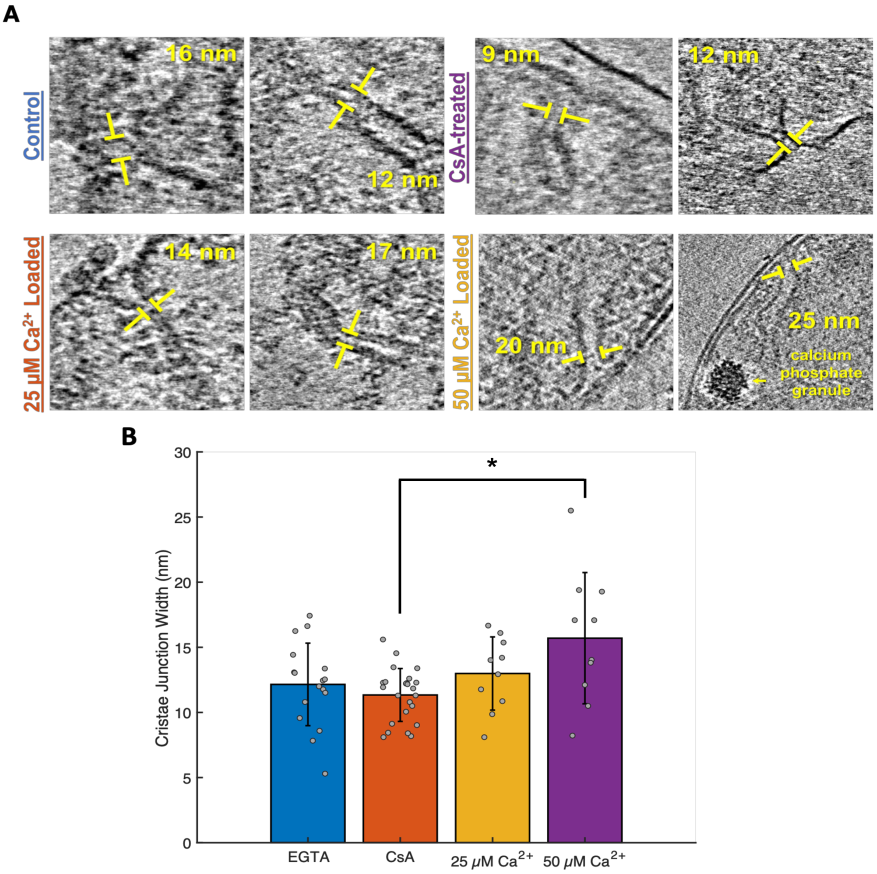

Figure 5.5: Calcium overload widens cristae junctions. A) To visualize the widening effect of calcium overload on cristae junctions, over 10 cristae junctions (n $\geq$ 10) for each condition were analyzed using cryo-EM tomography. Representative micrographs illustrate the yellow regions that confine the cristae junctions. B) 3D reconstructed cristae junctions for a given condition. C) The bars are plotted as means of the data with error bars representing the standard error of the mean. Grey dots represent individual data points for the cristae junctions measured. * Represents a statistical difference between the CsA and the 50 μM $CaCl_2$ group with a p-value of 0.0237.

ATP production, as previously suggested by the functional and structural data presented in **Chapters 3** and **4**.

Digging deeper into the cristae junction width, we observed a smaller increase in cristae junction width following the 25 μM $CaCl_2$ addition compared to the 50 μM $CaCl_2$ bolus. However, this effect is significant compared to CsA and the control group. Both calcium concentrations decrease the matrix density in a concentration-dependent manner. This effect is clearly visible in the examination of the 3D reconstructed models, where the differences in

the cristae network between the control and the 50 µM calcium-treated groups are particularly striking. It is worth noting that the control group appears to have a less defined cristae network compared to the rest of the model, but this is due to limitations in the resolution of the imaging technique used to generate the 3D models. Overall, these findings suggest that calcium overload has a significant impact on mitochondrial morphology and function, with potential implications for a range of pathological conditions.

The preliminary data presented in this section strongly supports the notion that calcium overload can induce changes in mitochondrial morphology, specifically affecting the cristae network. Higher levels of calcium can lead to deleterious effects on the matrix density and ultimately impact the integrity of the cristae. The impact of calcium phosphate deposits on the mitochondrial matrix is also apparent, resulting in looser and thinner matrices in mitochondria loaded with calcium compared to control or CsA-treated mitochondria. This observation is consistent with previously discussed data on the effects of high levels of calcium on mitochondrial structure and function in **Chapters 3** and **4**. Interestingly, the CsA treatment seems to enhance the cristae network despite having an aberrant outer mitochondrial membrane (OMM) structure. However, gathering tomograms for the CsA condition with either calcium concentration proved to be challenging due to the absence of the OMM, spreading of mitochondria across the carbon grids, or electron diffraction causing the matrix to look dense and dark. Thus, making it difficult to reconstruct in 3D space (**Appendix B**). This effect is not unknown, as previously recorded in **Chapter 3**.

The findings also raise new questions about how calcium impairs mitochondrial structure and the role of cristae-stabilizing proteins such as MICOS in this process. Studies have shown that disrupting MICOS can lead to fragmented cristae networks and alterations in cristae connections to the inner boundary membrane (IBM) [329]. Moreover, the phenomenon of the

permeability transition pore (PTP), which can lead to mitochondrial rupture and cytochrome c release, may be preceded by cristae destabilization resulting from the accumulation of calcium phosphate deposits. Studies performed in HeLa cells have suggested that cytochrome c and OPA1 are co-released following swelling prior to permeabilization induced by calcium overload [347]. Cells lacking OPA1 facilitated cyt. c release prior to permeabilization, suggesting that OPA1 influences mitochondrial structure that is independent of fusion [347]. These findings highlight the complex interplay between calcium overload, mitochondrial structure, and function, and underscore the need for further investigation in this area.

Chapter 6

Mitochondria: A Two-Pronged Attack on Calcium-Induced Impairment in Structure and Function, Combating ROS as a Druggable Target

6.1 Overall drug screening objective

Mitochondria are the primary source of energy metabolites for nearly all eukaryotic cells. Due to their nature, they are at an extreme risk of free radical sensitized calcium toxicity. This puts them at the center of many diseases and pathologies, particularly ischemia/reperfusion (I/R) injury. A drug screen, consisting of approximately 5,000 compounds from the NCI diversity set V library and the PKIS (GSK) kinase library, was achieved through the Assay Development and Drug Repurposing Core (ADDRC) of Michigan State University. In this chapter, the identified compounds selected as potential novel candidates for protecting mitochondria from calcium overload will be presented. Although the drugs mentioned in this chapter are currently available on the market, none of them have been specifically designed or approved for targeting the mitochondria. Thus, presenting a significant opportunity for drug repurposing in the field of mitochondrial medicine.

The aim this drug screen was to 1) develop and optimize a protocol for quantifying drug efficacy on mitochondrial calcium tolerance, 2) perform an initial 5,000 compound screen,

and 3) test for ability of compounds that make it past the initial screen for protection against calcium overload in a pro-oxidative environment. In this project, a fluorescent-based assay was tested and developed to quantify the ability of mitochondria to take up and retain calcium. The overarching goal of this study is to facilitate a rational approach to identify new therapeutic targets and develop novel therapies to correct or prevent calcium-induced mitochondrial dysfunction that leads to tissue injuries.

6.2 Introduction

Heart disease is the number one killer in the U.S. and worldwide [348]. The projected disease costs in the U.S. including health care services, medicines, and lost productivity due to death extend well into the 10's of billions of dollars with no foreseeable decline [349, 350]. The exact cause of death is multifaceted but nearly always results from an acute myocardial infarction, i.e., a heart attack. During a heart attack, blood flow to the heart is reduced or completely cut off. As discussed in **Chapter 1**, this alters metabolism and disrupts mitochondrial energy homeostasis [221, 351–365]. Paradoxically, the necessary act of reestablishing blood flow contributes up to half of the total damage [366]. The damage incurred after reperfusion is known as I/R injury [367]. There are four types of injuries associated with I/R injury with each contributing to the development of heart failure [365, 367, 368]. Of these injuries, the most detrimental is known as lethal reperfusion injury [369] which arises due to calcium-induced mitochondrial dysfunction. And although this injury is intensely studied at the basic science level and in clinical trials [370], the best treatments available are insufficient [371] and no clinically effective therapy exists. One of the major contributing factors in cell death during a heart attack is the disruption in mitochondrial function that occurs

after reperfusion. This phenomenon is known as mitochondrial permeability transition pore (PTP) [372–374]. The mitochondrial PTP is characterized by the opening of a calcium-dependent, free radical sensitized, proteinaceous molecular pore. However, as discussed in in previous chapters, the molecular identify of this pore thus far remains elusive [375]. When this pore is open, mitochondria transform from ATP producers into ATP consumers [376]. During ischemia, the disruption in energy metabolism disturbs calcium homeostasis resulting in elevated cytosolic calcium. It is at this time, mitochondria become loaded with toxic levels of calcium. Upon reperfusion, the sudden surge of available oxygen hyper-energizes the mitochondria, and they produce a rapid burst of free radicals [377]. Thus, the system is hit with a one-two punch which induces mitochondrial PTP, leads to cell death, and begins the downward spiral of heart failure. Therefore, any effective therapy must 1) protect mitochondria against situations conducive for calcium overload and 2) maintain this protection during oxidative stress conditions. There have been over 30 clinical trials on I/R injury over the past few decades [367]; however, there has been no real translational successes. These failures are attributed to a variety of factors [368, 371], but a common denominator is a lack of specific and effective therapies. The success of this project will enable the development of new and effective therapeutic strategies targeting IR injury, a clinically relevant phenomenon. Such a therapy would have an enormous commercial value. The overall study objective is shown in **Figure 6.1**.

As I/R injury is involved in many pathophysiological diseases and conditions such as neurological disorders, aging, response to toxins, cancer, muscular dystrophy, and I/R injury [209, 378], compounds identified during this study are not exclusive to cardiac tissue. This opens up an enormous opportunity to develop a whole class of therapies targeting organ-specific diseases.

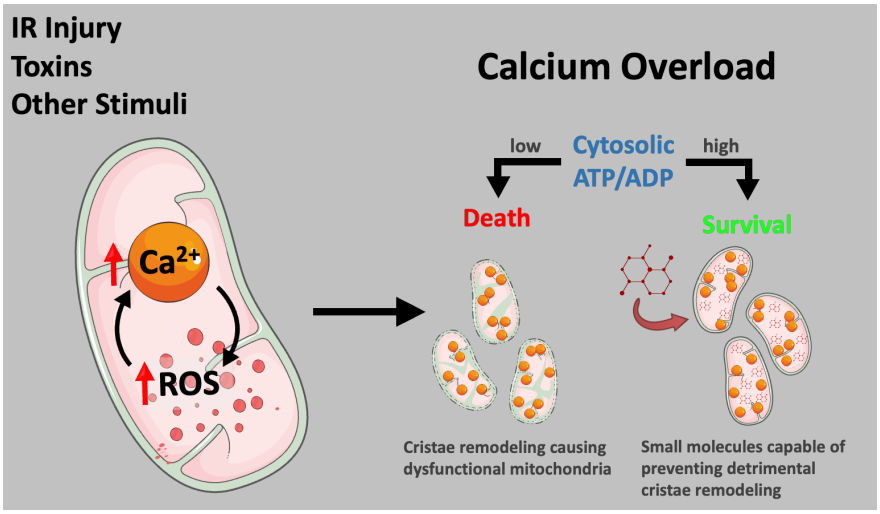

Figure 6.1: Overall study objective.

At the onset of a heart attack, the disruption of blood flow to the tissue begins a series of events that, if left untreated, results in massive cell death. Early treatment is essential for optimal recovery. However, the seemingly random nature of heart attacks makes time-to-need treatments impossible. Aside from preemptive treatment plans like diet and exercise, the most promising approach to treating a heart attack is in the hospital setting during balloon angioplasty and thrombolytic therapies. Therefore, our approach is to identify and develop a drug to deliver to the myocardium at the site of injury during these procedures. Our group expects this drug to dramatically reduce cell death and thus lower the prevalence of heart failure.

Figure 6.2 represents the rationale for the drug screen. As shown, calcium overload leads to a dramatic and significant decrease in mitochondrial respiratory function and loss of calcium homeostasis. However, the drug cyclosporin A enables mitochondria to stably sequester calcium and partially preserve metabolic function. Unfortunately, clinical trials using this drug produced negative or neutral results [379, 380]. Therefore, a new drug that is as effective is not only desirable, but also necessary. And given that the molecular

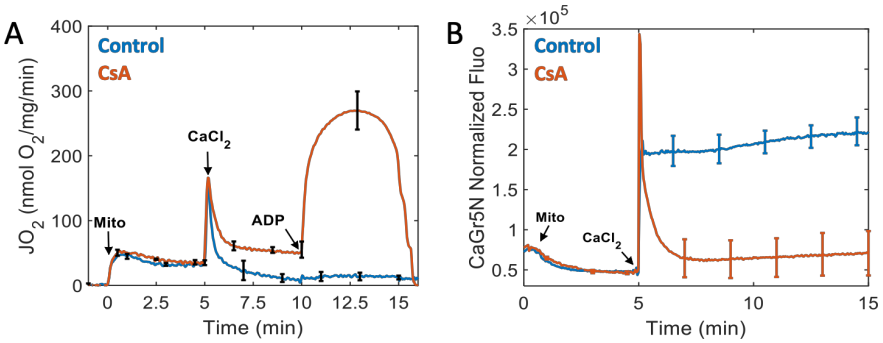

Figure 6.2: Representative trace of the effects of calcium overload on mitochondrial function. A) Calcium overload disrupts mitochondrial respiration and CsA rescues it. B) Calcium release following calcium uptake in control but not in CsA-treated mitochondria.

mechanism of calcium sequestration and its effects on bioenergetics are not well understood [78, 381], a drug screen is an ideal method to find a suitable alternative.

6.3 Initial drug screen

The ADDRC drug library screen for mitoprotectants followed the protocol optimization. This pilot screen consisted of approximately 5,000 compounds from the NCI diversity library, PKIS kinase library, as well as subsets of known drugs for drug-repurposing studies. A 'positive hit' was considered successful if the drug promotes calcium uptake and prevents calcium release from the mitochondria as detected by the calcium-sensitive fluorescent dye (**Figure 6.3**). The CsA positive control was used in the initial drug screen, whereas the "negative control" was non-CsA treated mitochondria.

A diagram for the intended protocol is shown in **Figure 6.4**. The first part shows the feasibility and protocol optimization used in the primary screen. A successful outcome was defined as being able to verify stable calcium uptake in the presence of cyclosporin A and no calcium uptake in the presence of ruthenium red (RR).

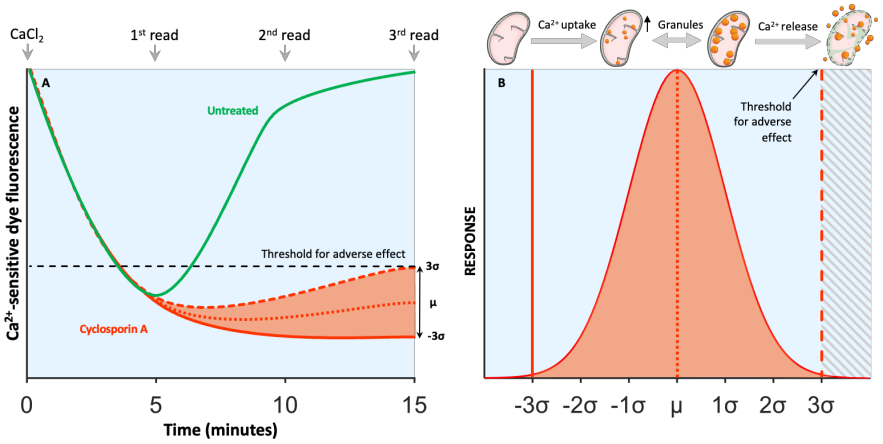

Figure 6.3: Screening protocol. Drug efficacy will be quantified by monitoring the ability of mitochondria to handle a large bolus of calcium. Drug responses will be compared to the positive control (cyclosporin A). Fluorescent values outside 3σ above the mean of the positive control fluorescence will be considered a negative result. An ideal compound will lead to low calcium levels.

6.4 Feasibility and optimization

I used a well-designed calcium uptake protocol to screen for mitoprotectants in the MSU Drug Discovery compound GSK and NCI libraries. In this assay, I detected mitochondrial calcium uptake using the fluorescent calcium dye, Calcium Green 5N. This dye was selected because it has a KD value in the low micromolar range, making it suitable for the purpose of this study. It is relevant to note that the calcium concentration range used in this assay is between 50 - 150 μM, and using a dye with a lower affinity, in the nanomolar range, would result in a saturated signal. Conversely, a dye with a higher KD value in the high micromolar range would not be sensitive enough to detect changes following calcium addition. When calcium overload disrupts mitochondrial function, mitochondria do not take up and stably sequester calcium (**Figures 6.2** and **6.3**). Prior to the initial screen, I demonstrated feasibility and optimized our protocol using a spectrophotometric-based assay. This is routinely done in the lab; however, assays are done in 2 mL cuvettes as opposed to microplate wells. However, the assay was successfully scaled down for high-throughput screening using the ADDRC's Biotek

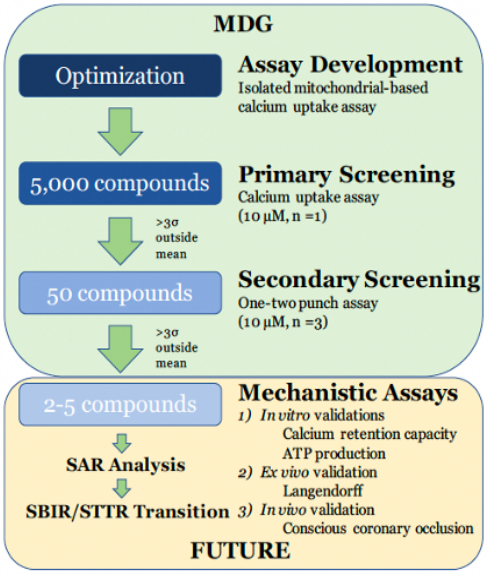

Figure 6.4: Decision tree.

Synergy Neo Plate Reader. In this assay, freshly isolated mitochondria were loaded in a 384-well microplate and their ability to take up and sequester a large calcium bolus was quantified in the presence of the mitoprotective agent CsA, as the positive control and MCU inhibitor RR, as the negative control, to impede calcium uptake. Freshly isolated mitochondria from guinea pig hearts are an ideal choice because *i*) they are routinely isolated in the lab, *ii*) there is enough mitochondria per heart to fill multiple 384-well plates, and *iii*) they are directly relevant to the aims of the proposed drug screen. To identify the optical calcium levels, calcium doses in the range of 50 to 150 μM were tested, which have previously shown to be in a range capable of inducing mitochondrial PTP. Here, we identified the 100 μM to be sufficient to induce PTP. Background fluctuations were determined by wells containing mitochondria devoid of calcium and calcium loaded wells in the absence of mitochondria. To avoid variable dye loading in each well, the dye was added to the respiratory buffer before dispersing in the wells.

6.5 Materials and Methods

Mitochondria isolation and protein quantification

Cardiac mitochondria were isolated from guinea pig hearts using differential centrifugation as described previously [382]. Briefly, Hartley albino guinea pigs weighing 350 – 450 g (4 – 6 weeks) were injected with 500 units/mL of heparin into the intraperitoneal cavity to prevent blood clotting during the cardiac mitochondrial isolation. Before heart excision, animals were deeply anesthetized with 4 – 5 % isoflurane. Prior to decapitation by guillotine, we checked both eye lid and paw pinch reflexes to confirm animals were fully sedated. Following decapitation, a thoracotomy was performed. The heart was then perfused with cold cardioplegia solution and homogenized as described elsewhere [382]. To prepare the mitochondrial suspension, we quantified the mitochondrial protein content using the BIO-RAD Bovine Serum Albumin (BSA) Standard Set Kit and the BCA assay, and diluted it to a working concentration of 40 mg/mL, which was maintained on ice for the duration of the experiment (approximately 6 hours). We also neutralized the substrate stock solutions to pH 7.0.

Mitochondrial quality control

The mitochondrial quality was determined using the Oxygraph 2 k (Oroboros Instruments Corp., Innsbruck, Austria) under constant stirring. The O2k chambers were loaded with 2 mL respiratory buffer containing 130 mM KCl, 5 mM K_2HPO_4, 20 mM MOPS, and 1 mM $MgCl_2$, 1 mM EGTA, 0.1 % (w/v) BSA at a pH of 7.1 and 37 °C. All subsequent experiments were done using this buffer and temperature. The respiratory control ratio (maximal ADP-stimulated rate divided by the leak rate) was collected for each experiment as a measure of mitochondrial quality. Only mitochondria with an RCR value greater than

or equal to 16 were used in the experiments. At 0 min, 5 mM sodium pyruvate and 1 mM L-malate were added followed by 0.1 mg/mL mitochondria. The rate of oxygen consumption by mitochondria only in the presence of substrates defines leak state (state 2) in these experiments. At 5 min a bolus of ADP (500 μM) was added to induce maximal ADP-stimulated respiration. This defines the maximal ADP-stimulated rate (state 3) in these experiments.

Calcium tolerance assay

The calcium tolerance was determined using the Oxygraph 2 k (Oroboros Instruments Corp., Innsbruck, Austria) loaded with the respiratory buffer as described above. At 0 min, 5 mM sodium pyruvate and 1 mM L-malate were added followed by 0.1 mg/mL mitochondria. At 5 min, different chambers were treated with a bolus of 25 μM $CaCl_2$ and 50 μM $CaCl_2$. At 10 min, a bolus of ADP (500 μM) was added to induce maximal ADP-stimulated respiration.

High-throughput screen

All of the solutions described below are three times the working concentration. An 8 mL buffer solution (Buffer 1) was freshly prepared in a black opaque 45 mL Falcon tube containing 15 mM sodium pyruvate and 3 mM L-malate, 3 μM Calcium Green-5N (from Molecular Probes), and 0.6 mg/mL mitochondria, as shown in **Figure 6.5**. This buffer solution was prepared shortly before beginning the assay to minimize mitochondrial degradation. All of the solutions were kept on ice and mixed gently to avoid bubbles. One mM Calcium Green 5N stocks were freshly prepared, and 30 μL were aliquoted into black opaque microtubes kept at -80 °C. A 20 μL stock solution of 5.2 mM CsA was freshly prepared and diluted with

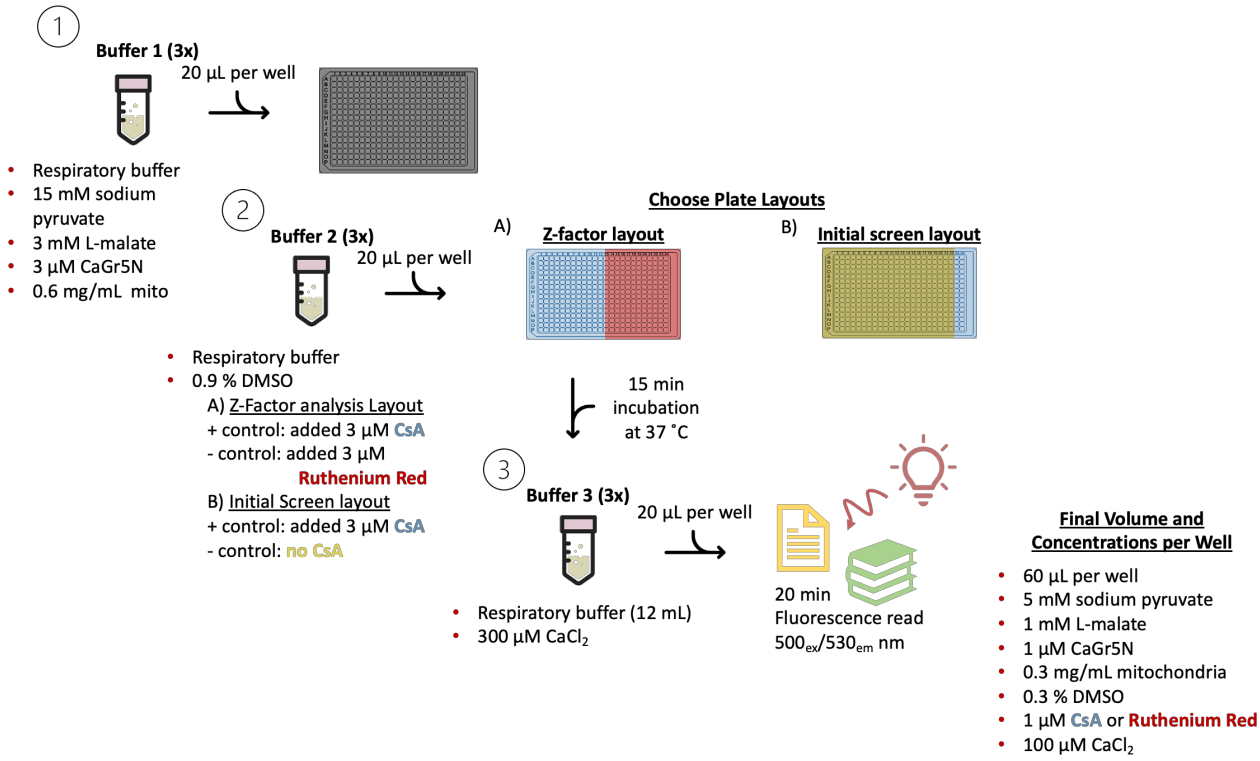

Figure 6.5: Schematic representation of the High-throughput screening protocol.

respiration buffer for each experiment. The microtubes were thawed shortly before starting the experiments to minimize dye decomposition and hydrolysis. The cassette tubing was rinsed and filled with 70 % EtOH to minimize surface evaporation, and it was washed with ddH_2O before priming Buffer 1 or 3. A 12 mL solution containing 0.9 % DMSO and respiration buffer was prepared (Buffer 2). A 3 μM CsA final concentration was prepared by aliquoting 6 mL from Buffer 2 and mixing it gently. This is our positive control solution. The remaining Buffer 2 solution was used as the negative control, containing either 3 μM Ruthenium Red (RR) for the Z-factor calculation layout or control mitochondria for the drug screening assay (**Figure 6.5**).

A Corning® 384-Well Solid Black plate was used, and wells A1-P12 were filled with 20 μL of the control solution (Buffer 2), while wells A13-P24 were filled with 3 μM cyclosporin A. Buffers 1 and 3 (described below) were dispensed using the BioTek EL406 Washer Dispenser.

Before priming the cassette with Buffer 1, the tubing was washed with 100 mL of ddH_2O. Buffer 1 was gently mixed to homogenize and resuspend the mitochondrial solution. The 384-well plate was loaded with 20 μL of Buffer 1 solution, quickly inserted into the preheated (37 °C) Biotek Synergy Neo Plate Reader, and set to linearly shake for 30 seconds. The plate was incubated for 15 mins at 37 °C to stabilize the mitochondrial signal. Meanwhile, a 300 μM $CaCl_2$ solution was freshly prepared in respiration buffer (Buffer 3) as shown in **Figure 6.5**. Before priming the cassette with Buffer 3, the tubing was washed as described above. After 15 minutes of incubation, the 384-well plate was removed, and 20 μL of Buffer 3 solution was added per well. The final concentrations for the reagents were 0.3 mg/mL mitochondria, 1 μM Calcium Green 5N, 3 μM CsA, 5 mM sodium pyruvate and 1 mM L-malate, 100 μM $CaCl_2$, and 0.3 % DMSO. The plate was quickly inserted into the preheated (37 °C) Biotek Synergy Neo Plate Reader, set to linearly shake for 30 seconds, and a 20-minute fluorescence kinetic read was performed at a minimum interval of 1 read per minute, with excitation at 500 nm and emission at 530 nm (**Figure 6.5**).

All measurements were done at least in triplicate. The ADDRC drug library was used to screen approximately 5,000 compounds from the NCI diversity set V library and the PKIS (GSK) kinase library. The initial concentration for these libraries was 2 mM, and the working concentration was 0.015 mM and 0.007 mM for the NCI diversity and GSK library, respectively. Sets of 384-well plates were initially loaded with 20 μL of respiration buffer. The compound library was loaded onto the 384-well plates with a Beckman Coulter Biomek FX^p. The last two columns were loaded with 3 μM CsA (positive control). Buffer 1 was prepared, primed on the cassette, and 20 μL was loaded onto the 384-well plate, as discussed above. To minimize fluorescence, the plate was covered in aluminum foil and incubated for 15 minutes following a linear shake for 30 seconds inside the Biotek Synergy Neo Plate Reader

preheated to 37 °C. Similarly, Buffer 2 was prepared, and 20 μL was loaded on the 384-well plate, as discussed above. The plate was quickly inserted into the Biotek Synergy Neo Plate Reader preheated to 37 °C and set to linearly shake for 30 seconds. A 20-min fluorescence kinetic read was performed with the minimum interval (1 read per min) by exciting at 500 nm and emitting at 530 nm. Drug hits were confirmed in duplicates.

Reagents

All reagents were purchased from Sigma Aldrich unless stated otherwise. All the reagents were diluted with respiration buffer unless stated otherwise.

6.6 Results

Protocol Optimization, Feasibility, and Z-Factor Analysis

When mitochondria are suspended in the wells of a 384-well plate, the signal initially drifts due to minor mitochondrial swelling and other kinetic adaptations to the new environment resulting from the sudden rise in temperature. As part of the optimization, it was crucial to determine where the fluorescence signal stabilizes to obtain accurate results. The fluorescence signal was measured over a period of ∼17 minutes as shown in a representative trace in **Figure 6.6A**. The last 5 data points of this measurement were averaged to determine the fluorescence for the positive (CsA) and negative (RR) controls. The environment and assay conditions have a large effect size when it comes to mitochondrial calcium toxicity. Therefore, we tested calcium doses ranging from 50 to 150 μM to determine the calcium toxicity threshold in this experimental platform. We found that mitochondria can tolerate

a 50 μM $CaCl_2$ bolus but fully permeabilize at higher concentrations (**Figure 6.2B**). As expected, mitochondria did not uptake calcium in the presence of the negative control RR. Robust calcium uptake was observed when the positive control CsA was present, even at the highest calcium load. Altogether, these results suggest that 100 μM $CaCl_2$ is a suitable concentration to compromise mitochondrial function.

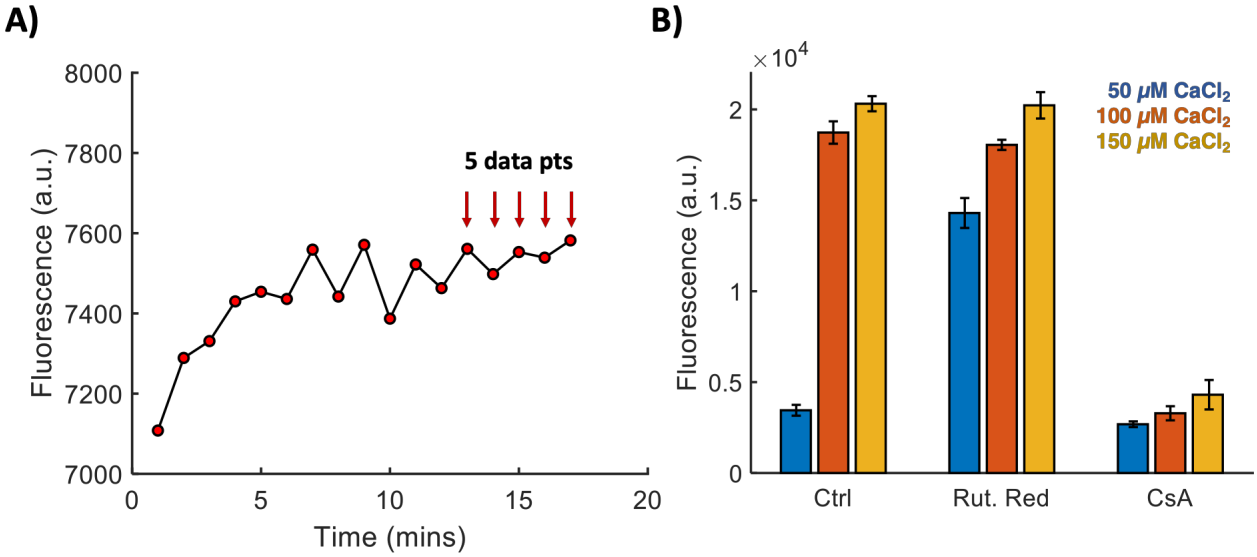

Figure 6.6: A) Representative trace of signal stability after 11 minutes. The last 5 data points were averaged to determine the Z-factor in the following assay for CsA-treated and control mitochondria. B) Representative trace to determine the toxic calcium bolus. RR and CsA are the negative and positive controls, respectively. Error bars represent the mean values obtained from the last 5 points averaged from minute 11 to 17 for $n = 4$ technical replicates. The presented data was obtained for a final volume of 45 μL per well.

Since the solvent for all the drugs in the compound library was DMSO, we tested whether DMSO affects our experimental setup (**Figure 6.7**). We found that DMSO percentages below 0.5 % did not significantly impair calcium uptake; however, solvent concentrations at 0.5 % and above led to premature permeabilization. For example, the fluorescence signal almost doubles at 50 μM $CaCl_2$ for every $\sim$0.5 % increase in DMSO. DMSO concentrations across the board had no effect on the signal for the 100 and 150 μM $CaCl_2$ boluses. Moreover, the RR results reveal that the solvent does not interfere with the dye's fluorescent signal.

When CsA is present, mitochondria are capable of taking up and storing the vast majority of the calcium challenge regardless of DMSO concentration.

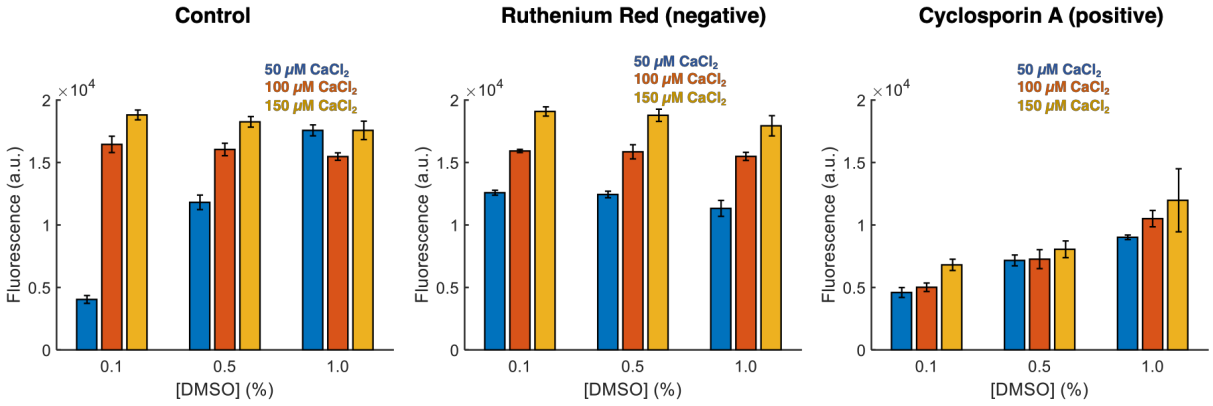

Figure 6.7: DMSO compromises mitochondrial function at increasing concentrations. Mitochondria were exposed to a 50, 100, and 150 μM $CaCl_2$ bolus in the presence or absence of RR and CsA. Error bars are the mean values obtained from the last 5 point averaged from minute 11 to 17 for $n = 4$ technical replicates. The data presented was obtained for a final volume of 45 μL per well.

After optimizing the screening assay and selecting the 100 μM $CaCl_2$ bolus as the toxic load, we performed the Z-factor analysis (**Figure 6.8**). It is important to note that the fluorescence signal intensities in **Figures 6.6** and **6.7** are lower than those in **Figure 6.8A** and **6.8B** due to the higher number of fluorescent molecules present in the assay buffer. This is because Calcium Green 5N, a non-ratiometric molecular dye, was used as the fluorophore, and the assay volume was increased from 45 μL to 60 μL to achieve ~0.3 % DMSO in the initial screen, which also increases the number of Calcium Green 5N fluorophores in the well.

The Z-factor measures how well the assay separates the signal values from the positive and negative controls and is commonly used as a measure of the assay's signal-to-noise (S/N) ratio. For the Z-factor and initial screen assay, the "negative" control is the untreated group, and the "positive" control is the CsA-treated group. A value of 1 indicates the assay has a perfect separation between the positive and negative controls, while a value of 0 reflects no

separation. If the Z-factor is negative, it indicates poor separation between the groups and is not suitable for high-throughput screening (HTS). The statistical parameter to evaluate the quality of the S/N ratio was calculated as follows:

$$\text{Z-factor} = 1 - \frac{3(\text{SD}{+\text{Ctrl}} + \text{SD}{-\text{Ctrl}})}{\mu_{+\text{Ctrl}} - \mu_{-\text{Ctrl}}} \tag{6.1}$$

Where SD is the standard deviation and μ is the mean for the positive and negative controls respectively (**Equation 6.1**). In HTS, a Z-factor value of at least 0.5 is considered acceptable for the separation between the controls. In this study, the Z-factor value obtained was 0.79, indicating good separation among the controls, and thus, demonstrates the suitability of this assay for a HTS (as shown in **Figure 6.8C**). To perform the HTS, a 384-well plate was divided into two halves: 192 wells were filled with control, and the other 192 wells were filled with 1 μM CsA as shown by the representative heatmap in **Figure 6.8A**.

High-throughput screening assay results

A total of 11 hits were identified from the ∼5,000 compounds screened from the GSK Kinase and NCI Diversity libraries. These results are listed below (**Table 6.1**). Compounds were considered effective when fluorescent values at least 3σ above the value obtained with CsA (negative control). The assay Z-factors for the NCI Diversity and GSK kinase libraries ranged between ∼0.6 to 0.7. The strongest hits came from the GSK kinase library as shown in the % Fluorescence and Sigma value columns from **Table 6.1**.

The web tool SwissTargetPrediction was used to predict potential protein targets using structural or ligand-based information [383]. The mechanisms of action for the novel compounds are not well understood. Protein targets are predicted based on the SwissTar-

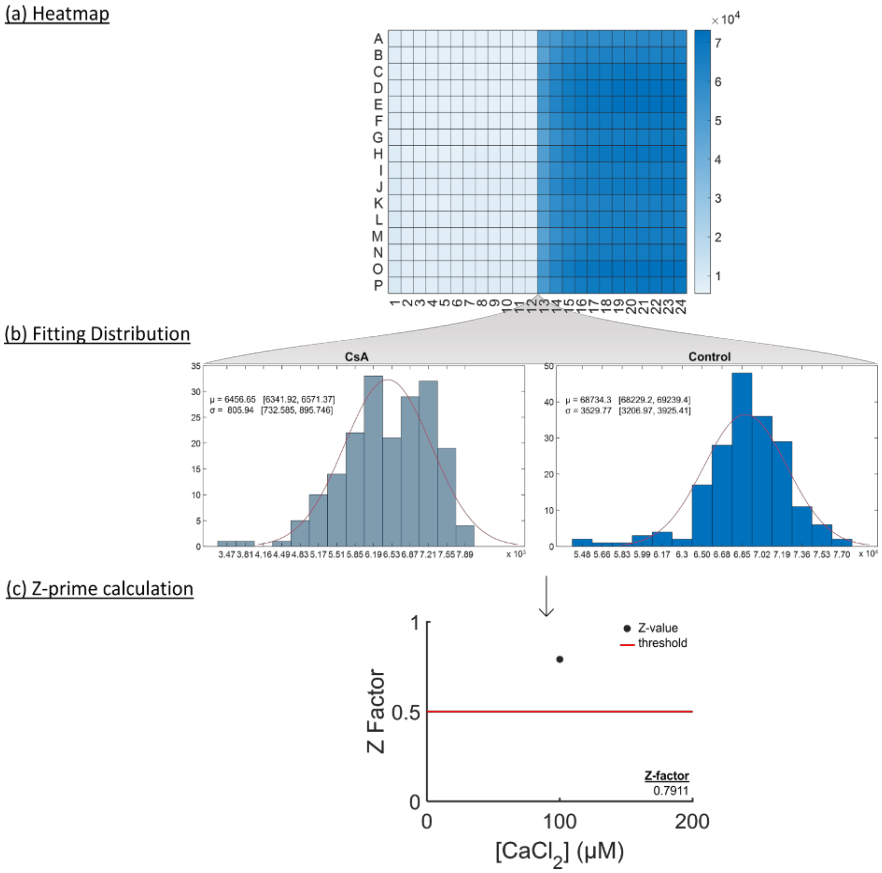

Figure 6.8: The Z-factor was obtained by analyzing plate reader signals at 15 minutes into the read. Positive control CsA resulted in lower fluorescence due to reduced mitochondrial calcium uptake, while untreated mitochondria showed increased fluorescence due to calcium release following permeabilization. The signal for CsA-treated mitochondria was 10.6 times higher than the control group. The coefficients of variation were 12 % and 5 % for the CsA treatment and control, respectively. The Z-factor was 0.7911, well above the acceptable threshold of 0.5, and was calculated based on a sample size of 6.

getPrediction database, and the most likely targets are assumed to be bioactive and from the *Homo sapiens* species. A list of target proteins known to associate with mitochondria is given in **Tables 6.1** and **6.2**. It is important to note that specific protein expression, molecular diversity, and function vary among cells, tissues, and organisms. The list includes both frequently and less frequently predicted targets. In the following discussion, I will focus on the most frequently observed targets, such as members of the phosphodiesterase (PDEs) family and glycogen synthase kinase-3β (GSK-3β), while also mentioning some of the less

Compound	Structure	Library	% Fluorescence	Sigma	Potential Protein Targets[1]
MSU-9549	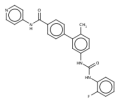	GSK Kinase	93.64	9.92	• Phosphodiesterase: PDE2A, 4A and 4B, 5A • p-53 binding protein minute double minute 2 (MDM2)
MSU-9433	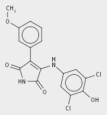	GSK Kinase	43.55	3.03	• Glycogen synthase kinase 3-beta (GSK3B) • NAD-dependent deacetylase sirtuin-1 (SIRT1) • Phosphodiesterase: PDE5A, 7A, 10A • Apoptosis regulator Bcl-X (BCL2L1) • Matrix metalloproteinases: MMP3, 12, and 13
MSU-9397	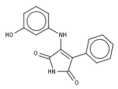	GSK Kinase	48.47	3.37	• Phosphodiesterase: PDE2A, 4B and 4D, 10A • glutathione S-transferase alpha 1 (GSTA1) • Huntingtin (HTT) • Matrix metalloproteinase 13 (MMP13)

Table 6.1: List of novel compounds from the GSK library. The % Fluorescence represents the fluorescence signal relative to the negative standard, which corresponds to untreated mitochondria. The σ value column represents the standard deviation of the fluorescent signal relative to the negative standard. The predicted protein targets for the novel compounds from the web tool SwissTargetPrediction[1] database [383]. The predictions are based on the *H. sapiens* species.

common ones to provide a comprehensive understanding of the results.

Phosphodiesterase Inhibitors and Mitochondrial Function

The GSK library contains the most promising compounds for protecting against calcium overload. All of these compounds have the potential to inhibit various members of the PDE family, which is a superfamily containing 11 structurally related proteins with distinct functions [384]. PDEs regulate the secondary messengers cAMP and cGMP signaling by catalyzing the hydrolysis of phosphodiester bonds [385]. Due to their molecular diversity, some PDEs are cAMP- or cGMP-specific and are activated or inhibited by cAMP or cGMP. A comprehensive review of the PDEs' structural differences, tissue expression, function, and selective inhibitors can be found in ref. [384]. The discovery of soluble adenylyl cyclase (sAC) in the mitochondrial matrix has led to a better understanding of the role of cAMP in regulating mitochondrial function [386]. Recent research suggests that cAMP is the rate-limiting

Compound	Structure	Library	% Fluorescence	Sigma	Potential Protein Targets[1]
MSU-4732	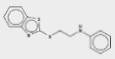	NCI Diversity	30.85	3.18	• Phosphodiesterase: PDE2A, 4A, 5A, 7A, 10A • Hypoxia-inducible factor 1 alpha (HIF1A) • Quinone reductase 2 (NQO2) • Translocator protein (TSPO) • Matrix metalloproteinases: MMP1, 2, 8, 9, 13 and 14
MSU-4575	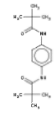	NCI Diversity	28.71	3.37	• Glycogen synthase kinase 3-beta (GSK3B) • Hexokinase Type IV (GCK) • CaM Kinase II (CAMK2D) • Phosphodiesterase: 4A-D, 5A p-53 binding protein minute double minute 2 (MDM2)
MSU-4571	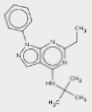	NCI Diversity	28.61	3.36	• Phosphodiesterase 7A (PDE7A) • Translocator protein (TSPO) • Matrix metalloproteinase: MMP2 and MMP9 • Quinone reductase: NQO1 and NQO2 Caspase 5 and 7 (CASP5 and 7)
MSU-4656	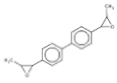	NCI Diversity	28.32	3.32	• Glycogen synthase kinase 3-beta (GSK3B) • Hexokinase Type IV (GCK) • Phosphodiesterase: 3A and 3B, 4A and 4B, 10A
MSU-4814	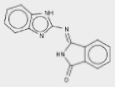	NCI Diversity	28.23	3.31	• Glycogen synthase kinase 3-beta (GSK3B) • Phosphodiesterase: PDE4B, 10A • Bcl2-antagonist of cell death (BAD)
MSU-4734	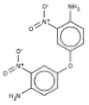	NCI Diversity	27.13	3.18	• Glycogen synthase kinase 3-beta (GSK3B) • Phosphodiesterase: PDE4B and 4D, 5A • Sodium/hydrogen exchanger 1 (SLC9A1)
MSU-4653	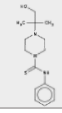	NCI Diversity	26.79	3.13	• Phosphodiesterase: PDE2A and 10A
MSU-5052		NCI Diversity	22.93	3.01	• Phosphodiesterase 10A (PDE10A) • Sodium/hydrogen exchanger 1 (SLC9A1) • Bcl2-antagonist of cell death (BAD) • Translocator protein (TSPO)

Table 6.2: List of novel compounds from the NCI library. The predicted protein targets for the novel compounds from the web tool SwissTargetPrediction[1] database [383]. The predictions are based on the *H. sapiens* species.

step for matrix calcium accumulation via the exchange protein directly activated by cAMP 1 (Epac1) and the mitochondrial calcium uniporter (MCU) [386]. Moreover, cAMP stimulates oxidative phosphorylation (OXPHOS), which increases ATP production [387]. These findings highlight the critical role of cAMP signaling in regulating mitochondrial metabolism. Additionally, cAMP is involved in cardiac function and pathogenesis, as well as the mitochondrial permeability transition pore (PTP) [388, 389]. It has been documented that cAMP signaling protects against necrosis and apoptosis, thereby playing a crucial role in maintain-

ing mitochondrial integrity [386]. Given that PDEs regulate cAMP production, their role in regulating mitochondrial function has been a topic of interest in recent studies. Like cAMP, they are linked to cardiomyopathies and mitochondrial structure [390]. For instance, PDE2A2 is localized within the mitochondrial matrix and is thought to regulate ATP production by degrading cAMP levels generated through sAC [387, 390]. However, a recent study suggests that PDE2A2 localizes outside the mitochondrial matrix and controls cytoplasmic cAMP and protein kinase A-dependent dynamin-related protein 1 (Drp1) phosphorylation [390]. This is intriguing because the GTPase Drp1 is a main regulator of mitochondrial fission. Altogether, PDEs are also localized in the mitochondria and provide regulatory actions by controlling structure and function. Recently, the effects of three PDEs (2-4) in isolated rodent cardiac mitochondria was studied [386]. While PDE4 is predominantly expressed in rodents, PDE2 showed the largest cAMP-degrading activity followed by PDE3 and PDE4 [386, 389]. Interestingly, the overexpressed PDE2 transgenic mice models had an increased sensitivity to swelling and loss of membrane potential upon calcium exposure relative to the control group. This is intriguing given a recent report on the overexpression of PDE2A in human heart failure [391]. A study on isolated rat hearts showed that inhibition of PDE4 enhanced the inotropic effects by activating SERCA2a [392]. Whereas a porcine model of heart failure show that PDE inhibitors can induce arrhythmogenic events [389]. While the acute application of PDEs has antihypertrophic and cardioprotective action, long-term use of PDEs in clinical trials increased cardiovascular mortality [393, 394]. The therapeutic action of these drugs can be related to the specific PDEs they target and their relative expression in cardiac tissue. For instance, PDE3 is the most common phosphodiesterase expressed in the human heart. PDE3A is found to control cardiac contractility and calcium handling [384]. Whereas PDE3B expression is not limited to cardiomyocytes and found to regulate

angiogenesis, lipid metabolism, and insulin signaling [384]. Hence, a drug inhibiting PDE3A might induce arrhythmogenic events relative to an inhibitor targeting PDE3B or another PDE exerting less cardiac function. Therefore, the positive and negative off-target effects induced by PDE inhibition must be carefully considered. In conclusion, the complex interplay between PDEs, cAMP signaling, and mitochondrial function highlights the potential of PDE inhibitors as a promising avenue for protecting against calcium overload and related cardiac pathologies, while also emphasizing the need for further research to fully understand their mechanisms of action and potential risks.

GSK-3 β inhibition might confer calcium overload protection The glycogen synthase kinase-3 beta (GSK-3 β) appeared in roughly half of the small molecules identified in **Table 6.1**. GSK3 is a serine/threonine kinase that controls cell proliferation, gene transcription, protein synthesis, regulation of glycogen synthesis, among other cellular processes [395]. GSK3 exists as two isoforms GSK-3 α and GSK-3 β encoded by two different genes with some overlapping and distinct functions [396]. Evidence on GSK-3 β inhibition highlights the potential clinical application in many diseases including as a mediator in anticancer immune response, Alzheimer's disease, and Parkinson's disease [397, 398]. The versatility of GSK-3 β inhibition could be attributed to the close to 100 proteins identified to be phosphorylated by GSK-3 β [397, 398]. In the context of mitochondria, GSK-3 β regulates all aspects of mitochondrial function including biogenesis, bioenergetics, motility, and apoptosis [398]. This makes it a strong candidate for establishing a mechanism of action against calcium-mediated PTP activity. Aspects of GSK-3 β were discussed in Chapter 1 whereby PTP formation following calcium overload is formed by the interaction of VDAC, Cyp-D, and the ANT. The proposed model of this mode of PTP regulation suggests that Cyp-D and ANT interaction can be impeded by GSK3 β inhibition or inactivated by phosphorylation

at Ser9 [399]. A study led by Gomez et al. assessed the involvement of GSK-3 β in PTP formation in ischemic hearts from mice following postconditioning [400]. Results suggest that postconditioning increased the threshold at which PTP formation in isolated mitochondria ensues in response to Ca^{2+}. This protective effect was not detected in transgenic mice expressing GSKS9A that cannot be inactivated by phosphorylation [400]. However, transgenic mice expressing a non-phosphorylatable form of GSKS9A did not exhibit this protective effect [400]. Taken together, this suggests GSK-3 β regulates PTP formation following Ca^{2+} overload insults. In support of the abovementioned PTP model, Nishihara et al. conducted a co-immunoprecipitation study to assess the interaction of phosphorylated GSK-3 β with PTP regulators including VDAC, ANT, and Cyp-D. In a study conducted on rat hearts, GSK-3 β phosphorylation was induced through ischemic preconditioning and erythropoietin-receptor activation of PKC and PI3K/Akt. The study found that phosphorylated GSK-3 β co-immunoprecipitated with ANT but not VDAC [204]. Additionally, the interaction between ANT and Cyp-D was disrupted by 40 % along with a 50 % increase in the interaction between phosphorylated GSK-3 β and ANT [204]. Altogether, these results provide a potential mechanism of action for the hit compounds by which inhibited or phosphorylated GSK-3 β interacts with PTP modulators to increase the threshold for Ca^{2+}-induced PTP.

Other targets

Another potential target is a protein called mouse double minute 2 (MDM2) which has been recently shown to modulate respiratory complex I activity independently of p53 [401]. It has been classified as an oncogene and a tumor suppressor [401]. It negatively regulates the p53 tumor suppressor and has been recently shown to be transported actively into the mi-

tochondria following hypoxic and ROS insults [402]. MDM2 also represses the transcription of NADH-dehydrogenase 6 and complex I activity in H1299 lung cancer cells [402]. A recent study provided a mechanism of action for the decreased mitochondrial respiration and ROS generation in which MDM2 directly binds to the NADH:ubiquinone oxidoreductase 75 kDa Fe-S protein 1 (NDUFS1) and destabilizes complex I activity and supercomplex assembly [401].

Furthermore, studies looking at vascular calcification suggest that the transcriptional activation of MDM2 is elevated in calcified human coronary arteries and in mouse models [403]. The effect of increased transcription increases the E3 ligase activity, which is essential for vascular calcification. Interestingly, elevated inorganic phosphate (Pi) in vascular smooth muscle cells (VSMCs) induces calcium phosphate deposits, which in turn upregulate MDM2 expression [403]. Similarly, a study investigating the effects of α-lipoic acid in VSMCs showed that elevated Pi led to decreased $\Delta\Psi_m$ and ATP production, ROS elevation, and disrupted mitochondrial structure [404]. In addition, these events were often followed by cytochrome c release and other pro-apoptotic events [404]. Altogether, this suggests a role for MDM2 in mitochondrial structure, function, and ROS generation independently of p53 binding. Two out of 11 were predicted to interact with this target, including the most active compound (**Table 6.1**: MSU-9549 and MSU-4575).

Matrix metalloproteinases (MMPs) have emerged as an interesting therapeutic target due to their role in the degradation of extracellular matrix proteins, which contributes to tissue remodeling and repair [405]. MMPs are Ca^{2+}-dependent Zn^{2+}-containing endopeptidases that are also found within cardiac mitochondria, and their activation can disrupt mitochondrial function and lead to loss of cardiac contractility following ischemia/reperfusion (I/R) injury [212, 222, 406]. This disruption is due to MMP-mediated degradation of mito-

chondrial proteins, including those involved in oxidative phosphorylation, which ultimately impairs energy production in the cell. Moshal et al. hypothesized that MMP activation and expression induces the formation of the mitochondrial permeability transition pore (PTP) and causes contractile dysfunction, as demonstrated in C57BL/6J mice fed with an elevated level of homocysteine diet [212]. Therefore, MMP inhibition may represent a potential strategy to protect cardiac mitochondria against Ca^{2+}-induced PTP activity, and the screened mitoprotectants MSU-9433, MSU-9397, MSU-4732, and MSU-4571 could act through this mechanism to preserve mitochondrial integrity (**Tables 6.1** and **6.2**). Hence, targeting MMPs represents a promising approach to mitigate the deleterious effects of I/R injury on mitochondrial function and cardiac contractility.

Overall, understanding how the screened compounds protect against Ca^{2+} overload is important for developing effective therapies. Further investigation is needed to confirm their mechanisms of action and detect any off-target effects. Assays to detect and characterize protein interactions are necessary for gaining insights into their protective effects. Therefore, comprehensive understanding of these mechanisms is crucial for developing potential therapies for calcium overload-related disorders.

Future directions: The one-two punch study

Although PTP is primarily induced by calcium overload, oxidative stress lowers the calcium threshold necessary to induce MPT [407]. A major contributor of I/R injury is the post-reperfusion burst of free radicals. Hence, compounds that passed the first screen must also preserve mitochondrial integrity in calcium overload conditions in pro-oxidative environments. As a future direction, if more than two compounds from **Table 6.1** are identified, they should be ranked based on which compound lowers the buffer calcium the most. To en-

sure compounds do not interact with Calcium Green 5N, the fluorescence should be measured in the presence of the drug without mitochondria. To screen for a one-two punch resistance, the optimized protocol must be used while including two types of pro-oxidants to test if the compounds identified in **Table 6.1** are still effective during oxidative stress. The first will be the redox cycler MitoPQ. This compound produces superoxide inside mitochondria proportional to its concentration [396].

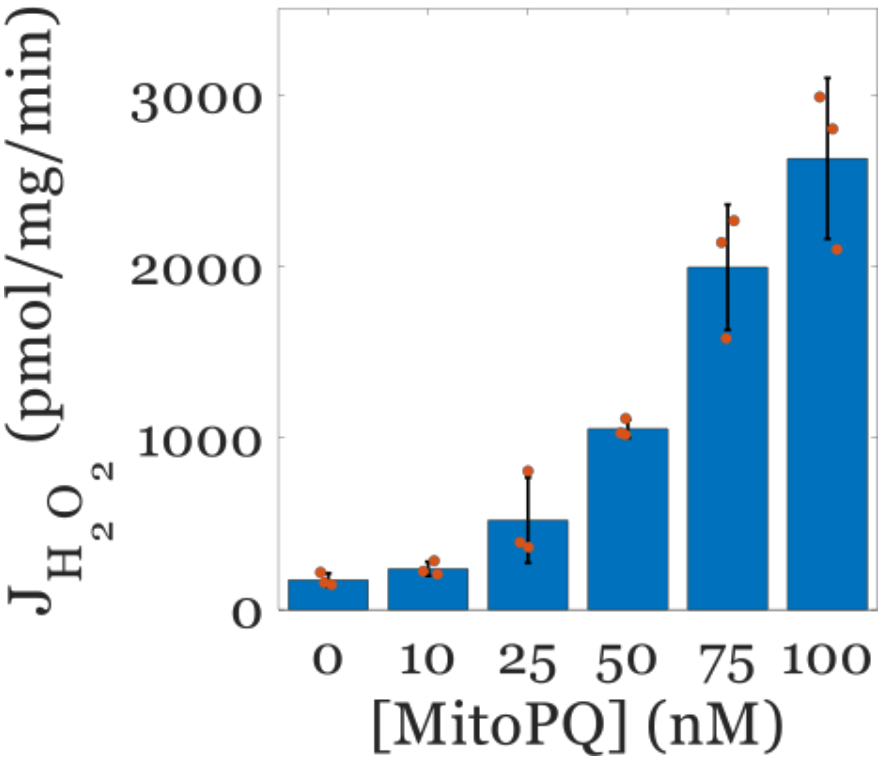

Figure 6.9: Mitochondrial ROS emission can be adjusted using the MitoPQ.

Preliminary data suggests the rate of ROS emission is controllable and a function of the concentration of MitoPQ (**Figure 6.9**). The second to consider is the lipid peroxide, tert-butyl hydroperoxide. A positive hit is considered successful if the drug achieves to preserve mitochondrial integrity in calcium overload conditions in pro-oxidative environments. The same positive and negative controls used for the protocol optimization should be used. In future studies, one should use additional *in vitro*, *ex vivo*, and *in vivo* experiments methods in

an acute and chronic settings to validate drug efficacy alluded to by our screen. For instance, screens can be employed in whole cells (e.g., H9c2, C2C12 or other myocyte lines) and compared with the results herein obtained from isolated mitochondria. For the *in vitro* studies, calcium retention capacity and ATP production rates must be quantified using the isolated mitochondrial preparation to determine the impact of the compounds on the mitochondrial function. For the *ex vivo* method, the Langendorff isolated heart perfusion platform can be utilized with the goal of monitoring cardiac function post-infarct in the acute setting. The hemodynamic function, infarct size, and mitochondrial viability can be quantified after a global ischemic insult with and without select compounds that make it past the screenings. For the chronic studies, *in vivo* conscious coronary occlusion model can be included. Coronary artery occlusion can be performed in guinea pigs by tying off the left coronary artery above the left anterior descending artery and circumflex artery branch point. In this model, occluding and pacing the guinea pig hearts, can cause significant cardiac damage. Longitudinal follow up studies 4 to 8 weeks post-treatment should be considered to monitor cardiac function, hypertrophy, scarring, and assess mitochondrial function. Importantly, control animals not receiving treatment must be included. Ultimately, data from each experimental level should reinforce one another and provide a comprehensive understanding of the molecular and metabolic effects of each prospective drug.

Chapter 7

Conclusion

This thesis provides a comprehensive approach to understanding the role of calcium overload in cardiac mitochondrial bioenergetics and its impact on the permeability transition pore (PTP) in the context of ischemia/reperfusion (I/R) injury. It sheds light on the complex mechanisms of calcium storage and ultrastructural changes associated with mitochondrial dysfunction resulting from calcium overload. By focusing on identifying preventative measures before reaching the point of no return, this work contributes to the development of therapeutic and preventative measures aimed at mitigating the severe effects of PTP following pathological mitochondrial calcium overload.

The thesis begins by providing a historical perspective on the role of mitochondrial PTP and its relevance in pathophysiology. The review emphasizes that previously proposed components and models of pore formation remain crucial for understanding its regulation. However, it also notes that these models have not been conclusively proven, and the molecular identity of the pore is yet to be fully elucidated.

Here, I present a unique proposal that focuses on preventing PTP before reaching the point of no return. Specifically, it highlights that high levels of calcium accumulation in the mitochondrial matrix cause structural alterations that negatively impact mitochondrial function through cristae remodeling. Although this work does not investigate how calcium uptake alters cristae-stabilizing proteins, it speculates on how such alterations could desta-

bilize the cristae. Therefore, future studies should aim to address the problem at its core by examining the molecular mechanisms underlying these structural alterations. Overall, this thesis makes a valuable contribution to the field by presenting novel insights into the regulation of PTP and identifying potential avenues for future research.

While sodium pyruvate and L-malate were used as the primary substrates in most of the experiments presented, previous studies in our lab have shown that the regulation of calcium varies with the presence of additional substrates, such as succinate (see **Appendix C.1**) and fatty acids [408]. This finding is particularly relevant given that a normal, healthy heart derives a significant proportion of its high-energy phosphates from fatty acids (approximately 60-90 %), with carbohydrates and lactate compensating for the rest [409]. While fatty acid metabolism yields more ATP per molecule than glycolysis, it also consumes more oxygen, which can exacerbate I/R injury under anoxic conditions [410].

These results underscore the importance of regulating both fatty acid and glucose metabolism in cardiomyocytes, especially during I/R injury. In our discussion, I mentioned that complex I is larger in size compared to complex II. The size difference between these complexes may have implications for their susceptibility to calcium phosphate deposits, as complex I may be more susceptible due to its larger size. This is consistent with our previous finding that mitochondria energized with succinate, which feeds directly into complex II, are more resistant to calcium overload. One possibility is that calcium phosphate deposits affect complex I activity mechanically or pose a limit on the diffusion barrier of reducing equivalents like NADH. Hence, energizing mitochondria with succinate does not present the same hindrance and allows respiration to continue until the mitochondrial structure begins to compromise following calcium accumulation and calcium phosphate deposit formation. Moving forward, future research should explore the effects of a broader range of substrates, alone and in com-

bination, on mitochondrial function and structure during calcium overload. Such studies will provide critical insights into how to reduce or mitigate the severe effects of PTP following pathological mitochondrial calcium overload. This will lead to the development of more effective therapeutic and preventative measures.

The experiments conducted in **Chapter 2** provided valuable insights into the role of PTP and calcium overload in cardiac mitochondrial bioenergetics. This chapter explains the observed ATP production decoupling following calcium overload and suggests that increasing calcium loads decrease the amount of ATP molecules produced for the same number of O_2 molecules. The respiratory ratios (JO_2) were used to estimate the effect of calcium overload on oxygen utilization during OXPHOS in the absence or presence of CsA. The results showed that CsA tends to lower the duration of OXPHOS to baseline without impacting the estimated ATP/O_2 ratio, dampening the effect of increasing calcium loads on ATP production. The fact that this effect persists at very low calcium levels suggests that CsA might be modulating the mitochondrial structure. One possible mechanism is that CsA might interact with metalloproteases that are known to activate by calcium to destabilize proteins regulating cristae junction structures. Hence, further experiments will need to be conducted to determine whether CsA regulates metalloprotease activity. Interestingly, CsA had little to no effect on the O_2 cost and ATP production, suggesting that PTP is not relevant in this scenario.

The preliminary findings that calcium phosphate complexes are the main components of the mitochondrial calcium sequestration system shed new lights on potential mechanisms prior to PTP activity. The formation of these calcium phosphate complexes can be described by the biochemical reaction shown in **Appendix C.2**. This reaction is charge and atom balanced and works for many calcium phosphate species (e.g. tricalcium phosphate, hy-

droxyapatite, and octacalcium phosphate). Using this reaction, a mathematical expression describing the mitochondrial calcium buffering power can be derived as shown in **Appendix C.2**. In this equation, two components of calcium buffering are explicitly modeled. The first component consists of prototypical buffers that includes protein, lipid, metabolite, and other binding sites in the matrix. The second component consists of calcium phosphate complexes. To experimentally quantify the calcium buffering power, the rates of total and free calcium flux into or out of the mitochondrial matrix must be simultaneously measured. After correction for compartment volume differences, their ratio:

$$\frac{[Ca^{2+}]_{tot}}{[Ca^{2+}]_{rate}} \tag{7.1}$$

gives the calcium buffering power of the mitochondrial matrix. Details of this method are described in Bazil et al [214]. An application of this method is shown in **Appendix C.3** explaining two conditions thought to regulate this system i) modulators that enhance buffering (CsA) or ii) diminish it (tert-butyl hydroperoxide, t-BuOOH). These data revealed that modulators that increase calcium uptake also increase the calcium buffering power; whereas, modulators that decrease calcium uptake, diminish the buffering power. These findings shed light on a previously unknown mode of regulation and provided evidence of the protective role of agents like CsA in the presence of calcium loads that induce PTP activity.

To test the hypothesis that CsA modulates mitochondrial function and calcium sequestration, cryo-EM imaging was used in **Chapter 3**. The results showed that calcium overload led to concentration-dependent calcium phosphate deposits, which could potentially induce cristae destabilization and explain the observed mitochondrial dysfunction prior to the onset of PTP. These findings shed light on the mechanisms underlying tissue damage during

I/R injury and suggest that mitochondria play a crucial role in the apoptotic response to reperfusion. Details of the cryo-EM imaging and data can be found in **Appendix A**.

To support this hypothesis, a model was derived in **Chapter 4** from the classic conservation law and free energy minimization, which described the dynamics of pattern formation and phase separation of the mitochondrial ultrastructure in the presence of calcium phosphate deposits. The morphological changes observed with this model correlated with the loss of mitochondrial function and ATP production rates observed in previous experiments and with the 3D reconstructed models in the presence and absence of calcium. Overall, this study provided an understanding of how calcium overload impairs mitochondrial function and the devastating consequences to mitochondrial structure.

However, this model is in its nascent stages and requires further expansion. For example, the model only considers the changes between cristae or matrix expansion, without considering any fluxes going in or out of the system. Therefore, depending on how the system is initialized, it can cause either the matrix or cristae to expand, depending on which compartment the calcium phosphate deposits are located in. However, since the calcium phosphate deposits are positioned in the mitochondrial matrix, the computational model is constrained to push the system towards matrix expansion. To enhance the computational model, the next steps would be to integrate the fluxes of different molecules, ions, and energy within the mitochondrial matrix and cristae. This would enable a more comprehensive representation of the dynamic changes in mitochondrial structure and function. Moreover, the model could be expanded to incorporate other factors that may contribute to mitochondrial dysfunction, such as reactive oxygen species and changes in pH. It would be crucial to validate the model with experimental data obtained from *in vitro* and *in vivo* studies to ensure that it accurately predicts the observed morphological changes and alterations in mitochondrial function.

Additionally, the model could be utilized to identify potential therapeutic targets or drug candidates for the treatment of mitochondrial dysfunction and related diseases. Overall, the continued refinement of the model is expected to provide valuable insights into the intricate mechanisms that govern mitochondrial function and dysfunction, and ultimately lead to the development of novel therapeutic interventions for mitochondrial diseases.

Altogether, the structural insights gained in **Chapter 4** shed light on the mechanisms underlying pathological mitochondrial calcium overload and the subsequent loss of function, paving the way for further investigations into potential therapeutic strategies aimed at mitigating the devastating effects of PTP on mitochondrial ultrastructure and bioenergetics.

In **Chapter 5**, the study further explores the effects of calcium overload on mitochondrial structure and function. Specifically, the chapter focuses on changes in cristae structures and the effect of calcium phosphate deposits on the mitochondrial matrix. The data presented in this chapter provide a strong case for why ATP production is impaired, as previously suggested by the functional and structural data presented in the previous chapters. The chapter also briefly discusses the effect of CsA on the mitochondrial outer membrane, although the CsA-treated group in the presence of calcium was not included in the report due to data collection feasibility.

Upon observation, it was noticed that CsA exhibits two different configurations following calcium uptake: one where it appears spread across the hole and grid, resembling a "spaghetti meatball" with its inner membrane preserved, and another where the mitochondrion looks normal with a dense matrix. It was observed that mitochondria looking like "spaghetti meatball" have many granules and the outer membrane is entirely lost, while normal-looking mitochondria have barely visible granules. Based on these observations, multiple explanations can be suggested. Firstly, the formation of calcium phosphate deposits leads to matrix

expansion, but since CsA preserves the cristae junction integrity, only the outer membrane is lost, and not the inner membrane. Secondly, CsA-treated mitochondria without big or multiple solid granules may have fewer mitochondrial calcium uniporters (MCU), which is the main route for calcium uptake. Hence, less or lack thereof of MCU would lead to fewer calcium phosphate deposits, as discussed in **Chapter 3**.

Regarding the potential effects of CsA on mitochondrial membrane adherence during cryo-EM, it is possible that the addition of CsA may alter the stability of the mitochondrial membrane, thereby affecting its ability to adhere to a carbon grid during sample preparation. In the blotting step, a thin layer of sample solution containing the mitochondria is applied to a carbon grid, which is then plunge-frozen in liquid ethane. If the CsA treatment does indeed affect membrane stability, it could result in fewer intact mitochondria being imaged. However, further confirmation is required to support this hypothesis.

Additional future aims for this chapter include conducting studies on mitochondria isolated from I/R-injured hearts to assess the effects of calcium overload and modulators on cristae stability, and changes in mitochondrial function during calcium overload should be run in parallel with cryo-EM sample vitrification to get a view of cristae structure and intactness. The complete analysis of calcium phosphate granule size, distribution, and formation must then be compared with the cristae data to link mitochondrial function with calcium sequestration. These results will establish if treatments preserving cristae can confer protection against calcium overload in I/R-injured hearts.

In **Chapter 6**, the focus is on screening for compounds that can protect mitochondria from the detrimental effects of calcium overload and reactive oxygen species (ROS). The study is a crucial step in identifying potential drug candidates or therapeutic targets for the treatment of mitochondrial dysfunction and related diseases. The screening process involved

testing approximately 5,000 compounds, and 11 were identified that passed the initial screening for protection against calcium overload. However, the study faced significant challenges in obtaining the compounds from pharmaceutical companies or medicinal chemists, which prevented the further progression of the study.

It is important to note that the rationale behind screening for compounds that protect against both calcium overload and reactive oxygen species is highly relevant in the context of I/R injury. I/R injury is a phenomenon that occurs when blood flow to an organ is interrupted (ischemia) and then restored (reperfusion), leading to a paradoxical injury effect that is centered on the mitochondria. The formation of the PTP phenomenon is a major contributor to I/R injury, which is sensitized mainly by these two components - calcium overload and oxidative stress. Therefore, the screening of compounds that can protect against both calcium overload and oxidative stress is a critical step in developing potential therapeutic strategies to mitigate the effects of I/R injury.

It is worth noting that although the libraries of compounds tested in this study exist, none have been tested or repurposed as a mitoprotectant before. Despite the obstacles faced, the study provided valuable insights into the potential mechanisms of action for the identified compounds. The compounds were subjected to a SwissADME analysis to predict their molecular and metabolic effects. The analysis proposed several potential mechanisms of action, which should be validated through future experiments. These experiments should be conducted in a pro-oxidative environment, with and without calcium, and at various experimental levels to reinforce one another and elucidate the molecular and metabolic effects of each prospective drug.

Overall, the study highlights the critical role that calcium overload and ROS play in mitochondrial dysfunction and the development of related diseases. The identification of

potential drug candidates and therapeutic targets provides new ideas for the development of effective treatments for mitochondrial dysfunction. The insights provided by the study may also aid in the development of preventative measures aimed at reducing the risk of mitochondrial dysfunction and related diseases.

Taken as a whole, this thesis lays the foundation for a comprehensive investigation of the role of mitochondrial calcium overload in cardiac I/R injury and the potential protective strategies against it. The experimental data presented in this thesis provides important insights into the mechanisms underlying mitochondrial dysfunction and structural changes induced by calcium overload. The proposed future studies will further advance our understanding of the complex interplay between mitochondrial function, calcium overload, and reactive oxygen species in cardiac I/R injury. The potential protective compounds identified in this study provide a promising starting point for the development of novel therapeutic strategies for the treatment of cardiac ischemia-reperfusion injury. Ultimately, the findings presented in this thesis have important implications for the development of targeted therapeutic interventions aimed at preserving mitochondrial function and protecting against cardiac I/R injury.

BIBLIOGRAPHY

[1] S. J. Beck et al. "Deregulation of mitochondrial F1FO-ATP synthase via OSCP in Alzheimer's disease". In: *Nat Commun* 7 (2016), page 11483. ISSN: 2041-1723. DOI: 10.1038/ncomms11483. URL: https://www.ncbi.nlm.nih.gov/pubmed/27151236 (cited on page 5).

[2] H. Du et al. "Cyclophilin D deficiency attenuates mitochondrial and neuronal perturbation and ameliorates learning and memory in Alzheimer's disease". In: *Nat Med* 14.10 (2008), pages 1097–105. ISSN: 1546-170X. DOI: 10.1038/nm.1868. URL: https://www.ncbi.nlm.nih.gov/pubmed/18806802 (cited on pages 5, 51).

[3] J. W. Elrod et al. "Cyclophilin D controls mitochondrial pore-dependent Ca(2+) exchange, metabolic flexibility, and propensity for heart failure in mice". In: *J Clin Invest* 120.10 (2010), pages 3680–7. ISSN: 1558-8238. DOI: 10.1172/JCI43171. URL: https://www.ncbi.nlm.nih.gov/pubmed/20890047 (cited on page 5).

[4] J. L. Martin et al. "Mitochondrial mechanisms and therapeutics in ischaemia reperfusion injury". In: *Pediatr Nephrol* 34.7 (2019), pages 1167–1174. ISSN: 1432-198X. DOI: 10.1007/s00467-018-3984-5. URL: https://www.ncbi.nlm.nih.gov/pubmed/29860579 (cited on pages 5, 6).

[5] L. J. Martin et al. "GNX-4728, a novel small molecule drug inhibitor of mitochondrial permeability transition, is therapeutic in a mouse model of amyotrophic lateral sclerosis". In: *Front Cell Neurosci* 8 (2014), page 433. ISSN: 1662-5102. DOI: 10.3389/fncel.2014.00433. URL: https://www.ncbi.nlm.nih.gov/pubmed/25565966 (cited on page 5).

[6] L. J. Martin et al. "Mitochondrial permeability transition pore regulates Parkinson's disease development in mutant ?-synuclein transgenic mice". In: *Neurobiol Aging* 35.5 (2014), pages 1132–52. ISSN: 1558-1497. DOI: 10.1016/j.neurobiolaging.2013.11.008. URL: https://www.ncbi.nlm.nih.gov/pubmed/24325796 (cited on page 5).

[7] A. Sun et al. "Mitochondrial aldehyde dehydrogenase 2 plays protective roles in heart failure after myocardial infarction via suppression of the cytosolic JNK/p53 pathway in mice". In: *J Am Heart Assoc* 3.5 (2014), e000779. ISSN: 2047-9980. DOI: 10.1161/JAHA.113.000779. URL: https://www.ncbi.nlm.nih.gov/pubmed/25237043 (cited on page 5).

[8] T. Kalogeris et al. "Cell biology of ischemia/reperfusion injury". In: *Int Rev Cell Mol Biol* 298 (2012), pages 229–317. ISSN: 1937-6448. DOI: 10.1016/B978-0-12-394309-5.00006-7. URL: https://www.ncbi.nlm.nih.gov/pubmed/22878108 (cited on page 6).

[9] T. Kalogeris et al. “Ischemia/Reperfusion”. In: *Compr Physiol* 7.1 (2016), pages 113–170. ISSN: 2040-4603. DOI: 10.1002/cphy.c160006. URL: https://www.ncbi.nlm.nih.gov/pubmed/28135002 (cited on page 6).

[10] C. Steenbergen, T. A. Fralix, and E. Murphy. “Role of increased cytosolic free calcium concentration in myocardial ischemic injury”. In: *Basic Res Cardiol* 88.5 (1993), pages 456–70. ISSN: 0300-8428. DOI: 10.1007/BF00795412. URL: https://www.ncbi.nlm.nih.gov/pubmed/8117251 (cited on page 6).

[11] C. Steenbergen et al. “Cardioprotection and altered mitochondrial adenine nucleotide transport”. In: *Basic Res Cardiol* 104.2 (2009), pages 149–56. ISSN: 1435-1803. DOI: 10.1007/s00395-009-0002-x. URL: https://www.ncbi.nlm.nih.gov/pubmed/19242642 (cited on page 6).

[12] D. J. Hausenloy, M. R. Duchen, and D. M. Yellon. “Inhibiting mitochondrial permeability transition pore opening at reperfusion protects against ischaemia-reperfusion injury”. In: *Cardiovasc Res* 60.3 (2003), pages 617–25. ISSN: 0008-6363. DOI: 10.1016/j.cardiores.2003.09.025. URL: https://www.ncbi.nlm.nih.gov/pubmed/14659807 (cited on page 6).

[13] G. Kroemer, B. Dallaporta, and M. Resche-Rigon. “The mitochondrial death/life regulator in apoptosis and necrosis”. In: *Annu Rev Physiol* 60 (1998), pages 619–42. ISSN: 0066-4278. DOI: 10.1146/annurev.physiol.60.1.619. URL: https://www.ncbi.nlm.nih.gov/pubmed/9558479 (cited on page 6).

[14] N. Manhas et al. “Computationally modeling mammalian succinate dehydrogenase kinetics identifies the origins and primary determinants of ROS production”. In: *J Biol Chem* 295.45 (2020), pages 15262–15279. ISSN: 1083-351X. DOI: 10.1074/jbc.RA120.014483. URL: https://www.ncbi.nlm.nih.gov/pubmed/32859750 (cited on page 6).

[15] C. P. Baines. “The mitochondrial permeability transition pore and ischemia-reperfusion injury”. In: *Basic Res Cardiol* 104.2 (2009), pages 181–8. ISSN: 1435-1803. DOI: 10.1007/s00395-009-0004-8. URL: https://www.ncbi.nlm.nih.gov/pubmed/19242640 (cited on pages 6, 7).

[16] E. J. Griffiths and A. P. Halestrap. “Mitochondrial non-specific pores remain closed during cardiac ischaemia, but open upon reperfusion”. In: *Biochem J* 307 (Pt 1).Pt 1 (1995), pages 93–8. ISSN: 0264-6021. DOI: 10.1042/bj3070093. URL: https://www.ncbi.nlm.nih.gov/pubmed/7717999 (cited on pages 6, 7).

[17] Q. V. Duong et al. “Identifying Site-Specific Superoxide and Hydrogen Peroxide Production Rates From the Mitochondrial Electron Transport System Using a Compu-

tational Strategy". In: *Function (Oxf)* 2.6 (2021), zqab050. ISSN: 2633-8823. DOI: 10.1093/function/zqab050. URL: https://www.ncbi.nlm.nih.gov/pubmed/35330793 (cited on pages 6, 44).

[18] A. Görlach et al. "Calcium and ROS: A mutual interplay". In: *Redox Biol* 6 (2015), pages 260–271. ISSN: 2213-2317. DOI: 10.1016/j.redox.2015.08.010. URL: https://www.ncbi.nlm.nih.gov/pubmed/26296072 (cited on page 7).

[19] K. W. CLELAND. "Permeability of isolated rat heart sarcosomes". In: *Nature* 170.4325 (1952), pages 497–9. ISSN: 0028-0836. DOI: 10.1038/170497a0. URL: https://www.ncbi.nlm.nih.gov/pubmed/12993213 (cited on page 7).

[20] F. E. HUNTER and L. FORD. "Inactivation of oxidative and phosphorylative systems in mitochondria by preincubation with phosphate and other ions". In: *J Biol Chem* 216.1 (1955), pages 357–69. ISSN: 0021-9258. URL: https://www.ncbi.nlm.nih.gov/pubmed/13252035 (cited on page 7).

[21] J. RAAFLAUB. "[Swelling of isolated mitochondria of the liver and their susceptibility to physicochemical influences]". In: *Helv Physiol Pharmacol Acta* 11.2 (1953), pages 142–56. ISSN: 0367-6242. URL: https://www.ncbi.nlm.nih.gov/pubmed/13095885 (cited on page 7).

[22] M. Carraro et al. "Molecular nature and regulation of the mitochondrial permeability transition pore(s), drug target(s) in cardioprotection". In: *J Mol Cell Cardiol* 144 (2020), pages 76–86. ISSN: 1095-8584. DOI: 10.1016/j.yjmcc.2020.05.014. URL: https://www.ncbi.nlm.nih.gov/pubmed/32454060 (cited on pages 8, 11, 23, 30).

[23] A. P. Halestrap and A. M. Davidson. "Inhibition of Ca2(+)-induced large-amplitude swelling of liver and heart mitochondria by cyclosporin is probably caused by the inhibitor binding to mitochondrial-matrix peptidyl-prolyl cis-trans isomerase and preventing it interacting with the adenine nucleotide translocase". In: *Biochem J* 268.1 (1990), pages 153–60. ISSN: 0264-6021. DOI: 10.1042/bj2680153. URL: https://www.ncbi.nlm.nih.gov/pubmed/2160810 (cited on pages 8, 10, 15, 51).

[24] J. W. Elrod and J. D. Molkentin. "Physiologic functions of cyclophilin D and the mitochondrial permeability transition pore". In: *Circ J* 77.5 (2013), pages 1111–22. ISSN: 1347-4820. DOI: 10.1253/circj.cj-13-0321. URL: https://www.ncbi.nlm.nih.gov/pubmed/23538482 (cited on pages 8, 15, 17, 22).

[25] I. Szabó and M. Zoratti. "The mitochondrial megachannel is the permeability transition pore". In: *J Bioenerg Biomembr* 24.1 (1992), pages 111–7. ISSN: 0145-479X. DOI: 10.

1007/BF00769537. URL: https://www.ncbi.nlm.nih.gov/pubmed/1380498 (cited on page 8).

[26] U. De Marchi et al. "Electrophysiological characterization of the Cyclophilin D-deleted mitochondrial permeability transition pore". In: *Mol Membr Biol* 23.6 (2006), pages 521–30. ISSN: 0968-7688. DOI: 10.1080/09687860600907644. URL: https://www.ncbi.nlm.nih.gov/pubmed/17127624 (cited on pages 9, 62).

[27] I. Szabó and M. Zoratti. "The giant channel of the inner mitochondrial membrane is inhibited by cyclosporin A". In: *J Biol Chem* 266.6 (1991), pages 3376–9. ISSN: 0021-9258. URL: https://www.ncbi.nlm.nih.gov/pubmed/1847371 (cited on pages 9, 52).

[28] V. Mavridou et al. "Substrate binding in the mitochondrial ADP/ATP carrier is a stepwise process guiding the structural changes in the transport cycle". In: *Nat Commun* 13.1 (2022), page 3585. ISSN: 2041-1723. DOI: 10.1038/s41467-022-31366-5. URL: https://www.ncbi.nlm.nih.gov/pubmed/35739110 (cited on pages 10, 11).

[29] A. Rück et al. "Reconstituted adenine nucleotide translocase forms a channel for small molecules comparable to the mitochondrial permeability transition pore". In: *FEBS Letters* 426.1 (2020), pages 97–101. ISSN: 0968-0004. DOI: 10.1016/j.tibs.2019.11.001. URL: https://www.ncbi.nlm.nih.gov/pubmed/31787485 (cited on pages 11, 27, 52).

[30] D. R. Hunter and R. A. Haworth. "The Ca2+-induced membrane transition in mitochondria. I. The protective mechanisms". In: *Arch Biochem Biophys* 195.2 (1979), pages 453–9. ISSN: 0003-9861 (Print) 0003-9861 (Linking). URL: https://www.ncbi.nlm.nih.gov/pubmed/383019 (cited on pages 11, 12).

[31] N. Brustovetsky and M. Klingenberg. "Mitochondrial ADP/ATP carrier can be reversibly converted into a large channel by Ca2+". In: *Biochemistry* 35.26 (1996), pages 8483–8. ISSN: 0006-2960. DOI: 10.1021/bi960833v. URL: https://www.ncbi.nlm.nih.gov/pubmed/8679608 (cited on pages 12, 27).

[32] X. R. Chapa-Dubocq et al. "Crosstalk between adenine nucleotide transporter and mitochondrial swelling: experimental and computational approaches". In: *Cell Biol Toxicol* (2022). ISSN: 1573-6822. DOI: 10.1007/s10565-022-09724-2. URL: https://www.ncbi.nlm.nih.gov/pubmed/35606662 (cited on page 12).

[33] C. P. Baines. "The molecular composition of the mitochondrial permeability transition pore". In: *J Mol Cell Cardiol* 46.6 (2009), pages 850–7. ISSN: 1095-8584. DOI: 10.1016/j.yjmcc.2009.02.007. URL: https://www.ncbi.nlm.nih.gov/pubmed/19233198 (cited on page 12).

[34] J. E. Kokoszka et al. "The ADP/ATP translocator is not essential for the mitochondrial permeability transition pore". In: *Nature* 427.6973 (2004), pages 461–5. ISSN: 1476-4687. DOI: 10.1038/nature02229. URL: https://www.ncbi.nlm.nih.gov/pubmed/14749836 (cited on page 12).

[35] J. Karch et al. "Inhibition of mitochondrial permeability transition by deletion of the ANT family and CypD". In: *Sci Adv* 5.8 (2019), eaaw4597. ISSN: 2375-2548. DOI: 10.1126/sciadv.aaw4597. URL: https://www.ncbi.nlm.nih.gov/pubmed/31489369 (cited on page 13).

[36] I. Szabó and M. Zoratti. "The mitochondrial permeability transition pore may comprise VDAC molecules. I. Binary structure and voltage dependence of the pore". In: *FEBS Lett* 330.2 (1993), pages 201–5. ISSN: 0014-5793. DOI: 10.1016/0014-5793(93)80273-w. URL: https://www.ncbi.nlm.nih.gov/pubmed/7689983 (cited on page 13).

[37] M. Colombini. "The VDAC channel: Molecular basis for selectivity". In: *Biochim Biophys Acta* 1863.10 (2016), pages 2498–502. ISSN: 0006-3002. DOI: 10.1016/j.bbamcr.2016.01.019. URL: https://www.ncbi.nlm.nih.gov/pubmed/26826035 (cited on page 14).

[38] E. M. Krammer, F. Homblé, and M. Prévost. "Molecular origin of VDAC selectivity towards inorganic ions: a combined molecular and Brownian dynamics study". In: *Biochim Biophys Acta* 1828.4 (2013), pages 1284–92. ISSN: 0006-3002. DOI: 10.1016/j.bbamem.2012.12.018. URL: https://www.ncbi.nlm.nih.gov/pubmed/23313453 (cited on page 14).

[39] M. W. McEnery et al. "Isolation of the mitochondrial benzodiazepine receptor: association with the voltage-dependent anion channel and the adenine nucleotide carrier". In: *Proc Natl Acad Sci U S A* 89.8 (1992), pages 3170–4. ISSN: 0027-8424. DOI: 10.1073/pnas.89.8.3170. URL: https://www.ncbi.nlm.nih.gov/pubmed/1373486 (cited on page 14).

[40] K. W. Kinnally et al. "Mitochondrial benzodiazepine receptor linked to inner membrane ion channels by nanomolar actions of ligands". In: *Proc Natl Acad Sci U S A* 90.4 (1993), pages 1374–8. ISSN: 0027-8424. DOI: 10.1073/pnas.90.4.1374. URL: https://www.ncbi.nlm.nih.gov/pubmed/7679505 (cited on page 14).

[41] M. Crompton et al. "Mitochondrial intermembrane junctional complexes and their involvement in cell death". In: *Biochimie* 84.2-3 (2002), pages 143–52. ISSN: 0300-9084. DOI: 10.1016/s0300-9084(02)01368-8. URL: https://www.ncbi.nlm.nih.gov/pubmed/12022945 (cited on pages 14, 16).

[42] M. Crompton, S. Virji, and J. M. Ward. "Cyclophilin-D binds strongly to complexes of the voltage-dependent anion channel and the adenine nucleotide translocase to form the permeability transition pore". In: *Eur J Biochem* 258.2 (1998), pages 729–35. ISSN: 0014-2956. DOI: 10.1046/j.1432-1327.1998.2580729.x. URL: https://www.ncbi.nlm.nih.gov/pubmed/9874241 (cited on pages 14, 16).

[43] K. Woodfield et al. "Direct demonstration of a specific interaction between cyclophilin-D and the adenine nucleotide translocase confirms their role in the mitochondrial permeability transition". In: *Biochem J* 336 (Pt 2).Pt 2 (1998), pages 287–90. ISSN: 0264-6021. DOI: 10.1042/bj3360287. URL: https://www.ncbi.nlm.nih.gov/pubmed/9820802 (cited on pages 14, 16).

[44] G. A. Porter and G. Beutner. "Cyclophilin D, Somehow a Master Regulator of Mitochondrial Function". In: *Biomolecules* 8.4 (2018). ISSN: 2218-273X. DOI: 10.3390/biom8040176. URL: https://www.ncbi.nlm.nih.gov/pubmed/30558250 (cited on pages 15, 21, 44).

[45] M. Crompton, H. Ellinger, and A. Costi. "Inhibition by cyclosporin A of a Ca2+-dependent pore in heart mitochondria activated by inorganic phosphate and oxidative stress". In: *Biochem J* 255.1 (1988), pages 357–60. ISSN: 0264-6021. URL: https://www.ncbi.nlm.nih.gov/pubmed/3196322 (cited on page 15).

[46] T. Nakagawa et al. "Cyclophilin D-dependent mitochondrial permeability transition regulates some necrotic but not apoptotic cell death". In: *Nature* 434.7033 (2005), pages 652–8. ISSN: 1476-4687. DOI: 10.1038/nature03317. URL: https://www.ncbi.nlm.nih.gov/pubmed/15800626 (cited on page 15).

[47] A. C. Schinzel et al. "Cyclophilin D is a component of mitochondrial permeability transition and mediates neuronal cell death after focal cerebral ischemia". In: *Proc Natl Acad Sci U S A* 102.34 (2005), pages 12005–10. ISSN: 0027-8424. DOI: 10.1073/pnas.0505294102. URL: https://www.ncbi.nlm.nih.gov/pubmed/16103352 (cited on page 15).

[48] A. Tanveer et al. "Involvement of cyclophilin D in the activation of a mitochondrial pore by Ca2+ and oxidant stress". In: *Eur J Biochem* 238.1 (1996), pages 166–72. ISSN: 0014-2956. DOI: 10.1111/j.1432-1033.1996.0166q.x. URL: https://www.ncbi.nlm.nih.gov/pubmed/8665934 (cited on page 15).

[49] M. Burnouf-Radosevich and T. Burnouf. "Chromatographic preparation of a therapeutic highly purified von Willebrand factor concentrate from human cryoprecipitate". In: *Vox Sang* 62.1 (1992), pages 1–11. ISSN: 0042-9007. DOI: 10.1111/j.1423-0410.1992.tb01159.x. URL: https://www.ncbi.nlm.nih.gov/pubmed/1580062 (cited on page 15).

[50] I. Marzo et al. “Bax and adenine nucleotide translocator cooperate in the mitochondrial control of apoptosis”. In: *Science* 281.5385 (1998), pages 2027–31. ISSN: 0036-8075. DOI: 10.1126/science.281.5385.2027. URL: https://www.ncbi.nlm.nih.gov/pubmed/9748162 (cited on page 15).

[51] J. G. Pastorino, N. Shulga, and J. B. Hoek. “Mitochondrial binding of hexokinase II inhibits Bax-induced cytochrome c release and apoptosis”. In: *J Biol Chem* 277.9 (2002), pages 7610–8. ISSN: 0021-9258. DOI: 10.1074/jbc.M109950200. URL: https://www.ncbi.nlm.nih.gov/pubmed/11751859 (cited on page 15).

[52] D. Zhang and J. S. Armstrong. “Bax and the mitochondrial permeability transition cooperate in the release of cytochrome c during endoplasmic reticulum-stress-induced apoptosis”. In: *Cell Death Differ* 14.4 (2007), pages 703–15. ISSN: 1350-9047. DOI: 10.1038/sj.cdd.4402072. URL: https://www.ncbi.nlm.nih.gov/pubmed/17170750 (cited on page 15).

[53] D. Zhang et al. “The mitochondrial permeability transition regulates cytochrome c release for apoptosis during endoplasmic reticulum stress by remodeling the cristae junction”. In: *J Biol Chem* 283.6 (2008), pages 3476–3486. ISSN: 0021-9258. DOI: 10.1074/jbc.M707528200. URL: https://www.ncbi.nlm.nih.gov/pubmed/18056990 (cited on page 15).

[54] Y. Li et al. “Cyclophilin-D promotes the mitochondrial permeability transition but has opposite effects on apoptosis and necrosis”. In: *Biochem J* 383.Pt 1 (2004), pages 101–9. ISSN: 1470-8728. DOI: 10.1042/BJ20040669. URL: https://www.ncbi.nlm.nih.gov/pubmed/15233627 (cited on page 15).

[55] C. P. Baines et al. “Loss of cyclophilin D reveals a critical role for mitochondrial permeability transition in cell death”. In: *Nature* 434.7033 (2005), pages 658–62. ISSN: 1476-4687. DOI: 10.1038/nature03434. URL: https://www.ncbi.nlm.nih.gov/pubmed/15800627 (cited on page 15).

[56] J. Banerjee and S. Ghosh. “Bax increases the pore size of rat brain mitochondrial voltage-dependent anion channel in the presence of tBid”. In: *Biochem Biophys Res Commun* 323.1 (2004), pages 310–4. ISSN: 0006-291X. DOI: 10.1016/j.bbrc.2004.08.094. URL: https://www.ncbi.nlm.nih.gov/pubmed/15351738 (cited on page 15).

[57] C. P. Baines et al. “Voltage-dependent anion channels are dispensable for mitochondrial-dependent cell death”. In: *Nat Cell Biol* 9.5 (2007), pages 550–5. ISSN: 1465-7392. DOI: 10.1038/ncb1575. URL: https://www.ncbi.nlm.nih.gov/pubmed/17417626 (cited on pages 16, 17).

[58] G. Beutner et al. “Complexes between porin, hexokinase, mitochondrial creatine kinase and adenylate translocator display properties of the permeability transition pore. Implication for regulation of permeability transition by the kinases”. In: *Biochim Biophys Acta* 1368.1 (1998), pages 7–18. ISSN: 0006-3002. DOI: 10.1016/s0005-2736(97)00175-2. URL: https://www.ncbi.nlm.nih.gov/pubmed/9459579 (cited on page 17).

[59] M. Bonora, C. Giorgi, and P. Pinton. “Molecular mechanisms and consequences of mitochondrial permeability transition”. In: *Nat Rev Mol Cell Biol* 23.4 (2022), pages 266–285. ISSN: 1471-0080. DOI: 10.1038/s41580-021-00433-y. URL: https://www.ncbi.nlm.nih.gov/pubmed/34880425 (cited on pages 17, 19, 44).

[60] J. Hunter F. E. and L. Ford. “Inactivation of oxidative and phosphorylative systems in mitochondria by preincubation with phosphate and other ions”. In: *J Biol Chem* 216.1 (1955), pages 357–69. ISSN: 0021-9258 (Print) 0021-9258 (Linking). URL: https://www.ncbi.nlm.nih.gov/pubmed/13252035 (cited on pages 17, 44).

[61] A. Carrer et al. “Modulation and Pharmacology of the Mitochondrial Permeability Transition: A Journey from F-ATP Synthase to ANT”. In: *Molecules* 26.21 (2021). ISSN: 1420-3049. DOI: 10.3390/molecules26216463. URL: https://www.ncbi.nlm.nih.gov/pubmed/34770872 (cited on pages 17, 22, 27).

[62] K. Herick, R. Krämer, and H. Lühring. “Patch clamp investigation into the phosphate carrier from Saccharomyces cerevisiae mitochondria”. In: *Biochim Biophys Acta* 1321.3 (1997), pages 207–20. ISSN: 0006-3002. DOI: 10.1016/s0005-2728(97)00050-9. URL: https://www.ncbi.nlm.nih.gov/pubmed/9393638 (cited on pages 17, 18).

[63] G. Fiermonte, V. Dolce, and F. Palmieri. “Expression in Escherichia coli, functional characterization, and tissue distribution of isoforms A and B of the phosphate carrier from bovine mitochondria”. In: *J Biol Chem* 273.35 (1998), pages 22782–7. ISSN: 0021-9258. DOI: 10.1074/jbc.273.35.22782. URL: https://www.ncbi.nlm.nih.gov/pubmed/9712911 (cited on page 17).

[64] A. W. Leung, P. Varanyuwatana, and A. P. Halestrap. “The mitochondrial phosphate carrier interacts with cyclophilin D and may play a key role in the permeability transition”. In: *J Biol Chem* 283.39 (2008), pages 26312–23. ISSN: 0021-9258. DOI: 10.1074/jbc.M805235200. URL: https://www.ncbi.nlm.nih.gov/pubmed/18667415 (cited on pages 17, 18).

[65] S. Chalmers and D. G. Nicholls. “The relationship between free and total calcium concentrations in the matrix of liver and brain mitochondria”. In: *J Biol Chem* 278.21 (2003), pages 19062–70. ISSN: 0021-9258 (Print) 0021-9258 (Linking). DOI: 10.1074/

jbc.M212661200. URL: https://www.ncbi.nlm.nih.gov/pubmed/12660243 (cited on pages 17, 39, 41, 42).

[66] V. Zara et al. "Biogenesis of the mitochondrial phosphate carrier". In: *Eur J Biochem* 198.2 (1991), pages 405–10. ISSN: 0014-2956. DOI: 10.1111/j.1432-1033.1991.tb16029.x. URL: https://www.ncbi.nlm.nih.gov/pubmed/2040301 (cited on page 17).

[67] J. A. Mayr et al. "Mitochondrial phosphate-carrier deficiency: a novel disorder of oxidative phosphorylation". In: *Am J Hum Genet* 80.3 (2007), pages 478–84. ISSN: 0002-9297. DOI: 10.1086/511788. URL: https://www.ncbi.nlm.nih.gov/pubmed/17273968 (cited on page 17).

[68] S. Alcalá et al. "A high-throughput screening for mammalian cell death effectors identifies the mitochondrial phosphate carrier as a regulator of cytochrome c release". In: *Oncogene* 27.1 (2008), pages 44–54. ISSN: 1476-5594. DOI: 10.1038/sj.onc.1210600. URL: https://www.ncbi.nlm.nih.gov/pubmed/17621274 (cited on page 18).

[69] M. Crompton and A. Costi. "Kinetic evidence for a heart mitochondrial pore activated by Ca2+, inorganic phosphate and oxidative stress. A potential mechanism for mitochondrial dysfunction during cellular Ca2+ overload". In: *Eur J Biochem* 178.2 (1988), pages 489–501. ISSN: 0014-2956. DOI: 10.1111/j.1432-1033.1988.tb14475.x. URL: https://www.ncbi.nlm.nih.gov/pubmed/2850179 (cited on page 18).

[70] E. Basso et al. "Phosphate is essential for inhibition of the mitochondrial permeability transition pore by cyclosporin A and by cyclophilin D ablation". In: *J Biol Chem* 283.39 (2008), pages 26307–11. ISSN: 0021-9258. DOI: 10.1074/jbc.C800132200. URL: https://www.ncbi.nlm.nih.gov/pubmed/18684715 (cited on page 18).

[71] M. Gutiérrez-Aguilar et al. "Genetic manipulation of the cardiac mitochondrial phosphate carrier does not affect permeability transition". In: *J Mol Cell Cardiol* 72 (2014), pages 316–25. ISSN: 1095-8584. DOI: 10.1016/j.yjmcc.2014.04.008. URL: https://www.ncbi.nlm.nih.gov/pubmed/24768964 (cited on page 18).

[72] V. Giorgio et al. "Cyclophilin D modulates mitochondrial F0F1-ATP synthase by interacting with the lateral stalk of the complex". In: *J Biol Chem* 284.49 (2009), pages 33982–8. ISSN: 1083-351X. DOI: 10.1074/jbc.M109.020115. URL: https://www.ncbi.nlm.nih.gov/pubmed/19801635 (cited on pages 18, 20, 21, 23, 44).

[73] A. I. Jonckheere, J. A. Smeitink, and R. J. Rodenburg. "Mitochondrial ATP synthase: architecture, function and pathology". In: *J Inherit Metab Dis* 35.2 (2012), pages 211–25. ISSN: 1573-2665. DOI: 10.1007/s10545-011-9382-9. URL: https://www.ncbi.nlm.nih.gov/pubmed/21874297 (cited on pages 19, 20).

[74] M. Campanella et al. "Regulation of mitochondrial structure and function by the F1Fo-ATPase inhibitor protein, IF1". In: *Cell Metab* 8.1 (2008), pages 13–25. ISSN: 1932-7420. DOI: 10.1016/j.cmet.2008.06.001. URL: https://www.ncbi.nlm.nih.gov/pubmed/18590689 (cited on pages 20, 21).

[75] M. Campanella et al. "IF(1): setting the pace of the F(1)F(o)-ATP synthase". In: *Trends Biochem Sci* 34.7 (2009), pages 343–50. ISSN: 0968-0004. DOI: 10.1016/j.tibs.2009.03.006. URL: https://www.ncbi.nlm.nih.gov/pubmed/19559621 (cited on pages 20, 44).

[76] C. Anselmi, K. M. Davies, and J. D. Faraldo-Gómez. "Mitochondrial ATP synthase dimers spontaneously associate due to a long-range membrane-induced force". In: *J Gen Physiol* 150.5 (2018), pages 763–770. ISSN: 1540-7748. DOI: 10.1085/jgp.201812033. URL: https://www.ncbi.nlm.nih.gov/pubmed/29643173 (cited on pages 20, 44).

[77] K. Jung and M. Pergande. "Influence of cyclosporin A on the respiration of isolated rat kidney mitochondria". In: *FEBS Lett* 183.1 (1985), pages 167–9. ISSN: 0014-5793. DOI: 10.1016/0014-5793(85)80977-7. URL: https://www.ncbi.nlm.nih.gov/pubmed/2858411 (cited on pages 22, 44).

[78] S. Malyala et al. "Ca2+-Pi precipitation inhibits mitochondrial energy metabolism". In: *PLoS computational biology* 15.1 (2019). DOI: 10.1371/journal.pcbi.1006719 (cited on pages 22, 33, 34, 42, 44, 50, 59, 60, 70, 75, 81, 85, 94, 95, 97, 130).

[79] J. O. Strubbe-Rivera et al. "The mitochondrial permeability transition phenomenon elucidated by cryo-EM reveals the genuine impact of calcium overload on mitochondrial structure and function". In: *Sci Rep* 11.1 (2021), page 1037. ISSN: 2045-2322. DOI: 10.1038/s41598-020-80398-8. URL: https://www.ncbi.nlm.nih.gov/pubmed/33441863 (cited on pages 22, 26, 116).

[80] A. Joshi et al. "The mitochondrial HSP90 paralog TRAP1 forms an OXPHOS-regulated tetramer and is involved in mitochondrial metabolic homeostasis". In: *BMC Biol* 18.1 (2020), page 10. ISSN: 1741-7007. DOI: 10.1186/s12915-020-0740-7. URL: https://www.ncbi.nlm.nih.gov/pubmed/31987035 (cited on page 22).

[81] B. H. Kang et al. "Regulation of tumor cell mitochondrial homeostasis by an organelle-specific Hsp90 chaperone network". In: *Cell* 131.2 (2007), pages 257–70. ISSN: 0092-8674. DOI: 10.1016/j.cell.2007.08.028. URL: https://www.ncbi.nlm.nih.gov/pubmed/17956728 (cited on page 22).

[82] I. Masgras et al. "The Chaperone TRAP1 As a Modulator of the Mitochondrial Adaptations in Cancer Cells". In: *Front Oncol* 7 (2017), page 58. ISSN: 2234-943X. DOI:

10.3389/fonc.2017.00058. URL: https://www.ncbi.nlm.nih.gov/pubmed/28405578 (cited on page 22).

[83] V. Giorgio et al. "Dimers of mitochondrial ATP synthase form the permeability transition pore". In: *Proc Natl Acad Sci U S A* 110.15 (2013), pages 5887–92. ISSN: 1091-6490. DOI: 10.1073/pnas.1217823110. URL: https://www.ncbi.nlm.nih.gov/pubmed/23530243 (cited on page 23).

[84] S. Hurst, J. Hoek, and S. S. Sheu. "Mitochondrial Ca". In: *J Bioenerg Biomembr* 49.1 (2017), pages 27–47. ISSN: 1573-6881. DOI: 10.1007/s10863-016-9672-x. URL: https://www.ncbi.nlm.nih.gov/pubmed/27497945 (cited on page 23).

[85] C. Gerle. "On the structural possibility of pore-forming mitochondrial FoF1 ATP synthase". In: *Biochim Biophys Acta* 1857.8 (2016), pages 1191–1196. ISSN: 0006-3002. DOI: 10.1016/j.bbabio.2016.03.008. URL: https://www.ncbi.nlm.nih.gov/pubmed/26968896 (cited on page 23).

[86] G. Beutner, R. E. Alanzalon, and G. A. Porter. "Cyclophilin D regulates the dynamic assembly of mitochondrial ATP synthase into synthasomes". In: *Sci Rep* 7.1 (2014), page 14488. ISSN: 1083-351X. DOI: 10.1074/jbc.M114.549634. URL: https://www.ncbi.nlm.nih.gov/pubmed/24692541 (cited on pages 23, 24).

[87] C. Chen et al. "Mitochondrial ATP synthasome: three-dimensional structure by electron microscopy of the ATP synthase in complex formation with carriers for Pi and ADP/ATP". In: *J Biol Chem* 279.30 (2004), pages 31761–8. ISSN: 0021-9258. DOI: 10.1074/jbc.M401353200. URL: https://www.ncbi.nlm.nih.gov/pubmed/15166242 (cited on page 23).

[88] M. Strauss et al. "Dimer ribbons of ATP synthase shape the inner mitochondrial membrane". In: *EMBO J* 27.7 (2008), pages 1154–60. ISSN: 1460-2075. DOI: 10.1038/emboj.2008.35. URL: https://www.ncbi.nlm.nih.gov/pubmed/18323778 (cited on page 23).

[89] S. Cogliati et al. "Mitochondrial cristae shape determines respiratory chain supercomplexes assembly and respiratory efficiency". In: *Cell* 155.1 (2013), pages 160–71. ISSN: 1097-4172. DOI: 10.1016/j.cell.2013.08.032. URL: https://www.ncbi.nlm.nih.gov/pubmed/24055366 (cited on page 23).

[90] A. Hahn et al. "Structure of a Complete ATP Synthase Dimer Reveals the Molecular Basis of Inner Mitochondrial Membrane Morphology". In: *Mol Cell* 63.3 (2016), pages 445–56. ISSN: 1097-4164. DOI: 10.1016/j.molcel.2016.05.037. URL: https://www.ncbi.nlm.nih.gov/pubmed/27373333 (cited on page 23).

[91] I. Wittig and H. Schägger. "Supramolecular organization of ATP synthase and respiratory chain in mitochondrial membranes". In: *Biochim Biophys Acta* 1787.6 (2009), pages 672–80. ISSN: 0006-3002. DOI: 10.1016/j.bbabio.2008.12.016. URL: https://www.ncbi.nlm.nih.gov/pubmed/19168025 (cited on page 23).

[92] K. Azuma, K. Ikeda, and S. Inoue. "Functional Mechanisms of Mitochondrial Respiratory Chain Supercomplex Assembly Factors and Their Involvement in Muscle Quality". In: *Int J Mol Sci* 21.9 (2020). ISSN: 1422-0067. DOI: 10.3390/ijms21093182. URL: https://www.ncbi.nlm.nih.gov/pubmed/32365950 (cited on page 24).

[93] J. Gu et al. "The architecture of the mammalian respirasome". In: *Nature* 537.7622 (2016), pages 639–43. ISSN: 1476-4687. DOI: 10.1038/nature19359. URL: https://www.ncbi.nlm.nih.gov/pubmed/27654917 (cited on page 24).

[94] J. A. Letts, K. Fiedorczuk, and L. A. Sazanov. "The architecture of respiratory supercomplexes". In: *Nature* 537.7622 (2016), pages 644–648. ISSN: 1476-4687. DOI: 10.1038/nature19774. URL: https://www.ncbi.nlm.nih.gov/pubmed/27654913 (cited on pages 24, 52).

[95] G. V. Novack et al. "Mitochondrial Supercomplexes: Physiological Organization and Dysregulation in Age-Related Neurodegenerative Disorders". In: *Front Endocrinol (Lausanne)* 11 (2020), page 600. ISSN: 1664-2392. DOI: 10.3389/fendo.2020.00600. URL: https://www.ncbi.nlm.nih.gov/pubmed/33042002 (cited on page 24).

[96] T. Miura, M. Nishihara, and T. Miki. "Drug development targeting the glycogen synthase kinase-3beta (GSK-3beta)-mediated signal transduction pathway: role of GSK-3beta in myocardial protection against ischemia/reperfusion injury". In: *J Pharmacol Sci* 109.2 (2009), pages 162–7. ISSN: 1347-8613. DOI: 10.1254/jphs.08r27fm. URL: https://www.ncbi.nlm.nih.gov/pubmed/19179805 (cited on page 24).

[97] A. Rasola et al. "Activation of mitochondrial ERK protects cancer cells from death through inhibition of the permeability transition". In: *Proc Natl Acad Sci U S A* 107.2 (2010), pages 726–31. ISSN: 1091-6490. DOI: 10.1073/pnas.0912742107. URL: https://www.ncbi.nlm.nih.gov/pubmed/20080742 (cited on page 24).

[98] R. J. Parks et al. "Cyclophilin D-mediated regulation of the permeability transition pore is altered in mice lacking the mitochondrial calcium uniporter". In: *Cardiovasc Res* 115.2 (2019), pages 385–394. ISSN: 1755-3245. DOI: 10.1093/cvr/cvy218. URL: https://www.ncbi.nlm.nih.gov/pubmed/30165576 (cited on page 25).

[99] S. Hurst et al. "Phosphorylation of cyclophilin D at serine 191 regulates mitochondrial permeability transition pore opening and cell death after ischemia-reperfusion". In: *Cell*

Death Dis 11.8 (2020), page 661. ISSN: 2041-4889. DOI: 10.1038/s41419-020-02864-5. URL: https://www.ncbi.nlm.nih.gov/pubmed/32814770 (cited on page 25).

[100] J. Carroll et al. "Persistence of the permeability transition pore in human mitochondria devoid of an assembled ATP synthase". In: *Proc Natl Acad Sci U S A* 116.26 (2019), pages 12816–12821. ISSN: 1091-6490. DOI: 10.1073/pnas.1904005116. URL: https://www.ncbi.nlm.nih.gov/pubmed/31213546 (cited on pages 25, 53).

[101] J. He et al. "Permeability transition in human mitochondria persists in the absence of peripheral stalk subunits of ATP synthase". In: *Proc Natl Acad Sci U S A* 114.34 (2017), pages 9086–9091. ISSN: 1091-6490. DOI: 10.1073/pnas.1711201114. URL: https://www.ncbi.nlm.nih.gov/pubmed/28784775 (cited on page 25).

[102] J. He et al. "Persistence of the mitochondrial permeability transition in the absence of subunit c of human ATP synthase". In: *Proc Natl Acad Sci U S A* 114.13 (2017), pages 3409–3414. ISSN: 1091-6490. DOI: 10.1073/pnas.1702357114. URL: https://www.ncbi.nlm.nih.gov/pubmed/28289229 (cited on page 25).

[103] P. Bernardi, M. Carraro, and G. Lippe. "The mitochondrial permeability transition: Recent progress and open questions". In: *FEBS* 289.22 (2017), pages 7051–7074. ISSN: 2045-2322. DOI: 10.1038/s41598-017-14795-x. URL: https://www.ncbi.nlm.nih.gov/pubmed/29101324 (cited on page 26).

[104] P. Bernardi. "Mechanisms for Ca". In: *Proc Natl Acad Sci U S A* 117.6 (2020). ISSN: 1091-6490. DOI: 10.1073/pnas.1921035117. URL: https://www.ncbi.nlm.nih.gov/pubmed/31992648 (cited on pages 26, 40).

[105] J. E. Walker, J. Carroll, and J. He. "Reply to Bernardi: The mitochondrial permeability transition pore and the ATP synthase". In: *Proc Natl Acad Sci U S A* 117.6 (2020), pages 2745–2746. ISSN: 1091-6490. DOI: 10.1073/pnas.1921409117. URL: https://www.ncbi.nlm.nih.gov/pubmed/31992647 (cited on page 26).

[106] L. L. Walkon, J. O. Strubbe-Rivera, and J. N. Bazil. "Calcium Overload and Mitochondrial Metabolism". In: *Biomolecules* 12.12 (2022). ISSN: 2218-273X. DOI: 10.3390/biom12121891. URL: https://www.ncbi.nlm.nih.gov/pubmed/36551319 (cited on page 26).

[107] M. A. Neginskaya et al. "ATP Synthase C-Subunit-Deficient Mitochondria Have a Small Cyclosporine A-Sensitive Channel, but Lack the Permeability Transition Pore". In: *Cell Rep* 26.1 (2019), 11–17.e2. ISSN: 2211-1247. DOI: 10.1016/j.celrep.2018.12.033. URL: https://www.ncbi.nlm.nih.gov/pubmed/30605668 (cited on page 27).

[108] M. J. Bround, D. M. Bers, and J. D. Molkentin. "A 20/20 view of ANT function in mitochondrial biology and necrotic cell death". In: *J Mol Cell Cardiol* 144 (2020), A3–A13. ISSN: 1095-8584. DOI: 10.1016/j.yjmcc.2020.05.012. URL: https://www.ncbi.nlm.nih.gov/pubmed/32454061 (cited on page 27).

[109] L. He and J. J. Lemasters. "Regulated and unregulated mitochondrial permeability transition pores: a new paradigm of pore structure and function?" In: *FEBS Lett* 512.1-3 (2002), pages 1–7. ISSN: 0014-5793. DOI: 10.1016/s0014-5793(01)03314-2. URL: https://www.ncbi.nlm.nih.gov/pubmed/11852041 (cited on page 28).

[110] D. Penzo et al. "Effects of fatty acids on mitochondria: implications for cell death". In: *Biochim Biophys Acta* 1555.1-3 (2002), pages 160–5. ISSN: 0006-3002. DOI: 10.1016/s0005-2728(02)00272-4. URL: https://www.ncbi.nlm.nih.gov/pubmed/12206909 (cited on pages 29, 30).

[111] A. AYu et al. "The ATP/ADP-antiporter is involved in the uncoupling effect of fatty acids on mitochondria". In: *Eur J Biochem* 182.3 (1989), pages 585–92. ISSN: 0014-2956. DOI: 10.1111/j.1432-1033.1989.tb14867.x. URL: https://www.ncbi.nlm.nih.gov/pubmed/2546761 (cited on pages 29, 44).

[112] M. M. Levachev et al. "[Energy metabolism in the pigeon during self-warming after hypothermia]". In: *Biokhimiia* 30.4 (1965), pages 864–74. ISSN: 0320-9725. URL: https://www.ncbi.nlm.nih.gov/pubmed/5882167 (cited on page 29).

[113] K. R. Laskowski and R. R. Russell. "Uncoupling proteins in heart failure". In: *Curr Heart Fail Rep* 5.2 (2008), pages 75–9. ISSN: 1546-9549. DOI: 10.1007/s11897-008-0013-1. URL: https://www.ncbi.nlm.nih.gov/pubmed/18765077 (cited on page 29).

[114] S. Shanmughapriya et al. "SPG7 Is an Essential and Conserved Component of the Mitochondrial Permeability Transition Pore". In: *Mol Cell* 60.1 (2015), pages 47–62. ISSN: 1097-4164. DOI: 10.1016/j.molcel.2015.08.009. URL: https://www.ncbi.nlm.nih.gov/pubmed/26387735 (cited on page 30).

[115] V. Baderna et al. "A novel AFG3L2 mutation close to AAA domain leads to aberrant OMA1 and OPA1 processing in a family with optic atrophy". In: *Acta Neuropathol Commun* 8.1 (2020), page 93. ISSN: 2051-5960. DOI: 10.1186/s40478-020-00975-w. URL: https://www.ncbi.nlm.nih.gov/pubmed/32600459 (cited on page 30).

[116] E. Fontaine et al. "Regulation of the permeability transition pore in skeletal muscle mitochondria. Modulation By electron flow through the respiratory chain complex i". In: *J Biol Chem* 273.20 (1998), pages 12662–8. ISSN: 0021-9258. DOI: 10.1074/jbc.273.20.12662. URL: https://www.ncbi.nlm.nih.gov/pubmed/9575229 (cited on page 31).

[117] V. Adam-Vizi and C. Chinopoulos. “Bioenergetics and the formation of mitochondrial reactive oxygen species”. In: *Trends Pharmacol Sci* 27.12 (2006), pages 639–45. ISSN: 0165-6147. DOI: 10.1016/j.tips.2006.10.005. URL: https://www.ncbi.nlm.nih.gov/pubmed/17056127 (cited on page 32).

[118] G. Barja and A. Herrero. “Localization at complex I and mechanism of the higher free radical production of brain nonsynaptic mitochondria in the short-lived rat than in the longevous pigeon”. In: *J Bioenerg Biomembr* 30.3 (1998), pages 235–43. ISSN: 0145-479X. DOI: 10.1023/a:1020592719405. URL: https://www.ncbi.nlm.nih.gov/pubmed/9733090 (cited on page 32).

[119] G. Krishnamoorthy and P. C. Hinkle. “Studies on the electron transfer pathway, topography of iron-sulfur centers, and site of coupling in NADH-Q oxidoreductase”. In: *J Biol Chem* 263.33 (1988), pages 17566–75. ISSN: 0021-9258. URL: https://www.ncbi.nlm.nih.gov/pubmed/2846570 (cited on page 32).

[120] L. Kussmaul and J. Hirst. “The mechanism of superoxide production by NADH-Q oxidoreductase (complex I) from bovine heart mitochondria”. In: *Proc Natl Acad Sci U S A* 103.20 (2006), pages 7607–12. ISSN: 0027-8424. DOI: 10.1073/pnas.0510977103. URL: https://www.ncbi.nlm.nih.gov/pubmed/16682634 (cited on page 32).

[121] L. K. Kwong and R. S. Sohal. “Substrate and site specificity of hydrogen peroxide generation in mouse mitochondria”. In: *Arch Biochem Biophys* 350.1 (1998), pages 118–26. ISSN: 0003-9861. DOI: 10.1006/abbi.1997.0489. URL: https://www.ncbi.nlm.nih.gov/pubmed/9466828 (cited on page 32).

[122] J. O. Strubbe-Rivera et al. “Modeling the Effects of Calcium Overload on Mitochondrial Ultrastructural Remodeling”. In: *Appl Sci (Basel)* 11.5 (2021). ISSN: 2076-3417. DOI: 10.3390/app11052071. URL: https://www.ncbi.nlm.nih.gov/pubmed/33898062 (cited on pages 33–35, 40, 42, 44, 45, 50).

[123] M. R. Duchen. “Mitochondria and calcium: from cell signalling to cell death”. In: *J Physiol* 529 Pt 1.Pt 1 (2000), pages 57–68. ISSN: 0022-3751. DOI: 10.1111/j.1469-7793.2000.00057.x. URL: https://www.ncbi.nlm.nih.gov/pubmed/11080251 (cited on pages 33, 74).

[124] V. Petronilli et al. “Regulation of the permeability transition pore, a voltage-dependent mitochondrial channel inhibited by cyclosporin A”. In: *Biochim Biophys Acta* 1187.2 (1994), pages 255–9. ISSN: 0006-3002. DOI: 10.1016/0005-2728(94)90122-8. URL: https://www.ncbi.nlm.nih.gov/pubmed/7521212 (cited on pages 33, 40).

[125] V. Petronilli et al. “Physiological effectors modify voltage sensing by the cyclosporin A-sensitive permeability transition pore of mitochondria”. In: *J Biol Chem* 268.29 (1993), pages 21939–45. ISSN: 0021-9258. URL: https://www.ncbi.nlm.nih.gov/pubmed/8408050 (cited on pages 33–35, 40, 42, 45, 48, 50, 51, 59, 62, 73, 75).

[126] B. Glancy and R. S. Balaban. “Role of mitochondrial Ca2+ in the regulation of cellular energetics”. In: *Biochemistry* 51.14 (2012), pages 2959–73. ISSN: 1520-4995. DOI: 10.1021/bi2018909. URL: https://www.ncbi.nlm.nih.gov/pubmed/22443365 (cited on pages 33, 41).

[127] A. Carrer et al. “Defining the molecular mechanisms of the mitochondrial permeability transition through genetic manipulation of F-ATP synthase”. In: *Nat Commun* 12.1 (2021), page 4835. ISSN: 2041-1723. DOI: 10.1038/s41467-021-25161-x. URL: https://www.ncbi.nlm.nih.gov/pubmed/34376679 (cited on pages 34, 35, 45, 46, 75).

[128] S. Austin et al. “MICSI is the Ca2+/H+ antiporter of mammalian mitochondria”. Journal Article. BioRxiv, 1965. URL: https://www.ncbi.nlm.nih.gov/pubmed/5849818 (cited on pages 34, 39, 40).

[129] B. Duvvuri and C. Lood. “Mitochondrial Calcification”. In: *Immunometabolism* 3.1 (2021). ISSN: 2084-6835. DOI: 10.20900/immunometab20210008. URL: https://www.ncbi.nlm.nih.gov/pubmed/33604080 (cited on pages 34, 40, 42).

[130] E. Basso et al. “Phosphate is essential for inhibition of the mitochondrial permeability transition pore by cyclosporin A and by cyclophilin D ablation”. In: *J Biol Chem* 283.39 (2008), pages 26307–11. ISSN: 0021-9258. DOI: 10.1074/jbc.C800132200. URL: https://www.ncbi.nlm.nih.gov/pubmed/18684715 (cited on pages 34, 46).

[131] M. J. Bround, D. M. Bers, and J. D. Molkentin. “A 20/20 view of ANT function in mitochondrial biology and necrotic cell death”. In: *J Mol Cell Cardiol* 144 (2020), A3–A13. ISSN: 1095-8584. DOI: 10.1016/j.yjmcc.2020.05.012. URL: https://www.ncbi.nlm.nih.gov/pubmed/32454061 (cited on pages 34, 39, 74).

[132] T. M. Bauer and E. Murphy. “Role of Mitochondrial Calcium and the Permeability Transition Pore in Regulating Cell Death”. In: *Circ Res* 126.2 (2020), pages 280–293. ISSN: 1524-4571. DOI: 10.1161/CIRCRESAHA.119.316306. URL: https://www.ncbi.nlm.nih.gov/pubmed/31944918 (cited on pages 35, 40, 73).

[133] A. P. Halestrap. “What is the mitochondrial permeability transition pore?” In: *J Mol Cell Cardiol* 46.6 (2009), pages 821–31. ISSN: 1095-8584. DOI: 10.1016/j.yjmcc.2009.02.021. URL: https://www.ncbi.nlm.nih.gov/pubmed/19265700 (cited on page 35).

[134] J. R. Kremer, D. N. Mastronarde, and J. R. McIntosh. "Computer visualization of three-dimensional image data using IMOD". In: *J Struct Biol* 116.1 (1996), pages 71–6. ISSN: 1047-8477. DOI: 10.1006/jsbi.1996.0013. URL: https://www.ncbi.nlm.nih.gov/pubmed/8742726 (cited on pages 38, 45, 51, 118).

[135] B. R. Alevriadou et al. "Molecular nature and physiological role of the mitochondrial calcium uniporter channel". In: *Am J Physiol Cell Physiol* 320.4 (2021), pages C465–C482. ISSN: 1522-1563. DOI: 10.1152/ajpcell.00502.2020. URL: https://www.ncbi.nlm.nih.gov/pubmed/33296287 (cited on pages 38, 78).

[136] K. N. Belosludtsev et al. "Mitochondrial Ca2+ Transport: Mechanisms, Molecular Structures, and Role in Cells". In: *Biochemistry (Mosc)* 84.6 (2019), pages 593–607. ISSN: 1608-3040. DOI: 10.1134/S0006297919060026. URL: https://www.ncbi.nlm.nih.gov/pubmed/31238859 (cited on pages 38, 51).

[137] G. Csordás et al. "MICU1 controls both the threshold and cooperative activation of the mitochondrial Ca²? uniporter". In: *Cell Metab* 17.6 (2013), pages 976–987. ISSN: 1932-7420. DOI: 10.1016/j.cmet.2013.04.020. URL: https://www.ncbi.nlm.nih.gov/pubmed/23747253 (cited on page 38).

[138] D. De Stefani, M. Patron, and R. Rizzuto. "Structure and function of the mitochondrial calcium uniporter complex". In: *Biochim Biophys Acta* 1853.9 (2015), pages 2006–11. ISSN: 0006-3002. DOI: 10.1016/j.bbamcr.2015.04.008. URL: https://www.ncbi.nlm.nih.gov/pubmed/25896525 (cited on page 38).

[139] T. E. Gunter et al. "Calcium and mitochondria". In: *FEBS Lett* 567.1 (2004), pages 96–102. ISSN: 0014-5793. DOI: 10.1016/j.febslet.2004.03.071. URL: https://www.ncbi.nlm.nih.gov/pubmed/15165900 (cited on pages 38, 73).

[140] J. Mishra et al. "The Mitochondrial Ca". In: *Handb Exp Pharmacol* 240 (2017). ISSN: 0171-2004. DOI: 10.1007/164_2017_1. URL: https://www.ncbi.nlm.nih.gov/pubmed/28194521 (cited on page 38).

[141] A. C. Wei et al. "Dynamics of matrix-free Ca2+ in cardiac mitochondria: two components of Ca2+ uptake and role of phosphate buffering". In: *J Gen Physiol* 139.6 (2012), pages 465–78. ISSN: 1540-7748. DOI: 10.1085/jgp.201210784. URL: https://www.ncbi.nlm.nih.gov/pubmed/22641641 (cited on pages 38, 39, 42).

[142] Y. Kirichok, G. Krapivinsky, and D. E. Clapham. "The mitochondrial calcium uniporter is a highly selective ion channel". In: *Nature* 427.6972 (2004), pages 360–4. ISSN: 1476-4687. DOI: 10.1038/nature02246. URL: https://www.ncbi.nlm.nih.gov/pubmed/14737170 (cited on page 38).

[143] R. K. Dash and D. A. Beard. "Analysis of cardiac mitochondrial Na+-Ca2+ exchanger kinetics with a biophysical model of mitochondrial Ca2+ handling suggests a 3:1 stoichiometry". In: *J Physiol* 586.13 (2008), pages 3267–85. ISSN: 1469-7793. DOI: 10.1113/jphysiol.2008.151977. URL: https://www.ncbi.nlm.nih.gov/pubmed/18467367 (cited on pages 39, 61, 74, 76).

[144] J. F. Garbincius and J. W. Elrod. "Mitochondrial calcium exchange in physiology and disease". In: *Physiol Rev* 102.2 (2022), pages 893–992. ISSN: 1522-1210. DOI: 10.1152/physrev.00041.2020. URL: https://www.ncbi.nlm.nih.gov/pubmed/34698550 (cited on page 39).

[145] K. K. Gunter, M. J. Zuscik, and T. E. Gunter. "The Na(+)-independent Ca2+ efflux mechanism of liver mitochondria is not a passive Ca2+/2H+ exchanger". In: *J Biol Chem* 266.32 (1991), pages 21640–8. ISSN: 0021-9258. URL: https://www.ncbi.nlm.nih.gov/pubmed/1939193 (cited on page 39).

[146] I. Drago, P. Pizzo, and T. Pozzan. "After half a century mitochondrial calcium in- and efflux machineries reveal themselves". In: *EMBO J* 30.20 (2011), pages 4119–25. ISSN: 1460-2075. DOI: 10.1038/emboj.2011.337. URL: https://www.ncbi.nlm.nih.gov/pubmed/21934651 (cited on pages 39, 51).

[147] P. Pizzo et al. "Mitochondrial Ca²? homeostasis: mechanism, role, and tissue specificities". In: *Pflugers Arch* 464.1 (2012), pages 3–17. ISSN: 1432-2013. DOI: 10.1007/s00424-012-1122-y. URL: https://www.ncbi.nlm.nih.gov/pubmed/22706634 (cited on pages 39, 77).

[148] R. Rizzuto and T. Pozzan. "Microdomains of intracellular Ca2+: molecular determinants and functional consequences". In: *Physiol Rev* 86.1 (2006), pages 369–408. ISSN: 0031-9333. DOI: 10.1152/physrev.00004.2005. URL: https://www.ncbi.nlm.nih.gov/pubmed/16371601 (cited on pages 39, 51).

[149] D. E. Wingrove and T. E. Gunter. "Kinetics of mitochondrial calcium transport. I. Characteristics of the sodium-independent calcium efflux mechanism of liver mitochondria". In: *J Biol Chem* 261.32 (1986), pages 15159–65. ISSN: 0021-9258. URL: https://www.ncbi.nlm.nih.gov/pubmed/3771569 (cited on pages 39, 73).

[150] D. E. Wingrove and T. E. Gunter. "Kinetics of mitochondrial calcium transport. II. A kinetic description of the sodium-dependent calcium efflux mechanism of liver mitochondria and inhibition by ruthenium red and by tetraphenylphosphonium". In: *J Biol Chem* 261.32 (1986), pages 15166–71. ISSN: 0021-9258. URL: https://www.ncbi.nlm.nih.gov/pubmed/2429966 (cited on page 39).

[151] D. M. Bers. "Altered cardiac myocyte Ca regulation in heart failure". In: *Physiology (Bethesda)* 21 (2006), pages 380–7. ISSN: 1548-9213. DOI: 10.1152/physiol.00019.2006. URL: https://www.ncbi.nlm.nih.gov/pubmed/17119150 (cited on pages 39, 59).

[152] C. C. Hale et al. "Sodium-calcium exchange crystallization". In: *Ann N Y Acad Sci* 976 (2002), pages 100–2. ISSN: 0077-8923. DOI: 10.1111/j.1749-6632.2002.tb04725.x. URL: https://www.ncbi.nlm.nih.gov/pubmed/12502545 (cited on page 39).

[153] L. Boyman and W. J. Lederer. "How the mitochondrial calcium uniporter complex (MCU". In: *Proc Natl Acad Sci U S A* 117.37 (2020), pages 22634–22636. ISSN: 1091-6490. DOI: 10.1073/pnas.2015886117. URL: https://www.ncbi.nlm.nih.gov/pubmed/32879002%20https://www.pnas.org/doi/pdf/10.1073/pnas.2015886117 (cited on page 39).

[154] G. Szanda et al. "Mitochondrial Ca2+ uptake with and without the formation of high-Ca2+ microdomains". In: *Cell Calcium* 40.5-6 (2006), pages 527–37. ISSN: 0143-4160. DOI: 10.1016/j.ceca.2006.08.019. URL: https://www.ncbi.nlm.nih.gov/pubmed/17069884 (cited on pages 39, 75).

[155] G. S. Williams et al. "Mitochondrial calcium uptake". In: *Proc Natl Acad Sci U S A* 110.26 (2013), pages 10479–86. ISSN: 1091-6490. DOI: 10.1073/pnas.1300410110. URL: https://www.ncbi.nlm.nih.gov/pubmed/23759742 (cited on pages 39, 75).

[156] L. Boyman and W. J. Lederer. "How the mitochondrial calcium uniporter complex (MCUcx) works". In: *Proc Natl Acad Sci U S A* 117.37 (2020), pages 22634–22636. ISSN: 1091-6490 (Electronic) 0027-8424 (Linking). DOI: 10.1073/pnas.2015886117. URL: https://www.ncbi.nlm.nih.gov/pubmed/32879002 (cited on page 39).

[157] X. Zhang et al. "Substrate- and Calcium-Dependent Differential Regulation of Mitochondrial Oxidative Phosphorylation and Energy Production in the Heart and Kidney". In: *Cells* 11.1 (2021). ISSN: 2073-4409. DOI: 10.3390/cells11010131. URL: https://www.ncbi.nlm.nih.gov/pubmed/35011693 (cited on page 40).

[158] P. Bernardi and V. Petronilli. "The permeability transition pore as a mitochondrial calcium release channel: a critical appraisal". In: *J Bioenerg Biomembr* 28.2 (1996), pages 131–8. ISSN: 0145-479X. DOI: 10.1007/BF02110643. URL: https://www.ncbi.nlm.nih.gov/pubmed/9132411 (cited on page 40).

[159] C. Chinopoulos and V. Adam-Vizi. "Mitochondrial Ca2+ sequestration and precipitation revisited". In: *FEBS J* 277.18 (2010), pages 3637–51. ISSN: 1742-4658. DOI: 10.1111/j.1742-4658.2010.07755.x. URL: https://www.ncbi.nlm.nih.gov/pubmed/20659160 (cited on pages 40, 41).

[160] P. Bernardi. "Mitochondrial transport of cations: channels, exchangers, and permeability transition". In: *Physiol Rev* 79.4 (1999), pages 1127–55. ISSN: 0031-9333. DOI: 10.1152/physrev.1999.79.4.1127. URL: https://www.ncbi.nlm.nih.gov/pubmed/10508231 (cited on pages 40, 41).

[161] N. Wu et al. "Blocking the mitochondrial permeability transition pore with cyclosporine-A can restore cardioprotection of ischemic postconditioning in hypercholesterolemic rat heart". In: *Eur Rev Med Pharmacol Sci* 19.3 (2015), pages 446–54. ISSN: 2284-0729. URL: https://www.ncbi.nlm.nih.gov/pubmed/25720717 (cited on page 40).

[162] D. Poburko, J. Santo-Domingo, and N. Demaurex. "Dynamic regulation of the mitochondrial proton gradient during cytosolic calcium elevations". In: *J Biol Chem* 286.13 (2011), pages 11672–84. ISSN: 1083-351X. DOI: 10.1074/jbc.M110.159962. URL: https://www.ncbi.nlm.nih.gov/pubmed/21224385 (cited on page 41).

[163] E. L. Seifert et al. "The mitochondrial phosphate carrier: Role in oxidative metabolism, calcium handling and mitochondrial disease". In: *Biochem Biophys Res Commun* 464.2 (2015), pages 369–75. ISSN: 1090-2104. DOI: 10.1016/j.bbrc.2015.06.031. URL: https://www.ncbi.nlm.nih.gov/pubmed/26091567 (cited on pages 41, 57).

[164] C. Garcia-Perez, G. Hajnoczky, and G. Csordas. "Physical coupling supports the local Ca2+ transfer between sarcoplasmic reticulum subdomains and the mitochondria in heart muscle". In: *J Biol Chem* 283.47 (2008), pages 32771–80. ISSN: 0021-9258 (Print) 0021-9258 (Linking). DOI: 10.1074/jbc.M803385200. URL: https://www.ncbi.nlm.nih.gov/pubmed/18790739 (cited on pages 41, 42, 70, 75).

[165] E. Camors, V. Monceau, and D. Charlemagne. "Annexins and Ca2+ handling in the heart". In: *Cardiovasc Res* 65.4 (2005), pages 793–802. ISSN: 0008-6363. DOI: 10.1016/j.cardiores.2004.11.010. URL: https://www.ncbi.nlm.nih.gov/pubmed/15721859 (cited on pages 41, 43).

[166] E. Carafoli, C. S. Rossi, and A. L. Lehninger. "Uptake of adenine nucleotides by respiring mitochondria during active accumulation of Ca2+ and phosphate". In: *J Biol Chem* 240 (1965), pages 2254–61. ISSN: 0021-9258. URL: https://www.ncbi.nlm.nih.gov/pubmed/14299656 (cited on pages 43, 75).

[167] J. Bandorowicz-Pikuła et al. "[Annexins in mitochondria]". In: *Postepy Biochem* 62.2 (2016), pages 216–223. ISSN: 0032-5422. URL: https://www.ncbi.nlm.nih.gov/pubmed/28132474 (cited on page 43).

[168] J. N. Bazil et al. "Modeling the calcium sequestration system in isolated guinea pig cardiac mitochondria". In: *J Bioenerg Biomembr* 45.3 (2013), pages 177–88. ISSN: 1573-

6881 (Electronic) 0145-479X (Linking). DOI: 10.1007/s10863-012-9488-2. URL: https://www.ncbi.nlm.nih.gov/pubmed/23180139 (cited on page 43).

[169] J. Bandorowicz-Pikula, R. Buchet, and S. Pikula. "Annexins as nucleotide-binding proteins: facts and speculations". In: *Bioessays* 23.2 (2001), pages 170–8. ISSN: 0265-9247 (Print) 0265-9247 (Linking). DOI: 10.1002/1521-1878(200102)23:2<170::AID-BIES1024>3.0.CO;2-#. URL: https://www.ncbi.nlm.nih.gov/pubmed/11169590 (cited on page 43).

[170] A. Szewczyk and S. Pikula. "Adenosine 5'-triphosphate: an intracellular metabolic messenger". In: *Biochim Biophys Acta* 1365.3 (1998), pages 333–53. ISSN: 0006-3002 (Print) 0006-3002 (Linking). DOI: 10.1016/s0005-2728(98)00094-2. URL: https://www.ncbi.nlm.nih.gov/pubmed/9711292 (cited on page 43).

[171] M. Chlystun et al. "Regulation of mitochondrial morphogenesis by annexin A6". In: *PLoS One* 8.1 (2013), e53774. ISSN: 1932-6203. DOI: 10.1371/journal.pone.0053774. URL: https://www.ncbi.nlm.nih.gov/pubmed/23341998 (cited on pages 43, 62).

[172] V. Gerke, C. E. Creutz, and S. E. Moss. "Annexins: linking Ca2+ signalling to membrane dynamics". In: *Nat Rev Mol Cell Biol* 6.6 (2005), pages 449–61. ISSN: 1471-0072. DOI: 10.1038/nrm1661. URL: https://www.ncbi.nlm.nih.gov/pubmed/15928709 (cited on page 43).

[173] U. Rescher and V. Gerke. "Annexins–unique membrane binding proteins with diverse functions". In: *J Cell Sci* 117.Pt 13 (2004), pages 2631–9. ISSN: 0021-9533. DOI: 10.1242/jcs.01245. URL: https://www.ncbi.nlm.nih.gov/pubmed/15169834 (cited on page 43).

[174] C. Croissant et al. "Annexins and Membrane Repair Dysfunctions in Muscular Dystrophies". In: *Int J Mol Sci* 22.10 (2021). ISSN: 1422-0067. DOI: 10.3390/ijms22105276. URL: https://www.ncbi.nlm.nih.gov/pubmed/34067866 (cited on page 43).

[175] V. G. Sophia N. Koerdt Arsila P.K. Ashraf. "Chapter Three - Annexins and Plasma Membrane Repair". In: *Plasma Membrane Repair*. Edited by L. O. Andrade. Volume 84. Elsevier: Zoe Kruze, 2019. Chapter 3, pages 43–65. ISBN: 978-0-12-817760-0. DOI: 10.1016/bs.ctm.2019.07.006 (cited on pages 43, 61, 76).

[176] M. R. Hayden. "The Mighty Mitochondria Are Unifying Organelles and Metabolic Hubs in Multiple Organs of Obesity, Insulin Resistance, Metabolic Syndrome, and Type 2 Diabetes: An Observational Ultrastructure Study". In: *Int J Mol Sci* 23.9 (2022). ISSN: 1422-0067 (Electronic) 1422-0067 (Linking). DOI: 10.3390/ijms23094820. URL: https://www.ncbi.nlm.nih.gov/pubmed/35563211 (cited on page 44).

[177] A. Knapp-Wilson et al. “Maintenance of complex I and its supercomplexes by NDUF-11 is essential for mitochondrial structure, function and health”. In: *J Cell Sci* 134.13 (2021). ISSN: 1477-9137 (Electronic) 0021-9533 (Linking). DOI: 10.1242/jcs.258399. URL: https://www.ncbi.nlm.nih.gov/pubmed/34106255 (cited on page 44).

[178] D. H. Mendelsohn et al. “Structural Analysis of Mitochondrial Dynamics-From Cardiomyocytes to Osteoblasts: A Critical Review”. In: *Int J Mol Sci* 23.9 (2022). ISSN: 1422-0067 (Electronic) 1422-0067 (Linking). DOI: 10.3390/ijms23094571. URL: https://www.ncbi.nlm.nih.gov/pubmed/35562962 (cited on page 44).

[179] I. Mendez-Lopez et al. “Progressive Mitochondrial SOD1(G93A) Accumulation Causes Severe Structural, Metabolic and Functional Aberrations through OPA1 Downregulation in a Mouse Model of Amyotrophic Lateral Sclerosis”. In: *Int J Mol Sci* 22.15 (2021). ISSN: 1422-0067 (Electronic) 1422-0067 (Linking). DOI: 10.3390/ijms22158194. URL: https://www.ncbi.nlm.nih.gov/pubmed/34360957 (cited on page 44).

[180] E. Mishra and M. K. Thakur. “Alterations in hippocampal mitochondrial dynamics are associated with neurodegeneration and recognition memory decline in old male mice”. In: *Biogerontology* 23.2 (2022), pages 251–271. ISSN: 1573-6768 (Electronic) 1389-5729 (Linking). DOI: 10.1007/s10522-022-09960-3. URL: https://www.ncbi.nlm.nih.gov/pubmed/35266060 (cited on page 44).

[181] I. Mukherjee, M. Ghosh, and M. Meinecke. “MICOS and the mitochondrial inner membrane morphology - when things get out of shape”. In: *FEBS Lett* 595.8 (2021), pages 1159–1183. ISSN: 1873-3468 (Electronic) 0014-5793 (Linking). DOI: 10.1002/1873-3468.14089. URL: https://www.ncbi.nlm.nih.gov/pubmed/33837538 (cited on page 44).

[182] E. A. Munn. *The structure of mitochondria*. London ; New York: Academic Press, 2004. DOI: 10.1023/B:JOBB.0000041753.52832.f3. URL: https://www.ncbi.nlm.nih.gov/pubmed/15377857 (cited on page 44).

[183] S. Ranjbarvaziri et al. “Altered Cardiac Energetics and Mitochondrial Dysfunction in Hypertrophic Cardiomyopathy”. In: *Circulation* 144.21 (2021), pages 1714–1731. ISSN: 1524-4539 (Electronic) 0009-7322 (Linking). DOI: 10.1161/CIRCULATIONAHA.121.053575. URL: https://www.ncbi.nlm.nih.gov/pubmed/34672721 (cited on page 44).

[184] A. Azzi and G. F. Azzone. “Swelling and shrinkage phenomena in liver mitochondria. I. Large amplitude swelling induced by inorganic phosphate and by ATP”. In: *Biochim Biophys Acta* 105.2 (1965). Azzi, A Azzone, GF, pages 253–264. ISSN: 0006-3002. URL: https://www.ncbi.nlm.nih.gov/pubmed/5849818 (cited on page 44).

[185] J. RAAFLAUB. "[Swelling of isolated mitochondria of the liver and their susceptibility to physicochemical influences]". In: *Helv Physiol Pharmacol Acta* 11.2 (1953), pages 142–56. ISSN: 0367-6242. URL: https://www.ncbi.nlm.nih.gov/pubmed/13095885 (cited on page 44).

[186] A. R. CROFTS and J. B. CHAPPELL. "CALCIUM ION ACCUMULATION AND VOLUME CHANGES OF ISOLATED LIVER MITOCHONDRIA. REVERSAL OF CALCIUM ION-INDUCED SWELLING". In: *Biochem J* 95 (1965), pages 387–92. ISSN: 0264-6021. DOI: 10.1042/bj0950387. URL: https://www.ncbi.nlm.nih.gov/pubmed/14340089 (cited on page 44).

[187] A. L. Lehninger. "Reversal of various types of mitochondrial swelling by adenosine triphosphate". In: *J Biol Chem* 234 (1959), pages 2465–71. ISSN: 0021-9258 (Print) 0021-9258 (Linking). URL: https://www.ncbi.nlm.nih.gov/pubmed/14415396 (cited on page 44).

[188] A. L. LEHNINGER and L. F. REMMERT. "An endogenous uncoupling and swelling agent in liver mitochondria and its enzymic formation". In: *J Biol Chem* 234 (1959), pages 2459–64. ISSN: 0021-9258. URL: https://www.ncbi.nlm.nih.gov/pubmed/14415393 (cited on pages 44, 52).

[189] C. R. Hackenbrock and A. I. Caplan. "Ion-induced ultrastructural transformations in isolated mitochondria. The energized uptake of calcium". In: *J Cell Biol* 42.1 (1969), pages 221–34. ISSN: 0021-9525. URL: https://www.ncbi.nlm.nih.gov/pubmed/5795884 (cited on pages 44, 52).

[190] C. Giorgi et al. "Mitochondrial Ca(2+) and apoptosis". In: *Cell Calcium* 52.1 (2012), pages 36–43. ISSN: 1532-1991 (Electronic) 0143-4160 (Linking). DOI: 10.1016/j.ceca.2012.02.008. URL: https://www.ncbi.nlm.nih.gov/pubmed/22480931 (cited on pages 45, 51).

[191] S. G. Wolf et al. "3D visualization of mitochondrial solid-phase calcium stores in whole cells". In: *Elife* 6 (2017). ISSN: 2050-084X (Electronic) 2050-084X (Linking). DOI: 10.7554/eLife.29929. URL: https://www.ncbi.nlm.nih.gov/pubmed/29106371 (cited on pages 49, 62, 72).

[192] R. A. Kloner et al. "Ultrastructural evidence of microvascular damage and myocardial cell injury after coronary artery occlusion: which comes first?" In: *Circulation* 62.5 (1980), pages 945–52. ISSN: 0009-7322 (Print) 0009-7322 (Linking). DOI: 10.1161/01.cir.62.5.945. URL: https://www.ncbi.nlm.nih.gov/pubmed/7418179 (cited on page 50).

[193] N. Afzal et al. “Effect of crista morphology on mitochondrial ATP output: A computational study”. In: *Curr Res Physiol* 4 (2021), pages 163–176. ISSN: 2665-9441 (Electronic) 2665-9441 (Linking). DOI: 10.1016/j.crphys.2021.03.005. URL: https://www.ncbi.nlm.nih.gov/pubmed/34396153 (cited on page 50).

[194] S. Ghosh et al. “Effects of altered cellular ultrastructure on energy metabolism in diabetic cardiomyopathy: an in silico study”. In: *Philos Trans R Soc Lond B Biol Sci* 377.1864 (2022), page 20210323. ISSN: 1471-2970 (Electronic) 0962-8436 (Linking). DOI: 10.1098/rstb.2021.0323. URL: https://www.ncbi.nlm.nih.gov/pubmed/36189807 (cited on page 50).

[195] S. Ghosh et al. “Insights on the impact of mitochondrial organisation on bioenergetics in high-resolution computational models of cardiac cell architecture”. In: *PLoS Comput Biol* 14.12 (2018), e1006640. ISSN: 1553-7358 (Electronic) 1553-734X (Linking). DOI: 10.1371/journal.pcbi.1006640. URL: https://www.ncbi.nlm.nih.gov/pubmed/30517098 (cited on page 50).

[196] A. P. Halestrap and P. Pasdois. “The role of the mitochondrial permeability transition pore in heart disease”. In: *Biochim Biophys Acta* 1787.11 (2009), pages 1402–15. ISSN: 0006-3002 (Print) 0006-3002 (Linking). DOI: 10.1016/j.bbabio.2008.12.017. URL: https://www.ncbi.nlm.nih.gov/pubmed/19168026 (cited on pages 51, 52).

[197] R. S. Balaban. “Cardiac energy metabolism homeostasis: role of cytosolic calcium”. In: *J Mol Cell Cardiol* 34.10 (2002), pages 1259–71. ISSN: 0022-2828 (Print) 0022-2828 (Linking). DOI: 10.1006/jmcc.2002.2082. URL: https://www.ncbi.nlm.nih.gov/pubmed/12392982 (cited on pages 51, 75).

[198] V. Eisner, M. Picard, and G. Hajnoczky. “Mitochondrial dynamics in adaptive and maladaptive cellular stress responses”. In: *Nat Cell Biol* 20.7 (2018), pages 755–765. ISSN: 1476-4679 (Electronic) 1465-7392 (Linking). DOI: 10.1038/s41556-018-0133-0. URL: https://www.ncbi.nlm.nih.gov/pubmed/29950571 (cited on page 51).

[199] B. Glancy et al. “Effect of calcium on the oxidative phosphorylation cascade in skeletal muscle mitochondria”. In: *Biochemistry* 52.16 (2013), pages 2793–809. ISSN: 1520-4995 (Electronic) 0006-2960 (Linking). DOI: 10.1021/bi3015983. URL: https://www.ncbi.nlm.nih.gov/pubmed/23547908 (cited on pages 51, 59).

[200] C. A. Mannella, W. J. Lederer, and M. S. Jafri. “The connection between inner membrane topology and mitochondrial function”. In: *J Mol Cell Cardiol* 62 (2013), pages 51–7. ISSN: 1095-8584 (Electronic) 0022-2828 (Linking). DOI: 10.1016/j.yjmcc.2013.05.001. URL: https://www.ncbi.nlm.nih.gov/pubmed/23672826 (cited on page 51).

[201] S. Marchi, S. Patergnani, and P. Pinton. "The endoplasmic reticulum-mitochondria connection: one touch, multiple functions". In: *Biochim Biophys Acta* 1837.4 (2014), pages 461–9. ISSN: 0006-3002 (Print) 0006-3002 (Linking). DOI: 10.1016/j.bbabio.2013.10.015. URL: https://www.ncbi.nlm.nih.gov/pubmed/24211533 (cited on page 51).

[202] P. Bonsi et al. "Mitochondrial toxins in Basal Ganglia disorders: from animal models to therapeutic strategies". In: *Curr Neuropharmacol* 4.1 (2006), pages 69–75. ISSN: 1570-159X (Print) 1570-159X (Linking). URL: https://www.ncbi.nlm.nih.gov/pubmed/18615133 (cited on pages 51, 52).

[203] P. Bernardi. "Mitochondrial transport of cations: channels, exchangers, and permeability transition". In: *Physiol Rev* 79.4 (1999), pages 1127–55. ISSN: 0031-9333 (Print) 0031-9333 (Linking). DOI: 10.1152/physrev.1999.79.4.1127. URL: https://www.ncbi.nlm.nih.gov/pubmed/10508231 (cited on pages 52, 62).

[204] J. B. Chappell and A. R. Crofts. "Calcium Ion Accumulation and Volume Changes of Isolated Liver Mitochondria. Calcium Ion-Induced Swelling". In: *Biochem J* 95 (1965), pages 378–86. ISSN: 0264-6021 (Print) 0264-6021 (Linking). URL: https://www.ncbi.nlm.nih.gov/pubmed/14340088 (cited on pages 52, 146).

[205] J. Hunter F. E. et al. "Studies on the Mechanism of Ascorbate-Induced Swelling and Lysis of Isolated Liver Mitochandria". In: *J Biol Chem* 239 (1964), pages 604–13. ISSN: 0021-9258 (Print) 0021-9258 (Linking). URL: https://www.ncbi.nlm.nih.gov/pubmed/14169167 (cited on page 52).

[206] D. R. Hunter and R. A. Haworth. "The Ca2+-induced membrane transition in mitochondria. I. The protective mechanisms". In: *Arch Biochem Biophys* 195.2 (1979), pages 453–9. ISSN: 0003-9861 (Print) 0003-9861 (Linking). URL: https://www.ncbi.nlm.nih.gov/pubmed/383019 (cited on pages 52, 73).

[207] M. Crompton, H. Ellinger, and A. Costi. "Inhibition by cyclosporin A of a Ca2+-dependent pore in heart mitochondria activated by inorganic phosphate and oxidative stress". In: *Biochem J* 255.1 (1988), pages 357–60. ISSN: 0264-6021 (Print) 0264-6021 (Linking). URL: https://www.ncbi.nlm.nih.gov/pubmed/3196322 (cited on pages 52, 73).

[208] D. R. Hunter, R. A. Haworth, and J. H. Southard. "Relationship between configuration, function, and permeability in calcium-treated mitochondria". In: *J Biol Chem* 251.16 (1976), pages 5069–77. ISSN: 0021-9258. URL: https://www.ncbi.nlm.nih.gov/pubmed/134035 (cited on page 52).

[209] K. H. Lim et al. “The effects of ischaemic preconditioning, diazoxide and 5 hydroxydecanoate on rat heart mitochondrial volume and respiration”. In: *J Physiol* 545.3 (2002). ISSN: 0022-3751. DOI: 10.1113/jphysiol.2002.031484. URL: https://www.ncbi.nlm.nih.gov/pubmed/12482899 (cited on pages 52, 128).

[210] S. Marchi et al. “Downregulation of the mitochondrial calcium uniporter by cancer-related miR-25”. In: *Curr Biol* 23.1 (2013), pages 58–63. ISSN: 1879-0445 (Electronic) 0960-9822 (Linking). DOI: 10.1016/j.cub.2012.11.026. URL: https://www.ncbi.nlm.nih.gov/pubmed/23246404 (cited on page 52).

[211] C. P. Baines and M. Gutiérrez-Aguilar. “The still uncertain identity of the channel-forming unit(s) of the mitochondrial permeability transition pore”. In: *Cell Calcium* 73 (2018), pages 121–130. ISSN: 1532-1991. DOI: 10.1016/j.ceca.2018.05.003. URL: https://www.ncbi.nlm.nih.gov/pubmed/29793100 (cited on pages 53, 61, 73, 76).

[212] C. Chinopoulos. “Mitochondrial permeability transition pore: Back to the drawing board”. In: *Neurochem Int* 117 (2018), pages 49–54. ISSN: 1872-9754 (Electronic) 0197-0186 (Linking). DOI: 10.1016/j.neuint.2017.06.010. URL: https://www.ncbi.nlm.nih.gov/pubmed/28647376 (cited on pages 53, 147, 148).

[213] L. C. Wollenman et al. “The effect of respiration buffer composition on mitochondrial metabolism and function”. In: *PLoS One* 12.11 (2017), e0187523. ISSN: 1932-6203 (Electronic) 1932-6203 (Linking). DOI: 10.1371/journal.pone.0187523. URL: https://www.ncbi.nlm.nih.gov/pubmed/29091971 (cited on pages 53–55).

[214] J. N. Bazil et al. “Modeling the calcium sequestration system in isolated guinea pig cardiac mitochondria”. In: *J Bioenerg Biomembr* 45.3 (2013), pages 177–88. ISSN: 1573-6881 (Electronic) 0145-479X (Linking). DOI: 10.1007/s10863-012-9488-2. URL: https://www.ncbi.nlm.nih.gov/pubmed/23180139 (cited on pages 59, 75, 154, 232).

[215] N. Brustovetsky et al. “Increased susceptibility of striatal mitochondria to calcium-induced permeability transition”. In: *J Neurosci* 23.12 (2003), pages 4858–67. ISSN: 1529-2401 (Electronic) 0270-6474 (Linking). DOI: 10.1523/JNEUROSCI.23-12-04858.2003. URL: https://www.ncbi.nlm.nih.gov/pubmed/12832508 (cited on page 59).

[216] J. D. Pandya, V. N. Nukala, and P. G. Sullivan. “Concentration dependent effect of calcium on brain mitochondrial bioenergetics and oxidative stress parameters”. In: *Front Neuroenergetics* 5 (2013), page 10. ISSN: 1662-6427 (Print) 1662-6427 (Linking). DOI: 10.3389/fnene.2013.00010. URL: https://www.ncbi.nlm.nih.gov/pubmed/24385963 (cited on page 59).

[217] M. Bonora et al. “Comprehensive analysis of mitochondrial permeability transition pore activity in living cells using fluorescence-imaging-based techniques”. In: *Nat Protoc* 11.6 (2016), pages 1067–80. ISSN: 1750-2799. DOI: 10.1038/nprot.2016.064. URL: https://www.ncbi.nlm.nih.gov/pubmed/27172167 (cited on pages 61, 76).

[218] A. M. McGee and C. P. Baines. “Phosphate is not an absolute requirement for the inhibitory effects of cyclosporin A or cyclophilin D deletion on mitochondrial permeability transition”. In: *Biochem J* 443.1 (2012), pages 185–91. ISSN: 1470-8728. DOI: 10.1042/BJ20111881. URL: https://www.ncbi.nlm.nih.gov/pubmed/22236255 (cited on page 61).

[219] F. Di Lisa et al. “Opening of the mitochondrial permeability transition pore causes depletion of mitochondrial and cytosolic NAD+ and is a causative event in the death of myocytes in postischemic reperfusion of the heart”. In: *J Biol Chem* 276.4 (2001), pages 2571–5. ISSN: 0021-9258. DOI: 10.1074/jbc.M006825200. URL: https://www.ncbi.nlm.nih.gov/pubmed/11073947 (cited on page 61).

[220] S. Chalmers and D. G. Nicholls. “The relationship between free and total calcium concentrations in the matrix of liver and brain mitochondria”. In: *J Biol Chem* 278.21 (2003), pages 19062–70. ISSN: 0021-9258 (Print) 0021-9258 (Linking). DOI: 10.1074/jbc.M212661200. URL: http://www.ncbi.nlm.nih.gov/pubmed/12660243 (cited on pages 62, 74).

[221] P. Bernardi. “Modulation of the mitochondrial cyclosporin A-sensitive permeability transition pore by the proton electrochemical gradient. Evidence that the pore can be opened by membrane depolarization”. In: *J Biol Chem* 267.13 (1992), pages 8834–9. ISSN: 0021-9258 (Print) 0021-9258 (Linking). URL: https://www.ncbi.nlm.nih.gov/pubmed/1374381 (cited on pages 62, 127).

[222] S. G. Wolf et al. “3D visualization of mitochondrial solid-phase calcium stores in whole cells”. In: *Elife* 6 (2017). ISSN: 2050-084X (Electronic) 2050-084X (Linking). DOI: 10.7554/eLife.29929. URL: https://www.ncbi.nlm.nih.gov/pubmed/29106371 (cited on pages 70, 75, 147).

[223] N. Eliaz and N. Metoki. “Calcium Phosphate Bioceramics: A Review of Their History, Structure, Properties, Coating Technologies and Biomedical Applications”. In: *Materials (Basel)* 10.4 (2017). ISSN: 1996-1944 (Print) 1996-1944 (Linking). DOI: 10.3390/ma10040334. URL: https://www.ncbi.nlm.nih.gov/pubmed/28772697 (cited on pages 70, 76).

[224] S. Jiang et al. “Amorphous calcium phosphate phase-mediated crystal nucleation kinetics and pathway”. In: *Faraday Discuss* 179 (2015), pages 451–61. ISSN: 1364-5498

(Electronic) 1359-6640 (Linking). DOI: 10.1039/c4fd00212a. URL: https://www.ncbi.nlm.nih.gov/pubmed/25876510 (cited on page 70).

[225] G. Mancardi et al. "Detection of Posner's clusters during calcium phosphate nucleation: a molecular dynamics study". In: *Journal of Materials Chemistry B* 7274.5 (2017), page 12. DOI: 10.1039/c7tb01199g. URL: https://pubs.rsc.org/en/content/articlepdf/2017/tb/c7tb01199g (cited on page 70).

[226] A. Onuma K.; Ito. "Cluster Growth Model for Hydroxyapatite". In: *Chem. Mater* 10 (1998), page 6. DOI: 10.1021/cm980062c (cited on page 70).

[227] P. Bernardi et al. "From ATP to PTP and Back: A Dual Function for the Mitochondrial ATP Synthase". In: *Circ Res* 116.11 (2015), pages 1850–62. ISSN: 1524-4571 (Electronic) 0009-7330 (Linking). DOI: 10.1161/CIRCRESAHA.115.306557. URL: https://www.ncbi.nlm.nih.gov/pubmed/25999424 (cited on page 73).

[228] M. Opalinska and H. Janska. "AAA Proteases: Guardians of Mitochondrial Function and Homeostasis". In: *Cells* 7.10 (2018). ISSN: 2073-4409 (Print) 2073-4409 (Linking). DOI: 10.3390/cells7100163. URL: https://www.ncbi.nlm.nih.gov/pubmed/30314276 (cited on page 74).

[229] D. Arnoult et al. "Release of OPA1 during apoptosis participates in the rapid and complete release of cytochrome c and subsequent mitochondrial fragmentation". In: *J Biol Chem* 280.42 (2005), pages 35742–50. ISSN: 0021-9258 (Print) 0021-9258 (Linking). DOI: 10.1074/jbc.M505970200. URL: https://www.ncbi.nlm.nih.gov/pubmed/16115883 (cited on page 74).

[230] C. Frezza et al. "OPA1 controls apoptotic cristae remodeling independently from mitochondrial fusion". In: *Cell* 126.1 (2006), pages 177–89. ISSN: 0092-8674. DOI: 10.1016/j.cell.2006.06.025. URL: https://www.ncbi.nlm.nih.gov/pubmed/16839885 (cited on page 74).

[231] C. Glytsou et al. "Optic Atrophy 1 Is Epistatic to the Core MICOS Component MIC60 in Mitochondrial Cristae Shape Control". In: *Cell Rep* 17.11 (2016), pages 3024–3034. ISSN: 2211-1247. DOI: 10.1016/j.celrep.2016.11.049. URL: https://www.ncbi.nlm.nih.gov/pubmed/27974214 (cited on page 74).

[232] L. Scorrano et al. "A distinct pathway remodels mitochondrial cristae and mobilizes cytochrome c during apoptosis". In: *Dev Cell* 2.1 (2002), pages 55–67. ISSN: 1534-5807. URL: https://www.ncbi.nlm.nih.gov/pubmed/11782314 (cited on pages 74, 77, 111).

[233] S. De La Fuente et al. “Spatial Separation of Mitochondrial Calcium Uptake and Extrusion for Energy-Efficient Mitochondrial Calcium Signaling in the Heart”. In: *Cell Rep* 24.12 (2018), 3099–3107 e4. ISSN: 2211-1247 (Electronic). DOI: 10.1016/j.celrep.2018.08.040. URL: https://www.ncbi.nlm.nih.gov/pubmed/30231993 (cited on page 75).

[234] V. Lukyanenko, A. Chikando, and W. J. Lederer. “Mitochondria in cardiomyocyte Ca2+ signaling”. In: *Int J Biochem Cell Biol* 41.10 (2009), pages 1957–71. ISSN: 1878-5875 (Electronic) 1357-2725 (Linking). DOI: 10.1016/j.biocel.2009.03.011. URL: https://www.ncbi.nlm.nih.gov/pubmed/19703657 (cited on pages 75, 84).

[235] M. Bonora et al. “Role of the c subunit of the FO ATP synthase in mitochondrial permeability transition”. In: *Cell Cycle* 12.4 (2013), pages 674–83. ISSN: 1551-4005 (Electronic) 1551-4005 (Linking). DOI: 10.4161/cc.23599. URL: https://www.ncbi.nlm.nih.gov/pubmed/23343770 (cited on pages 76, 113).

[236] M. Hessenberger et al. “Regulated membrane remodeling by Mic60 controls formation of mitochondrial crista junctions”. In: *Nat Commun* 8 (2017), page 15258. ISSN: 2041-1723 (Electronic) 2041-1723 (Linking). DOI: 10.1038/ncomms15258. URL: https://www.ncbi.nlm.nih.gov/pubmed/28561061 (cited on page 77).

[237] N. Ikon and R. O. Ryan. “Cardiolipin and mitochondrial cristae organization”. In: *Biochim Biophys Acta Biomembr* 1859.6 (2017), pages 1156–1163. ISSN: 0005-2736 (Print) 0005-2736 (Linking). DOI: 10.1016/j.bbamem.2017.03.013. URL: https://www.ncbi.nlm.nih.gov/pubmed/28336315 (cited on page 77).

[238] C. T. Brighton and R. M. Hunt. “Histochemical localization of calcium in growth plate mitochondria and matrix vesicles”. In: *Fed Proc* 35.2 (1976), pages 143–7. ISSN: 0014-9446 (Print) 0014-9446 (Linking). URL: https://www.ncbi.nlm.nih.gov/pubmed/1248647 (cited on page 78).

[239] E. Carafoli, C. S. Rossi, and A. L. Lehninger. “Cation and Anion Balance during Active Accumulation of Ca++ and Mg++ by Isolated Mitochondria”. In: *J Biol Chem* 239 (1964), pages 3055–61. ISSN: 0021-9258 (Print) 0021-9258 (Linking). URL: http://www.ncbi.nlm.nih.gov/pubmed/14217896 (cited on page 78).

[240] J. W. Greenawalt, C. S. Rossi, and A. L. Lehninger. “Effect of Active Accumulation of Calcium and Phosphate Ions on the Structure of Rat Liver Mitochondria”. In: *J Cell Biol* 23 (1964), pages 21–38. ISSN: 0021-9525. URL: https://www.ncbi.nlm.nih.gov/pubmed/14228516 (cited on page 78).

[241] T. Kristian et al. “Heterogeneity of the calcium-induced permeability transition in isolated non-synaptic brain mitochondria”. In: *J Neurochem* 83.6 (2002), pages 1297–

308. ISSN: 0022-3042 (Print) 0022-3042 (Linking). DOI: 10.1046/j.1471-4159.2002.01238.x. URL: https://www.ncbi.nlm.nih.gov/pubmed/12472884 (cited on page 78).

[242] T. Kristian et al. "Calcium-induced precipitate formation in brain mitochondria: composition, calcium capacity, and retention". In: *J Neurochem* 102.4 (2007), pages 1346–56. ISSN: 0022-3042 (Print) 0022-3042 (Linking). DOI: 10.1111/j.1471-4159.2007.04626.x. URL: http://www.ncbi.nlm.nih.gov/pubmed/17663756 (cited on page 78).

[243] W. C. Stanley, F. A. Recchia, and G. D. Lopaschuk. "Myocardial Substrate Metabolism in the Normal and Failing Heart". In: *Physiological reviews* 85.3 (2005), pages 1093–1129. DOI: 10.1152/physrev.00006.2004 (cited on page 81).

[244] B. Glancy and R. S. Balaban. "Role of Mitochondrial Ca2+ in the Regulation of Cellular Energetics". In: *Biochemistry* 51.14 (2012), pages 2959–2973. DOI: 10.1021/bi2018909 (cited on page 81).

[245] J. G. McCormack and R. M. Denton. "The role of intramitochondrial Ca2+ in the regulation of oxidative phosphorylation in mammalian tissues". In: *Biochemical Society transactions* 21.3 (1993), pages 793–799. DOI: 10.1042/bst0210793 (cited on page 81).

[246] A. P. Wescott et al. "Voltage-energized Calcium-sensitive ATP Production by Mitochondria". In: *Nature metabolism* 1.10 (2019), pages 975–984. DOI: 10.1038/s42255-019-0126-8 (cited on pages 81, 95, 98).

[247] S. Abou-Khalil, W. H. Abou-Khalil, and A. A. Yunis. "Inhibition by Ca2+ of oxidative phosphorylation in myeloid tumor mitochondria". In: *Archives of biochemistry and biophysics* 209.2 (1981), pages 460–464. DOI: 10.1016/0003-9861(81)90303-9 (cited on pages 81, 94).

[248] R. Moreno-Sánchez. "Inhibition of oxidative phosphorylation by a Ca2+-induced diminution of the adenine nucleotide translocator". In: *Biochimica et biophysica acta* 724.2 (1983), pages 278–285. DOI: 10.1016/0005-2728(83)90146-9 (cited on pages 81, 94).

[249] J. D. Pandya, V. N. Nukala, and P. G. Sullivan. "Concentration dependent effect of calcium on brain mitochondrial bioenergetics and oxidative stress parameters". In: *Frontiers in neuroenergetics* 5.NA (2013), pages 10–10. DOI: 10.3389/fnene.2013.00010 (cited on pages 81, 94).

[250] K. A. Rasbach et al. "Identification and optimization of a novel inhibitor of mitochondrial calpain 10". In: *Journal of medicinal chemistry* 52.1 (2008), pages 181–188. DOI: 10.1021/jm800735d (cited on pages 81, 94).

[251] I. Roman, A. F. Clark, and P. D. Swanson. "The interaction of calcium transport and ADP phosphorylation in brain mitochondria". In: *Membrane biochemistry* 4.1 (1981), pages 1–9. DOI: 10.3109/09687688109065419 (cited on pages 81, 94).

[252] J. Thompson et al. "Activation of mitochondrial calpain and increased cardiac injury: beyond AIF release". In: *American journal of physiology. Heart and circulatory physiology* 310.3 (2015), pages 376–84. DOI: 10.1152/ajpheart.00748.2015 (cited on pages 81, 94).

[253] R. F. W. Thorne and F. L. Bygrave. "Inhibition by calcium of adenine nucleotide translocation in mitochondria isolated from Ehrlich ascites tumour cells". In: *FEBS letters* 41.1 (1974), pages 118–121. DOI: 10.1016/0014-5793(74)80968-3 (cited on pages 81, 94).

[254] T. V. Vygodina et al. "Cytochrome c oxidase inhibition by calcium at physiological ionic composition of the medium: Implications for physiological significance of the effect". In: *Biochimica et biophysica acta. Bioenergetics* 1858.12 (2017), pages 982–990. DOI: 10.1016/j.bbabio.2017.08.011 (cited on pages 81, 94).

[255] L. C. Wollenman et al. "The effect of respiration buffer composition on mitochondrial metabolism and function". In: *PloS one* 12.11 (2017), e0187523–NA. DOI: 10.1371/journal.pone.0187523 (cited on pages 81, 85, 94, 95, 116).

[256] P. A. Bernard and R. S. Cockrell. "Calcium transport by rat brain mitochondria and oxidation of 2-oxoglutarate". In: *Biochimica et biophysica acta* 766.3 (1984), pages 549–553. DOI: 10.1016/0005-2728(84)90113-0 (cited on pages 81, 94).

[257] N. Brustovetsky et al. "Calcium-induced cytochrome c release from CNS mitochondria is associated with the permeability transition and rupture of the outer membrane". In: *Journal of neurochemistry* 80.2 (2002), pages 207–218. DOI: 10.1046/j.0022-3042.2001.00671.x (cited on pages 81, 94).

[258] Q. V. Duong et al. "Calcium Overload Decreases Net Free Radical Emission in Cardiac Mitochondria". In: *Mitochondrion* 51.NA (2020), pages 126–139. DOI: 10.1016/j.mito.2020.01.005 (cited on pages 81, 85, 94, 95, 97).

[259] M. M. Fagian, L. C. P. da Silva, and A. E. Vercesi. "Inhibition of oxidative phosphorylation by Ca2+ or Sr2+: A competition with Mg2+ for the formation of adenine nucleotide complexes". In: *Biochimica et biophysica acta* 852.2-3 (1986), pages 262–268. DOI: 10.1016/0005-2728(86)90231-8 (cited on pages 81, 94).

[260] B. D. Fink et al. “Regulation of ATP production: dependence on calcium concentration and respiratory state”. In: *American journal of physiology. Cell physiology* 313.2 (2017), pages C146–C153. DOI: 10.1152/ajpcell.00086.2017 (cited on pages 81, 94).

[261] L. Hardy et al. “Reoxygenation-dependent decrease in mitochondrial NADH:CoQ reductase (complex I) activity in the hypoxic/reoxygenated rat heart”. In: *The Biochemical journal* 274.1 (1991), pages 133–137. DOI: 10.1042/bj2740133 (cited on pages 81, 94).

[262] J. C. K. Lai and A. J. L. Cooper. “Brain alpha-ketoglutarate dehydrogenase complex: kinetic properties, regional distribution, and effects of inhibitors”. In: *Journal of neurochemistry* 47.5 (1986), pages 1376–1386. DOI: 10.1111/j.1471-4159.1986.tb00768.x (cited on pages 81, 94).

[263] J. C. K. Lai, J. C. DiLorenzo, and K.-F. R. Sheu. “Pyruvate dehydrogenase complex is inhibited in calcium-loaded cerebrocortical mitochondria”. In: *Neurochemical research* 13.11 (1988), pages 1043–1048. DOI: 10.1007/bf00973148 (cited on pages 81, 94).

[264] T. Bauer and E. Murphy. “Role of Mitochondrial Calcium and the Permeability Transition Pore in Regulating Cell Death”. In: *Circulation research* 126.2 (2020), pages 280–293. DOI: 10.1161/circresaha.119.316306 (cited on page 81).

[265] A. Rasola and P. Bernardi. “Mitochondrial permeability transition in Ca(2+)-dependent apoptosis and necrosis”. In: *Cell calcium* 50.3 (2011), pages 222–233. DOI: 10.1016/j.ceca.2011.04.007 (cited on page 81).

[266] J. O. Strubbe-Rivera et al. “The mitochondrial permeability transition phenomenon elucidated by cryo-EM reveals the genuine impact of calcium overload on mitochondrial structure and function”. In: *Scientific reports* 11.1 (2021), 1037–NA. DOI: 10.1038/s41598-020-80398-8 (cited on pages 81, 105).

[267] M. Liesa and O. S. Shirihai. “Mitochondrial dynamics in the regulation of nutrient utilization and energy expenditure”. In: *Cell metabolism* 17.4 (2013), pages 491–506. DOI: 10.1016/j.cmet.2013.03.002 (cited on page 82).

[268] C. Montemurro et al. “Cell cycle-related metabolism and mitochondrial dynamics in a replication-competent pancreatic beta-cell line”. In: *Cell cycle (Georgetown, Tex.)* 16.21 (2017), pages 2086–2099. DOI: 10.1080/15384101.2017.1361069 (cited on page 82).

[269] T. M. Moore et al. “The impact of exercise on mitochondrial dynamics and the role of Drp1 in exercise performance and training adaptations in skeletal muscle”. In: *Molec-*

ular metabolism 21.NA (2018), pages 51–67. DOI: 10.1016/j.molmet.2018.11.012 (cited on page 82).

[270] L. Pernas and L. Scorrano. "Mito-Morphosis: Mitochondrial Fusion, Fission, and Cristae Remodeling as Key Mediators of Cellular Function". In: *Annual review of physiology* 78.1 (2015), pages 505–531. DOI: 10.1146/annurev-physiol-021115-105011 (cited on page 82).

[271] A. K. Kondadi et al. "Cristae undergo continuous cycles of membrane remodelling in a MICOS-dependent manner". In: *EMBO reports* 21.3 (2020), 49776–NA. DOI: 10.15252/embr.201949776 (cited on page 82).

[272] S. Cogliati et al. "Mitochondrial Cristae Shape Determines Respiratory Chain Supercomplexes Assembly and Respiratory Efficiency". In: *Cell* 155.1 (2013), pages 160–171. DOI: 10.1016/j.cell.2013.08.032 (cited on page 82).

[273] K. Eydt et al. "Cristae architecture is determined by an interplay of the MICOS complex and the F1FO ATP synthase via Mic27 and Mic10". In: *Microbial cell (Graz, Austria)* 4.8 (2017), pages 259–272. DOI: 10.15698/mic2017.08.585 (cited on page 82).

[274] C. Glytsou et al. "Optic Atrophy 1 Is Epistatic to the Core MICOS Component MIC60 in Mitochondrial Cristae Shape Control". In: *Cell reports* 17.11 (2016), pages 3024–3034. DOI: 10.1016/j.celrep.2016.11.049 (cited on page 82).

[275] I. Kaurov et al. "The Diverged Trypanosome MICOS Complex as a Hub for Mitochondrial Cristae Shaping and Protein Import". In: *Current biology : CB* 28.21 (2018), 3393–3407.e5. DOI: 10.1016/j.cub.2018.09.008 (cited on page 82).

[276] C. Frezza et al. "OPA1 Controls Apoptotic Cristae Remodeling Independently from Mitochondrial Fusion". In: *Cell* 126.1 (2006), pages 177–189. DOI: 10.1016/j.cell.2006.06.025 (cited on page 82).

[277] T. Varanita et al. "The Opa1-Dependent Mitochondrial Cristae Remodeling Pathway Controls Atrophic, Apoptotic, and Ischemic Tissue Damage". In: *Cell metabolism* 21.6 (2015), pages 834–844. DOI: 10.1016/j.cmet.2015.05.007 (cited on page 82).

[278] K. M. Davies et al. "Structure of the yeast F1Fo-ATP synthase dimer and its role in shaping the mitochondrial cristae". In: *Proceedings of the National Academy of Sciences of the United States of America* 109.34 (2012), pages 13602–13607. DOI: 10.1073/pnas.1204593109 (cited on pages 82, 104).

[279] R. Quintana-Cabrera et al. “The cristae modulator Optic atrophy 1 requires mitochondrial ATP synthase oligomers to safeguard mitochondrial function”. In: *Nature communications* 9.1 (2018), pages 3399–3399. DOI: 10.1038/s41467-018-05655-x (cited on page 82).

[280] K. Salewskij et al. “The spatio-temporal organization of mitochondrial F1FO ATP synthase in cristae depends on its activity mode”. In: *Biochimica et biophysica acta. Bioenergetics* 1861.1 (2019), pages 148091–148091. DOI: 10.1016/j.bbabio.2019.148091 (cited on pages 82, 92).

[281] A. Olichon et al. “OPA1 alternate splicing uncouples an evolutionary conserved function in mitochondrial fusion from a vertebrate restricted function in apoptosis”. In: *Cell death and differentiation* 14.4 (2006), pages 682–692. DOI: 10.1038/sj.cdd.4402048 (cited on pages 82, 93).

[282] R. Kojima et al. “Maintenance of Cardiolipin and Crista Structure Requires Cooperative Functions of Mitochondrial Dynamics and Phospholipid Transport”. In: *Cell reports* 26.3 (2019), pages 518–528. DOI: 10.1016/j.celrep.2018.12.070 (cited on page 82).

[283] T. K. Rainbolt et al. “Reciprocal Degradation of YME1L and OMA1 Adapts Mitochondrial Proteolytic Activity during Stress”. In: *Cell reports* 14.9 (2016), pages 2041–2049. DOI: 10.1016/j.celrep.2016.02.011 (cited on page 82).

[284] C. Merkwirth et al. “Prohibitins control cell proliferation and apoptosis by regulating OPA1-dependent cristae morphogenesis in mitochondria”. In: *Genes and development* 22.4 (2008), pages 476–488. DOI: 10.1101/gad.460708 (cited on page 82).

[285] T. Tatsuta, K. Model, and T. Langer. “Formation of Membrane-bound Ring Complexes by Prohibitins in Mitochondria”. In: *Molecular biology of the cell* 16.1 (2004), pages 248–259. DOI: 10.1091/mbc.e04-09-0807 (cited on page 82).

[286] J. Demongeot et al. “An open issue: The inner mitochondrial membrane (IMM) as a free boundary problem”. In: *Biochimie* 89.9 (2007), pages 1049–1057. DOI: 10.1016/j.biochi.2007.04.009 (cited on page 83).

[287] Z. Y. Tam, Y. H. Cai, and R. Gunawan. “Elucidating Cytochrome c Release from Mitochondria: Insights from an In Silico Three-Dimensional Model”. In: *Biophysical journal* 99.10 (2010), pages 3155–3163. DOI: 10.1016/j.bpj.2010.09.041 (cited on page 83).

[288] C. E. J. Dieteren et al. “Solute diffusion is hindered in the mitochondrial matrix”. In: *Proceedings of the National Academy of Sciences of the United States of America* 108.21 (2011), pages 8657–8662. DOI: 10.1073/pnas.1017581108 (cited on page 83).

[289] F. Elías-Wolff et al. “Curvature sensing by cardiolipin in simulated buckled membranes”. In: *Soft matter* 15.4 (2019), pages 792–802. DOI: 10.1039/c8sm02133c (cited on page 83).

[290] N. Khalifat et al. “Lipid packing variations induced by pH in cardiolipin-containing bilayers: the driving force for the cristae-like shape instability”. In: *Biochimica et biophysica acta* 1808.11 (2011), pages 2724–2733. DOI: 10.1016/j.bbamem.2011.07.013 (cited on page 83).

[291] N. Khalifat et al. “Membrane deformation under local pH gradient: mimicking mitochondrial cristae dynamics”. In: *Biophysical journal* 95.10 (2008), pages 4924–4933. DOI: 10.1529/biophysj.108.136077 (cited on page 83).

[292] D. H. Song et al. “Biophysical significance of the inner mitochondrial membrane structure on the electrochemical potential of mitochondria”. In: *Physical review. E, Statistical, nonlinear, and soft matter physics* 88.6 (2013), pages 062723–062723. DOI: 10.1103/physreve.88.062723 (cited on page 83).

[293] D. H. Song et al. “Effects of Local pH on the Formation and Regulation of Cristae Morphologies”. In: *Physical review. E, Statistical, nonlinear, and soft matter physics* 90.2 (2014), 022702–NA. DOI: 10.1103/physreve.90.022702 (cited on page 83).

[294] A. A. Stuchebrukhov et al. “Kinetic advantage of forming respiratory supercomplexes”. In: *Biochimica et biophysica acta. Bioenergetics* 1861.7 (2020), pages 148193–148193. DOI: 10.1016/j.bbabio.2020.148193 (cited on pages 83, 94, 97).

[295] V. M. Sukhorukov and J. Bereiter-Hahn. “Anomalous Diffusion Induced by Cristae Geometry in the Inner Mitochondrial Membrane”. In: *PloS one* 4.2 (2009), e4604–NA. DOI: 10.1371/journal.pone.0004604 (cited on pages 83, 94).

[296] M. E. Gurtin. “Generalized Ginzburg-Landau and Cahn-Hilliard equations based on a microforce balance”. In: *Physica D: Nonlinear Phenomena* 92.3 (1996), pages 178–192. DOI: 10.1016/0167-2789(95)00173-5 (cited on page 83).

[297] J. Kim, K. Kang, and J. Lowengrub. “Conservative multigrid methods for Cahn-Hilliard fluids”. In: *Journal of Computational Physics* 193.2 (2004), pages 511–543. DOI: 10.1016/j.jcp.2003.07.035 (cited on page 83).

[298] J. Shen and X. Yang. "Numerical approximations of Allen-Cahn and Cahn-Hilliard equations". In: *Discrete and Continuous Dynamical Systems - A* 28.4 (2010), pages 1669–1691. DOI: 10.3934/dcds.2010.28.1669 (cited on page 83).

[299] G. W. Wei and Y. Zhou. "Variational methods for biomolecular modeling. In Variational Methods in Molecular Modeling". In: *Springer* (2017), pages 181–221 (cited on page 83).

[300] G. Landolfi. "New results on the Canham–Helfrich membrane model via the generalized Weierstrass representation". In: *Journal of Physics A: Mathematical and General* 36.48 (2003), pages 11937–11954. DOI: 10.1088/0305-4470/36/48/003 (cited on page 83).

[301] I. S. Aranson and L. Kramer. "The world of the complex Ginzburg-Landau equation". In: *Reviews of Modern Physics* 74.1 (2002), pages 99–143. DOI: 10.1103/revmodphys.74.99 (cited on page 83).

[302] C. H. Taubes. "The existence of a non-minimal solution to the SU (2) Yang-Mills-Higgs equations on ? 3 . Part I". In: *Communications in Mathematical Physics* 86.2 (1982), pages 257–298. DOI: 10.1007/bf01206014 (cited on page 83).

[303] S. Dai and K. Promislow. "Geometric evolution of bilayers under the functionalized cahn-hilliard equation". In: *Proceedings of the Royal Society A: Mathematical, Physical and Engineering Sciences* 469.2153 (2013), pages 20120505–20120505. DOI: 10.1098/rspa.2012.0505 (cited on page 83).

[304] A. Novick-Cohen and L. A. Segel. "Nonlinear aspects of the Cahn-Hilliard equation". In: *Physica D: Nonlinear Phenomena* 10.3 (1984), pages 277–298. DOI: 10.1016/0167-2789(84)90180-5 (cited on page 84).

[305] R. L. Pego. "Front migration in the nonlinear Cahn-Hilliard equation". In: *Proc. R. Soc. Lond. A Math. Phys. Sci.* 422 (1997), pages 261–278 (cited on page 84).

[306] S. Guan, C. H. Lai, and G.-W. Wei. "Geometry and boundary control of pattern formation and competition". In: *Physica D: Nonlinear Phenomena* 176.1 (2003), pages 19–43. DOI: 10.1016/s0167-2789(02)00737-6 (cited on page 84).

[307] P. W. Bates and P. C. Fife. "The dynamics of nucleation for the Cahn-Hilliard equation". In: *SIAM Journal on Applied Mathematics* 53.4 (1993), pages 990–1008. DOI: 10.1137/0153049 (cited on page 84).

[308] L. Gránásy and D. W. Oxtoby. "Cahn–Hilliard theory with triple-parabolic free energy. II. Nucleation and growth in the presence of a metastable crystalline phase". In: *The*

Journal of Chemical Physics 112.5 (2000), pages 2410–2419. DOI: 10.1063/1.480807 (cited on page 84).

[309] P. Boyanova and M. Neytcheva. "Efficient numerical solution of discrete multicomponent Cahn-Hilliard systems". In: *Computers and Mathematics with Applications* 67.1 (2014), pages 106–121. DOI: 10.1016/j.camwa.2013.10.013 (cited on page 84).

[310] Y. Li, J. I. Choi, and J. Kim. "Multi-component Cahn–Hilliard system with different boundary conditions in complex domains". In: *Journal of Computational Physics* 323.NA (2016), pages 1–16. DOI: 10.1016/j.jcp.2016.07.017 (cited on page 84).

[311] J. R. Kremer, D. N. Mastronarde, and J. R. McIntosh. "Computer Visualization of Three-Dimensional Image Data Using IMOD". In: *Journal of structural biology* 116.1 (1996), pages 71–76. DOI: 10.1006/jsbi.1996.0013 (cited on page 88).

[312] L. Azzolin et al. "The mitochondrial permeability transition from yeast to mammals". In: *FEBS letters* 584.12 (2010), pages 2504–2509. DOI: 10.1016/j.febslet.2010.04.023 (cited on page 95).

[313] P. Bernardi and F. Di Lisa. "The mitochondrial permeability transition pore: Molecular nature and role as a target in cardioprotection". In: *Journal of molecular and cellular cardiology* 78.NA (2014), pages 100–106. DOI: 10.1016/j.yjmcc.2014.09.023 (cited on page 95).

[314] S. Hurst, J. B. Hoek, and S.-S. Sheu. "Mitochondrial Ca(2+) and regulation of the permeability transition pore". In: *Journal of bioenergetics and biomembranes* 49.1 (2016), pages 27–47. DOI: 10.1007/s10863-016-9672-x (cited on page 95).

[315] R. J. Parks, E. Murphy, and J. C. Liu. "Mitochondrial permeability transition pore and calcium handling." In: *Methods Mol. Biol.* 1782 (2018), pages 187–196 (cited on page 95).

[316] C. A. Mannella. "Structure and dynamics of the mitochondrial inner membrane cristae". In: *Biochimica et biophysica acta* 1763.5 (2006), pages 542–548. DOI: 10.1016/j.bbamcr.2006.04.006 (cited on page 102).

[317] C. R. Hackenbrock. "Ultrastructural Bases for Metabolically Linked Mechanical Activity in Mitochondria I. Reversible Ultrastructural Changes with Change in Metabolic Steady State in Isolated Liver Mitochondria". In: *The Journal of cell biology* 30.2 (1966), pages 269–297. DOI: 10.1083/jcb.30.2.269 (cited on page 103).

[318] C. R. Hackenbrock. “Energy-linked ultrastructural transformations in isolated liver mitochondria and mitoplasts. Preservation of configurations by freeze-cleaving compared to chemical fixation”. In: *The Journal of cell biology* 53.2 (1972), pages 450–465. DOI: 10.1083/jcb.53.2.450 (cited on page 103).

[319] P. Mitchell. “Chemiosmotic coupling in oxidative and photosynthetic phosphorylation”. In: *Biochimica et biophysica acta* 1807.12 (2011), pages 1507–1538. DOI: 10.1016/j.bbabio.2011.09.018 (cited on page 103).

[320] B. A. Scalettar, J. R. Abney, and C. R. Hackenbrock. “Dynamics, structure, and function are coupled in the mitochondrial matrix”. In: *Proceedings of the National Academy of Sciences of the United States of America* 88.18 (1991), pages 8057–8061. DOI: 10.1073/pnas.88.18.8057 (cited on page 103).

[321] H. Rampelt et al. “Role of the mitochondrial contact site and cristae organizing system in membrane architecture and dynamics”. In: *Biochimica et biophysica acta. Molecular cell research* 1864.4 (2016), pages 737–746. DOI: 10.1016/j.bbamcr.2016.05.020 (cited on page 104).

[322] F. P. Prince. “Lamellar and tubular associations of the mitochondrial cristae: unique forms of the cristae present in steroid-producing cells”. In: *Mitochondrion* 1.4 (2002), pages 381–389. DOI: 10.1016/s1567-7249(01)00038-1 (cited on page 104).

[323] M. Harner et al. “An evidence based hypothesis on the existence of two pathways of mitochondrial crista formation”. In: *eLife* 5.NA (2016), 18853–NA. DOI: 10.7554/elife.18853 (cited on page 104).

[324] B. Gottschalk et al. “MICU1 controls cristae junction and spatially anchors mitochondrial Ca2+ uniporter complex”. In: *Nature communications* 10.1 (2019), pages 3732–3732. DOI: 10.1038/s41467-019-11692-x (cited on pages 104, 105).

[325] Y. Kushnareva et al. “Loss of OPA1 disturbs cellular calcium homeostasis and sensitizes for excitotoxicity”. In: *Cell death and differentiation* 20.2 (2012), pages 353–365. DOI: 10.1038/cdd.2012.128 (cited on page 105).

[326] S. Modi et al. “Miro clusters regulate ER-mitochondria contact sites and link cristae organization to the mitochondrial transport machinery”. In: *Nature communications* 10.1 (2019), pages 4399–4399. DOI: 10.1038/s41467-019-12382-4 (cited on page 105).

[327] M. Waldeck-Weiermair et al. “Rearrangement of MICU1 multimers for activation of MCU is solely controlled by cytosolic Ca 2”. In: *Scientific reports* 5.1 (2015). DOI: 10.1038/srep15602 (cited on page 105).

[328] L.-J. Wang et al. “Drosophila MICOS knockdown impairs mitochondrial structure and function and promotes mitophagy in muscle tissue”. In: *Biology open* 9.12 (2020), NA–NA. DOI: 10.1242/bio.054262 (cited on page 105).

[329] H. Rampelt et al. “Role of the mitochondrial contact site and cristae organizing system in membrane architecture and dynamics”. In: *Biochim Biophys Acta Mol Cell Res* 1864.4 (2017), pages 737–746. ISSN: 0167-4889 (Print) 0167-4889 (Linking). DOI: 10.1016/j.bbamcr.2016.05.020. URL: https://www.ncbi.nlm.nih.gov/pubmed/27614134 (cited on pages 110, 124).

[330] T. D. Pham et al. “Cristae remodeling causes acidification detected by integrated graphene sensor during mitochondrial outer membrane permeabilization”. In: *Sci Rep* 6 (2016), page 35907. ISSN: 2045-2322 (Electronic) 2045-2322 (Linking). DOI: 10.1038/srep35907. URL: https://www.ncbi.nlm.nih.gov/pubmed/27786282 (cited on page 111).

[331] M. Song et al. “Mitochondrial fission and fusion factors reciprocally orchestrate mitophagic culling in mouse hearts and cultured fibroblasts”. In: *Cell Metab* 21.2 (2015), pages 273–286. ISSN: 1932-7420 (Electronic) 1550-4131 (Print) 1550-4131 (Linking). DOI: 10.1016/j.cmet.2014.12.011. URL: https://www.ncbi.nlm.nih.gov/pubmed/25600785 (cited on pages 111, 112).

[332] H. M. Cho and W. Sun. “Molecular cross talk among the components of the regulatory machinery of mitochondrial structure and quality control”. In: *Exp Mol Med* 52.5 (2020), pages 730–737. ISSN: 2092-6413 (Electronic) 1226-3613 (Print) 1226-3613 (Linking). DOI: 10.1038/s12276-020-0434-9. URL: https://www.ncbi.nlm.nih.gov/pubmed/32398745 (cited on pages 111, 113).

[333] C. R. Chang et al. “A lethal de novo mutation in the middle domain of the dynamin-related GTPase Drp1 impairs higher order assembly and mitochondrial division”. In: *J Biol Chem* 285.42 (2010), pages 32494–503. ISSN: 1083-351X (Electronic) 0021-9258 (Print) 0021-9258 (Linking). DOI: 10.1074/jbc.M110.142430. URL: https://www.ncbi.nlm.nih.gov/pubmed/20696759 (cited on pages 111, 112).

[334] H. Xian and Y.-C. Liou. “Functions of outer mitochondrial membrane proteins: mediating the crosstalk between mitochondrial dynamics and mitophagy”. In: *Cell Death Differentiation* 28.3 (2021), pages 827–842. ISSN: 1476-5403. DOI: 10.1038/s41418-020-00657-z. URL: https://www.ncbi.nlm.nih.gov/pubmed/33208889 (cited on page 112).

[335] J. M. Quiles and A. B. Gustafsson. “The role of mitochondrial fission in cardiovascular health and disease”. In: *Nat Rev Cardiol* 19.11 (2022), pages 723–736. ISSN: 1759-5010 (Electronic) 1759-5002 (Linking). DOI: 10.1038/s41569-022-00703-y. URL: https://www.ncbi.nlm.nih.gov/pubmed/35523864 (cited on page 112).

[336] H. Otera et al. “Mff is an essential factor for mitochondrial recruitment of Drp1 during mitochondrial fission in mammalian cells”. In: *J Cell Biol* 191.6 (2010), pages 1141–58. ISSN: 1540-8140 (Electronic) 0021-9525 (Print) 0021-9525 (Linking). DOI: 10.1083/jcb.201007152. URL: https://www.ncbi.nlm.nih.gov/pubmed/21149567 (cited on page 112).

[337] W. Song et al. “Mutant huntingtin binds the mitochondrial fission GTPase dynamin-related protein-1 and increases its enzymatic activity”. In: *Nat Med* 17.3 (2011). ISSN: 1546-170X (Electronic) 1078-8956 (Print) 1078-8956 (Linking). DOI: 10.1038/nm.2313. URL: https://www.ncbi.nlm.nih.gov/pubmed/21336284 (cited on page 112).

[338] Y. Ikeda et al. “Endogenous Drp1 mediates mitochondrial autophagy and protects the heart against energy stress”. In: *Circ Res* 116.2 (2015), pages 264–78. ISSN: 1524-4571 (Electronic) 0009-7330 (Linking). DOI: 10.1161/CIRCRESAHA.116.303356. URL: https://www.ncbi.nlm.nih.gov/pubmed/25332205 (cited on page 112).

[339] Z. Song et al. “Mitofusins and OPA1 mediate sequential steps in mitochondrial membrane fusion”. In: *Mol Biol Cell* 20.15 (2009), pages 3525–32. ISSN: 1939-4586 (Electronic) 1059-1524 (Print) 1059-1524 (Linking). DOI: 10.1091/mbc.e09-03-0252. URL: https://www.ncbi.nlm.nih.gov/pubmed/19477917 (cited on page 113).

[340] S. Jang and S. Javadov. “OPA1 regulates respiratory supercomplexes assembly: The role of mitochondrial swelling”. In: *Mitochondrion* 51 (2020), pages 30–39. ISSN: 1872-8278 (Electronic) 1567-7249 (Print) 1567-7249 (Linking). DOI: 10.1016/j.mito.2019.11.006. URL: https://www.ncbi.nlm.nih.gov/pubmed/31870826 (cited on pages 113, 114).

[341] B. Gottschalk, C. T. Madreiter-Sokolowski, and W. F. Graier. “Cristae junction as a fundamental switchboard for mitochondrial ion signaling and bioenergetics”. In: *Cell Calcium* 101 (2022), page 102517. ISSN: 1532-1991 (Electronic) 0143-4160 (Linking). DOI: 10.1016/j.ceca.2021.102517. URL: https://www.ncbi.nlm.nih.gov/pubmed/34915234 (cited on pages 113, 114).

[342] P. Mishra et al. “Proteolytic cleavage of Opa1 stimulates mitochondrial inner membrane fusion and couples fusion to oxidative phosphorylation”. In: *Cell Metab* 19.4 (2014), pages 630–41. ISSN: 1932-7420 (Electronic) 1550-4131 (Print) 1550-4131 (Linking). DOI: 10.1016/j.cmet.2014.03.011. URL: https://www.ncbi.nlm.nih.gov/pubmed/24703695 (cited on page 113).

[343] B. Gottschalk et al. “MICU1 controls cristae junction and spatially anchors mitochondrial Ca(2+) uniporter complex”. In: *Nat Commun* 10.1 (2019), page 3732. ISSN: 2041-1723 (Electronic) 2041-1723 (Linking). DOI: 10.1038/s41467-019-11692-x. URL: https://www.ncbi.nlm.nih.gov/pubmed/31427612 (cited on pages 114, 115).

[344] W. Basu Ball, J. K. Neff, and V. M. Gohil. "The role of nonbilayer phospholipids in mitochondrial structure and function". In: *FEBS Lett* 592.8 (2018), pages 1273–1290. ISSN: 1873-3468 (Electronic) 0014-5793 (Print) 0014-5793 (Linking). DOI: 10.1002/1873-3468.12887. URL: https://www.ncbi.nlm.nih.gov/pubmed/29067684 (cited on page 114).

[345] A. N. Antony et al. "MICU1 regulation of mitochondrial Ca(2+) uptake dictates survival and tissue regeneration". In: *Nat Commun* 7 (2016), page 10955. ISSN: 2041-1723 (Electronic) 2041-1723 (Linking). DOI: 10.1038/ncomms10955. URL: https://www.ncbi.nlm.nih.gov/pubmed/26956930 (cited on page 115).

[346] Z. Dong et al. "Mitochondrial Ca(2+) Uniporter Is a Mitochondrial Luminal Redox Sensor that Augments MCU Channel Activity". In: *Mol Cell* 65.6 (2017), 1014–1028 e7. ISSN: 1097-4164 (Electronic) 1097-2765 (Print) 1097-2765 (Linking). DOI: 10.1016/j.molcel.2017.01.032. URL: https://www.ncbi.nlm.nih.gov/pubmed/28262504 (cited on page 115).

[347] D. Arnoult et al. "Release of OPA1 during apoptosis participates in the rapid and complete release of cytochrome c and subsequent mitochondrial fragmentation". In: *J Biol Chem* 280.42 (2005), pages 35742–50. ISSN: 0021-9258 (Print) 0021-9258 (Linking). DOI: 10.1074/jbc.M505970200. URL: https://www.ncbi.nlm.nih.gov/pubmed/16115883 (cited on page 125).

[348] E. J. Benjamin et al. "Heart Disease and Stroke Statistics-2019 Update: A Report From the American Heart Association". In: *Circulation* 139.10 (2019), e56–e528. ISSN: 1524-4539. DOI: 10.1161/CIR.0000000000000659. URL: https://www.ncbi.nlm.nih.gov/pubmed/30700139 (cited on page 127).

[349] C. D. Fryar, T. C. Chen, and X. Li. "Prevalence of uncontrolled risk factors for cardiovascular disease: United States, 1999-2010". In: *NCHS Data Brief* 103 (2012), pages 1–8. ISSN: 1941-4927. URL: https://www.ncbi.nlm.nih.gov/pubmed/23101933 (cited on page 127).

[350] M. A. Konstam. "Heart Failure Costs, Minority Populations, and Outcomes: Targeting Health Status, Not Utilization, to Bend the Cost-Effectiveness Curve". In: *JACC Heart Fail* 6.5 (2018), pages 398–400. ISSN: 2213-1787. DOI: 10.1016/j.jchf.2018.02.005. URL: https://www.ncbi.nlm.nih.gov/pubmed/29655823 (cited on page 127).

[351] E. Braunwald and R. A. Kloner. "Myocardial reperfusion: a double-edged sword?" In: *J Clin Invest* 76.5 (1985), pages 1713–9. ISSN: 0021-9738. DOI: 10.1172/JCI112160. URL: https://www.ncbi.nlm.nih.gov/pubmed/4056048 (cited on page 127).

[352] A. Johri and M. F. Beal. "Mitochondrial dysfunction in neurodegenerative diseases". In: *J Pharmacol Exp Ther* 342.3 (2012), pages 619–30. ISSN: 1521-0103. DOI: 10.1124/jpet.112.192138. URL: https://www.ncbi.nlm.nih.gov/pubmed/22700435 (cited on page 127).

[353] G. Lascaratos et al. "Mitochondrial dysfunction in glaucoma: understanding genetic influences". In: *Mitochondrion* 12.2 (2012), pages 202–12. ISSN: 1872-8278. DOI: 10.1016/j.mito.2011.11.004. URL: https://www.ncbi.nlm.nih.gov/pubmed/22138560 (cited on page 127).

[354] P. Newsholme, C. Gaudel, and M. Krause. "Mitochondria and diabetes. An intriguing pathogenetic role". In: *Adv Exp Med Biol* 942 (2012), pages 235–47. ISSN: 0065-2598. DOI: 10.1007/978-94-007-2869-1_10. URL: https://www.ncbi.nlm.nih.gov/pubmed/22399425 (cited on page 127).

[355] B. ORourke, J. E. Van Eyk, and D. B. Foster. "Mitochondrial protein phosphorylation as a regulatory modality: implications for mitochondrial dysfunction in heart failure". In: *Congest Heart Fail* 17.6 (2011), pages 269–82. ISSN: 1751-7133. DOI: 10.1111/j.1751-7133.2011.00266.x. URL: https://www.ncbi.nlm.nih.gov/pubmed/22103918 (cited on page 127).

[356] P. S. Puri et al. "Alterations in energy metabolism and ultrastructure upon reperfusion of the ischemic myocardium after coronary occlusion". In: *Am J Cardiol* 36.2 (1975), pages 234–43. ISSN: 0002-9149. URL: https://www.ncbi.nlm.nih.gov/pubmed/1080352 (cited on page 127).

[357] D. M. Small et al. "Oxidative stress, anti-oxidant therapies and chronic kidney disease". In: *Nephrology (Carlton)* 17.4 (2012), pages 311–21. ISSN: 1440-1797. DOI: 10.1111/j.1440-1797.2012.01572.x. URL: https://www.ncbi.nlm.nih.gov/pubmed/22288610 (cited on page 127).

[358] A. K. Camara, M. Bienengraeber, and D. F. Stowe. "Mitochondrial approaches to protect against cardiac ischemia and reperfusion injury". In: *Front Physiol* 2 (2011), page 13. ISSN: 1664-042X. DOI: 10.3389/fphys.2011.00013. URL: https://www.ncbi.nlm.nih.gov/pubmed/21559063 (cited on page 127).

[359] R. Chandra, F. G. Baumann, and R. A. Goldman. "Myocardial reperfusion, a cause of ischemic injury during cardiopulmonary bypass". In: *Surgery* 80.2 (1976), pages 266–76. ISSN: 0039-6060. URL: https://www.ncbi.nlm.nih.gov/pubmed/941098 (cited on page 127).

[360] J. R. Colca and D. L. Feinstein. "Altering mitochondrial dysfunction as an approach to treating Alzheimers disease". In: *Adv Pharmacol* 64 (2012), pages 155–76. ISSN: 1557-8925. DOI: 10.1016/B978-0-12-394816-8.00005-2. URL: https://www.ncbi.nlm.nih.gov/pubmed/22840747 (cited on page 127).

[361] M. Cozzolino and M. T. Carrì. "Mitochondrial dysfunction in ALS". In: *Prog Neurobiol* 97.2 (2012), pages 54–66. ISSN: 1873-5118. DOI: 10.1016/j.pneurobio.2011.06.003. URL: https://www.ncbi.nlm.nih.gov/pubmed/21827820 (cited on page 127).

[362] K. A. Fox, S. R. Bergmann, and B. E. Sobel. "Pathophysiology of myocardial reperfusion". In: *Annu Rev Med* 36 (1985), pages 125–44. ISSN: 0066-4219. DOI: 10.1146/annurev.me.36.020185.001013. URL: https://www.ncbi.nlm.nih.gov/pubmed/2859828 (cited on page 127).

[363] I. Grattagliano et al. "Role of mitochondria in nonalcoholic fatty liver disease–from origin to propagation". In: *Clin Biochem* 45.9 (2012), pages 610–8. ISSN: 1873-2933. DOI: 10.1016/j.clinbiochem.2012.03.024. URL: https://www.ncbi.nlm.nih.gov/pubmed/22484459 (cited on page 127).

[364] D. J. Hausenloy and D. M. Yellon. "Myocardial ischemia-reperfusion injury: a neglected therapeutic target". In: *J Clin Invest* 123.1 (2013), pages 92–100. ISSN: 1558-8238. DOI: 10.1172/JCI62874. URL: https://www.ncbi.nlm.nih.gov/pubmed/23281415 (cited on page 127).

[365] R. B. JENNINGS et al. "Myocardial necrosis induced by temporary occlusion of a coronary artery in the dog". In: *Arch Pathol* 70 (1960), pages 68–78. ISSN: 0363-0153. URL: https://www.ncbi.nlm.nih.gov/pubmed/14407094 (cited on page 127).

[366] D. J. Hausenloy and D. M. Yellon. "Time to take myocardial reperfusion injury seriously". In: *N Engl J Med* 359.5 (2008), pages 518–20. ISSN: 1533-4406. DOI: 10.1056/NEJMe0803746. URL: https://www.ncbi.nlm.nih.gov/pubmed/18669431 (cited on page 127).

[367] D. M. Yellon and D. J. Hausenloy. "Myocardial reperfusion injury". In: *N Engl J Med* 357.11 (2007), pages 1121–35. ISSN: 1533-4406. DOI: 10.1056/NEJMra071667. URL: https://www.ncbi.nlm.nih.gov/pubmed/17855673 (cited on pages 127, 128).

[368] D. J. Hausenloy et al. "Ischaemic conditioning and targeting reperfusion injury: a 30 year voyage of discovery". In: *Basic Res Cardiol* 111.6 (2016), page 70. ISSN: 1435-1803. DOI: 10.1007/s00395-016-0588-8. URL: https://www.ncbi.nlm.nih.gov/pubmed/27766474 (cited on pages 127, 128).

[369] A. P. Halestrap. "A pore way to die: the role of mitochondria in reperfusion injury and cardioprotection". In: *Biochem Soc Trans* 38.4 (2010), pages 841–60. ISSN: 1470-8752. DOI: 10.1042/BST0380841. URL: https://www.ncbi.nlm.nih.gov/pubmed/20658967 (cited on page 127).

[370] R. Bolli et al. "Myocardial protection at a crossroads: the need for translation into clinical therapy". In: *Circ Res* 95.2 (2004), pages 125–34. ISSN: 1524-4571. DOI: 10.1161/01.RES.0000137171.97172.d7. URL: https://www.ncbi.nlm.nih.gov/pubmed/15271864 (cited on page 127).

[371] H. Bulluck, D. M. Yellon, and D. J. Hausenloy. "Reducing myocardial infarct size: challenges and future opportunities". In: *Heart* 102.5 (2016), pages 341–8. ISSN: 1468-201X. DOI: 10.1136/heartjnl-2015-307855. URL: https://www.ncbi.nlm.nih.gov/pubmed/26674987 (cited on pages 127, 128).

[372] R. A. Haworth and D. R. Hunter. "The Ca2+-induced membrane transition in mitochondria. II. Nature of the Ca2+ trigger site". In: *Arch Biochem Biophys* 195.2 (1979), pages 460–7. ISSN: 0003-9861. DOI: 10.1016/0003-9861(79)90372-2. URL: https://www.ncbi.nlm.nih.gov/pubmed/38751 (cited on page 128).

[373] D. R. Hunter and R. A. Haworth. "The Ca2+-induced membrane transition in mitochondria. I. The protective mechanisms". In: *Arch Biochem Biophys* 195.2 (1979), pages 453–9. ISSN: 0003-9861. DOI: 10.1016/0003-9861(79)90371-0. URL: https://www.ncbi.nlm.nih.gov/pubmed/383019 (cited on page 128).

[374] D. R. Hunter and R. A. Haworth. "The Ca2+-induced membrane transition in mitochondria. III. Transitional Ca2+ release". In: *Arch Biochem Biophys* 195.2 (1979), pages 468–77. ISSN: 0003-9861. DOI: 10.1016/0003-9861(79)90373-4. URL: https://www.ncbi.nlm.nih.gov/pubmed/112926 (cited on page 128).

[375] C. Chinopoulos. "Mitochondrial permeability transition pore: Back to the drawing board". In: *Neurochem Int* 117 (2018), pages 49–54. ISSN: 1872-9754. DOI: 10.1016/j.neuint.2017.06.010. URL: https://www.ncbi.nlm.nih.gov/pubmed/28647376 (cited on page 128).

[376] E. J. Griffiths and A. P. Halestrap. "Mitochondrial non-specific pores remain closed during cardiac ischaemia, but open upon reperfusion". In: *Biochem J* 307 (Pt 1).Pt 1 (1995), pages 93–8. ISSN: 0264-6021. DOI: 10.1042/bj3070093. URL: https://www.ncbi.nlm.nih.gov/pubmed/7717999 (cited on page 128).

[377] E. T. Chouchani et al. "Ischaemic accumulation of succinate controls reperfusion injury through mitochondrial ROS". In: *Nature* 515.7527 (2014), pages 431–435. ISSN: 1476-

4687. DOI: 10.1038/nature13909. URL: https://www.ncbi.nlm.nih.gov/pubmed/25383517 (cited on page 128).

[378] H. N. Fridolfsson et al. "Mitochondria-localized caveolin in adaptation to cellular stress and injury". In: *FASEB J* 26.11 (2012), pages 4637–49. ISSN: 1530-6860. DOI: 10.1096/fj.12-215798. URL: https://www.ncbi.nlm.nih.gov/pubmed/22859372 (cited on page 128).

[379] G. Campo et al. "Data on administration of cyclosporine, nicorandil, metoprolol on reperfusion related outcomes in ST-segment Elevation Myocardial Infarction treated with percutaneous coronary intervention". In: *Data Brief* 14 (2017), pages 197–205. ISSN: 2352-3409 (Print) 2352-3409 (Electronic) 2352-3409 (Linking). DOI: 10.1016/j.dib.2017.07.033. URL: https://www.ncbi.nlm.nih.gov/pubmed/28795098 (cited on page 129).

[380] T. T. Cung et al. "Cyclosporine before PCI in Patients with Acute Myocardial Infarction". In: *N Engl J Med* 373.11 (2015), pages 1021–31. ISSN: 1533-4406. DOI: 10.1056/NEJMoa1505489. URL: https://www.ncbi.nlm.nih.gov/pubmed/26321103 (cited on page 129).

[381] Q. V. Duong et al. "Calcium overload decreases net free radical emission in cardiac mitochondria". In: *Mitochondrion* 51 (2020), pages 126–139. ISSN: 1872-8278. DOI: 10.1016/j.mito.2020.01.005. URL: https://www.ncbi.nlm.nih.gov/pubmed/31982614 (cited on page 130).

[382] L. C. Wollenman et al. "The effect of respiration buffer composition on mitochondrial metabolism and function". In: *PLoS One* 12.11 (2017), e0187523. ISSN: 1932-6203 (Electronic) 1932-6203 (Linking). DOI: 10.1371/journal.pone.0187523. URL: https://www.ncbi.nlm.nih.gov/pubmed/29091971 (cited on page 133).

[383] A. Daina, O. Michielin, and V. Zoete. "SwissTargetPrediction: updated data and new features for efficient prediction of protein targets of small molecules". In: *Nucleic Acids Res* 47.W1 (2019), W357–W364. ISSN: 1362-4962. DOI: 10.1093/nar/gkz382. URL: https://www.ncbi.nlm.nih.gov/pubmed/31106366 (cited on pages 140, 142, 143).

[384] D. H. Maurice et al. "Advances in targeting cyclic nucleotide phosphodiesterases". In: *Nat Rev Drug Discov* 13.4 (2014), pages 290–314. ISSN: 1474-1784. DOI: 10.1038/nrd4228. URL: https://www.ncbi.nlm.nih.gov/pubmed/24687066 (cited on pages 142, 144, 145).

[385] A. T. Bender and J. A. Beavo. "Cyclic nucleotide phosphodiesterases: molecular regulation to clinical use". In: *Pharmacol Rev* 58.3 (2006), pages 488–520. ISSN: 0031-6997.

DOI: 10.1124/pr.58.3.5. URL: https://www.ncbi.nlm.nih.gov/pubmed/16968949 (cited on page 142).

[386] D. Liu et al. "PDE2 regulates membrane potential, respiration and permeability transition of rodent subsarcolemmal cardiac mitochondria". In: *Mitochondrion* 47 (2019), pages 64–75. ISSN: 1872-8278. DOI: 10.1016/j.mito.2019.05.002. URL: https://www.ncbi.nlm.nih.gov/pubmed/31100470 (cited on pages 142–144).

[387] R. Acin-Perez et al. "Cyclic AMP produced inside mitochondria regulates oxidative phosphorylation". In: *Cell Metab* 9.3 (2009), pages 265–76. ISSN: 1932-7420. DOI: 10.1016/j.cmet.2009.01.012. URL: https://www.ncbi.nlm.nih.gov/pubmed/19254571 (cited on pages 143, 144).

[388] M. Folkmanaite and M. Zaccolo. "Regulation of cardiac function by cyclic AMP nanodomains". In: *Biosci Rep* 43.2 (2023). ISSN: 1573-4935 (Electronic) 0144-8463 (Print) 0144-8463 (Linking). DOI: 10.1042/BSR20220953. URL: https://www.ncbi.nlm.nih.gov/pubmed/36749130 (cited on page 143).

[389] D. Mika et al. "Synergic PDE3 and PDE4 control intracellular cAMP and cardiac excitation-contraction coupling in a porcine model". In: *J Mol Cell Cardiol* 133 (2019), pages 57–66. ISSN: 1095-8584. DOI: 10.1016/j.yjmcc.2019.05.025. URL: https://www.ncbi.nlm.nih.gov/pubmed/31158360 (cited on pages 143, 144).

[390] S. Monterisi et al. "PDE2A2 regulates mitochondria morphology and apoptotic cell death via local modulation of cAMP/PKA signalling". In: *Elife* 6 (2017). ISSN: 2050-084X. DOI: 10.7554/eLife.21374. URL: https://www.ncbi.nlm.nih.gov/pubmed/28463107 (cited on page 144).

[391] H. Mehel et al. "Phosphodiesterase-2 is up-regulated in human failing hearts and blunts beta-adrenergic responses in cardiomyocytes". In: *J Am Coll Cardiol* 62.17 (2013), pages 1596–606. ISSN: 1558-3597. DOI: 10.1016/j.jacc.2013.05.057. URL: https://www.ncbi.nlm.nih.gov/pubmed/23810893 (cited on page 144).

[392] H. Huang et al. "Rolipram, a PDE4 Inhibitor, Enhances the Inotropic Effect of Rat Heart by Activating SERCA2a". In: *Front Pharmacol* 10 (2019), page 221. ISSN: 1663-9812. DOI: 10.3389/fphar.2019.00221. URL: https://www.ncbi.nlm.nih.gov/pubmed/30967774 (cited on page 144).

[393] E. Amsallem et al. "Phosphodiesterase III inhibitors for heart failure". In: *Cochrane Database Syst Rev* 2005.1 (2005), page CD002230. ISSN: 1469-493X. DOI: 10.1002/14651858.CD002230.pub2. URL: https://www.ncbi.nlm.nih.gov/pubmed/15674893 (cited on page 144).

[394] M. A. Movsesian and R. C. Kukreja. “Phosphodiesterase inhibition in heart failure”. In: *Handb Exp Pharmacol* 204 (2011), pages 237–49. ISSN: 0171-2004. DOI: 10.1007/978-3-642-17969-3_10. URL: https://www.ncbi.nlm.nih.gov/pubmed/21695643 (cited on page 144).

[395] G. Griebel et al. “The selective GSK3 inhibitor, SAR502250, displays neuroprotective activity and attenuates behavioral impairments in models of neuropsychiatric symptoms of Alzheimers disease in rodents”. In: *Sci Rep* 9.1 (2019), page 18045. ISSN: 2045-2322 (Electronic) 2045-2322 (Linking). DOI: 10.1038/s41598-019-54557-5. URL: https://www.ncbi.nlm.nih.gov/pubmed/31792284 (cited on page 145).

[396] S. M. Arciniegas Ruiz and H. Eldar-Finkelman. “Glycogen Synthase Kinase-3 Inhibitors: Preclinical and Clinical Focus on CNS-A Decade Onward”. In: *Front Mol Neurosci* 14 (2021), page 792364. ISSN: 1662-5099 (Print) 1662-5099 (Electronic) 1662-5099 (Linking). DOI: 10.3389/fnmol.2021.792364. URL: https://www.ncbi.nlm.nih.gov/pubmed/35126052 (cited on pages 145, 149).

[397] I. Sahin et al. “Glycogen synthase kinase-3 beta inhibitors as novel cancer treatments and modulators of antitumor immune responses”. In: *Cancer Biol Ther* 20.8 (2019), pages 1047–1056. ISSN: 1555-8576 (Electronic) 1538-4047 (Print) 1538-4047 (Linking). DOI: 10.1080/15384047.2019.1595283. URL: https://www.ncbi.nlm.nih.gov/pubmed/30975030 (cited on page 145).

[398] K. Yang et al. “The Key Roles of GSK-3-beta in Regulating Mitochondrial Activity”. In: *Cell Physiol Biochem* 44.4 (2017), pages 1445–1459. ISSN: 1421-9778 (Electronic) 1015-8987 (Linking). DOI: 10.1159/000485580. URL: https://www.ncbi.nlm.nih.gov/pubmed/29190615 (cited on page 145).

[399] A. Krishnankutty et al. “In vivo regulation of glycogen synthase kinase 3-beta activity in neurons and brains”. In: *Sci Rep* 7.1 (2017), page 8602. ISSN: 2045-2322 (Electronic) 2045-2322 (Linking). DOI: 10.1038/s41598-017-09239-5. URL: https://www.ncbi.nlm.nih.gov/pubmed/28819213 (cited on page 146).

[400] L. Gomez et al. “Inhibition of GSK3-beta by postconditioning is required to prevent opening of the mitochondrial permeability transition pore during reperfusion”. In: *Circulation* 117.21 (2008), pages 2761–8. ISSN: 1524-4539 (Electronic) 0009-7322 (Linking). DOI: 10.1161/CIRCULATIONAHA.107.755066. URL: https://www.ncbi.nlm.nih.gov/pubmed/18490522 (cited on page 146).

[401] R. Elkholi et al. “MDM2 Integrates Cellular Respiration and Apoptotic Signaling through NDUFS1 and the Mitochondrial Network”. In: *Mol Cell* 74.3 (2019), 452–465 e7. ISSN: 1097-4164 (Electronic) 1097-2765 (Print) 1097-2765 (Linking). DOI: 10.

1016/j.molcel.2019.02.012. URL: https://www.ncbi.nlm.nih.gov/pubmed/30879903 (cited on pages 146, 147).

[402] G. Arena et al. "Mitochondrial MDM2 Regulates Respiratory Complex I Activity Independently of p53". In: *Mol Cell* 69.4 (2018), 594–609 e8. ISSN: 1097-4164 (Electronic) 1097-2765 (Print) 1097-2765 (Linking). DOI: 10.1016/j.molcel.2018.01.023. URL: https://www.ncbi.nlm.nih.gov/pubmed/29452639 (cited on page 147).

[403] D. H. Kwon et al. "Regulation of MDM2 E3 ligase-dependent vascular calcification by MSX1/2". In: *Exp Mol Med* 53.11 (2021), pages 1781–1791. ISSN: 2092-6413 (Electronic) 1226-3613 (Print) 1226-3613 (Linking). DOI: 10.1038/s12276-021-00708-6. URL: https://www.ncbi.nlm.nih.gov/pubmed/34845330 (cited on page 147).

[404] H. Kim et al. "Alpha Lipoic acid attenuates vascular calcification via reversal of mitochondrial function and restoration of Gas6/Axl/Akt survival pathway". In: *J Cell Mol Med* 16.2 (2012), pages 273–86. ISSN: 1582-4934 (Electronic) 1582-1838 (Print) 1582-1838 (Linking). DOI: 10.1111/j.1582-4934.2011.01294.x. URL: https://www.ncbi.nlm.nih.gov/pubmed/21362131 (cited on page 147).

[405] R. P. Verma and C. Hansch. "Matrix metalloproteinases (MMPs): chemical-biological functions and (Q)SARs". In: *Bioorg Med Chem* 15.6 (2007), pages 2223–68. ISSN: 0968-0896 (Print) 0968-0896 (Linking). DOI: 10.1016/j.bmc.2007.01.011. URL: https://www.ncbi.nlm.nih.gov/pubmed/17275314 (cited on page 147).

[406] H. S. Sood, M. J. Cox, and S. C. Tyagi. "Generation of nitrotyrosine precedes activation of metalloproteinase in myocardium of hyperhomocysteinemic rats". In: *Antioxid Redox Signal* 4.5 (2002), pages 799–804. ISSN: 1523-0864 (Print) 1523-0864 (Linking). DOI: 10.1089/152308602760598954. URL: https://www.ncbi.nlm.nih.gov/pubmed/12470508 (cited on page 147).

[407] D. B. Zorov et al. "ROS-induced ROS release: a new phenomenon accompanying induction of the mPTP in cardiac myocytes". In: *J Exp Med* 192.7 (2000), pages 1001–14. ISSN: 0022-1007 (Print) 1540-9538 (Electronic) 0022-1007 (Linking). DOI: 10.1084/jem.192.7.1001. URL: https://www.ncbi.nlm.nih.gov/pubmed/11015441 (cited on page 148).

[408] Q. V. Duong et al. "Identifying Site-Specific Superoxide and Hydrogen Peroxide Production Rates From the Mitochondrial Electron Transport System Using a Computational Strategy". In: *Function (Oxf)* 2.6 (2021), zqab050. ISSN: 2633-8823 (Electronic) 2633-8823 (Linking). DOI: 10.1093/function/zqab050. URL: https://www.ncbi.nlm.nih.gov/pubmed/35330793 (cited on page 152).

[409] E. Murphy et al. “Kinetics and regulation of the glutamate-aspartate translocator in rat liver mitochondria”. In: *J Biol Chem* 254.17 (1979), pages 8369–76. ISSN: 0021-9258 (Print) 0021-9258 (Linking). URL: https://www.ncbi.nlm.nih.gov/pubmed/38250 (cited on page 152).

[410] J. R. Williamson. “Mitochondrial function in the heart”. In: *Annu Rev Physiol* 41 (1979), pages 485–506. ISSN: 0066-4278 (Print) 0066-4278 (Linking). DOI: 10.1146/annurev.ph.41.030179.002413. URL: https://www.ncbi.nlm.nih.gov/pubmed/373602 (cited on page 152).

Appendix A

Chapter 3 Supplemental Information

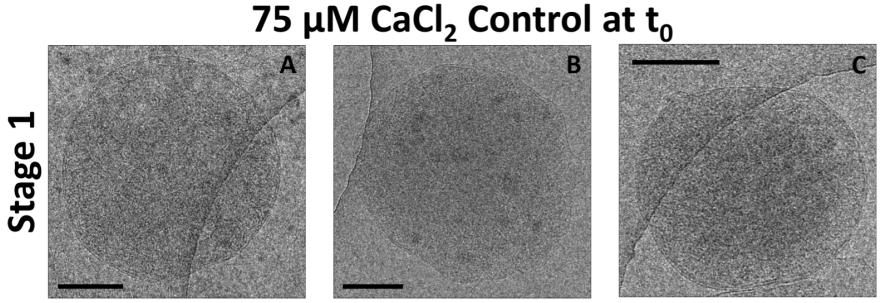

Figure A.1: Mitochondrial membrane morphology in the absence of calcium overload. Representative images before the addition of calcium in the absence of CsA. (A-C) Mitochondria are round with the outer and inner membrane clearly visible. In some instances, small calcium phosphate granules are observed. Granules form after mitochondria take up contaminate calcium. Samples were collected at t0 as described in **Figure 3.3**. Scale bars are 250 nm.

Respirometry analyses were performed to compare the effects of two calcium boluses (75 µM and 100 µM) on control and CsA groups. For each bolus, the control and CsA groups had a sample size of 3, resulting in a total of 6 observations.

A Levene's test was conducted for each bolus to assess the equality of variances between the two groups. The results indicated that there was no significant difference in variances between the control and CsA groups for both boluses (75 µM: $F(1,4) = 1.2966$, $p = 0.3184$ greater than $\alpha = 0.01$; 100 µM: $F(1,4) = 1.04$, $p = 0.3655$ greater than $\alpha = 0.01$), suggesting that the assumption of homogeneity of variances was met for both analyses.

A two-sample t-test with pooled variance was conducted for each bolus to compare the means of the control and CsA groups. For the 75 µM bolus, the t-test yielded a significant

result (t(4) = -9.3341, p = 0.0007334), indicating that there was a significant difference in means between the two groups. The effect size was large (Cohen's d = 7.62). For the 100 µM bolus, the t-test also yielded a significant result (t(4) = -19.6372, p = 0.00003966), indicating a significant difference in means between the two groups. The effect size was large (Cohen's d = 16.03). These findings are summarized below.

75 μM $CaCl_2$		**100 μM $CaCl_2$**	
Control	**CsA**	**Control**	**CsA**
59.67 (30.37)	536.41 (83.09)	31.00 (7.87)	451.01 (36.20)
Levene's test F(1,4) = 1.30 p = 0.318 Cohen's d = 7.62	t-test t(4) = -9.33 p = 0.0007	Levene's test F(1,4) = 1.04 p = 0.366 Cohen's d = 16.03	t-test t(4) = -19.64 p = 0.00004

Table A.1: T-test Results from the Respirometry Data Between Control and CsA-treated mitochondria.

To evaluate the impact of calcium overload on mitochondrial respiration, the average maximal respiration values of three independent samples were compared between control and CsA-treated samples after the addition of ADP. This approach provided a reliable measure of mitochondrial function, with values obtained from the trace around 2-3 minutes after the addition of ADP.

At 75 and 100 µM $CaCl_2$, the CsA-treated mitochondria achieved an average maximal respiration of 536.41 and 451.01 nmol O_2/mg mitochondrial protein/min, respectively, as shown in **Table A.1**. To determine the percentage of respiration activity in the control group compared to the CsA-treated samples in the presence of 75 µM or 100 µM $CaCl_2$ additions, the average maximal respiration values for the control group were divided by the average CsA maximal respiration in the presence of 75 µM or 100 µM $CaCl_2$ and then multiplied by 100. The standard deviation was calculated from the resulting values and

multiplied by 100.

The analysis revealed that for the 75 µM $CaCl_2$ addition, the control group displayed 11.12 % (mean) ± 4.63 % (stdev) of the maximal respiration activity in the CsA-treated group. For the 100 µM $CaCl_2$ addition, the control group displayed 6.87 % ± 1.42 %. These findings suggest that calcium overload can significantly impact mitochondrial respiration and that CsA partially protects mitochondrial function.

A Kolmogorov-Smirnov test was performed to compare calcium phosphate deposit number, size, and mitochondrion size between control and CsA. Table A.2 shows a comparison of these variables, summarizing the p-values, Kolmogorov-Smirnov (KS) statistics, and significance level for each comparison.

The results show that significant differences were observed between Ctrl and CsA at certain time points and calcium concentrations. Specifically, significant differences were observed for calcium phosphate deposit number and size at t0 for 75 µM $CaCl_2$, and at t1 and t3 for 100 µM $CaCl_2$. No significant differences were observed at t3 for 75 µM $CaCl_2$.

For mitochondrion size, significant differences were observed between Ctrl and CsA at t0 and t3 for 75 µM $CaCl_2$, and at t3 for 100 µM $CaCl_2$. No significant differences were observed at t1 for 100 µM $CaCl_2$.

These results suggest that CsA has significant effects on calcium phosphate deposit number and size, as well as mitochondrion size, at certain time points and calcium concentrations. However, one limitation of this study is the small sample size for the control group at t3 due to mitochondrial permeabilization, which may limit the generalizability of the findings. A summary of these results is provided below.

	Calcium Phosphate Deposit Number			
	Ctrl	CsA	Ctrl	CsA
$CaCl_2$ concentration	Time point	P-value	KS Stat	Significance ($\alpha \leq 0.01$)
75 µM	t0	0.006749677	0.354545455	significant
75 µM	t3	0.065134072	0.47972973	not significant
100 µM	t1	6.61E-08	0.764705882	significant
100 µM	t3	3.53E-10	0.987951807	significant

	Calcium Phosphate Deposit Size (nm)			
	Ctrl	CsA	Ctrl	CsA
$CaCl_2$ concentration	Time point	P-value	KS Stat	Significance ($\alpha \leq 0.01$)
75 µM	t0	0.006749677	0.354545455	significant
75 µM	t3	0.065134072	0.47972973	not significant
100 µM	t1	8.81E-06	0.647058824	significant
100 µM	t3	0.000300993	0.618473896	significant

	Mitochondrion Size (nm)			
	Ctrl	CsA	Ctrl	CsA
$CaCl_2$ concentration	Time point	P-value	KS Stat	Significance ($\alpha \leq 0.01$)
75 µM	t0	0.006749677	0.354545455	significant
75 µM	t3	0.065134072	0.47972973	not significant
100 µM	t1	0.037323497	0.367647059	not significant
100 µM	t3	0.006649247	0.497991968	significant

Table A.2: Comparison of Calcium Phosphate Deposit Number, Size, and Mitochondrion Size between Ctrl and CsA.

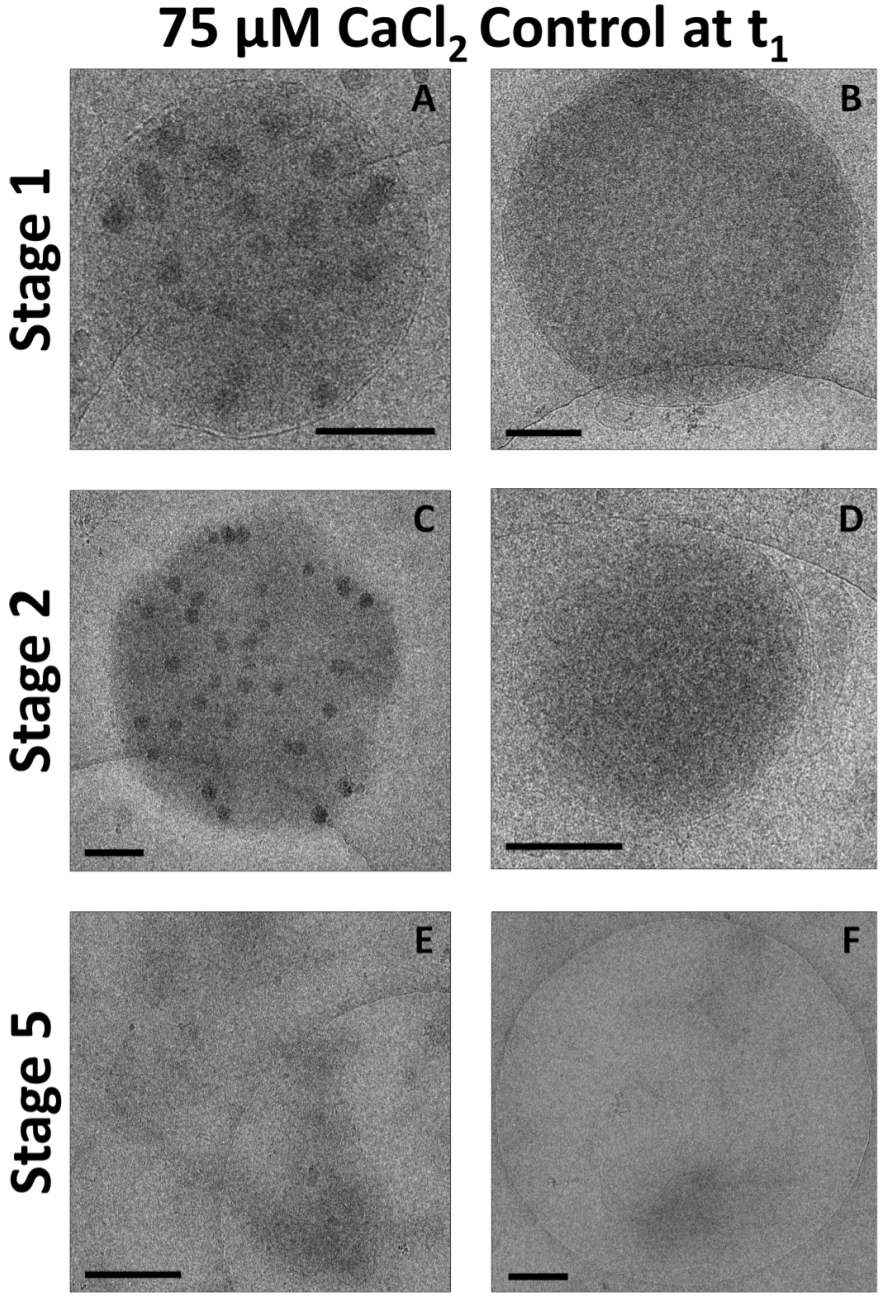

Figure A.2: Calcium uptake leads to the formation of large calcium phosphate granules, fragmentation the inner mitochondrial membrane, and rupture of the outer membrane Representative images of 1.5 mins (t1) after the addition of a 75 µM $CaCl_2$ bolus. (A and B) Mitochondria with preserved inner and outer membranes observed. (C and D) The beginning of mitochondrial fragmentation caused by calcium overload. (E and F) Absence of outer membrane with fragmented inner membranes. Scale bars are 250 nm.

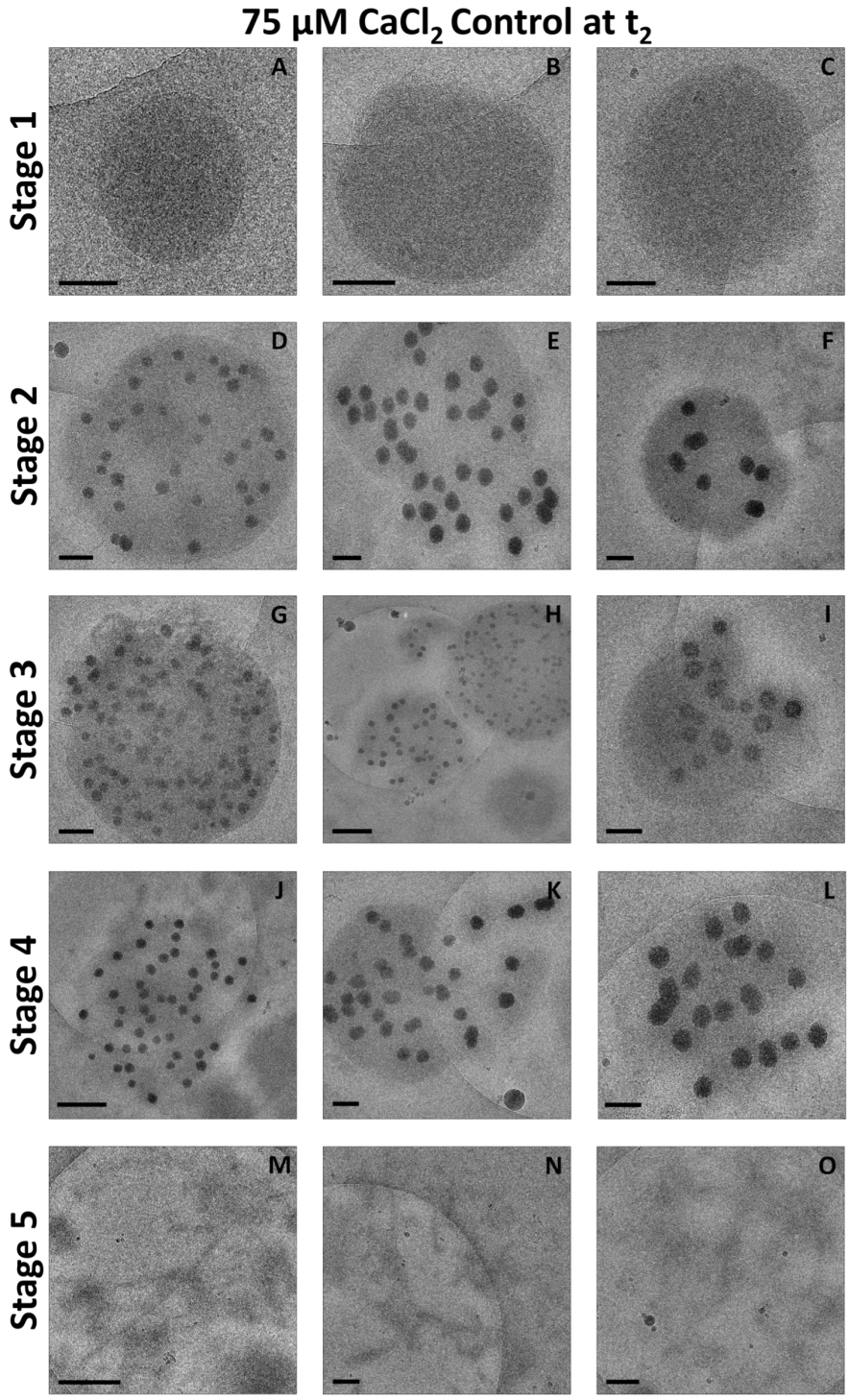

Figure A.3: Calcium accumulation induces localized ruptures of the outer membrane and complete mitochondrial fragmentation. Representative images of 4 mins (t2) after the addition of a 75 µM calcium chloride bolus. (A-D) Defined inner and outer membranes with granules present or absent. (D-F) Loss of outer membrane integrity. (G-I) Loss of the outer membrane begins initiating inner membrane fragmentation. (J-L) Complete loss of outer membrane with preserved granules. (M-O) Complete loss of inner and outer membranes. In this stage, the inner membrane is severely compromised and unable to maintain a membrane potential. Scale bars are 250 nm.

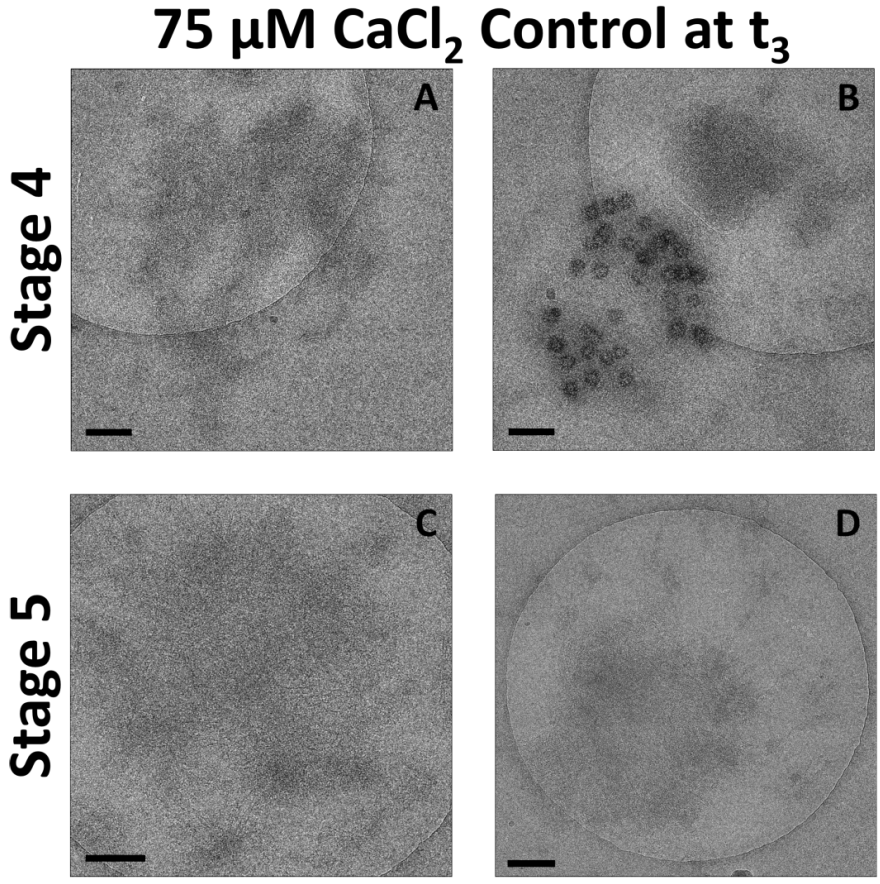

Figure A.4: Massive calcium overload results in severe mitochondrial fragmentation. Representative images of 10 mins (t3) after the addition of a 75 µM calcium chloride bolus. (A-B) Only a few mitochondria with clearly visible granules were observed. (C-D) The vast majority of images showed mitochondria that were partially or completely fragmented. Scale bars are 250 nm.

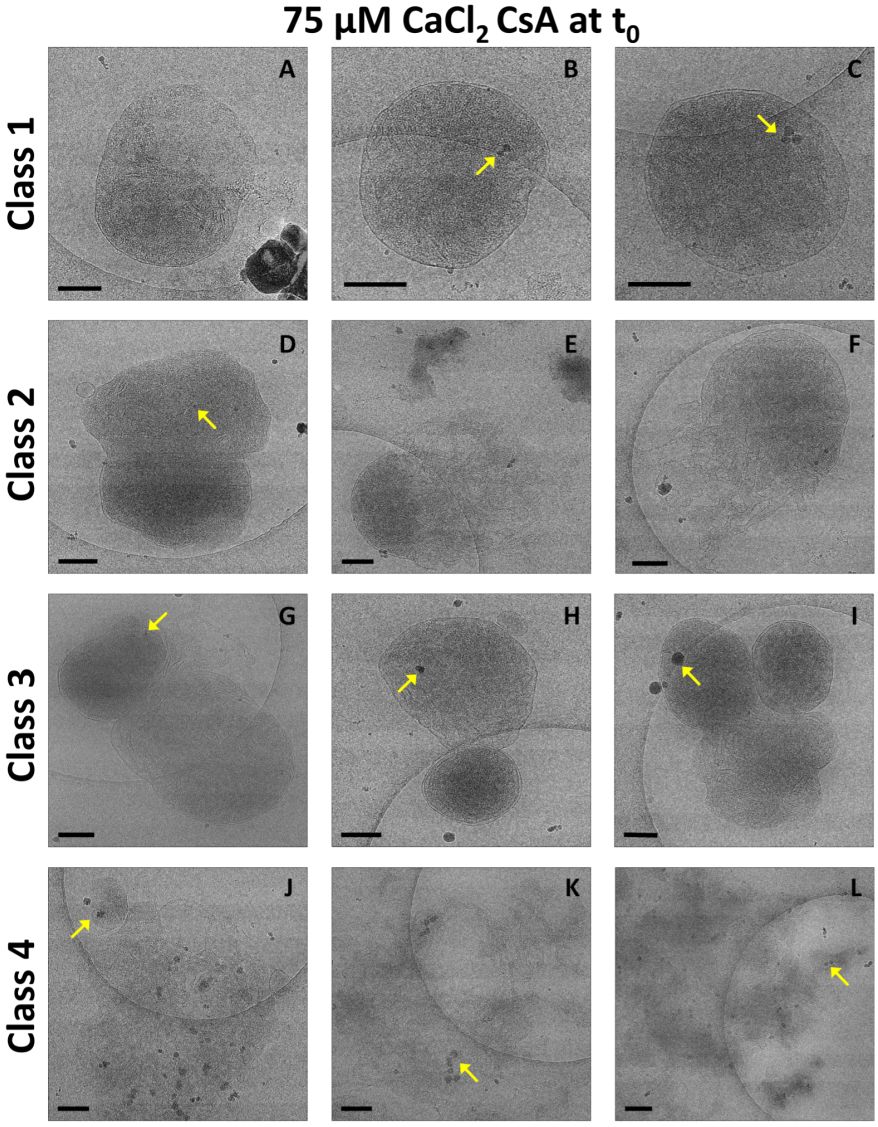

Figure A.5: CsA disrupts the outer membrane morphology, causes release of the inner membrane and tends to form mitochondrial clusters. Representative images before the addition of a 75 µM calcium bolus (t0) in the presence of 1 µM CsA. Mitochondria were energized with 5 mM sodium pyruvate and 1 mM L-malate. (A-C) CsA induced morphological changes in the outer mitochondrial membrane. There are mitochondria with calcium phosphate granules present as shown by the arrows. (D-F) While in others the inner membrane is released. (G-I) Clusters of mitochondria are commonly observed with treatment. (J-L) In some mitochondria, the outer membrane is completely lost. Scale bars are 250 nm.

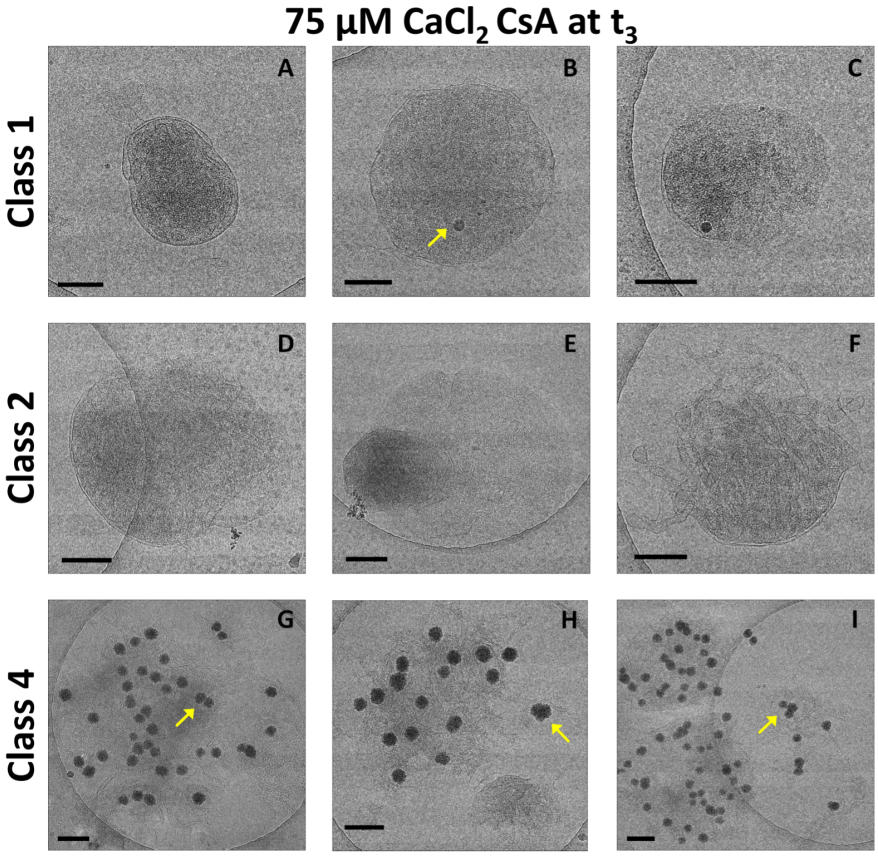

Figure A.6: In the presence of moderate calcium overload, CsA preserves inner mitochondrial membrane intactness. Representative images 10 mins after the addition of a 75 µM calcium bolus (t3) in the presence of 1 µM CsA. (A-C) Mitochondria with or without granules with defined inner and outer membranes. (D-F) There are mitochondria with visible cristae ejecting the inner membrane. (G-I) After losing the outer membrane, mitochondria spread the inner membrane across the carbon grid. Only 2 micrographs were found in clusters by the time point. However, the presence of mitochondria with unraveled inner membranes in the presence or absence of granules were increased at this time point. Scale bars are 250 nm. Arrows are pointing granules within the mitochondria.

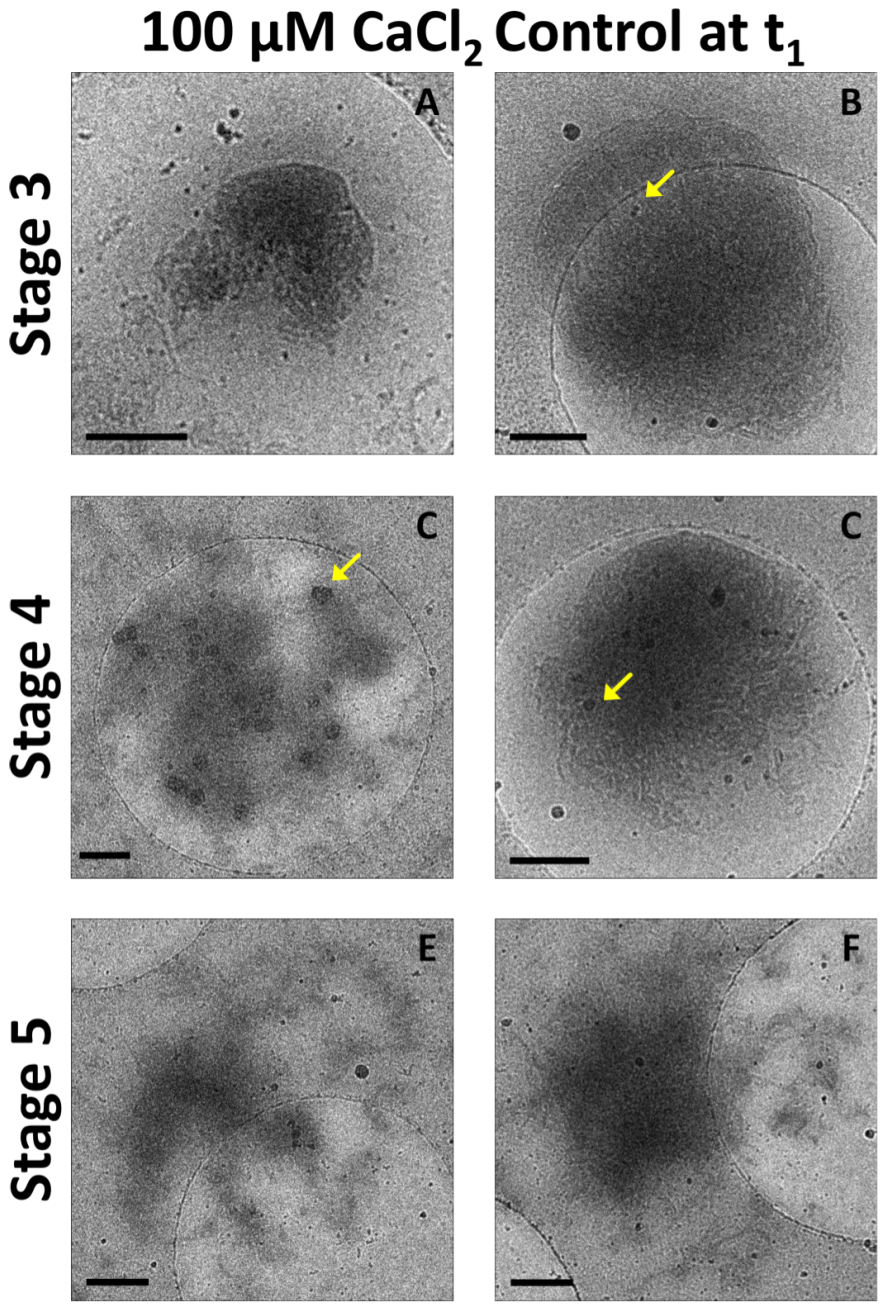

Figure A.7: Mitochondrial morphology is severely compromised and occurs more rapidly at greater calcium loads. Representative images from isolated mitochondria (0.1 mg/ml) acquired 1.5 mins (t1) after the addition of a 100 µM calcium chloride bolus. Most of the mitochondria were permeabilized under such high calcium load conditions. Only a few stages were identified at this early time point suggesting that membrane fragmentation rapidly occurs. This data is confirmed by the absorbance data where large amplitude swelling was observed. The formation of granules is seen in multiple mitochondria. Scale bars are 250 nm. Arrows are pointing granules within the mitochondria.

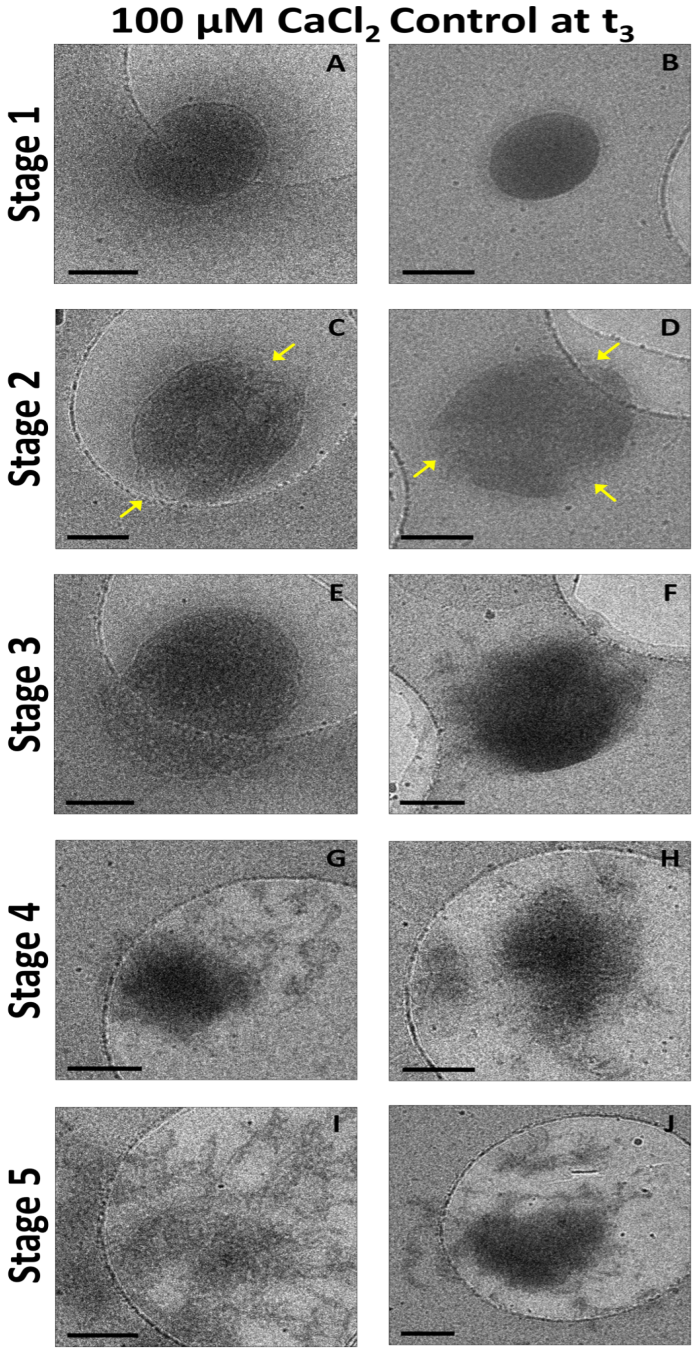

Figure A.8: Heterogeneous responses to high calcium loads leading to mitochondrial permeability transition. Representative images from isolated mitochondria (0.1 mg/ml) acquired 10 mins (t3) after the addition of a 100 µM calcium chloride bolus. There is a heterogeneous response in the mitochondrial population and multiple stages could be characterized despite being collected at this time-point. Some mitochondria displayed multiple regions of outer membrane rupture as shown by the arrows in stage 2. Scale bars are 250 nm.

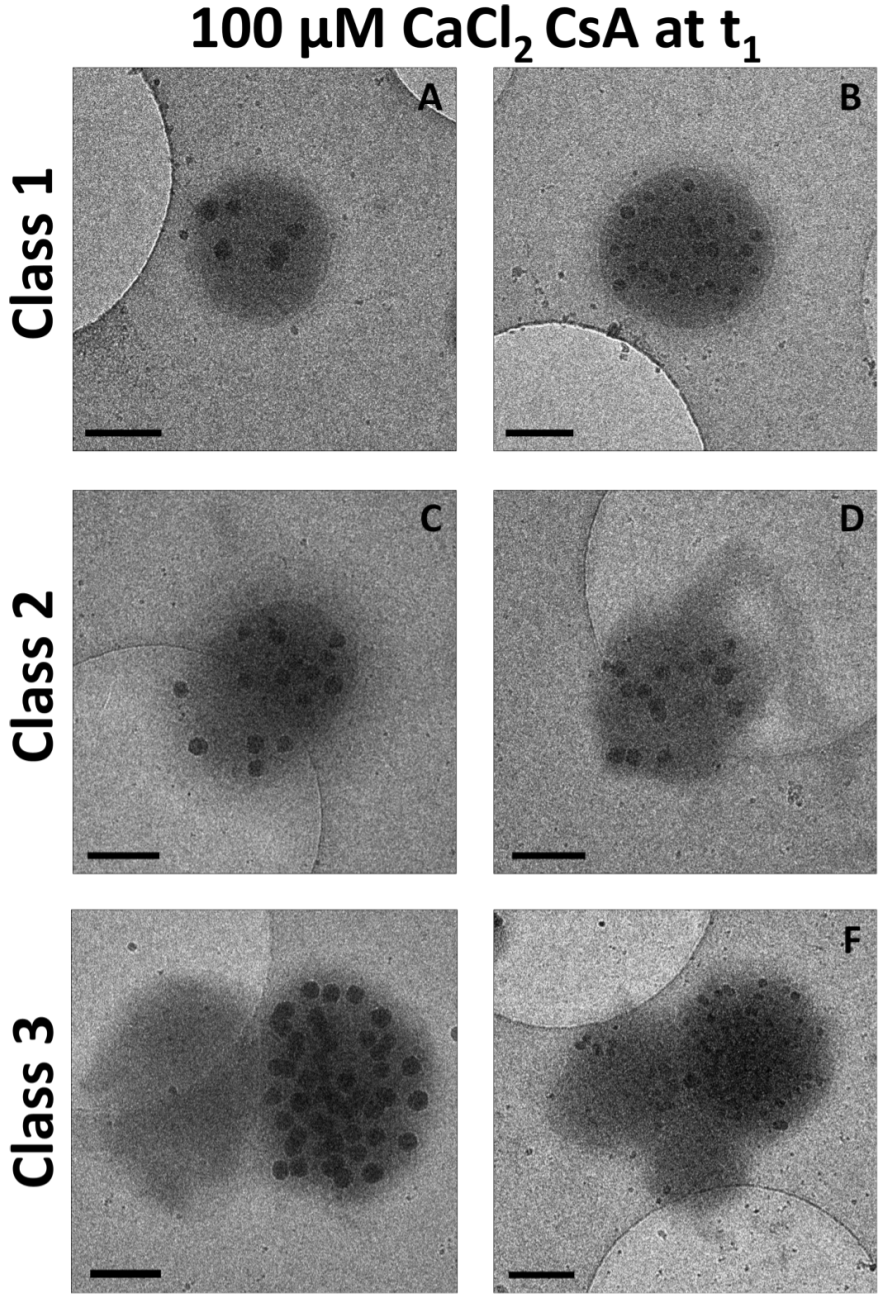

Figure A.9: In extreme calcium overload conditions, CsA preserves inner mitochondrial membrane intactness. Representative images before the addition of a 100 µM calcium bolus (t1) in the presence of 1 µM CsA. (A-B) The presence of calcium led to the formation of granules of various sizes varying between but not within mitochondrion. There is a heterogeneous response to the initial observed effect of CsA on membrane alterations. (C-D) The release of inner membrane is apparent in some mitochondrial micrographs. (E-F) While others show clusters of mitochondria as observed in the 75 µM calcium chloride bolus experiment. Scale bars are 250 nm.

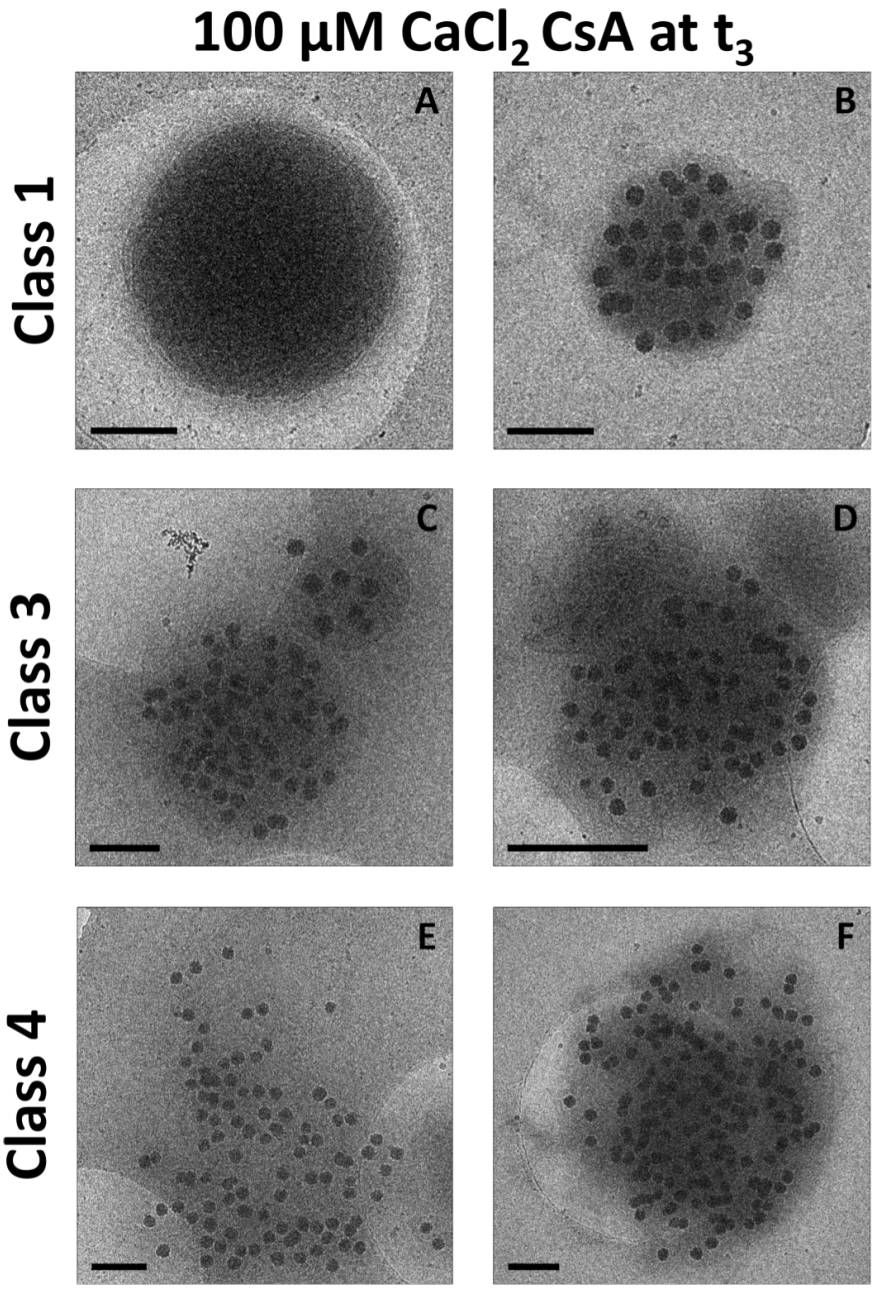

Figure A.10: Mitochondria remain functional at the highest calcium bolus in the presence of CsA. Representative images from isolated mitochondria (0.1 mg/ml) acquired 10 mins (t3) after the addition of a 100 µM calcium chloride bolus. (A-B) There is a heterogeneous response following the addition of a calcium bolus. (C-D) Mitochondrial clusters could be identified similar to the previous time points and calcium boluses in the presence of CsA treatment. (E-F) Also, mitochondria with protruded inner membranes without outer membranes were detected. Scale bars are 250 nm.

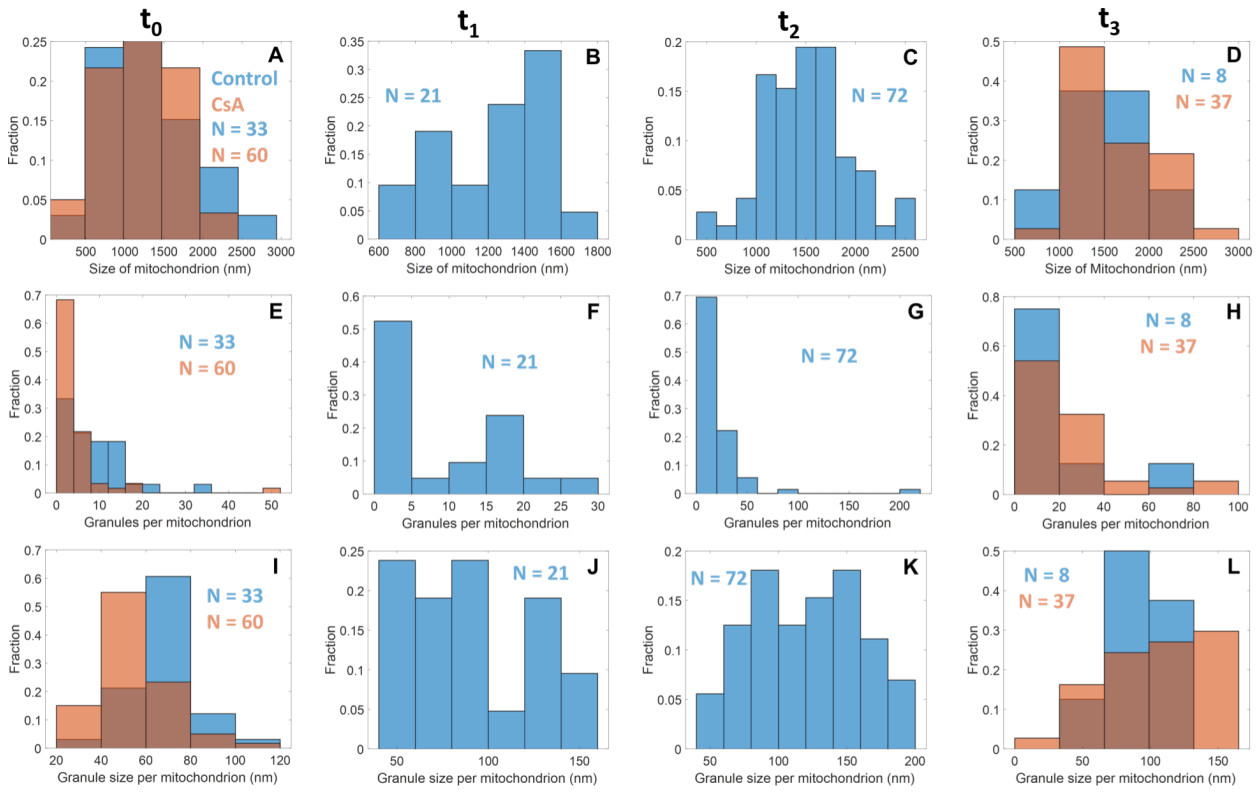

Figure A.11: CsA enhances the number and size of calcium phosphate granules per mitochondrion. The mitochondrial size, calcium phosphate granules size and number per mitochondrion were quantified for each time-point (t0 – t3) before and after the addition of a 75 µM calcium bolus in the presence or absence of CsA. (A) There are no differences in the mitochondrial size before the addition of calcium. (D) In contrast, CsA increased marginally their sizes. (E and I) Exposing the control mitochondrial suspension to calcium for longer periods increased the number and growth of granules. (H and L) However, 10 mins after the addition of calcium (t3) there is a marked decrease in size and number of granules suggesting mitochondrial fragmentation and permeabilization. Conversely, treated mitochondria developed granules of greater size and enhanced the number of granules per mitochondrion.

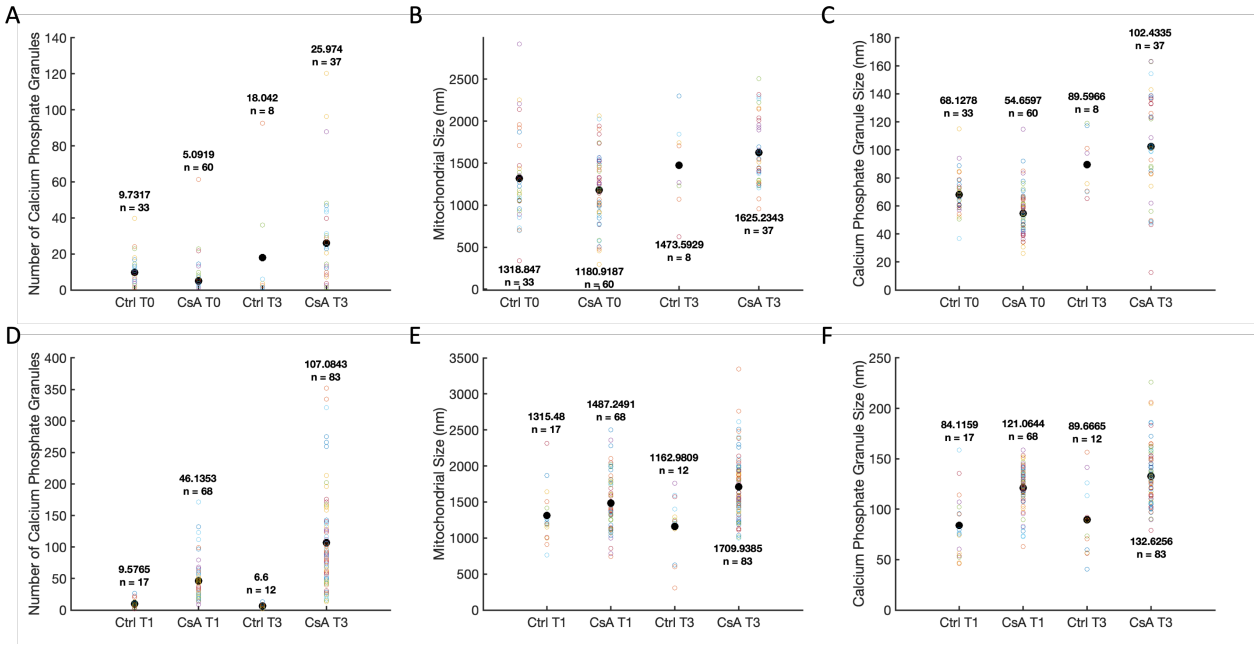

Figure A.12: A-C) Data corresponding to the 75 µM $CaCl_2$ condition. D-F) Data corresponding to the 100 uM $CaCl_2$ condition. The plotted data points represent the mean number of granules per mitochondrion for a given experimental condition. Each data point corresponds to the average value obtained from a set of individual observations. The black data point shown on top of each data set represents the mean value of the averaged points, and is accompanied by the corresponding "n" value which represents the number of mitochondria analyzed for that condition. This provides a visual representation of the distribution of data points around the mean, allowing for easy interpretation and comparison of the data between experimental conditions.

Appendix B

Chapter 5 Supplemental Information

Parameter	**Value**
P-value	0.08441
W	0.9647
Sample size (n)	59
Average ($\bar{x}$)	12.4547
Median	12.2587
Sample Standard Deviation (S)	2.8563
Sum of Squares	473.186
b	21.3652
Skewness	0.4147
Skewness Shape	0.183
Excess kurtosis	-0.2048
Kurtosis Shape	0.738

Table B.1: The Shapiro-Wilk was run using a normal distribution (right-tailed). The test did not showed a significance departure from the normality **Table B.1**. Since p-value is greater than α, the H_0 is accepted. Outliers were excluded using MATLAB default criteria of removing values more than three scaled median absolute deviations from the median. The p-value equals 0.08441. Hence, the chance of type I error (rejecting a correct H_0) is pretty high (8.44 %). The test statistic W falls within the region of acceptance (96 % out of 100 %).

Source	SS	df	MS	Prob >F
Groups	74.827	3	24.9423	0.0228
Error	398.359	55	7.2429	
Total	473.186	58		

Table B.2: The result of a One-way ANOVA. The p-value of 0.0228 suggested that there is a statistically significant difference among the means of the groups being compared.

Group 1	Group 2	$\bar{x}_{\text{diff}}$	SE	Lower CI	Upper CI
50 μM $CaCl_2$	25 μM $CaCl_2$	-1.0617	1.2396	3.5408	0.4882
50 μM $CaCl_2$	CsA	-3.2827	0.4085	2.4657	0.9816
50 μM $CaCl_2$	EGTA	-5.0040	2.0331	0.9378	0.2783
25 μM $CaCl_2$	CsA	-4.3317	1.6481	1.0356	0.3722
25 μM $CaCl_2$	EGTA	-6.0596	3.2727	-0.4857	0.0152
CsA	EGTA	-4.9007	1.6246	1.6515	0.5582

Table B.3: Results from Tukey-Kramer test after One-way ANOVA test to determine which groups are significantly different from each other. Results seemingly suggest that there's a statistical difference between the CsA and 50 μM $CaCl_2$ group with a p-value of 0.0237.

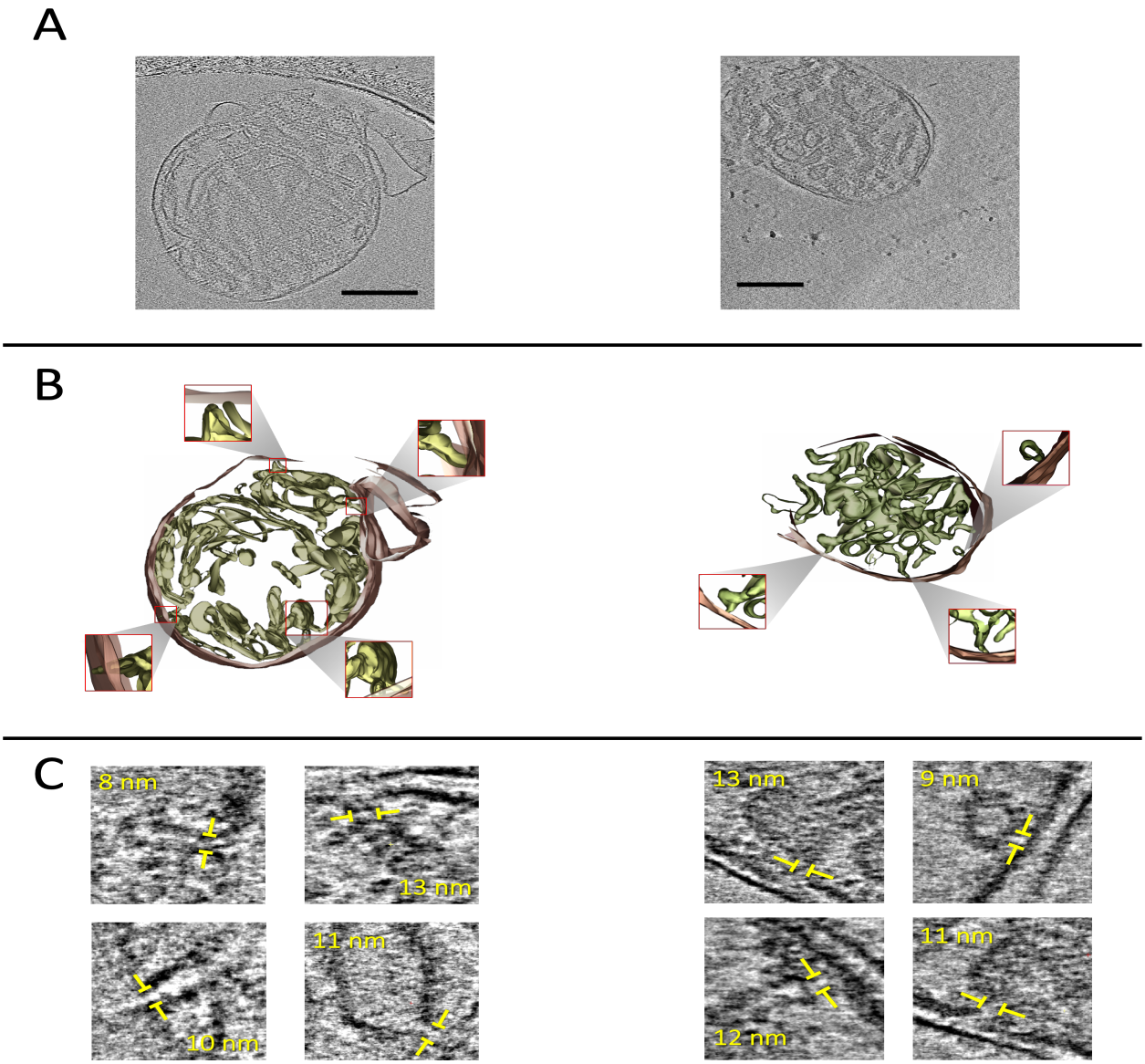

Figure B.1: CsA treated mitochondria. A) Representative micrographs with scale bars set at 250 nm. B) 3D reconstructed model showing the cristae junctions. C) Representative micrographs illustrating cristae junctions confined by the yellow regions.

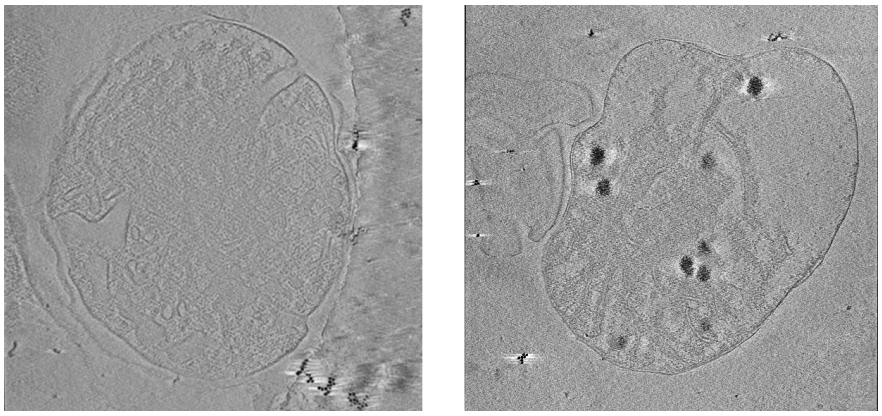

Figure B.2: Representative micrographs of two mitochondrion treated with EGTA (left) or a 50 μM $CaCl_2$ bolus of calcium (right) currently being 3D reconstructed.

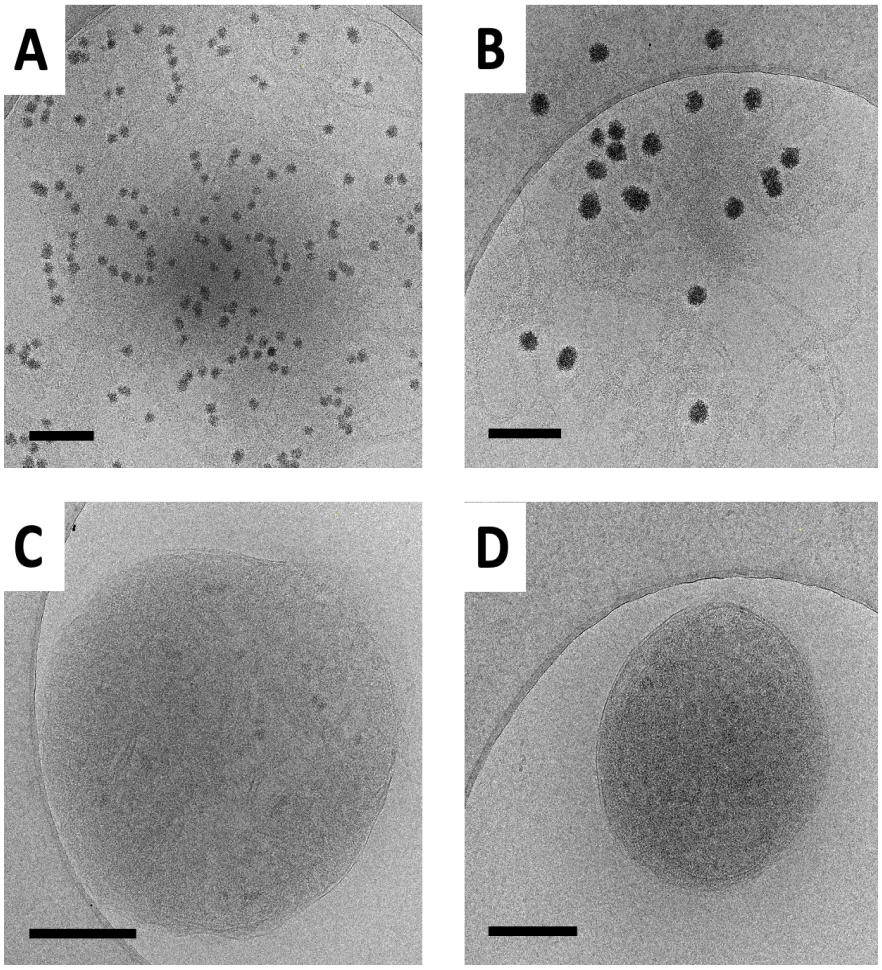

Figure B.3: CsA treatment altered the ultrastructure of the mitochondria following a 50 μM $CaCl_2$ bolus. The spread inner mitochondrial membrane can be observed across the carbon grid in panels A and B. However, in panels C and D, the outer membrane appears to be preserved. However, the matrix is very dense, making it difficult to appreciate key features like cristae, cristae junctions, and calcium phosphate granules. This makes CsA treated mitochondria with a 50 μM $CaCl_2$ bolus challenging to reconstruct in 3D space.

Appendix C

Chapter 7 Supplemental Information

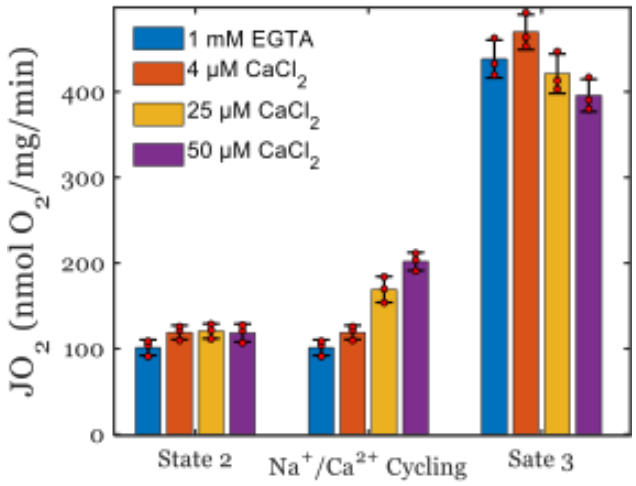

Figure C.1: Succinate supported ATP synthesis (State 3) is not affected by calcium overload. Mitochondria respiring on 10 mM succinate in the presence of 0.5 μM rotenone. Error bars represent the standard deviation for $n = 3$. The bar plots are the mean values and the dots represents the individual data points.

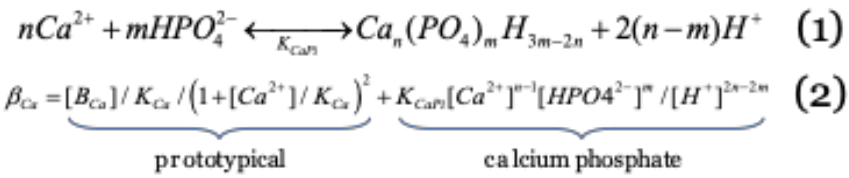

Figure C.2: Biochemical reaction explaining the formation of calcium phosphate complexes. Eq. 1 is a charge and atom balanced that works in multiple calcium phosphate species such as tricalcium phosphate, hydroxyapatite, and octacalcium phosphate. Using this reaction, a mathematical expression describing the mitochondrial calcium buffering power can be derived as shown in Eq. 2. In this equation, two components of calcium buffering are explicitly modeled. The first component consists of prototypical buffers that includes protein, lipid, metabolite, and other binding sites in the matrix. The second component consists of calcium phosphate complexes.

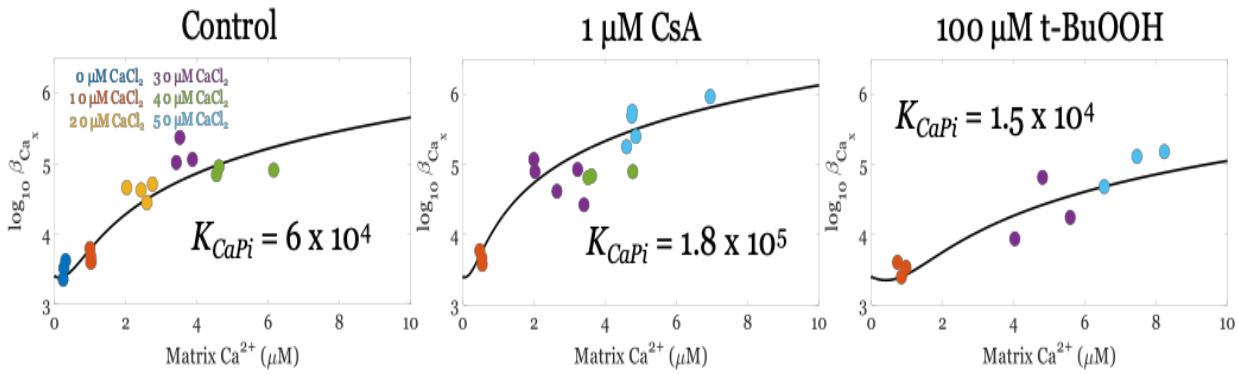

Figure C.3: CsA enhances mitochondrial calcium buffering while oxidative stress diminishes buffering. The mitochondrial calcium buffering power for the control is shown on the left. The Eq. 1 and 2 were obtained from the protocol described in Bazil et al [214]. In the middle, mitochondria were treated with 1 μM CsA. On the right, mitochondria were incubated in the presence of 100 μM tert-butyl hydroperoxide (t-BuOOH), a pro-oxidant. The parameter K_{CaPi} represents the strength of phosphate-dependent buffering. For the model predictions, K_{CaPi} is given in each panel with $[B_{Ca}]$ equal to 10 mM and K_{Ca} equal to 4 μM for all three conditions. The calcium:phosphate stoichiometry was fixed at 3:2.